VIBRATION CONTROL OF CONTINUOUS SYSTEMS
USING BOUNDARY CONSTRAINT

By

Assaad Awad Abbass

A DISSERTATION

Submitted to
Michigan State University
in partial fulfillment of the requirements
for the degree of

DOCTOR OF PHILOSOPHY

Mechanical Engineering

2012

ABSTRACT

VIBRATION CONTROL OF CONTINUOUS SYSTEMS USING BOUNDARY CONSTRAINT

By

Assaad Awad Abbass

Vibration suppression in continuous systems, namely strings and membranes, using boundary constraints was investigated. A problem of string vibration, where the string is subjected to a fixed boundary constraint, is studied first. The boundary constraint is in the form of a smooth obstacle and the string is assumed to wrap and unwrap around the obstacle during vibration. Assuming that wrapping of the string around the obstacle results in loss of kinetic energy due to inelastic collision and unwrapping conserves energy, the behavior of the string was investigated for different modes of oscillation and different obstacle shapes. The loss of energy is found to be greater for higher modes of oscillation and for obstacles that induce greater length of wrapping. Next, the vibration of the string subjected to a moving constraint near one boundary is investigated. The constraint is applied by a scabbard, which moves a small distance along the mean position of the string. The constraint is removed by moving the scabbard back to its original position and the change in energy of the string is investigated for different values of scabbard travel distance and time of application of the constraint. Unlike the fixed obstacle at the boundary, simulation results show that the energy of the string can increase or decrease depending on the time of application of the constraint. Based of this finding, a semi-active control strategy is proposed for vibration suppression. The control strategy is verified experimentally by substituting the scabbard-like actuator by a pair of solenoids. The experimental results show good match with results obtained through simulations. The control strategy developed for the string is extended to a circular

membrane. It is assumed that the membrane is fixed at its outer boundary and a zero displacement circular areal constraint is sequentially applied and removed. To investigate the effect of constraint application and removal on the energy of the membrane, the dynamics of constrained membranes is investigated. For arbitrary size and location of the constraint, the orthogonality of distinct modes is mathematically established and a procedure for accurate computation of the eigenfrequencies and mode shapes is presented. Assuming that the constraint is applied and removed instantaneously at arbitrary time intervals, the change in total energy is investigated for different sizes and locations of the constraint and for different times of application of the constraint. Similar to the vibrating string with the scabbard-like actuator, the results show that energy of the membrane can decrease or increase depending on the time of application of the constraint. Three different semi-active control strategies are presented to the vibration suppression of circular membrane. These control strategies have the potential for use in large space structures where high dimensional tolerances are required.

“ *The wind gasps with the midday heat,*
Like a nightmare in the late afternoon
And on the masts, it continues to fold, to spread for departure
The gulf is crowded with them–laborers roaming the seas
Barefoot, half-naked
And on the sand, by the gulf
A stranger sat–a baffled vision wanders the gulf
Destroying the pillars of light with the rising wail
Higher than the torrents roaring foam, than the clamor
A voice thunders in the abyss of my bereaved soul: Iraq
Like the crest rising, like a cloud, like tears to the eyes
The wind cries to me: Iraq
The wave howls at me: Iraq. Iraq. Nothing but Iraq
The sea is as wide as can be, and you are as distant
The sea is between you and me: Oh Iraq“

A Stranger by the Gulf: by Badr Shakir Al-Sayyab (1953)

To my family and my home country Iraq

ACKNOWLEDGMENTS

In the name of Allah, the Most Gracious and the Most Merciful, all praises to Allah for the strengths and His blessing in completing this work. I would like to express my most sincere gratitude to my advisor, Prof. Ranjan Mukherjee for his excellent guidance, consistent encouragement, I am greatly indebted to him for his invaluable inspiration. Special thanks go to Prof. Alejandro R. Diaz , Prof. Hassan Khalil and Prof. Steven W. Shaw for their willingness of being in my committee members despite their busy schedules. Also, I would like to thank my friends in the control lab for their help and support.

My gratitude extends to my parents for their support and encouragement. Their prayers for me during the course of this study have brought many blessings into my life. Special gratitude and appreciation are expressed to my family for their patience and support during my study. Last but not least, I also would like to thank my uncle Jawad Al-Sahlani and my two uncles families in United States for their help and support during my study.

TABLE OF CONTENTS

LIST OF TABLES

LIST OF FIGURES

Chapter 1

Introduction

1.1 Motivation and Objectives

The suppression of undesired vibration in industrial and engineering applications has been a fertile field of research for decades. Vibration occurs in structures when they are subjected to disturbances, regardless of the size of the structure. Some structures are huge such as bridges and skyscrapers whereas others structures are tiny such as MEMS devices and nano scale systems. To study vibration in mechanical systems, the systems are often modeled as discrete systems with finite degrees of freedom. For some other applications, the mechanical vibration occurs in systems that have infinite degrees of freedom, such systems are called *continuous systems*. Examples of continuous systems are strings, beams, plates and membranes which are widely used in many engineering applications such as space structures. In space applications, the weight and size play a crucial role in the cost of transportation and deployment. For this reason, aerospace companies prefer to use light weight flexible continuous systems as a substitute to heavier and rigid elements. For instance, the regular space telescope rigid mirrors are now substituted by thin deployable membrane mirrors that are much lighter in weight. The same is true for satellite antennas where large and lightweight inflatable antennas, as shown in Fig. 1.1, are replacing regular antennas. The new lightweight antennas are functionally efficient and can be folded into significantly smaller volume [4]. Although lightweight deployable structures have low cost transportation and deployment, they are prone to disturbances.

In general, vibration in continuous systems can be suppressed passively by changing the mass or stiffness in the systems, or actively, by sensing the states of the system and using feedback control. Passive control methods are not very effective and are not well suited for many applications. Active control methods are effective but they require many sensing and actuators complicated sensing and actuating mechanisms and complex mathematical models to compute the control effort. In this work, we present semi-control strategies to suppress the vibration in continuous systems namely, strings and circular membranes using boundary constraints. First, we investigate the energetics of string wrapping and unwrapping around fixed obstacle located at one of the boundaries where the obstacle represents a passive mechanism. Second, we present semi-active control strategy to suppress the vibration in string using a scabbard-like actuator that interacts with string near one of its boundaries. We present experimental verification to the control strategy based on the scabbard-like actuator control strategy. Third, we extend our semi-active control strategy to vibrating circular membranes. We use a small circular areal constraint that is applied sequentially on the membrane to suppress the vibration. We present the complete mathematical solution of the dynamic and energetics of circular membrane subjected to eccentric areal constraint and different control strategies are presented to the vibration suppression of circular membrane.

Figure 1.1: The spartan 207 inflatable antenna, NASA [4] “For interpretation of the references to color in this and all other figures, the reader is referred to the electronic version of this dissertation“

1.2 Vibration Control of Strings

1.2.1 Passive Control of Vibrating Strings

The dynamics of vibrating strings has been a subject of study for a very long time but the motion of strings vibrating against obstacles appeared in the technical literature relatively recently. Early work on this problem can be credited to Citrini [5] who considered point-shaped obstacles. The element of string that comes in contact with point-shaped obstacles can be assumed to be massless and hence the energy of the string, in the absence of damping, was assumed to remain conserved. Amerio [6] investigated the motion of a string vibrating against a rigid wall, parallel to the position of the string at rest. The motion of the string in the presence of the unilateral constraint was posed as a problem in impact. The nature of the impact was assumed to be elastic and the problem was formulated based on conservation of energy of the string. A number of other researchers have also based their work on the premise of energy conservation of the string. These include Schatzman [7], who investigated the existence and uniqueness of solutions for concave obstacles and Haraux and Cabannes [8], who established almost-periodic nature of solutions for straight and fixed obstacles.

In 1982, Burridge et al. [9] investigated the vibration of the sitar, an Indian stringed instrument. The sitar differs from the Western stringed instruments in that the bridge across which the strings pass form a broad support, rather than a well-defined edge. During vibration, the sitar string wraps and unwraps around the gentle slope of the bridge and the length of the vibrating part of the string varies during oscillation [9]. Burridge et al. [9] modeled the impact of the string with the bridge as perfectly inelastic, discarding the assumption of energy conservation of the string. Subsequently, Bamberger and Schatzman [10] proved the existence of solutions which do not conserve energy with arbitrary obstacles and Ahn [11] claimed energy loss of the string vibrating against flat obstacles. In conformity with earlier work by Citrini [5], Ahn [11] also showed that energy remains conserved for highly-peaked obstacles. Other work on string vibration against obstacles includes discretization [12] and finite difference methods [13] for numerical simulation, and study of nonlinear effects of varying amplitude and gravity [14] on extensible and non-extensible cables. In our work we investigate the vibration of a string against an obstacle located at its boundary. Similar to the work by Burridge, et al. [9], we assume the string to wrap and unwrap around the obstacle during each oscillation. The impact of the string during wrapping is assumed to be perfectly inelastic and the obstacle is implicitly assumed to be convex. The assumption of convexity of the obstacle is both convenient and practical. Assuming that the string vibrates in a single mode at all times, it is shown that energy loss is higher for higher modes of oscillation.

1.2.2 Active Control of String vibration

Several methods have been proposed in the literature for actively controlling string vibration. Some of these methods involve direct physical interaction with the string, using point or distributed forces, for example. Other methods are less intrusive and are based on tension variation or boundary control. In our work we propose to use a scabbard-like actuator that imposes a zero-displacement constraint over some length of the string from one boundary. Although this particular approach has not been proposed earlier, several papers in the literature have explored fundamentally similar ideas. Early work by Dutt and Ramakrishna [15] investigated the application of a distributed control force to minimize the energy of a part of the string while maintaining the energy of the uncontrolled part at a desired level. The work was later extended [16] to investigate optimal positions and magnitudes of the control forces. In our approach, the scabbard is intended to reduce the energy of the overall system while dissipating the energy of a short length of the string. When the scabbard is removed, the energy of the uncontrolled portion of the string is redistributed over the entire length and thus cyclic application and removal of the scabbard can lead to gradual dissipation of the total energy of the string. This idea is derived from earlier work on finite degree-of-freedom systems [17, 18] and has similarities with the work by Hebrard and Henrot [19], where exponential decay in the total energy is achieved by subjecting a portion of the string to constant damping. The zero-displacement constraint enforced by the scabbard can be viewed as impulsive actuation and in this regard our approach is similar to the approach proposed by Myshkis [20].

The scabbard-like actuator proposed in this study essentially moves one boundary of the string in the axial direction. Although vibration control using a scabbard has not been proposed earlier, the effect of moving the boundary and varying the length of the string has been investigated [21]. It has been shown that reducing the length of the string can increase its energy through compression of the propagating waves. Many researchers have also investigated transverse boundary control of vibrating strings. Shahruz and Kurmaji [22] designed a controller for a nonlinear model of axially moving strings using vertical control forces at one support. Fung, et al. [23] proposed an exponentially stabilizing mass-damper-spring controller and Li, et al. [24] proposed boundary velocity feedback to stabilize a nonlinear model obtained using Hamilton's principle. Do and Pan [25] studied boundary control of flexible marine risers; the controller was designed using Lyapunov's direct method and backstepping [26], and implemented using a hydraulic actuator. Zhang, et al. [27] designed boundary controllers for a general class of nonlinear string-actuator systems; a nonlinear distributed parameter model was used to account for large amplitude displacement and the associated variation in tension. Other boundary control methods include, for example, wave control [28, 29], wave cancellation [30, 31], and active sinks [32]. While wave control is a general methodology, wave cancellation refers to control using a boundary force that prevents reflection of the wave and active sinks is a strategy to make vibration modes inactive by applying a control force at some distance from the source of excitation. Our method is fundamentally different in that a zero displacement constraint is applied at the boundary.

Although there are many theoretical studies on the active control of vibrating strings, experimental results on control of string vibration have been scarce. This can be partly attributed to the fact that traditional strings have high internal damping and do not lend themselves well to vibration control experiments. Another challenge in performing vibration control experiments with strings relates to actuator placement. Unlike a beam, to which piezoelectric actuators can be easily mounted, it is inconvenient to mount actuators on a string. Many papers in the literature present experimental results, but they primarily consider axially moving strings; few papers consider strings that are not translating between supports. Baicu, et al. [33] developed an active boundary controller for the nonlinear model of an elastic cable; the angle of the cable at one boundary was sensed and its position was controlled to asymptotically decay modal vibration. A wave absorption strategy was developed by Saigo, et al. [29]; a voice-coil actuator was placed near a fixed boundary of the string to suppress vibration. For the experimental verification of scabbard like actuator method, we present a control methodology in which energy reduction is achieved through cyclic application and removal of a constraint. In our method, a zero-displacement constraint is enforced at one point on the string, close to one of its boundaries. This effectively results in two vibrating strings, one of which is much shorter in length than the other. The vibration of the shorter length string decays rapidly due to high internal damping and when the constraint is released, the remaining energy of the string is redistributed over its entire length; this allows the cycle of constraint application and removal to be repeated for vibration suppression.

1.3 Dynamics and Vibration Control of Membrane

The dynamics of a membrane is a classical problem in mechanical vibrations. Among the different types of membranes, circular membranes are the most commonly studied due to their large number of applications. From the study of musical notes of percussion instruments, circular membranes have been used to design diaphragms for condenser microphones, model the dynamics of the human ear [34], understand the vibration characteristics of membrane mirrors and gossamer structures [35], measure surface tension [36], and design ink-jet printers [37]. For a majority of these applications, unconstrained membrane models have been used. A constrained membrane is one in which a portion of the membrane does not undergo vibration, and an application where constrained membrane models have been used is waveguides. Early work on this subject dates back to the 1960's and 70's. Yee and Audeh [38], [1] used the point-matching method to determine eigenfrequencies of waveguides with eccentric cross-section. Davies and Muilwyk [39] and Steele [40] used the finite difference method to compute eigenvalues of waveguides with arbitrary cross-section. The Helmholtz equation, which describes the dynamics of waveguides, was solved by Arlett, et al. [41] and Gass [42] using finite element methods, by Laura [43] and Hine [44] using the Galerkin method, and by Bulley and Davies [45] using the Rayleigh-Ritz method.

The similarity between the differential equations of membranes and waveguides motivated the study of circular membranes with constraints in the 1970's and 80's. The eigenvalues of a circular membrane with an internal eccentric circular areal constraint were first computed by Nagaya [2] using Fourier series. Another solution to this problem was presented by Lin [46], who used Graf's addition theorem to transform the Bessel functions from one set of polar coordinates to another. Lin [46] missed a term in the final expression, which affected the results of calculation. The missing term was identified by Singh and Kothari [47] and Singh, et al. [3], who used Nagaya's approach together with Graf's addition theorem. Later, Nagaya and Hai [48] studied composite membranes with arbitrarily shaped inner and outer boundaries. S. Noga [49] presented numerical simulation for the free transversal vibrations of a systems of two annular and circular membranes connected by a Winkler elastic layer. Arokiasamy, A. [50] presented work for vibrating rectangular membrane by using computer graphics. E. Alvarado-Anell and et al. [51] presented simulation and animation of circular, rectangular and elliptical membranes by using computer MAPLE software. The circular membrane is also used for the modelling of human tympanum, where computer simulations are presented [52, 53].

The vibration of membranes remains an active subject of research with recent work focusing on complex boundary conditions and shapes, inhomogeneities, accuracy of solutions, and applications. Investigations of membranes with complex boundary conditions and shapes include the work by Laura and Gutierrez [54], Yu and Wang [55], Kang and Lee [56], and Chen, et al. [57]. Investigations of non-homogeneous membranes include the work by Cortinez and Laura [58] and Cap [59], and that of accuracy of solutions include the work by Zhao and Stevens [60]. Applications of membranes are diverse and membrane vibrations have been investigated in the context of micro-air vehicle wings [61], [62], [63], energy harvesting [64, 65]. Wang, O. [66] presented a study about the wave propagation in a piezoelectric coupled cylindrical membrane shell. Furthermore, membrane structures are used in many different applications such as concentrators, planar configurations, solar sails and optical applications [67]. Although many theoretical works in the literature investigated the vibration of membranes in general, only handful of studies are conducted to the experimental study of vibration in membranes, a thorough literature review about membrane experiments can be found in [67].

Some studies in the literature are conduct for the vibration control of membranes using different active control schemes. Grosso, Ronald P. and Yellin, Martin [68] investigated the vibration control of a membrane mirror assembly by using electrostatic actuators. Joo, I. [69] and [70] presented a study on the control of circular and rectangular membranes by reachability of movement states in fixed time. James D. Moore [71] presented a design and testing of a one-meter membrane mirror with active boundary control. Mauro V. Aguanno and et al. [72] presented an experimental work on investigation to demonstrate a full-field laser vibrometer system that could replace electro-mechanical scanning with electronic scanning within a programmable stand-alone and relatively low-cost digital camera. Recently, a study on the active vibration control of thin and flexible disc is presented by [73], where the thin disc is equipped with two piezoelectric circular patches: one of them works as a sensor and the other is used as an actuator for damping of the most vibrating modes in a specified bandwidth. Another recent work on the vibration suppression of membrane is presented by P. A. Tarazaga and et al. [74], who investigated the using of vibro-acoustic technique to suppress the vibration in a pressurized optical membrane mirror.

In our work we use a small areal circular boundary constraint that interacts actively with the membrane during its motion and suppresses the vibration through sequential applications and removals of the constraint. Application and removal of constraint requires a complete and accurate solution for dynamics of the membrane with and without constraint. As we have seen, a thorough review of the literature indicates that investigations of constrained membranes have been limited to computing the eigenfrequencies of vibration. Although accurate computation of the eigenfrequencies may be sufficient for many applications, it is not sufficient for accurate computation of the mode shapes and/or modal coefficients of a constrained membrane. Simulation of the dynamics requires computation of the modal coefficients using orthogonality property of the modes. The orthogonality property of modes is well-known but it has not been established mathematically for constrained membranes. We establish the orthogonality property of all modes of a circular membrane with an internal circular areal constraint for the first time in this work. The computation of the modal coefficients require accurate computation of the mode shapes and this requires proper choice of the number of angular modes. We present an algorithm that determines the appropriate number of angular modes for arbitrary size and location of the constraint. In addition to this algorithm, which computes the mode shapes, we provide an algorithm for computation of the modal coefficients for arbitrary initial conditions. Also, we investigate the effect of application and removal of the constraint on the energetics of the vibrating membrane and provide semi-active control strategies to suppress the vibrating in the membrane through cyclic application and removal of the constraint.

Our entire work in this dissertation is organized as follows; in Chapter 2 we present a passive control strategy for the string vibration by subjecting the string to an obstacle located at one boundary. A semi-active control strategy for the string vibration is presented in Chapter 3, where a scabbard-like actuator is used near one boundary to suppress the string vibration. In Chapter 4 ,we present experimental verification to the control strategy based on the scabbard-like actuator control strategy. Chapter 5 presents accurate dynamics and simulation of constrained membrane under arbitrary initial conditions. In Chapter 6 we use the analysis presented in Chapter 5 to investigate the energetics of the application and removal of the areal boundary constraint and three different control strategies are presented. Chapter 7 includes the concluding remarks and the future work.

Chapter 2

Vibration of a String Wrapping and Unwrapping Around an Obstacle

2.1 Introduction

In this chapter we investigate the vibration of a string against an obstacle located at its boundary. Similar to the work by Burridge, et al.[9], we assume the string to wrap and unwrap around the obstacle during each oscillation. The impact of the string during wrapping is assumed to be perfectly inelastic and the obstacle is implicitly assumed to be convex. The assumption of convexity of the obstacle is both convenient and practical. The obstacle constrains the motion of the string and in this regard the mechanism for energy loss is a continuous-system version of the energy dissipation methodology proposed for finite degree-of-freedom systems by Issa, et al.[18]. Since the energy of the string decreases even in the absence of damping, the obstacle can be regarded as a passive mechanism for vibration suppression and control. This chapter is organized as follows. A formal problem statement and a list of the assumptions made in our analysis is provided in Section 2.2. The analytical model for computing the geometry of the string as it wraps and unwraps around the obstacle during oscillation is presented in Section 2.3. In Section 2.4 we provide simulation results for percentage energy loss and length of wrapping during each cycle of oscillation for different modes with circular- and elliptic-shaped obstacles. Using numerical simulations, we show in Section 2.5 that percentage energy loss can be increased significantly by changing the orientation of the obstacle.

2.2 Problem Statement and Assumptions

Consider a string vibrating against an obstacle placed at one of its boundaries, as shown in Fig. 2.1. We investigate energy dissipation in the string under the following assumptions:

A1. The obstacle is rigid and has the following geometry

$$y = f(x), \qquad y(0) = 0, \qquad \left[\frac{dy}{dx}\right]_{x=0} = 0 \tag{2.1}$$

A2. The string is homogeneous and has a constant mass per unit length denoted by ρ. The tension in the string is equal to T and remains constant at all times. The string undergoes transverse vibration in the xy plane and is not affected by gravity.

A3. The amplitude of oscillation of the string is small and therefore the equation of motion of the string can be expressed by the standard relation [75]

$$\frac{\partial^2 y}{\partial x^2} = \frac{1}{c^2}\frac{\partial^2 y}{\partial t^2}, \qquad c \triangleq \sqrt{T/\rho} \tag{2.2}$$

where $y(x,t)$ is the displacement of the string at a distance x from the origin at time t.

A4. The string wraps around the obstacle during vibration. Over each time step during wrapping, a small element of the string comes to rest on the obstacle through perfectly inelastic collisions. The wrapping process continues till the freely vibrating portion of the string has no more kinetic energy.

A5. The surface of the obstacle is not sticky and the string unwraps from the obstacle without any loss of energy.

A6. At the initial time $t = 0$, the string has no contact with the obstacle. It is in its mean position with zero potential energy and kinetic energy equal to E_0.

A7. The string continues to vibrate in the mode in which it started its vibration at the initial time. This implies that each point of the string, not in contact with the obstacle, has the same frequency of vibration[1] at any instant of time, and the number of nodes[2] in the vibrating string remains constant.

A8. The string has no internal damping, *i.e.*, the energy of the string will remain conserved during free vibration.

[1] The frequency of the string is not constant; it varies with time and amplitude when the string wraps and unwraps around the obstacle.

[2] A node is a point with zero displacement. As the string wraps or unwraps around the obstacle, the location of the node(s) change and therefore node(s) have nonzero horizontal velocity.

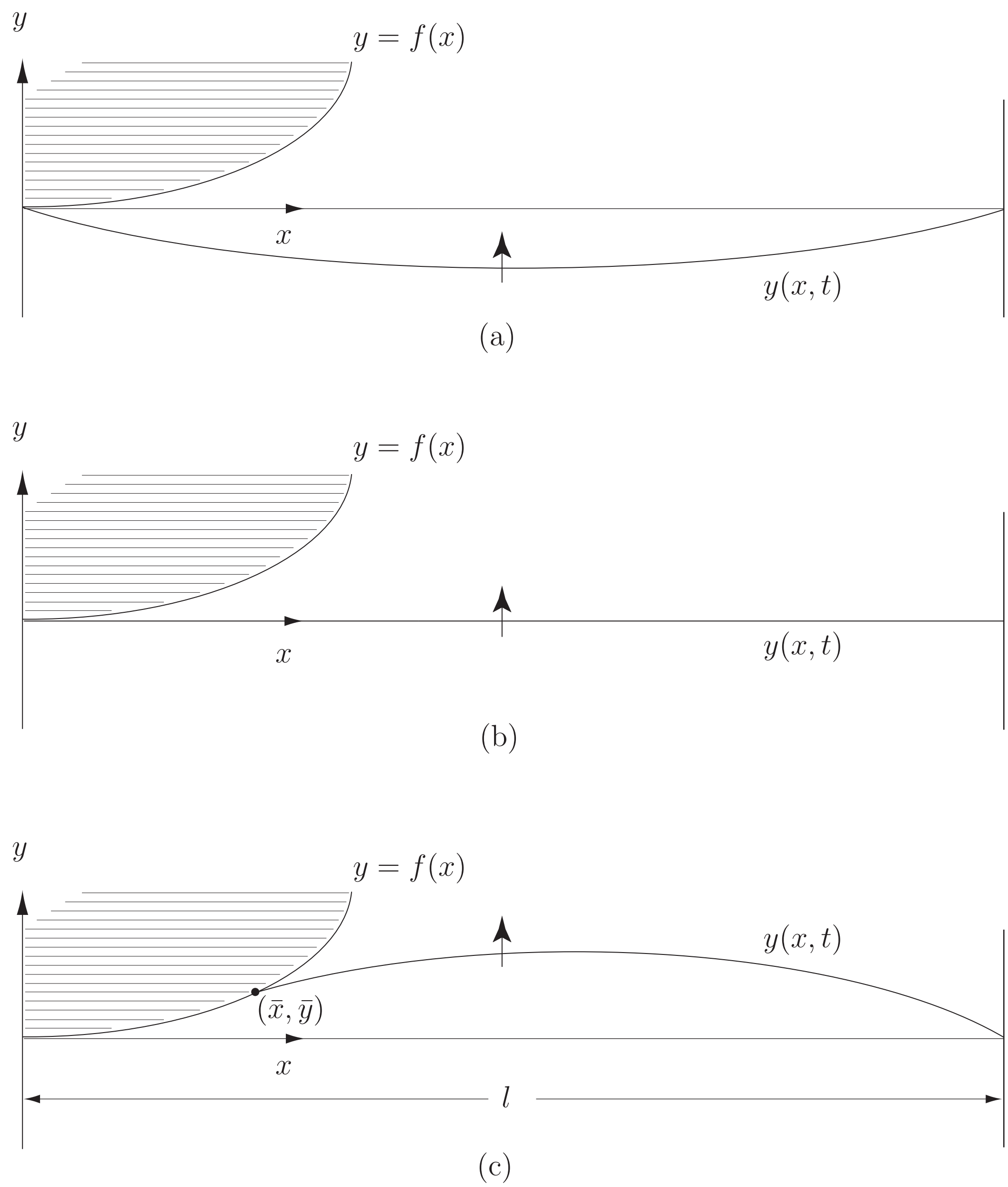

Figure 2.1: A string vibrating against an obstacle is shown in three configurations: (a) the string has both potential and kinetic energy and is not in contact with the obstacle, (b) the string has kinetic energy but no potential energy and is not in contact with the obstacle, (c) the string has both potential and kinetic energy and has wrapped around the obstacle. In a wrapped configuration, $(\bar{x}, \bar{y})$ denotes the coordinate where the string breaks contact with the obstacle

2.3 Analytical Model

2.3.1 Boundary conditions and general solution

A general solution to the partial differential equation in Eq. (2.2) can be written as [75]

$$y(x,t) = (\alpha_1 \sin \lambda x + \alpha_2 \cos \lambda x)\, (\alpha_3 \sin \omega t + \alpha_4 \cos \omega t) \tag{2.3}$$

where α_i, $i = 1, 2, 3, 4$ are constants, ω is the circular frequency and λ is the wave length and it is related to ω by the relation

$$\omega \triangleq c\lambda \tag{2.4}$$

At time $t = 0$, the string is at the mean position, *i.e.* $y(x, 0) \equiv 0$, per assumption A6. This implies $\alpha_4 = 0$. The solution in Eq. (2.3) can now be written as

$$y(x,t) = (A \sin \lambda x + B \cos \lambda x)\, \sin \omega t, \qquad A = \alpha_1\alpha_3, \qquad B = \alpha_2\alpha_3 \tag{2.5}$$

At the right boundary, the string satisfies the relation $y(l, t) = 0$ for all t. Using Eq. (2.5) we get

$$A \sin \lambda l + B \cos \lambda l = 0 \qquad \Longrightarrow \qquad B = -A \tan \lambda l \tag{2.6}$$

Substitution of Eq. (2.6) into Eq. (2.5) gives the solution

$$y(x,t) = A\,(\sin \lambda x - \tan \lambda l\, \cos \lambda x)\, \sin \omega t \tag{2.7}$$

We now consider the boundary conditions at the contact break point. From Fig. 2.1 we have

$$f(\bar{x}) = y(\bar{x}, t) \qquad \Longrightarrow \qquad f(\bar{x}) = A\left(\sin\lambda\bar{x} - \tan\lambda l\, \cos\lambda\bar{x}\right)\sin\omega t \tag{2.8}$$

Also, the string is tangential to the obstacle at the contact break point $x = \bar{x}$, *i.e.*,

$$f'(\bar{x}) = \frac{\partial y(\bar{x}, t)}{\partial x} \qquad \Longrightarrow \qquad f'(\bar{x}) = \lambda A\left(\cos\lambda\bar{x} + \tan\lambda l\, \sin\lambda\bar{x}\right)\sin\omega t \tag{2.9}$$

From Eqs. (2.8) and (2.9) we get

$$\tan\lambda(l - \bar{x}) = -\lambda\frac{f(\bar{x})}{f'(\bar{x})} \tag{2.10}$$

which indicates that λ can be computed from the value of $\bar{x}$. The solution of Eq. (2.10) is however not unique - each non-trivial value of λ corresponds to a mode of vibration of the string. Since λ is an implicit function of $\bar{x}$, we can rewrite Eq. (2.9) as follows

$$A\sin\omega t = g(\bar{x}), \qquad g(x) \triangleq \frac{f'(x)}{\lambda\left(\cos\lambda x + \tan\lambda l\, \sin\lambda x\right)} \tag{2.11}$$

Equation (2.11) can be used to compute t from the value of $\bar{x}$. The existence of the solution, however, depends on the magnitude of A. We now discuss the procedure for computing A.

Let the total energy of the string at any time t be denoted by E. Then,

$$E = E_{\text{pe}} + E_{\text{ke}} = E_{\text{pe}}^{\text{obs}} + E_{\text{pe}}^{\text{vib}} + E_{\text{ke}} \tag{2.12}$$

where $E_{\text{pe}}^{\text{obs}}$ is the potential energy of the string wrapped around the obstacle, $E_{\text{pe}}^{\text{vib}}$ is the potential energy of the freely vibrating string, E_{pe} is the total potential energy, and E_{ke} is the kinetic energy of the string. The total potential energy of the string is computed as the product of the tension T (which is assumed constant) and elongation of the string [76]. The elongation of the string is computed by integrating the strain of the string along the length wrapped around the obstacle and along the length of string vibrating freely. Thus, the total potential energy can be written as

$$E_{\text{pe}} = T\int dl = T\int (ds - dx) = T\int (\sqrt{dx^2 + dy^2} - dx) = T\int_0^l (\sqrt{1 + (dy/dx)^2} - 1)dx$$

and $E_{\text{pe}}^{\text{obs}}$ and $E_{\text{pe}}^{\text{vib}}$ can be written as

$$\begin{aligned} E_{\text{pe}}^{\text{obs}} &= T\int_0^{\bar{x}} (\sqrt{1 + (dy/dx)^2} - 1)dx \\ E_{\text{pe}}^{\text{vib}} &= T\int_{\bar{x}}^{l} (\sqrt{1 + (dy/dx)^2} - 1)dx \end{aligned}$$

Since the string conforms to the shape of the obstacle, $(dy/dx) = f'(x)$ for $x \in [0, \bar{x}]$. By expressing $(dy/dx) = y'(x,t)$ for $x \in [\bar{x}, l]$ and simplifying using Eqs. (2.7) and (2.11), we get

$$\begin{aligned} E_{\text{pe}}^{\text{obs}} &= T\int_0^{\bar{x}} \left[\sqrt{1 + \left[f'(x)\right]^2} - 1\right] dx \\ E_{\text{pe}}^{\text{vib}} &= T\int_{\bar{x}}^{l} \left[\sqrt{1 + \left[y'(x,t)\right]^2} - 1\right] dx \\ &\approx \frac{T}{2}\int_{\bar{x}}^{l} \left[y'(x,t)\right]^2 dx \end{aligned} \tag{2.13}$$

then

$$
\begin{aligned}
E_{\text{pe}}^{\text{vib}} &= \frac{T}{2}\lambda^2 A^2 \sin^2 \omega t \int_{\bar{x}}^{l} [\cos \lambda x + \tan \lambda l \sin \lambda x]^2 \, dx \\
&= \frac{1}{8} T\lambda A^2 \sin^2 \omega t \, \sec^2 \lambda l \Big\{ 2\lambda(l - \bar{x}) + \sin[2\lambda(l - \bar{x})] \Big\} \\
&= \frac{1}{8} T\lambda \sec^2 \lambda l \Big\{ 2\lambda(l - \bar{x}) + \sin[2\lambda(l - \bar{x})] \Big\} \big[g(\bar{x})\big]^2 \qquad (2.14)
\end{aligned}
$$

An element of string of length dx has a mass of $\rho \, dx$ and velocity is $\dot{y}(x, t)$. Thus, the kinetic energy of the freely vibrating string can be written and simplified as follows

$$
\begin{aligned}
E_{\text{ke}} &= \frac{1}{2} \int_{\bar{x}}^{l} \rho \big[\dot{y}(x, t)\big]^2 dx \\
&= \frac{\rho}{2} \omega^2 A^2 \cos^2 \omega t \int_{\bar{x}}^{l} [\sin \lambda x - \tan \lambda l \cos \lambda x]^2 \, dx \\
&= \frac{1}{8\lambda} \rho \, \omega^2 A^2 \cos^2 \omega t \, \sec^2 \lambda l \Big\{ 2\lambda(l - \bar{x}) - \sin[2\lambda(l - \bar{x})] \Big\} \\
&= \frac{1}{8\lambda} \rho \, \omega^2 \sec^2 \lambda l \Big\{ 2\lambda(l - \bar{x}) - \sin[2\lambda(l - \bar{x})] \Big\} \Big\{ A^2 - \big[g(\bar{x})\big]^2 \Big\} \qquad (2.15)
\end{aligned}
$$

From Eqs. (2.12), (2.13), (2.14) and (2.15) it is easy to verify that the energy expression has the form

$$
E = h(\bar{x}, A) \qquad (2.16)
$$

For a configuration in which the string is wrapped around the obstacle, the complete solution can be determined from the values of $\bar{x}$ and E using the four-step algorithm below:

1. Use Eq. (2.10) to determine the value of λ. Since Eq. (2.10) provides multiple non-trivial solutions that correspond to different modes of vibration, the solution corresponding to the initial mode of vibration should be chosen - see assumption A7.

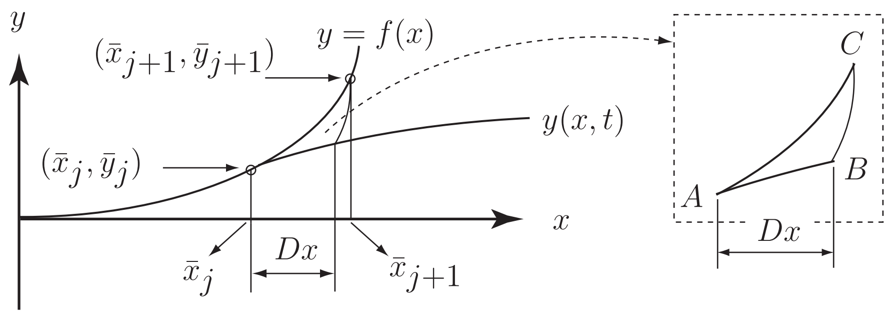

Figure 2.2: Small string segment Δx wraps around obstacle after perfectly inelastic collision. In the magnified image, AB denotes the small string segment of length Δx that wraps around the obstacle over the region AC

2. Use Eq. (2.4) to compute ω.

3. Compute A from Eq. (2.16) using the values of $\bar{x}$, E, λ and ω.

4. Compute the time t from Eq. (2.11) by substituting in the values of $\bar{x}$, A and λ.

The complete solution can now be described using Eqs. (2.1) and (2.7) as follows:

$$y(x,t) = \begin{cases} f(x) & : \quad x \in [0, \bar{x}] \\ A\,(\sin \lambda x - \tan \lambda l \, \cos \lambda x)\, \sin \omega t & : \quad x \in [\bar{x}, l\,] \end{cases} \tag{2.17}$$

2.3.2 Wrapping of the string

From our discussion in the last section we know that the geometry of the string can be determined from the values of $\bar{x}$ and E. In this section we discuss the method for computing these values at regular intervals of time. Let $\{\bar{x}_i, E_i\}$ denote the values of $\bar{x}$ and E at time $t = t_i$, $i = 0, 1, 2, \cdots, k$. We assume $t_0 = 0$. Then, from assumption A6, $\bar{x}_0 = 0$ and the value of E_0 is known. We will discuss the method for determining the value of t_k which denotes the time after which the string begins to unwrap.

Let us assume that for some $i = j$, $\{\bar{x}_j, E_j\}$ is known. We outline the method for computing $\{\bar{x}_{j+1}, E_{j+1}\}$ from the values of $\{\bar{x}_j, E_j\}$. Choose a small segment of the vibrating string that is expected to wrap around the obstacle over a small interval of time. Let the projection of this string segment AB on the x axis be Δx as shown in Fig. 2.2. The kinetic energy of this string segment, which will be lost due to inelastic collision, can be computed from Eq. (2.7) as follows

$$\begin{aligned} E_{\text{lost}} &= \frac{\rho}{2}\int_{\bar{x}_j}^{\bar{x}_j+\Delta x} \left[\dot{y}(x,t)\right]^2 dx \\ &= \frac{\rho}{2}\omega_j^2 A_j^2 \cos^2 \omega_j t_j \int_{\bar{x}_j}^{\bar{x}_j+\Delta x} \left[\sin\lambda_j x - \tan\lambda_j l \, \cos\lambda_j x\right]^2 dx \end{aligned} \tag{2.18}$$

where A_j, ω_j, λ_j and t_j denote values of A, ω, λ and t, respectively, derived for the pair $\{\bar{x}_j, E_j\}$. Using Eq. (2.18), E_{j+1} can be computed as follows

$$E_{j+1} = E_j - E_{\text{lost}}, \qquad j = 1, 2, \cdots, k-1 \tag{2.19}$$

To compute $\bar{x}_{j+1}$, $j = 1, 2, \cdots, k-1$, we make the following general assumption:

A9. With reference to Fig. 2.2, the potential energy of the vibrating string segment AB at time t_j is equal to the potential energy of the string segment AC wrapped on the obstacle at time t_{j+1}.

Using Eqs. (2.13) and (2.14) assumption A9 can be mathematically expressed as follows

$$\begin{aligned} &\int_{\bar{x}_j}^{\bar{x}_{j+1}} \left[\sqrt{1+\left[f'(x)\right]^2} - 1\right] dx = \int_{\bar{x}_j}^{\bar{x}_j+\Delta x} \left[\sqrt{1+\left[y'(x,t)\right]^2} - 1\right] dx \\ \approx\ & \frac{1}{2}\int_{\bar{x}_j}^{\bar{x}_j+\Delta x} \left[y'(x,t)\right]^2 dx \Longrightarrow \end{aligned}$$

$$\frac{1}{2}\int_{\bar{x}_j}^{\bar{x}_j+\Delta x}\Big[y'(x,t)\Big]^2\,dx = \frac{1}{2}\lambda_j^2 A_j^2 \sin^2\omega_j t_j \int_{\bar{x}_j}^{\bar{x}_j+\Delta x}\Big[\cos\lambda_j x + \tan\lambda_j l\,\sin\lambda_j x\Big]^2\,dx \tag{2.20}$$

Equation (2.20) can be used to determine $\bar{x}_{j+1}$. The values of A_{j+1}, ω_{j+1}, λ_{j+1} and t_{j+1} are computed from the values of $\bar{x}_{j+1}$ and E_{j+1}. The iterative process is terminated when the kinetic energy of the vibrating string segment becomes approximately equal to zero. At this time, which is denoted as t_k, the string stops wrapping and begins to unwrap.

2.3.3 Unwrapping of the string

Similar to wrapping, the geometry of the string during unwrapping is computed from the values of $\bar{x}$ and E. The string begins to unwrap at $t = t_k$; at this time the values of $\bar{x} = \bar{x}_k$ and $E = E_k$ are known. Let $\{\bar{x}_i, E_i\}$ denote the values of $\bar{x}$ and E at time $t = t_i$, $i = k, k+1, k+2, \cdots, l$, where t_l denotes the time when the string has unwrapped completely. We outline the method for computing $\{\bar{x}_{j+1}, E_{j+1}\}$ from the values of $\{\bar{x}_j, E_j\}$ for $k \le j \le l-1$. One chooses a small segment of the string that is expected to unwrap over a small interval of time. Then we let the projection of this string segment on the x axis be Δx. Then,

$$\bar{x}_{j+1} = \bar{x}_j - \Delta x, \qquad j = k, k+1, \cdots, l-1 \tag{2.21}$$

Since there is no loss of kinetic energy during unwrapping (see assumption A5), we have

$$E_{j+1} = E_j, \qquad j = k, k+1, \cdots, l-1 \tag{2.22}$$

The values of A_{j+1}, ω_{j+1}, λ_{j+1} and t_{j+1} are computed iteratively from the values of $\bar{x}_{j+1}$ and E_{j+1}. The iterative process is terminated at $t = t_l$ when the potential energy of the string is equal to its value at the mean position.

2.4 Numerical Simulations

Consider a string with

$$T = 1 \text{ N}, \qquad \rho = 0.025 \text{ kg/m}, \qquad l = 4 \text{ m} \tag{2.23}$$

The obstacle is assumed to be a circle of radius R and center coordinates $(x, y) \equiv (0, R)$, *i.e.*,

$$y = f(x) = R - \sqrt{R^2 - x^2}, \qquad 0 \leq x \leq R \tag{2.24}$$

It can be verified that $f(x)$ in Eq. (2.24) satisfies the boundary conditions in Eq. (2.1). For $R = 1$ m and $\Delta x = 0.001$ m, we compute the percentage loss of energy over one cycle of string oscillation for three different values of initial energy E_0 and for oscillation in the first, second, and third modes, respectively. These values are shown in table 2.1 together with the values of $\bar{x}_k$, which is a measure of the length of wrapping around the obstacle. For the special case of $E_0 = 0.5\ J$, we plot the percentage loss of energy for three consecutive cycles of string vibration in the first two modes. These plots are shown in Fig. 2.3. Figure 2.6 plots

Table 2.1: Percentage energy loss over one cycle of oscillation and $\bar{x}_k$ for different values of E_0 and three modes of oscillation, all with $R = 1\,m$

	Mode 1	Mode 2	Mode 3
$E_0 = 1.00\,J$	0.491%, 0.729 m	1.598%, 0.696 m	2.752%, 0.654 m
$E_0 = 0.50\,J$	0.256%, 0.596 m	0.861%, 0.569 m	1.547%, 0.537 m
$E_0 = 0.25\,J$	0.113%, 0.461 m	0.402%, 0.445 m	0.766%, 0.424 m

the decay in energy as a function of time for vibration in the first four modes with $E_0 = 0.5$ J. The following observations can be made from the plots in Figs. 2.3 and 2.6, and the data in table 2.1

- For any mode of oscillation, it can be seen that the percentage energy loss is higher for higher values of E_0. This is not surprising since higher values of E_0 results in higher kinetic energy and greater length of wrapping, as evident from the values of $\bar{x}_k$ in table 2.1, and consequently more energy loss through inelastic collision. The same argument can explain the reduction in the percentage loss of energy over consecutive cycles of vibration in Fig. 2.3.

- The percentage energy loss is higher for higher modes of oscillation for the same value of E_0. This is true for the same number of cycles (see Fig. 2.3) as well as for the same length of time (see Fig. 2.6) and is due to the fact that the velocities of the string associated with higher frequencies are higher in higher modes, and as a consequence the loss upon impact is higher. The value of $\bar{x}_k$ is less for the higher modes but this does not have a significant effect on the percentage of energy loss.

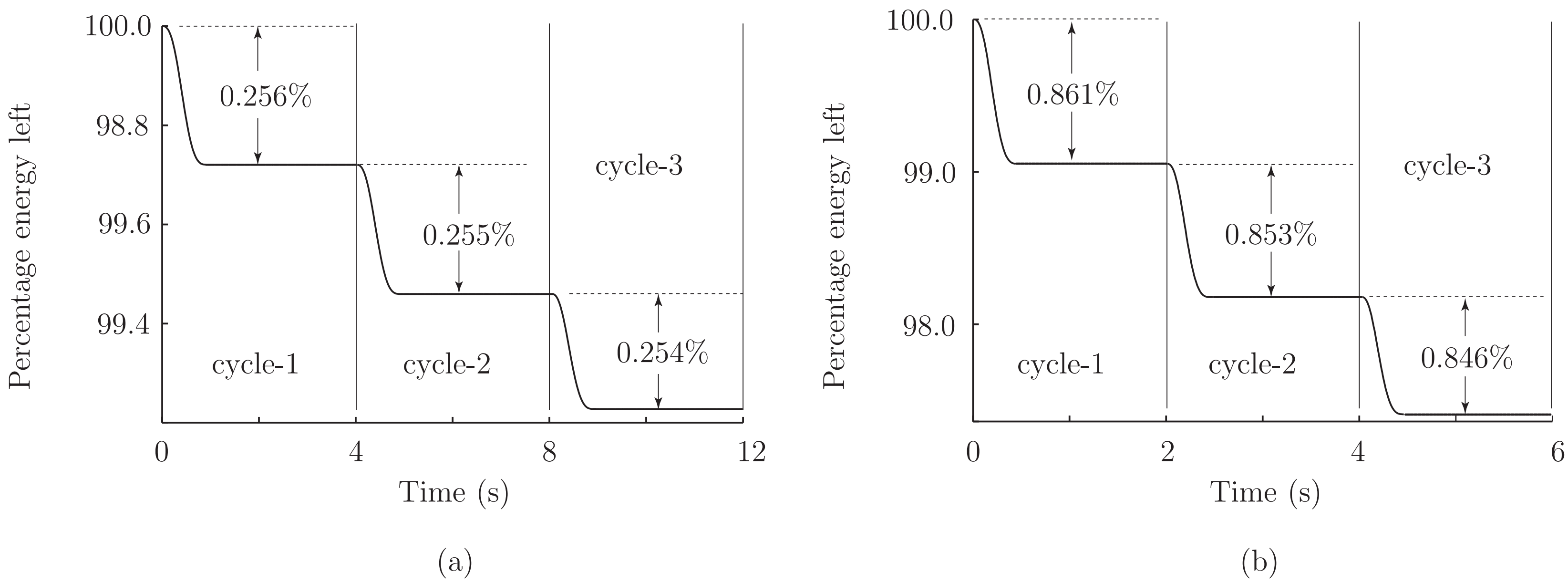

Figure 2.3: Plot of percentage energy content of the string over three consecutive cycles of vibration in (a) Mode 1, and (b) Mode 2. For both cases, the initial energy of the string was $E_0 = 0.5\ J$

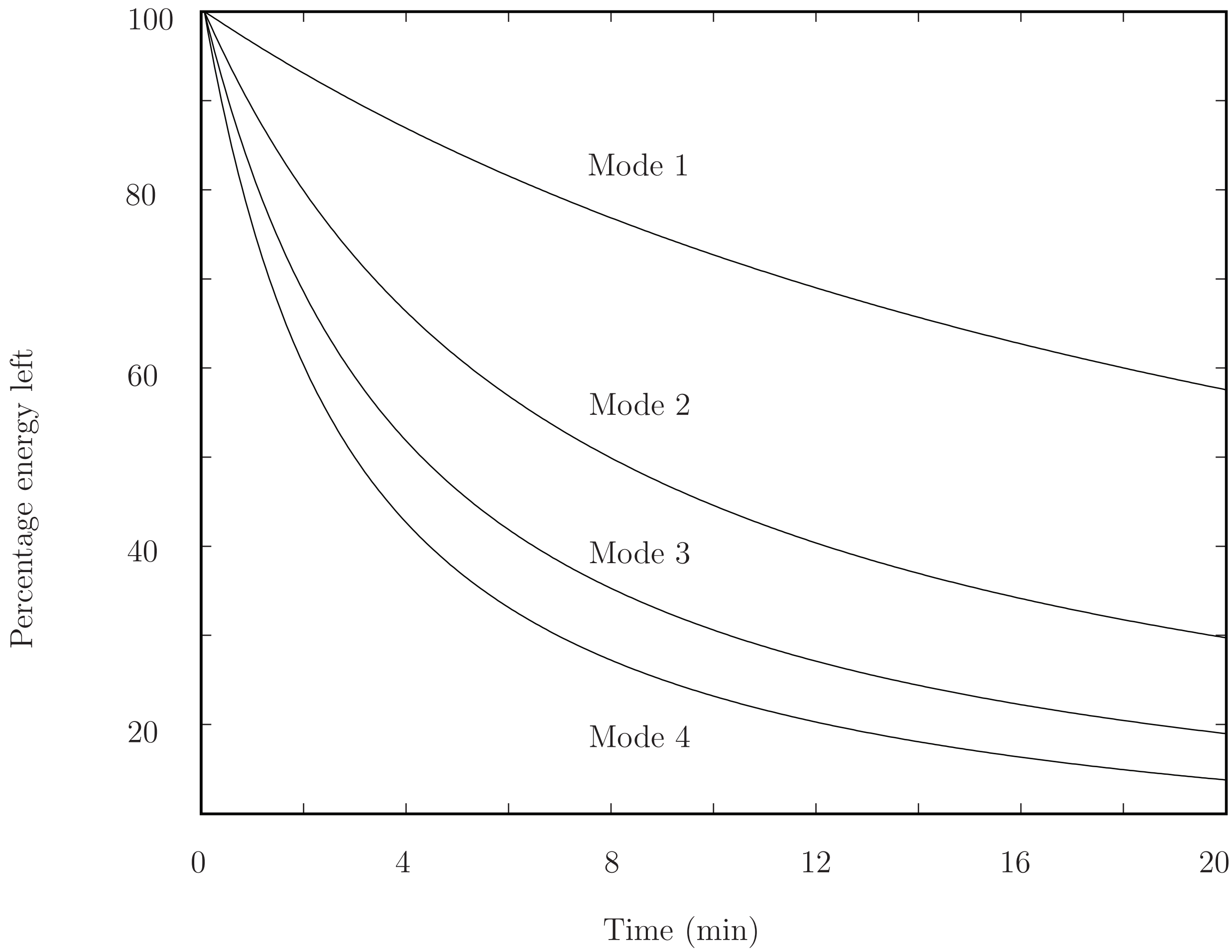

Figure 2.4: Exponential decay in the energy of a string wrapping and unwrapping around an obstacle. The plots show energy decay for single-mode vibration in the first four modes with $E_0 = 0.5\ J$

The geometry of the string at different points in time during one cycle of oscillation is shown in Fig. 2.5 for Mode 1 and Mode 2 with initial energy $E_0 = 0.5\ J$. It can be seen from these plots that a fixed point on the string moves in the y direction only when the string is not in contact with the obstacle but moves in both the x and y directions during wrapping and unwrapping. From the plot for Mode 2, it is also clear that a node is not a fixed point on the string. It is a point of zero displacement but has nonzero velocity during wrapping and unwrapping.

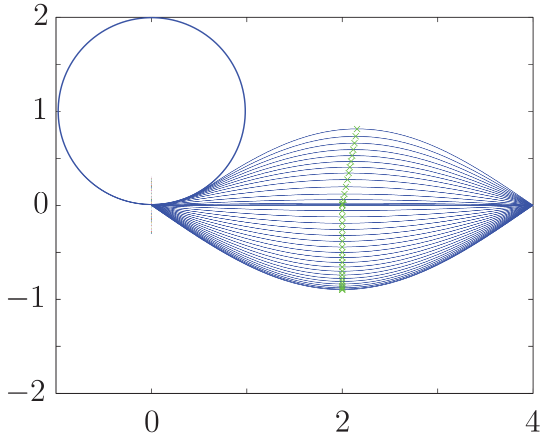

(a)

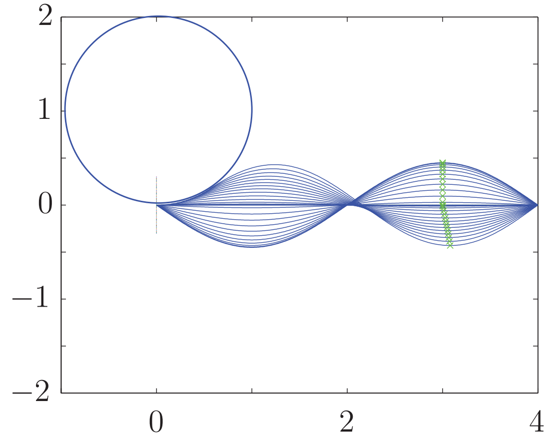

(b)

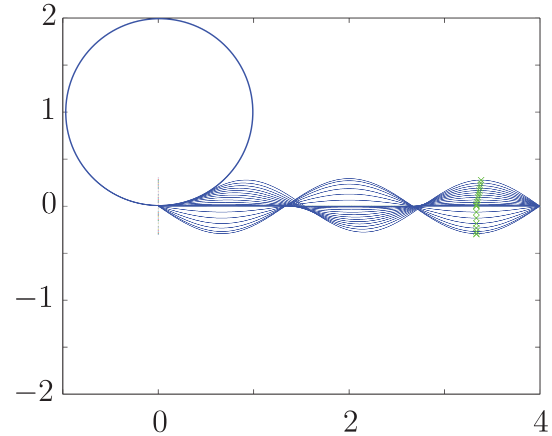

(c)

Figure 2.5: A string vibrating against a circular obstacle in (a) Mode 1 (b) Mode 2, and (c) Mode 3

To study the effect of the shape of the obstacle on percentage energy loss, we fix the value of the initial energy to $E_0 = 0.5\ J$ and study the following four cases where the obstacle is:

(a) a circle with $R = 0.5$ m

(b) a circle with $R = 1.0$ m

(c) a circle with $R = 1.5$ m

(d) an ellipse with semi-major and semi-minor axes lengths of 1.2 m and 1.0 m, respectively, and with the major axis aligned with the x axis

and satisfy the boundary conditions in Eq. (2.1). The results are shown in Table 2.2. It is clear from the results that for circular obstacles the percentage energy loss increases with increase in radius and vice versa. This is in agreement with the results expected for the limiting cases, namely, percentage energy loss is zero when the radius of the circle is zero and is equal to 100% when the radius is infinity. The ellipse in case (d) circumscribes the circle in case (b) and provides a lower slope for the wrapping curve. A comparison of the data for cases (b) and (d) indicates that a slight decrease in slope of the obstacle results in significantly higher percentage of energy loss.

Table 2.2: Percentage energy loss over one cycle of oscillation and $\bar{x}_k$ for obstacles of different shapes and sizes, all with $E_0 = 0.50\,J$

Case	Mode 1	Mode 2	Mode 3
(a)	0.029%, 0.295 m	0.113%, 0.291 m	0.237%, 0.286 m
(b)	0.256%, 0.596 m	0.861%, 0.569 m	1.547%, 0.537 m
(c)	0.915%, 0.897 m	2.549%, 0.815 m	3.887%, 0.737 m
(d)	0.665%, 0.803 m	2.021%, 0.750 m	3.278%, 0.692 m

2.5 Effect of Change in Slope of Obstacle

We consider the obstacle in Fig. 2.6 where the curve $y = g(x)$ is obtained by rotating the curve $y = f(x)$ in Fig. 2.1 clockwise by angle θ about point O. To deal with this problem, we modify assumptions A1 and A6 as follows:

A1. The obstacle is rigid and has the following geometry

$$y = f(x), \qquad y(0) = 0, \quad \left[\frac{dy}{dx}\right]_{x=0} = -\tan\theta \tag{2.25}$$

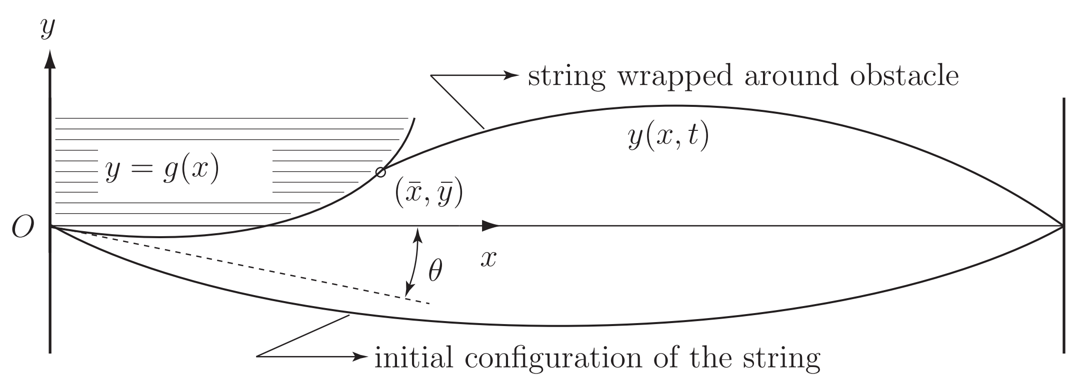

Figure 2.6: A string vibrating against an obstacle. The obstacle is identical to the one in Fig. 2.1 but rotated clockwise by angle θ about point O

A6. At the initial time $t = 0$, the string has no contact with the obstacle. It has zero kinetic energy and potential energy equal to E_0. The displacement of the string at the initial time corresponds to a single mode of free vibration as shown in Fig. 2.6.

The remaining assumptions, A2 through A5 and A6 through A9, are not changed. In table 2.3 we present simulation results for a string with

$$T = 1 \text{ N}, \qquad \rho = 0.025 \text{ kg/m}, \qquad l = 4 \text{ m}, \qquad E_0 = 0.50 \text{ J} \tag{2.26}$$

and a circular obstacle of radius $R = 1$ m. A comparison of the results indicates that percentage energy loss is significantly higher for higher values of θ.

Table 2.3: Percentage energy loss over one cycle of oscillation and $\bar{x}_k$ for two modes of oscillation with different values of θ

θ	Mode 1	Mode 2
0°	0.256%, 0.596 m	0.861%, 0.569 m
15°	1.486%, 0.866 m	3.478%, 0.841 m
30°	9.233%, 1.095 m	13.72%, 1.080 m

In this chapter, the string was assumed to have no damping. In reality, the string will have damping and this will enhance the rate of energy decay. The rate of energy decay will however not be constant even if the damping ratio of the string is constant. As the string wraps around the obstacle, its effective length decreases and frequency of vibration increases - this will increase the rate of energy decay which depends on the product of damping ratio and natural frequency.

Chapter 3

Vibration Control of a String Using A Scabbard-Like Actuator

3.1 Introduction

In this chapter, we investigate the dynamics and energetics of vibrating string with fixed ends subjected to moving constraint at one boundary. The constraint is applied by a scabbard that moves a small distance along the mean position of the string. The scabbard is moved instantaneously such that the position and velocity of the string outside the scabbard is unaffected immediately after application of the constraint, whereas the length of the string covered by the scabbard is brought to rest. The constraint is removed by moving the scabbard back to its original position and the change in energy of the string is investigated for different values of scabbard travel distance and time of application of the constraint. This chapter is organized as follows. A formal problem statement and a list of assumptions are provided in Section 3.2. Assuming that the string is vibrating in its fundamental mode, we use analytical methods in Section 3.3 to study the dynamics of the string and change in its energy after application of the constraint. The dynamics of the string and change in its energy after removal of the constraint is studied in Section 3.4. In Section 3.5 we present numerical simulation results for one cycle of constraint application and removal - these results indicate that the energy of the string can increase or decrease depending on the time of application of the constraint. In Section 3.6 we repeat the analyses of Sections 3.3 and 3.4 for arbitrary initial conditions of the string and develop a control strategy to reduce the energy of the string for every cycle of constraint application and removal. Numerical simulation results are then presented to demonstrate the efficacy of the control strategy.

3.2 Problem Statement and Assumptions

Consider the vibrating string in Fig. 3.1 (a), that passes through a scabbard located at its left boundary. At time $t = t_c$, the scabbard is moved instantaneously to the right by distance x_0 along the mean position of the string. This is shown in Fig. 3.1 (b). At some future time $t = t_r$, $t_r > t_c$, the scabbard is moved back to its original position. To investigate the effect of application and removal of the scabbard on the vibration of the string, we make the following simplifying assumptions:

A1. The string is homogeneous and has a constant mass per unit length denoted by ρ. The tension in the string is equal to T and remains constant at all times. The string undergoes transverse vibration in the xy plane and is not affected by gravity.

A2. The string is initially vibrating in its fundamental mode. This assumption will be removed and a general displacement profile of the string will be assumed in Section

3.6.

A3. The amplitude of oscillation of the string is small and therefore the equation of motion of the string can be expressed by the standard relation [75]

$$\left(\frac{\partial^2 y}{\partial x^2}\right) = \frac{1}{c^2}\left(\frac{\partial^2 y}{\partial t^2}\right), \qquad c \triangleq \sqrt{T/\rho} \tag{3.1}$$

where $y(x,t)$ is the displacement of the string at a distance x and time t.

A4. The string has no internal damping, *i.e.*, the energy of the string will remain conserved for free vibration.

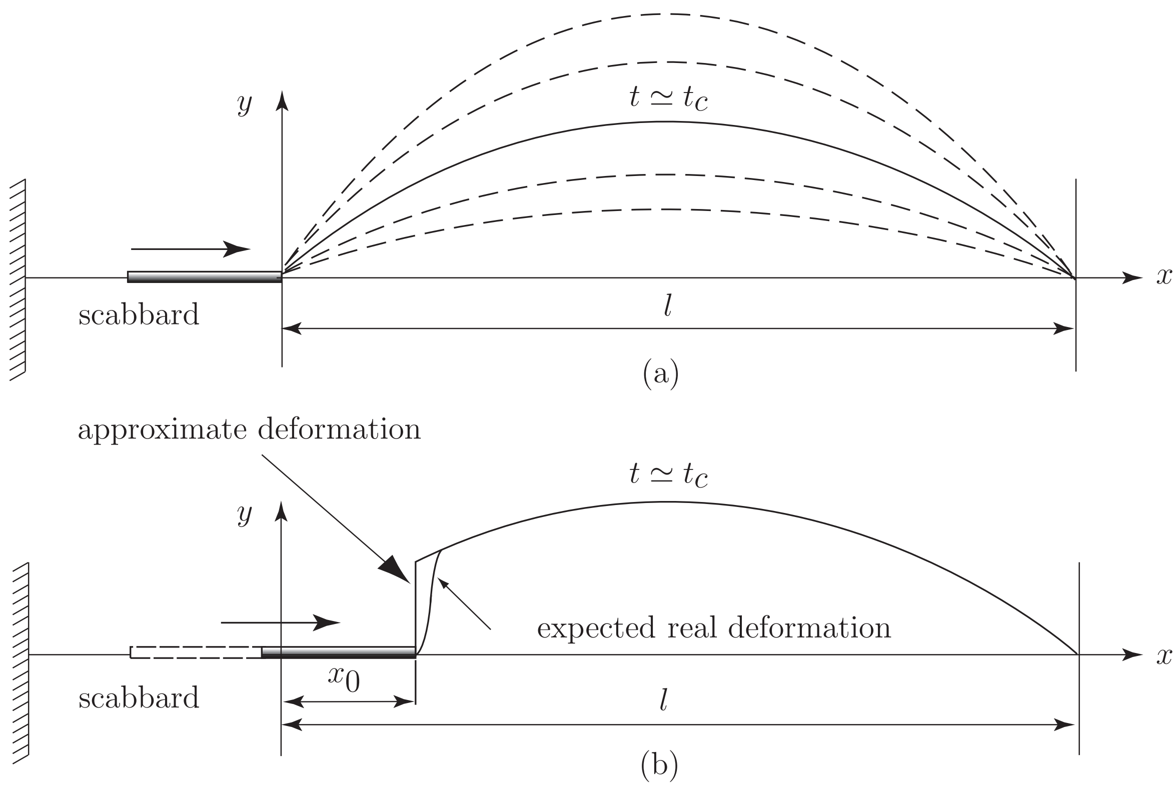

Figure 3.1: (a) A vibrating string (b) A zero-displacement constraint is applied to the string at time $t = t_c$ over the length segment $x \in [0, x_0)$ using a scabbard

A5. At time $t = t_c$, the scabbard is moved instantaneously to the right by a distance x_0 along the mean position of the string. The movement of the scabbard imposes a zero-displacement constraint over the length interval $x \in [0, x_0)$. The displacement and velocity of the string over the remaining interval $x \in [x_0, l]$ remains unchanged immediately after movement of the scabbard.

A6. The distance x_0 is small compared to the length of the string. Consequently, the discontinuity[1] in the displacement of the string at x_0 at time t_c, shown in Fig. 3.1 (b), will be small.

A7. At time $t = t_r$, $t_r > t_c$, the scabbard is instantaneously moved back to its original position, *i.e.*, to the left by a distance x_0 along the mean position of the string. The displacement and velocity of the string over the interval $x \in [x_0, l]$ remains unchanged immediately after movement of the scabbard.

3.3 Effect of Applying Constraint on the Dynamics of the String

3.3.1 Equation of motion after application of the constraint

The motion of the string prior to application of the constraint is shown in Fig. 3.1 (a) and is described by the equation

$$y_0(x,t) = A_0 \sin \lambda_0 x \sin \omega_0 t, \qquad \lambda_0 = (\pi/l), \quad \omega_0 = c\lambda_0 \tag{3.2}$$

[1]In reality, there will be no discontinuity in the string displacement. The same is true for the dynamic model since a finite number of Fourier coefficients will be used.

where A_0 is the amplitude, ω_0 is the circular frequency, and c is defined in Eq. (3.1).

To obtain the equation of motion of the string after the constraint has been applied, we solve Eq. (3.1) subject to initial and boundary conditions consistent with the constraint. A general solution to the partial differential equation in Eq. (3.1) is first written as [75]

$$y(x,t) = f(x)\, g(t) \tag{3.3}$$

where

$$\begin{aligned} f(x) &= A \sin \lambda x + B \cos \lambda x \\ g(t) &= C \sin \omega t + D \cos \omega t \end{aligned} \quad , \qquad \omega = c\lambda \tag{3.4}$$

where A, B, C and D are constants, and ω is the circular frequency. The boundary conditions for the constrained string, shown in Fig. 3.1 (b), give us the following relations

$$\begin{aligned} & y(x_0, t) = 0 \\ \Rightarrow\quad & (A \sin \lambda x_0 + B \cos \lambda x_0)\ (C \sin \omega t + D \cos \omega t) = 0 \\ \Rightarrow\quad & B = -A \tan \lambda x_0 \end{aligned} \tag{3.5}$$

$$\begin{aligned} & y(l, t) = 0 \\ \Rightarrow\quad & (A \sin \lambda l + B \cos \lambda l)\ (C \sin \omega t + D \cos \omega t) = 0 \\ \Rightarrow\quad & B = -A \tan \lambda l \end{aligned} \tag{3.6}$$

From Eqs. (3.5) and (3.6) we get

$$\tan \lambda x_0 = \tan \lambda l \quad \Rightarrow \quad \sin \lambda (l - x_0) = 0 \quad \Rightarrow \quad \lambda_n = \frac{n\pi}{l - x_0}, \;\; n = 1, 2, \cdots \tag{3.7}$$

By substituting the expressions for B and λ_n from Eqs. (3.6) and (3.7) in the expression for $f(x)$ in Eq. (3.4), we get

$$f(x) = A\left(\sin\lambda_n x - \tan\lambda_n l\, \cos\lambda_n x\right) = -\frac{A}{\cos\lambda_n l}\sin\lambda_n(l-x) \tag{3.8}$$

The general solution to Eq. (3.1) is obtained by substituting Eqs. (3.4) and (3.8) into Eq. (3.3):

$$y(x,t) = \begin{cases} 0 & : \; x \in [0, x_0) \\ \displaystyle\sum_{n=1}^{\infty} \sin\lambda_n(l-x)\big[C_n \sin c\lambda_n t + D_n \cos c\lambda_n t\big] & : \; x \in [x_0, l] \end{cases} \tag{3.9}$$

The constants C_n and D_n, $n = 1, 2, \cdots$, are determined from initial conditions. Without loss of generality, the time is first reset from $t = t_c$ to $t = 0$. Using assumption A5 in relation to the displacement and velocity of the string over the interval $x \in [x_0, l]$, we get

$$\begin{aligned} y(x,0) \;&=\; y_0(x,t_c) \;=\; A_0 \sin\lambda_0 x \sin\omega_0 t_c, \quad x \in [x_0, l] \\ \Rightarrow \;\sum_{n=1}^{\infty} & D_n \sin\lambda_n(l-x) = A_0 \sin\lambda_0 x \sin\omega_0 t_c, \quad x \in [x_0, l] \end{aligned}$$

$$\begin{aligned} \Rightarrow \;\; D_n &= \frac{2A_0}{(l-x_0)}\sin\omega_0 t_c \int_{x_0}^{l} \sin\lambda_0 x \,\sin\lambda_n(l-x)\, dx \\ &= (-1)^n \frac{2A_0\lambda_n}{(l-x_0)(\lambda_0^2-\lambda_n^2)} \sin\lambda_0 x_0 \,\sin\omega_0 t_c \end{aligned} \tag{3.10}$$

and,

$$\dot{y}(x,0) = \dot{y}_0(x,t_c) \;=\; A_0\omega_0 \,\sin\lambda_0 x\,\cos\omega_0 t_c, \qquad\qquad x \in [x_0, l]$$

$$\Rightarrow \quad \sum_{n=1}^{\infty} c\lambda_n C_n \,\sin\lambda_n(l-x) = A_0\omega_0 \,\sin\lambda_0 x\,\cos\omega_0 t_c, \quad x \in [x_0, l]$$

$$\begin{aligned}
\Rightarrow \quad C_n &= \frac{2A_0\omega_0}{nc\pi}\cos\omega_0 t_c \int_{x_0}^{l} \sin\lambda_0 x\,\sin\lambda_n(l-x)\,dx \\
&= (-1)^n \frac{2A_0\omega_0\lambda_n}{nc\pi(\lambda_0^2-\lambda_n^2)}\sin\lambda_0 x_0\,\cos\omega_0 t_c \qquad (3.11)
\end{aligned}$$

It is clear from Eqs. (3.10) and (3.11) that the values of the coefficients C_n and D_n, $n = 1, 2, \cdots$, depend on the values of x_0 and t_c. The motion of the string after application of the constraint is described by Eq. (3.9), and with the knowledge of these coefficients the motion is completely defined.

3.3.2 Energetics of constraint application

In this section we compute the change in the energy of the string due to application of the constraint. The energy of the string prior to application of the constraint is computed as follows [75]

$$E_0 = \frac{T}{2}\int_0^l \left[\frac{\partial y_0(x,t)}{\partial x}\right]^2 dx + \frac{\rho}{2}\int_0^l \left[\frac{\partial y_0(x,t)}{\partial t}\right]^2 dx \qquad (3.12)$$

By differentiating the expression for $y_0(x,t)$ in Eq. (3.2) with respect to x and t and substituting the relations in Eq. (3.12), we get

$$E_0 = \frac{T}{2}\frac{l}{2}A_0^2\lambda_0^2\,\sin^2\omega_0 t + \frac{\rho}{2}\frac{l}{2}A_0^2\omega_0^2\,\cos^2\omega_0 t \qquad (3.13)$$

Substituting the expressions for λ_0 and ω_0 from Eq. (3.2), λ_n from Eq. (3.7) and c from

Eq. (3.1) into Eq. (3.13), we get

$$E_0 = \frac{T\pi^2 A_0^2}{4l} \tag{3.14}$$

After the constraint has been applied, the energy of the string is given by the relation

$$E_c = \frac{T}{2}\int_{x_0}^{l}\left[\frac{\partial y(x,t)}{\partial x}\right]^2 dx + \frac{\rho}{2}\int_{x_0}^{l}\left[\frac{\partial y(x,t)}{\partial t}\right]^2 dx \tag{3.15}$$

If we define the time functions p_n, q_n, $n = 1, 2, \cdots$, as

$$\begin{aligned} p_n(t) &= C_n \sin c\lambda_n t + D_n \cos c\lambda_n t \\ q_n(t) &= C_n \cos c\lambda_n t - D_n \sin c\lambda_n t \end{aligned} \tag{3.16}$$

Eq. (3.15) can be rewritten as follows

$$\begin{aligned} E_c &= \frac{T}{2}\int_{x_0}^{l}\left[\sum_{n=1}^{\infty} p_n \lambda_n \cos \lambda_n (l-x)\right]^2 dx + \frac{\rho}{2}\int_{x_0}^{l}\left[\sum_{n=1}^{\infty} q_n \omega_n \sin \lambda_n (l-x)\right]^2 dx \\ &= \frac{T}{2}\int_{x_0}^{l}\left[\sum_{n=1}^{\infty} p_n^2 \lambda_n^2 \cos^2 \lambda_n (l-x)\right] dx + \frac{\rho}{2}\int_{x_0}^{l}\left[\sum_{n=1}^{\infty} q_n^2 \omega_n^2 \sin^2 \lambda_n (l-x)\right] dx \\ &\quad + \frac{T}{2}\int_{x_0}^{l}\left[\sum_{m=1}^{\infty}\sum_{\substack{n=1 \\ n\neq m}}^{\infty} p_m\, p_n\, \lambda_m\, \lambda_n \cos \lambda_m (l-x) \cos \lambda_n (l-x)\right] dx \\ &\quad + \frac{\rho}{2}\int_{x_0}^{l}\left[\sum_{m=1}^{\infty}\sum_{\substack{n=1 \\ n\neq m}}^{\infty} q_m\, q_n\, \omega_m\, \omega_n \sin \lambda_m (l-x) \sin \lambda_n (l-x)\right] dx \end{aligned} \tag{3.17}$$

Using the relation $(p_n^2 + q_n^2) = (C_n^2 + D_n^2)$, which can be easily shown from Eq. (3.16), the expression for λ_n in Eq. (3.7), and the identities

$$\int_{x_0}^{l} \cos^2 \lambda_n(l-x)dx = (l-x_0)/2, \qquad \int_{x_0}^{l} \cos \lambda_n(l-x) \cos \lambda_m(l-x)dx = 0$$
$$\int_{x_0}^{l} \sin^2 \lambda_n(l-x)dx = (l-x_0)/2, \qquad \int_{x_0}^{l} \sin \lambda_n(l-x) \sin \lambda_m(l-x)dx = 0$$

Eq. (3.17) is simplified to the form

$$E_c = \frac{T}{4}(l-x_0)\sum_{n=1}^{\infty} \lambda_n^2(p_n^2+q_n^2) = \frac{T\pi^2}{4(l-x_0)}\sum_{n=1}^{\infty} n^2(C_n^2+D_n^2) \tag{3.18}$$

The work done by the constraint is equal to the change in energy of the string, and is given by the relation

$$W_c = (E_c - E_0) = \frac{T\pi^2}{4(l-x_0)}\sum_{n=1}^{\infty} n^2(C_n^2+D_n^2) - \frac{T\pi^2 A_0^2}{4l} \tag{3.19}$$

From the expression for W_c in Eq. (3.19) and the expressions for C_n and D_n, $n = 1, 2, \cdots,$ in Eqs. 3.10) and (3.11), it is clear that the work done by the constraint depends on the values of x_0 and t_c. Through numerical simulations, it will be shown in Section 3.5 that the work done can be positive or negative, depending on the time of application of the constraint t_c.

3.4 Effect of Removing Constraint on the Dynamics of the String

Assume the constraint is removed during the string vibration at an arbitrary time $t = t_r$. In this section we investigate the effect of the constraint removal on the dynamics of the string and change in its energy. When the scabbard is removed instantaneously back, the string configuration which represents the initial displacement and velocity, will have two regions as shown in Fig. 3.2. The first region was covered by the scabbard and has zero velocity and displacement, and the second region is the configuration of the string at the instance of scabbard removal where the displacement and velocity are given by $y(t_r)$ and $\dot{y}(t_r)$ respectively.

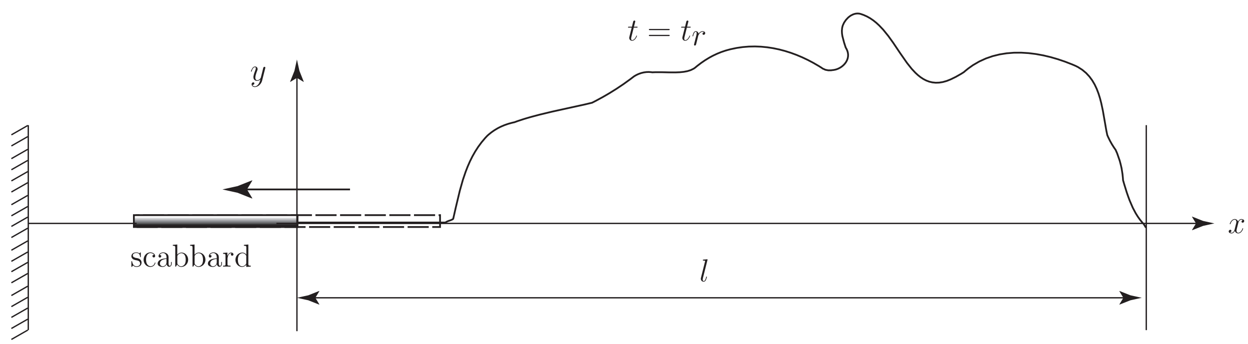

Figure 3.2: At time $t = t_r$, the scabbard is instantaneously moved back to its original position

3.4.1 Equation of motion after removal of the constraint

To obtain the equation of motion of the string after the constraint has been removed, we start from the general solution to the partial differential equation in Eq. (3.1), namely

$$y_r(x,t) = (\alpha \sin \Lambda x + \beta \cos \Lambda x)\,(\gamma \sin \Omega t + \delta \cos \Omega t), \qquad \Omega = c\Lambda \tag{3.20}$$

where $x \in [0, l]$, α, β, γ and δ are constants, and Ω is the circular frequency. The boundary conditions for the string, shown in Fig. 3.2, give us the following relations:

$$
\begin{aligned}
&y_r(0,t) = 0 \quad \Rightarrow \quad \beta = 0 \\
&y_r(l,t) = 0 \quad \Rightarrow \quad \sin \Lambda l = 0 \quad \Rightarrow \Lambda_k = (k\pi/l),\ k = 1, 2, \cdots
\end{aligned}
\tag{3.21}
$$

Substituting the relations in Eq. (3.21) into Eq. (3.20), we get

$$
y_r(x,t) = \sum_{k=1}^{\infty} \sin \Lambda_k x \big[\gamma_k \sin c\Lambda_k t + \delta_k \cos c\Lambda_k t\big], \quad x \in [0, l] \tag{3.22}
$$

The constants γ_k and δ_k, $k = 1, 2, \cdots$, are determined from initial conditions. Without loss of generality, the time is first reset from $t = t_r$ to $t = 0$. Using assumption A7 in relation to the displacement and velocity of the string over the interval $x \in [0, l]$, we get

$$
\begin{aligned}
y_r(x,0) &= y(x,t_r) \\
\Rightarrow \quad \sum_{k=1}^{\infty} \delta_k \sin \Lambda_k x &= \begin{cases} 0 & : \ x \in [0, x_0) \\ \displaystyle\sum_{n=1}^{\infty} \sin \lambda_n (l-x) \big[C_n \sin c\lambda_n t_r + D_n \cos c\lambda_n t_r\big] & : \ x \in [x_0, l] \end{cases} \\
\Rightarrow \quad \delta_k &= \frac{2}{l} \int_{x_0}^{l} \sum_{n=1}^{\infty} \sin \Lambda_k x \, \sin \lambda_n (l-x) \big[C_n \sin c\lambda_n t_r + D_n \cos c\lambda_n t_r\big] dx \\
&= \frac{2}{l} \sin \Lambda_k x_0 \sum_{n=1}^{\infty} (-1)^n \frac{\lambda_n}{\Lambda_k^2 - \lambda_n^2} \big[C_n \sin c\lambda_n t_r + D_n \cos c\lambda_n t_r\big]
\end{aligned}
\tag{3.23}
$$

and,

$$
\dot{y}_r(x,0) = \dot{y}(x,t_r) \Rightarrow
$$

similarly,

$$\sum_{k=1}^{\infty} c\Lambda_k \gamma_k \sin \Lambda_k x = \sum_{n=1}^{\infty} c\lambda_n \sin \lambda_n(l-x)\big[C_n \cos c\lambda_n t_r - D_n \sin c\lambda_n t_r\big] \quad : \quad x \in [x_0, l]$$

$$\begin{aligned}
\Rightarrow \quad \gamma_k &= \frac{2}{l\Lambda_k} \int_{x_0}^{l} \sum_{n=1}^{\infty} \lambda_n \sin \Lambda_k x \, \sin \lambda_n(l-x)\big[C_n \cos c\lambda_n t_r - D_n \sin c\lambda_n t_r\big] dx \\
&= \frac{2}{k\pi} \sin \Lambda_k x_0 \sum_{n=1}^{\infty} (-1)^n \frac{\lambda_n^2}{\Lambda_k^2 - \lambda_n^2} \big[C_n \cos c\lambda_n t_r - D_n \sin c\lambda_n t_r\big] \qquad (3.24)
\end{aligned}$$

The equation of motion of the string after removal of the constraint is given by Eq. (3.22), where δ_k and γ_k are defined by Eqs. (3.23) and (3.24), respectively.

3.4.2 Energetics of constraint removal

The change in energy of the string due to removal of the constraint can be computed in the same way as we computed the change in energy due to application of the constraint. The energy of the string after removal of the constraint is given by the relation

$$E_r = \frac{T}{2} \int_0^l \left[\frac{\partial y_r(x,t)}{\partial x}\right]^2 dx + \frac{\rho}{2} \int_0^l \left[\frac{\partial y_r(x,t)}{\partial t}\right]^2 dx \qquad (3.25)$$

Using Eqs. 3.22), (3.23) and (3.24) to compute the derivatives of $y_r(x,t)$ with respect to x and t, and substituting them in Eq. (3.25) and simplifying, we get the final expression

$$E_r = \frac{T\pi^2}{4l} \sum_{k=1}^{\infty} k^2(\gamma_k^2 + \delta_k^2) \qquad (3.26)$$

The change in energy due to removal of the constraint is computed as

$$W_r = (E_r - E_c) = \frac{T\pi^2}{4} \sum_{k=1}^{\infty} k^2 \left[\frac{(\gamma_k^2 + \delta_k^2)}{l} - \frac{(C_k^2 + D_k^2)}{(l - x_0)} \right] \tag{3.27}$$

In the next section we will use numerical simulations to show that the change in energy due to constraint removal is zero, *i.e.*, $W_r = 0$. This result is intuitive because removal of the constraint simply results in redistribution of the energy from its constrained length of $(l - x_0)$ to its original length l.

3.5 Simulation of One Cycle of Constraint Application and Removal

We consider a string of length $l = 4$ m, mass per unit length $\rho = 0.25$ kg/m, and tension $T = 1$ N, vibrating in its first mode with unit amplitude $A_0 = 0.1$ m. At $t = 0$ the string is assumed to pass through its mean position, and the equation of motion of the string is

$$y_0(x, t) = 0.1 \sin(\frac{\pi}{4}x) \sin(\frac{\pi}{2}t) \tag{3.28}$$

The time period of oscillation of the string is 4 sec and Fig. 3.3 (a) shows the shape of the string at different instants of time over the interval $t \in [1.0, 3.0]$ sec. The string is in its maximum potential energy configuration at $t = 1.0$ sec and $t = 3.0$ sec, and maximum kinetic energy configuration at $t = 2.0$ sec.

We first present simulation results for percentage change in energy due to constraint application for $x_0 \in \{0.0l, 0.01l, 0.02l, \cdots, 0.09l, 0.10l\}$ and $t_c \in [1.7, 2.3]$ sec. The results, shown in Fig. 3.3 (b), indicate that the energy of the string increases if the constraint is applied when the string is far away from the mean position, and decreases if the constraint is applied when the string is near its mean position, irrespective of the value of x_0. This can be explained as follows. Upon application of the constraint, the potential energy of the string increases. This increase is large when the string is far away from its mean position, and although the constraint removes the kinetic energy of a portion of the string, there is a net gain in energy. When the string is near its mean position, the increase in energy due to change in potential energy is small compared to the loss of kinetic energy and as a result the net change in energy is negative. When the string is at its mean position, there is no change in potential energy upon application of the constraint and consequently the energy loss is maximum in this configuration. For the same value of t_c, a larger value of x_0 results in a larger increase in potential energy and a larger decrease in kinetic energy. Consequently, a larger value of x_0 results in a larger percentage change in the energy. This can be verified from Fig. 3.3 (b). It should be noted that increase in energy due to movement of the boundary that reduces the length of the string was also observed by Zhu and Zheng [21].

Table 3.1: Comparison of values of E_c and E_r for $x_0 = 0.1l$ and $t_r = 0.8$ sec

No. of Fourier coefficients	E_c (J)	E_r (J)	error %
50	0.6124	0.6096	0.4723
100	0.6127	0.6110	0.2694
1000	0.6128	0.6123	0.0853

We next investigate the change in energy of the string due to removal of the constraint. Instead of computing the value of W_r in Eq. (3.27), we compute the values of E_c and E_r, which equal the energy of the string before and after removal of the constraint. Using

Eqs. (3.18) and (3.26), E_c and E_r are computed for varying number of Fourier coefficients. From this data (see Table 3.1) it is clear that E_c and E_r approach each other as the number of Fourier coefficients increase. Although the data corresponds to the specific case of $x_0 = 0.1l$ and $t_r = 0.8$ sec, the same trends can be observed for all values of x_0 and t_r.

Although constraint removal does not change the energy of the system, it resets the system for a new cycle of constraint application. In the next section we investigate the effect of application of the constraint on the dynamics of the string with arbitrary initial conditions such that sequential application and removal of constraints can be explored as a strategy for vibration suppression.

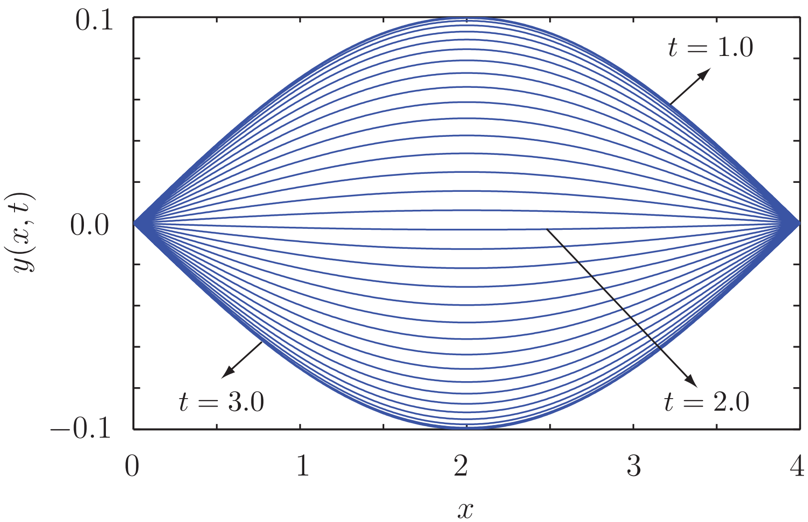

(a)

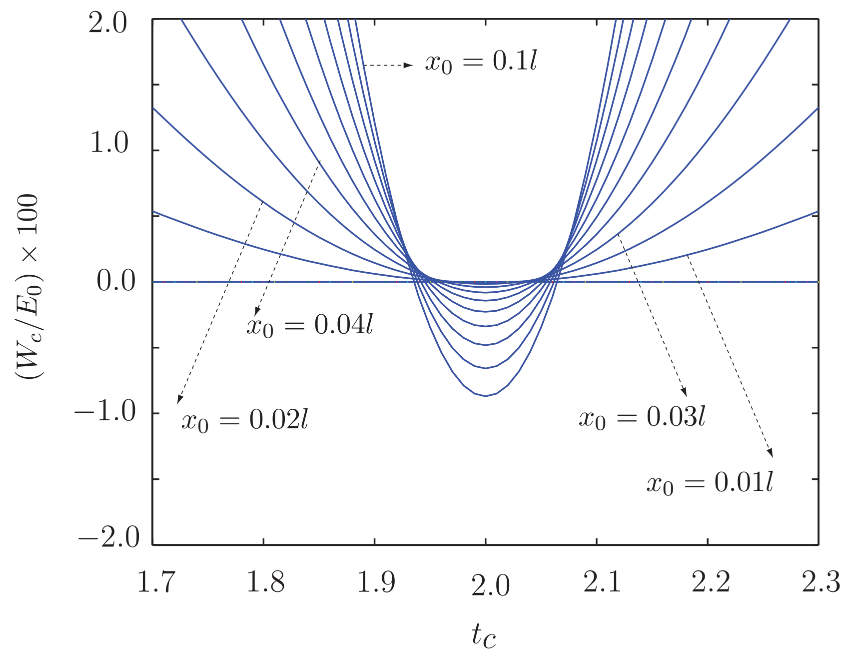

(b)

Figure 3.3: (a) Position of the string at different time instants (b) Percentage change in energy of the string due to application of the constraint for different values of x_0 and t_c

3.6 Sequential Application and Removal of Constraints

3.6.1 Dynamics of string with arbitrary initial conditions

In this section we relax assumption A2 and allow the string to have arbitrary initial conditions and then repeat the analysis of sections 3.4.2 and 3.5. Prior to application of the constraint, the equation of motion of the string has the form

$$y_0(x,t) = \sum_{k=1}^{\infty} \sin \Lambda_k x \big[\bar{\gamma}_k \sin c\Lambda_k t + \bar{\delta}_k \cos c\Lambda_k t\big], \quad x \in [0,l] \tag{3.29}$$

which is similar to Eq. (3.22) and satisfies the boundary conditions $y_0(0,t) = y_0(l,t) = 0$. In Eq. (3.29), the values of the coefficients $\bar{\gamma}_k$, $\bar{\delta}_k$, $k = 1, 2, \cdots$, are known. The energy of the string at the initial time is given by the relation

$$E_0 = \frac{T\pi^2}{4l} \sum_{k=1}^{\infty} k^2 (\bar{\gamma}_k^2 + \bar{\delta}_k^2) \tag{3.30}$$

which is similar to Eq. (3.26). After application of the constraint, the equation of motion of the string has the form

$$y(x,t) = \begin{cases} 0 & : \ x \in [0, x_0) \\ \displaystyle\sum_{n=1}^{\infty} \sin \lambda_n (l-x) \big[\bar{C}_n \sin c\lambda_n t + \bar{D}_n \cos c\lambda_n t\big] & : \ x \in [x_0, l] \end{cases} \tag{3.31}$$

which is identical to Eq. (3.9) except that the coefficients C_n and D_n, $n = 1, 2, \cdots$, have been replaced by $\bar{C}_n$ and $\bar{D}_n$. The constants $\bar{C}_n$ and $\bar{D}_n$, $n = 1, 2, \cdots$, are determined from initial conditions by repeating the procedure used in section 3.3.1. Without loss of generality, the time is reset from $t = t_c$ to $t = 0$, and the displacement and velocity of the string given by Eqs. (3.29) and (3.31) are compared over the interval $x \in [x_0, l]$:

$$\begin{aligned} y(x,0) \;=\; y_0(x,t_c) \;&=\; \sum_{k=1}^{\infty} \sin \Lambda_k x \big[\bar{\gamma}_k \sin c\Lambda_k t_c + \bar{\delta}_k \cos c\Lambda_k t_c\big], \quad x \in [x_0, l] \\ \Rightarrow \quad \sum_{n=1}^{\infty} \bar{D}_n \sin \lambda_n (l-x) &= \sum_{k=1}^{\infty} \sin \Lambda_k x \big[\bar{\gamma}_k \sin c\Lambda_k t_c + \bar{\delta}_k \cos c\Lambda_k t_c\big], \quad x \in [x_0, l] \end{aligned}$$

$$\begin{aligned} \Rightarrow \quad \bar{D}_n &= \frac{2}{l-x_0} \int_{x_0}^{l} \sum_{k=1}^{\infty} \sin \Lambda_k x \, \sin \lambda_n (l-x) \big[\bar{\gamma}_k \sin c\Lambda_k t_c + \bar{\delta}_k \cos c\Lambda_k t_c\big] dx \\ &= \frac{2}{l-x_0} \sum_{k=1}^{\infty} (-1)^n \frac{\lambda_n}{\Lambda_k^2 - \lambda_n^2} \sin \Lambda_k x_0 \big[\bar{\gamma}_k \sin c\Lambda_k t_c + \bar{\delta}_k \cos c\Lambda_k t_c\big] \end{aligned} \tag{3.32}$$

and,

$$\begin{aligned} \dot{y}(x,0) \;=\; \dot{y}_0(x,t_c) \;&=\; \sum_{k=1}^{\infty} c\Lambda_k \sin \Lambda_k x \big[\bar{\gamma}_k \cos c\Lambda_k t_c - \bar{\delta}_k \sin c\Lambda_k t_c\big], \quad x \in [x_0, l] \\ \Rightarrow \quad \sum_{n=1}^{\infty} c\lambda_n \bar{C}_n \sin \lambda_n (l-x) &= \sum_{k=1}^{\infty} c\Lambda_k \sin \Lambda_k x \big[\bar{\gamma}_k \cos c\Lambda_k t_c - \bar{\delta}_k \sin c\Lambda_k t_c\big], \quad x \in [x_0, l] \\ \Rightarrow \quad \bar{C}_n &= \frac{2}{l-x_0} \int_{x_0}^{l} \sum_{k=1}^{\infty} \frac{\Lambda_k}{\lambda_n} \sin \Lambda_k x \, \sin \lambda_n (l-x) \big[\bar{\gamma}_k \cos c\Lambda_k t_c - \bar{\delta}_k \sin c\Lambda_k t_c\big] dx \\ &= \frac{2}{nl} \sum_{k=1}^{\infty} (-1)^n \frac{k\lambda_n}{\Lambda_k^2 - \lambda_n^2} \sin \Lambda_k x_0 \big[\bar{\gamma}_k \cos c\Lambda_k t_c - \bar{\delta}_k \sin c\Lambda_k t_c\big] \end{aligned} \tag{3.33}$$

The total energy of the system after application of the constraint is given by the expression

$$E_c = \frac{T\pi^2}{4(l-x_0)} \sum_{n=1}^{\infty} n^2 (\bar{C}_n^2 + \bar{D}_n^2) \tag{3.34}$$

which is similar to the expression in Eq. (3.18). Using Eqs. (3.30) and (3.34), the change in energy due to constraint application can be expressed as

$$W_c = (E_c - E_0) = \frac{T\pi^2}{4}\sum_{n=1}^{\infty} n^2 \left[\frac{(\bar{C}_n^2 + \bar{D}_n^2)}{(l - x_0)} - \frac{(\bar{\gamma}_n^2 + \bar{\delta}_n^2)}{l}\right] \tag{3.35}$$

When the constraint is removed at $t = t_r > t_c$, the equation of motion of the string is described by Eq. (3.22), namely

$$y_r(x,t) = \sum_{k=1}^{\infty} \sin \Lambda_k x \left[\gamma_k \sin c\Lambda_k t + \delta_k \cos c\Lambda_k t\right], \quad x \in [0, l] \tag{3.36}$$

where γ_k, δ_k, $k = 1, 2, \cdots$, can be computed from Eqs. (3.23) and (3.24) after replacing C_n and D_n, $n = 1, 2, \cdots$, with $\bar{C}_n$ and $\bar{D}_n$, respectively, *i.e.*,

$$\begin{aligned} \delta_k &= \frac{2}{l} \sin \Lambda_k x_0 \sum_{n=1}^{\infty} (-1)^n \frac{\lambda_n}{\Lambda_k^2 - \lambda_n^2} \left[\bar{C}_n \sin c\lambda_n t_r + \bar{D}_n \cos c\lambda_n t_r\right] \\ \gamma_k &= \frac{2}{k\pi} \sin \Lambda_k x_0 \sum_{n=1}^{\infty} (-1)^n \frac{\lambda_n^2}{\Lambda_k^2 - \lambda_n^2} \left[\bar{C}_n \cos c\lambda_n t_r - \bar{D}_n \sin c\lambda_n t_r\right] \end{aligned} \tag{3.37}$$

The energy of the string after removal of the constraint is given by Eq. (3.26), namely

$$E_r = \frac{T\pi^2}{4l} \sum_{k=1}^{\infty} k^2 (\gamma_k^2 + \delta_k^2) \tag{3.38}$$

Similar to section 3.5, we rely on simulation results to claim $W_r = (E_r - E_c) = 0$. The net change in energy due to one cycle of constraint application and removal is therefore equal to

$$\Delta W = (W_c + W_r) = W_c = \frac{T\pi^2}{4}\sum_{n=1}^{\infty} n^2 \left[\frac{(\bar{C}_n^2 + \bar{D}_n^2)}{(l - x_0)} - \frac{(\bar{\gamma}_n^2 + \bar{\delta}_n^2)}{l}\right] \tag{3.39}$$

The effect of sequential application and removal of constraints can be investigated by defining $\bar{\gamma}_k = \gamma_k$, $\bar{\delta}_k = \delta_k$, $k = 1, 2, \cdots$, and $y_0(x,t) = y_r(x,t)$, and repeating the procedure outlined above.

3.6.2 Control strategy for vibration suppression

From our simulation results in section 3.5, we have seen that maximum reduction in energy is achieved if the constraint is applied when the displacement of the string is zero over the interval $[0, x_0)$. Since the string was assumed to be vibrating in its first mode, greater reduction in energy was achieved by simply choosing larger values of x_0. For arbitrary initial conditions, the displacement of the string can be uniformly zero only over a small length segment at some given time, and therefore, energy reduction can be ensured by choosing a small value of x_0. A small value of x_0 will result in less energy reduction but greater reduction in energy can be achieved by applying the constraint incrementally N times, for a total distance of Nx_0. Figure 3.4 shows a sensing scheme that can be employed to determine the time when the scabbard can move incrementally. The removal of the constraint will involve moving the scabbard to its original configuration after N applications of the constraint.

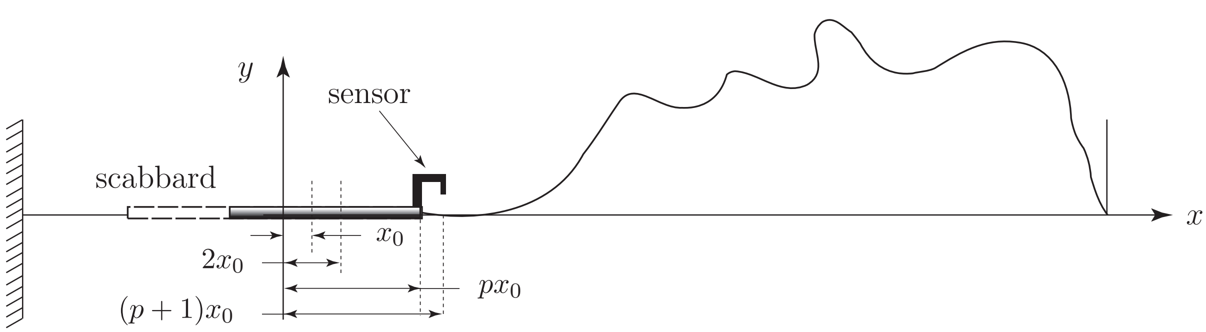

Figure 3.4: The sensor measures the displacement of the string at a distance x_0 from the tip of the scabbard. When this displacement is zero, the scabbard moves incrementally by distance x_0

In the sequel we provide the equations needed to describe the vibration of the string during the process of N applications and removal of the constraint. The initial conditions of the string are assumed to be arbitrary and hence its equation of motion is given by Eq. (3.29), namely

$$y_0(x,t) = \sum_{k=1}^{\infty} \sin \Lambda_k x \big[\bar{\gamma}_k \sin c\Lambda_k t + \bar{\delta}_k \cos c\Lambda_k t \big], \quad x \in [0,l] \tag{3.40}$$

We assume that the constraint is applied N times at $t = t_c^{(1)}, t_c^{(2)}, \cdots, t_c^{(N)}$, and removed at $t = t_r$, where $t_c^{(1)} < t_c^{(2)} < \cdots < t_c^{(N)} < t_r$. After the first application of the constraint, the equation of motion of the string has the form

$$y_1(x,t) = \begin{cases} 0 & : \ x \in [0, x_0) \\ \displaystyle\sum_{n=1}^{\infty} \sin \lambda_n^{(1)}(l-x) \big[\bar{C}_n^{(1)} \sin c\lambda_n^{(1)} t + \bar{D}_n^{(1)} \cos c\lambda_n^{(1)} t \big] & : \ x \in [x_0, l] \end{cases} \tag{3.41}$$

The above equation is identical to Eq. (3.31) with the only difference that $\bar{C}_n$ and $\bar{D}_n$, $n = 1, 2, \cdots$, and λ_n now have the superscript (1), which indicates that the constraint was applied at $t = t_c^{(1)}$. Using the same procedure as before, $y_0(x,t)$ and $y_1(x,t)$ in Eqs. (3.40) and (3.41) are compared over the interval $x \in [x_0, l]$ to determine $\bar{C}_n^{(1)}$ and $\bar{D}_n^{(1)}$

$$\bar{D}_n^{(1)} = \frac{2}{l - x_0} \sum_{k=1}^{\infty} (-1)^n \frac{\lambda_n^{(1)}}{\Lambda_k^2 - (\lambda_n^{(1)})^2} \sin \Lambda_k x_0 \big[\bar{\gamma}_k \sin c\Lambda_k t_c^{(1)} + \bar{\delta}_k \cos c\Lambda_k t_c^{(1)} \big] \tag{3.42}$$

and

$$\bar{C}_n^{(1)} = \frac{2}{nl} \sum_{k=1}^{\infty} (-1)^n \frac{k\lambda_n^{(1)}}{\Lambda_k^2 - (\lambda_n^{(1)})^2} \sin \Lambda_k x_0 \big[\bar{\gamma}_k \cos c\Lambda_k t_c^{(1)} - \bar{\delta}_k \sin c\Lambda_k t_c^{(1)} \big] \tag{3.43}$$

where

$$\lambda_n^{(p)} = \frac{n\pi}{l - px_0}, \quad p = 1, 2, \cdots, N \tag{3.44}$$

After the second application of the constraint, the equation of motion of the string has the form

$$y_2(x,t) = \begin{cases} 0 & : \; x \in [0, 2x_0) \\ \sum_{n=1}^{\infty} \sin \lambda_n^{(2)}(l-x)\big[\bar{C}_n^{(2)} \sin c\lambda_n^{(2)} t + \bar{D}_n^{(2)} \cos c\lambda_n^{(2)} t\big] & : \; x \in [2x_0, l] \end{cases} \tag{3.45}$$

By comparing $y_1(x,t)$ and $y_2(x,t)$ in Eqs. (3.41) and (3.45) over the interval $x \in [2x_0, l]$, $\bar{C}_n^{(2)}$ and $\bar{D}_n^{(2)}$, $n = 1, 2, \cdots$, are obtained as follows

$$\bar{D}_n^{(2)} = \frac{1}{l - 2x_0} \sum_{k=1}^{\infty} \big[\bar{C}_k^{(1)} \sin c\lambda_k^{(1)} t_c^{(2)} + \bar{D}_k^{(1)} \cos c\lambda_k^{(1)} t_c^{(2)}\big] U(k,1) \tag{3.46}$$

$$\bar{C}_n^{(2)} = \frac{1}{cn\pi} \sum_{k=1}^{\infty} c\lambda_k^{(1)} \big[\bar{C}_k^{(1)} \cos c\lambda_k^{(1)} t_c^{(2)} - \bar{D}_k^{(1)} \sin c\lambda_k^{(1)} t_c^{(2)}\big] U(k,1) \tag{3.47}$$

where

$$U(k,i) = \left\{\frac{\sin[(\lambda_n^{(i+1)} - \lambda_k^{(i)})(l-(i+1)x_0)]}{\lambda_n^{(i+1)} - \lambda_k^{(i)}}\right\} - \left\{\frac{\sin[(\lambda_n^{(i+1)} + \lambda_k^{(i)})(l-(i+1)x_0)]}{\lambda_n^{(i+1)} + \lambda_k^{(i)}}\right\} \tag{3.48}$$

The behavior of the string hereafter can be iteratively described by the relation

$$y_p(x,t) = \begin{cases} 0 & : \; x \in [0, px_0) \\ \sum_{n=1}^{\infty} \sin \lambda_n^{(p)}(l-x)\big[\bar{C}_n^{(p)} \sin c\lambda_n^{(p)} t + \bar{D}_n^{(p)} \cos c\lambda_n^{(p)} t\big] & : \; x \in [px_0, l] \end{cases} \tag{3.49}$$

where $p = 2, 3, \cdots, N$, and $\bar{C}_n^{(p)}$ and $\bar{D}_n^{(p)}$, $n = 1, 2, \cdots$, are given by the expressions

$$\begin{aligned} \bar{D}_n^{(p)} &= \frac{1}{l - px_0} \sum_{k=1}^{\infty} \big[\bar{C}_k^{(p-1)} \sin c\lambda_k^{(p-1)} t_c^{(p)} + \bar{D}_k^{(p-1)} \cos c\lambda_k^{(p-1)} t_c^{(p)}\big] U(k, p-1) \\ \bar{C}_n^{(p)} &= \frac{1}{cn\pi} \sum_{k=1}^{\infty} c\lambda_k^{(p-1)} \big[\bar{C}_k^{(p-1)} \cos c\lambda_k^{(p-1)} t_c^{(p)} - \bar{D}_k^{(p-1)} \sin c\lambda_k^{(p-1)} t_c^{(p)}\big] U(k, p-1) \end{aligned} \tag{3.50}$$

The scabbard is moved back to its original configuration after it reaches its maximum travel distance Nx_0, and this completes one cycle of constraint application and removal. The equation of motion of the string after constraint removal is given by Eq. (3.36), namely

$$y_r(x,t) = \sum_{k=1}^{\infty} \sin \Lambda_k x \big[\gamma_k \sin c\Lambda_k t + \delta_k \cos c\Lambda_k t\big], \quad x \in [0, l] \tag{3.51}$$

where γ_k, δ_k, $k = 1, 2, \cdots$, are defined in terms of $\bar{C}_n^{(N)}$ and $\bar{D}_n^{(N)}$ as follows

$$\delta_k = \frac{2}{l} \sin \Lambda_k N x_0 \sum_{n=1}^{\infty} (-1)^n \frac{\lambda_n^{(N)}}{\Lambda_k^2 - (\lambda_n^{(N)})^2} \big[\bar{C}_n^{(N)} \sin c\lambda_n^{(N)} t_r + \bar{D}_n^{(N)} \cos c\lambda_n^{(N)} t_r\big] \tag{3.52}$$

and

$$\gamma_k = \frac{2}{k\pi} \sin \Lambda_k N x_0 \sum_{n=1}^{\infty} (-1)^n \frac{(\lambda_n^{(N)})^2}{\Lambda_k^2 - (\lambda_n^{(N)})^2} \big[\bar{C}_n^{(N)} \cos c\lambda_n^{(N)} t_r - \bar{D}_n^{(N)} \sin c\lambda_n^{(N)} t_r\big] \tag{3.53}$$

Similar to Eq. (3.39), the work done in one cycle of constraint application and removal can be shown to be

$$\Delta W = (W_c + W_r) = W_c = \frac{T\pi^2}{4}\sum_{n=1}^{\infty} n^2 \left[\frac{\{(\bar{C}_n^{(N)})^2 + (\bar{D}_n^{(N)})^2\}}{(l - Nx_0)} - \frac{\{\bar{\gamma}_n^2 + \bar{\delta}_n^2\}}{l} \right] \tag{3.54}$$

Since the sensing scheme in Fig. 3.4 allows negative work to be done each time the scabbard is moved incrementally, the net work done in each cycle of constraint application and removal will be negative.

We define the work done after a number of constraint applications as the cost function, where

$$J = \sum_{k=0}^{N} E_{k+1} - E_k \tag{3.55}$$

where, E_{k+1} is total energy after k constraint application and E_k is the total energy before k constraint application. And the cost is $J = (E_1 - E_0) + (E_2 - E_1) + \cdots + (E_{N-1} - E_{N-2}) + (E_N - E_{N-1})$, then

$$J = E_N - E_0 \tag{3.56}$$

To perform the control, we sense the states during the motion by the mean of a sensor. Where the sensor reads the displacement at $x = (p+1)x_0$ i.e $\hat{y} = y((p+1)x_0, t)$ and $\dot{\hat{y}} = \dot{y}((p+1)x_0, t)$ as shown in Fig. 3.4, and the control strategy becomes

$$u_k = \begin{cases} x_0 & : \ |\hat{y}_k| \simeq 0, \ |\dot{\hat{y}}_k| > 0, \ t = t_k \\ 0 & : \ t = t_k + t_r \end{cases} \tag{3.57}$$

The condition of $|\hat{y}_k| \simeq 0$ guarantees the potential energy is minimum in the controlled segment, and $|\dot{\hat{y}}_k| > 0$ guarantees the kinetic energy $K_e > 0$ where K_e will be the reduction in total system energy. t_r is the time of constraint removal.

3.6.3 Numerical simulations

Similar to our example in section 3.5, we consider a string of length $l = 4$ m, mass per unit length $\rho = 0.25$ kg/m, and tension $T = 1$ N, vibrating in its first mode with amplitude $A_0 = 0.1$ m. At $t = 0$ the string is assumed to pass through its mean position, and the equation of motion of the string is therefore

$$y_0(x,t) = 0.1 \sin(\frac{\pi}{4}x)\, \sin(\frac{\pi}{2}t)$$

We simulate 12 cycles of constraint application and removal with constraint application occurring incrementally in each cycle with $x_0 = 0.05l$ and $N = 3$, as discussed in section 3.6.2. In each cycle, the constraints are applied at the earliest instant of time, when the string displacement is zero at the sensor[2] location. For the first cycle, this is illustrated with the help of Fig. 3.5, which shows the displacement and percentage energy loss of the string at different time instances.

The constraint can be removed at any time t_r, $t_r > t_c^{(3)}$, and there is flexibility in choosing t_r. In Table 3.2 and Fig. 3.6, we present simulation results for the two cases:

(A): the constraint is removed when the sensor measures zero displacement, and

(B): the constraint is removed when the sensor records the maximum displacement.

From the data in Table 3.2, it is clear that case (B) results in significantly higher reduction in energy in comparison to case (A). Although constraint removal does not change the

[2]The sensor measures the displacement of the string at a distance x_0 from the scabbard - see Fig. 3.4. Since x_0 is small, a zero sensor reading implies that the string has almost zero displacement over the entire interval $x \in [0, x_0)$.

overall energy of the string, the configuration of the string at the time of constraint removal determines how energy of the constrained string is redistributed over the entire length; and this has a significant effect on the rate of energy reduction in subsequent cycles of constraint application. Beginning with the last plots in Fig. 3.5 and Fig. 3.6 shows the configuration of the string at the instant of time when the constraint is removed in the first cycle for cases (A) and (B). It also shows the maximum displacement of the string after the completion of 12 cycles for the two cases. The maximum displacement plots corroborate that the energy content of the string for case (B) is much less than that of case (A). The plots in Fig. 3.6 can explain why case (B) results in higher reduction in energy. In case (B), the constraint is removed when the string has the maximum deformation. This effectively results in plucking of the string (without addition of energy), which excites the high-frequency modes of the string and transfer of energy into these modes. When a significant fraction of energy is funneled into the high-frequency modes, the scabbard is more effective in energy reduction since these modes have higher energy density than the low-frequency modes for the same amplitude of vibration. It can be verified from Fig. 3.6 that the string, after 12 cycles, predominantly vibrates in its first mode for case (A) but has many high-frequency components for case (B).

Table 3.2: Comparison of percentage energy loss of the string for cases (A) and (B) over 12 cycles of constraint application and removal

No.	1	2	3	4	5	6	7	8	9	10	11	12
(A)	0.88	5.52	9.83	15.94	16.33	16.37	16.46	16.50	16.54	16.58	16.60	16.64
(B)	0.88	3.78	9.07	17.14	23.56	31.42	44.14	46.19	46.95	47.25	56.32	57.25

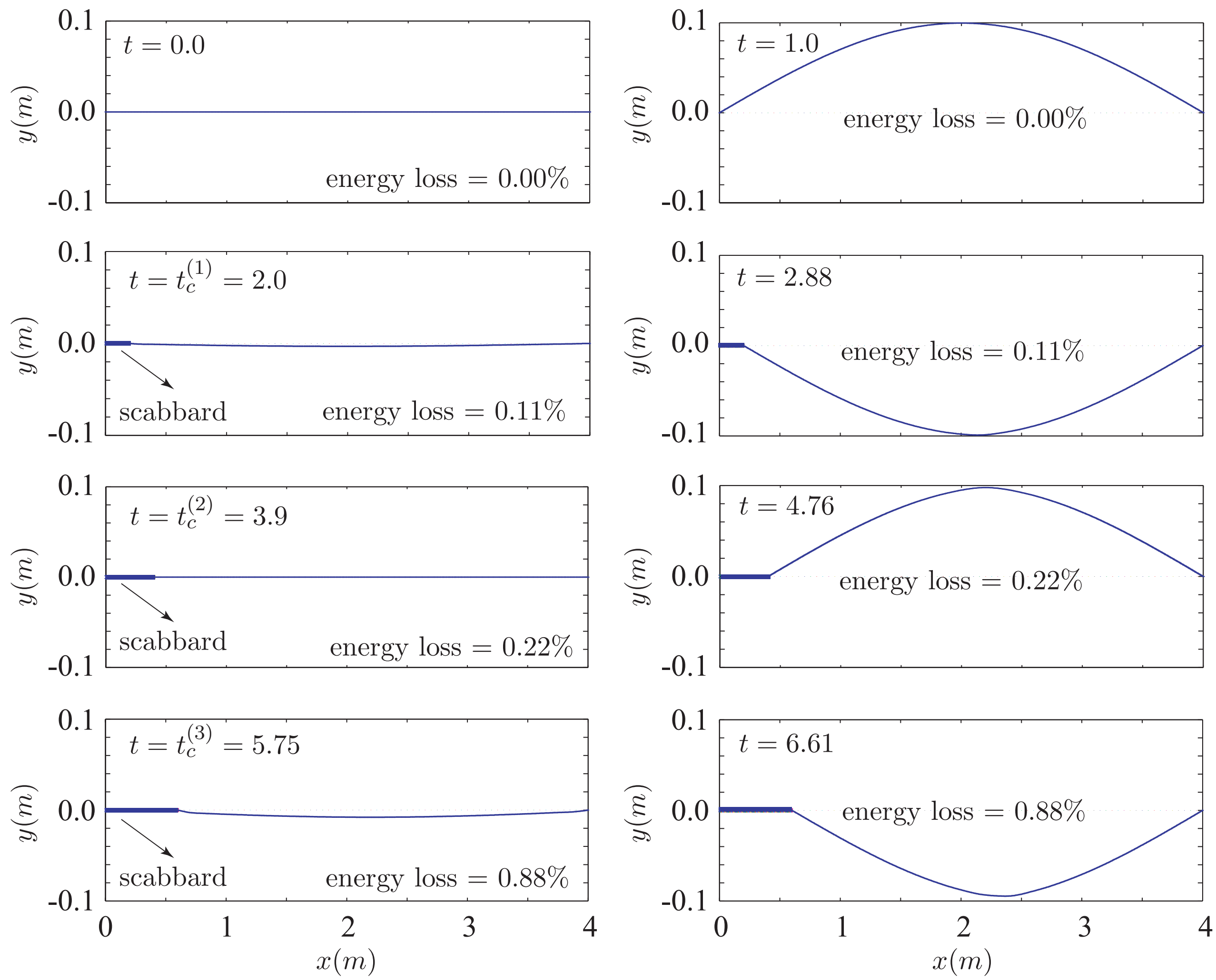

Figure 3.5: Displacement of the string and percentage energy loss at different time instants during the first cycle of constraint application

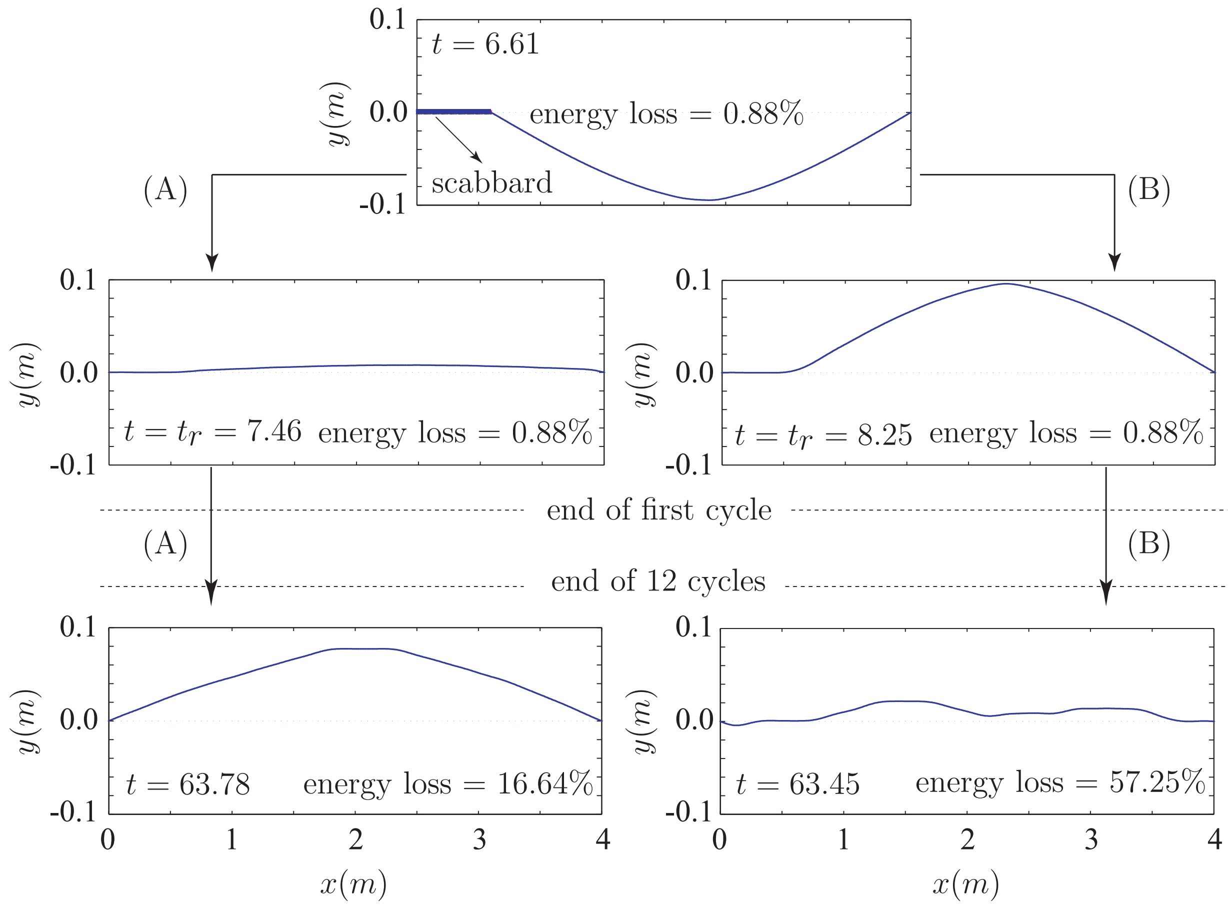

Figure 3.6: Displacement and percentage energy loss of the string at the end of the first cycle and after completion of 12 cycles of constraint application and removal for cases (A) and (B)

Chapter 4

Vibration Control of a String Through Cyclic Application and Removal of Constraints: Experimental Verification

4.1 Introduction

In Chapter 3 we presented a control strategy for the vibration control of string by using scabbard-like actuator. The scabbard-like actuator is difficult to implement in hardware and an alternate actuation mechanism is therefore proposed in this chapter. In this chapter we present an experimental control methodology that verifies the idea of the scabbard-like actuator method in which energy reduction is achieved through cyclic application and removal of a constraint. In our method, a zero-displacement constraint is enforced at one point on the string, close to one of its boundaries. This effectively results in two vibrating strings, one of which is much shorter in length than the other. The vibration of the shorter length string decays rapidly due to high internal damping and when the constraint is released, the remaining energy of the string is redistributed over its entire length; this allows the cycle of constraint application and removal to be repeated for vibration suppression. This chapter is organized as follows. In Section 4.2 we present the mathematical model of the effect of constraint application and removal, including change in energy of the string. This modeling effort is similar to the one presented in Chapter 3 but includes damping; the addition of damping allows us to compare simulation and experimental results. We use a stretched coil extension spring as a string in our experiments. A coil extension spring can easily store potential energy during stretching, and as a consequence has low damping - this makes it well-suited for vibration control experiments. Although a stretched coil extension spring was used earlier by Kashy, et al [77], we present experimental results to justify its use as a string. These results are presented in Section 4.3. Section 4.3 also contains experimental results that are used to identify the damping coefficient of the spring-string. Simulation and experimental results of vibration suppression are presented in Section 4.4 - these results establish the feasibility of vibration suppression through application and removal of constraints.

4.2 Cyclic Application and Removal of Constraint

4.2.1 Actuation and Sensing Mechanism

We propose the mechanism in Fig. 4.1 for constraint application and removal. It is comprised of a pair of solenoids that can impose a zero velocity constraint at one point on the string, located at a distance of x_0 from the boundary. An optical sensor, located at a distance of η from the solenoids, measures the distance of the string from its mean position. The solenoids are activated when the sensor indicates that the string is passing through its mean position, *i.e.* $y(x_0+\eta) = 0$. Since η is a small distance by design, the solenoids impose the zero velocity constraint when $y(x_0) \approx 0$, *i.e.*, the solenoids impose a zero displacement constraint. This is necessary to ensure that the constraint does not alter the equilibrium configuration of the string. The zero displacement constraint virtually results in two vibrating strings over the intervals $x \in [0, x_0)$ and $x \in (x_0, l]$. The distance x_0 is a small fraction of the total length l by design and consequently the string vibrating over the interval $x \in [0, x_0)$ will have a much higher natural frequency and damping. This implies that the energy of the shorter string will dissipate quickly and naturally, and subsequent de-activation of the solenoids will result in redistribution of the remaining energy of the string over its entire length. Each cycle of solenoid activation and de-activation (constraint application and removal) will reduce the energy of the string and eventually result in vibration suppression.

The actuation mechanism in Fig. 4.1 is fundamentally similar to the scabbard-like actuator in Chapter 3. By applying a zero displacement constraint over a small length of string that is passing through its mean position, the scabbard proposes to remove kinetic energy of the small string segment through impact. In contrast, the mechanism in Fig. 4.1 imposes a zero displacement constraint at one point of the string. This point is proximal to one fixed support and therefore the energy trapped in the string between the point of application of the constraint and the proximal support is dissipated naturally. The time required for natural dissipation depends on the distance of the point of application of the constraint and the proximal boundary - a smaller distance results in faster dissipation and vice versa.

The scabbard proposes to dissipate the energy of the small string segment instantaneously through impact, but it is difficult to implement.

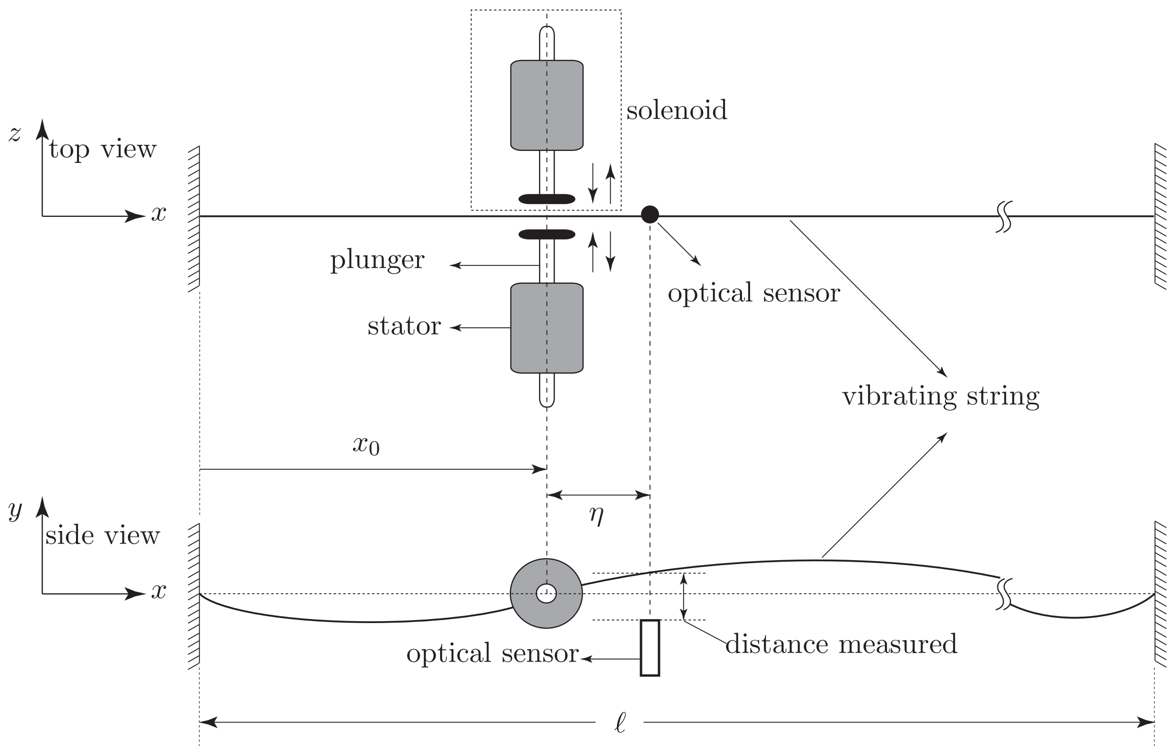

Figure 4.1: Actuation and sensing mechanism for application and removal of constraint

4.2.2 Mathematical Modeling

4.2.2.1 Linear model of vibrating string with damping

In this section we consider a mathematical model of the string and compute the change in energy of the string due to constraint application and constraint removal. To include damping, we consider the mathematical model from [78]

$$T\frac{\partial^2 y}{\partial x^2} = \rho\frac{\partial^2 y}{\partial t^2} + C\frac{\partial y}{\partial t} \tag{4.1}$$

where T is the tension, ρ is the mass per unit length, and C is the damping coefficient of the string. Through separation of variables $y(x,t) = X(x)\,\phi(t)$, we get

$$\frac{1}{X}\frac{\partial^2 X}{\partial x^2} = \frac{1}{\phi}\frac{1}{c^2}\left[\frac{\partial^2 \phi}{\partial t^2} + K\frac{\partial \phi}{\partial t}\right] = -\lambda^2, \qquad K \triangleq C/\rho, \qquad c \triangleq \sqrt{T/\rho}$$

where λ is constant. The above equation gives

$$\begin{aligned} \frac{\partial^2 X}{\partial x^2} + \lambda^2 X = 0 \quad &\Rightarrow \quad X(x) = \{\alpha \cos \lambda x + \beta \sin \lambda x\} \\ \frac{\partial^2 \phi}{\partial t^2} + K\frac{\partial \phi}{\partial t} + c^2\lambda^2\phi = 0 \quad &\Rightarrow \quad \phi(t) = e^{-\zeta\omega t}\left\{A\cos(\omega\sqrt{1-\zeta^2})t + B\sin(\omega\sqrt{1-\zeta^2})t\right\} \end{aligned}$$

and leads to the general solution

$$y(x,t) = e^{-\zeta\omega t}\{\alpha \cos \lambda x + \beta \sin \lambda x\}\left\{A\cos(\omega\sqrt{1-\zeta^2})t + B\sin(\omega\sqrt{1-\zeta^2})t\right\} \tag{4.2}$$

where

$$\omega \triangleq c\lambda, \qquad \zeta \triangleq K/(2c\lambda)$$

Assuming the string to be of length ℓ and applying the boundary conditions $y(0,t) = y(\ell,t) = 0$ or $X(0) = X(\ell) = 0$, we get

$$X(x) = \beta_n \sin \lambda_n x, \qquad \lambda_n = \frac{n\pi}{\ell}, \qquad n = 1, 2, \cdots, \infty$$

The general solution then takes the form

$$y(x,t) = \sum_{n=1}^{\infty} \phi_n(t) \sin \lambda_n x \tag{4.3}$$

where

$$\phi_n(t) = e^{-\zeta_n \omega_n t}\left\{A_n \cos(\omega_n\sqrt{1-\zeta_n^2})t + B_n \sin(\omega_n\sqrt{1-\zeta_n^2})t\right\}$$

and

$$\omega_n \triangleq c\lambda_n, \quad \zeta_n \triangleq K/(2c\lambda_n)$$

The total energy of the string is the sum of its potential and kinetic energy

$$E(t) = \frac{\rho}{2}\int_0^\ell \left[\frac{\partial y(x,t)}{\partial t}\right]^2 dx + \frac{T}{2}\int_0^\ell \left[\frac{\partial y(x,t)}{\partial x}\right]^2 dx \tag{4.4}$$

Substituting Eq. (4.3) into Eq. (4.4), we get

$$\begin{aligned} E(t) \;=\; & \frac{\rho}{2}\int_0^\ell \left[\sum_{n=1}^{\infty} \dot{\phi}_n(t)\sin\lambda_n x\right]\left[\sum_{m=1}^{\infty} \dot{\phi}_m(t)\sin\lambda_m x\right] dx \\ & +\frac{T}{2}\int_0^\ell \left[\sum_{n=1}^{\infty} \lambda_n\,\phi_n(t)\cos\lambda_n x\right]\left[\sum_{m=1}^{\infty} \lambda_m\,\phi_m(t)\cos\lambda_m x\right] dx \end{aligned}$$

Using the orthogonality property of the modes and simplifying, we get

$$E(t) = \frac{\rho\ell}{4}\sum_{n=1}^{\infty} \dot{\phi}_n^2(t) + \frac{T\ell}{4}\sum_{n=1}^{\infty} \lambda_n^2\,\phi_n^2(t) \tag{4.5}$$

4.2.2.2 Effect of constraint application

To obtain the equation of motion of the string after the constraint is applied, we solve Eq. (4.1) subject to initial and boundary conditions consistent with the constraint. Assuming the solution to be of the form $y_c(x,t) = \bar{X}(x)\,\bar{\phi}(t)$, where

$$\bar{X}(x) = \left\{\bar{\alpha}\cos\bar{\lambda}x + \bar{\beta}\sin\bar{\lambda}x\right\}$$

and

$$\bar{\phi}(t) = e^{-\bar{\zeta}\bar{\omega}t} \left\{ \bar{A}\cos(\bar{\omega}\sqrt{1-\bar{\zeta}^2})t + \bar{B}\sin(\bar{\omega}\sqrt{1-\bar{\zeta}^2})t \right\}$$

application of the boundary conditions $y_c(x_0, t) = y_c(\ell, t) = 0$ or $\bar{X}(x_0) = \bar{X}(\ell) = 0$ yields

$$\bar{X}(x) = \bar{\beta}_m \sin\bar{\lambda}_m(\ell - x), \qquad \bar{\lambda}_m = \frac{m\pi}{\ell - x_0}, \qquad m = 1, 2, \cdots, \infty$$

The constrained solution then takes the form

$$y_c(x,t) = \sum_{m=1}^{\infty} \bar{\phi}_m(t)\sin\bar{\lambda}_m(\ell - x) \tag{4.6}$$

where

$$\bar{\phi}_m(t) = e^{-\bar{\zeta}_m\bar{\omega}_m t} \left\{ \bar{A}_m\cos(\bar{\omega}_m\sqrt{1-\bar{\zeta}_m^2})t + \bar{B}_m\sin(\bar{\omega}_m\sqrt{1-\bar{\zeta}_m^2})t \right\}$$

and

$$\bar{\omega}_m \triangleq c\bar{\lambda}_m, \quad \bar{\zeta}_m \triangleq K/(2c\bar{\lambda}_m)$$

If the constraint is applied at time $t = t_c$, we have the following conditions:

A1. $y_c(x, 0) = y(x, t_c)$. From Eqs. (4.3) and (4.6) we can write

$$\sum_{m=1}^{\infty} \bar{A}_m \sin\bar{\lambda}_m(\ell - x) = \sum_{n=1}^{\infty} \phi_n(t_c)\sin\lambda_n x \tag{4.7}$$

where $\phi_n(t)$ was defined after Eq. (4.3). Multiplying both sides by $\sin\bar{\lambda}_m(\ell - x)$ and integrating with respect to x from x_0 to ℓ, we get

$$\begin{aligned}\bar{A}_m &= \frac{2}{\ell - x_0}\sum_{n=1}^{\infty}\phi_n(t_c)\int_{x_0}^{\ell}\sin\bar{\lambda}_m(\ell - x)\sin\lambda_n x\,dx \\ &= \frac{2}{\ell - x_0}\sum_{n=1}^{\infty}(-1)^m\phi_n(t_c)\frac{\bar{\lambda}_m}{\lambda_n^2 - \bar{\lambda}_m^2}\sin\lambda_n x_0 \qquad (4.8)\end{aligned}$$

A2. $\dot{y}_c(x,0) = \dot{y}(x,t_c)$. From Eqs. (4.3) and (4.6) we can again write

$$\sum_{m=1}^{\infty}\bar{\omega}_m\left(\sqrt{1-\bar{\zeta}_m^2}\,\bar{B}_m - \bar{\zeta}_m\bar{A}_m\right)\sin\bar{\lambda}_m(\ell - x) = \sum_{n=1}^{\infty}\dot{\phi}_n(t_c)\sin\lambda_n x \qquad (4.9)$$

Multiplying both sides by $\sin\bar{\lambda}_m(\ell - x)$, integrating with respect to x from x_0 to ℓ, we get

$$\bar{B}_m = \frac{1}{\bar{\omega}_m\sqrt{1-\bar{\zeta}_m^2}}\left[\bar{\zeta}_m\,\bar{\omega}_m\bar{A}_m + \frac{2}{\ell - x_0}\sum_{n=1}^{\infty}(-1)^m\dot{\phi}_n(t_c)\frac{\bar{\lambda}_m}{\lambda_n^2 - \bar{\lambda}_m^2}\sin\lambda_n x_0\right] \qquad (4.10)$$

where $\bar{A}_m$ is defined by Eq. (4.8).

The energy of the string after application of the constraint is given by the relation

$$E_c(t) = \frac{\rho}{2}\int_{x_0}^{\ell}\left[\frac{\partial y_c(x,t)}{\partial t}\right]^2 dx + \frac{T}{2}\int_{x_0}^{\ell}\left[\frac{\partial y_c(x,t)}{\partial x}\right]^2 dx \qquad (4.11)$$

Substituting Eq. (4.6) and simplifying using orthogonality property of the modes, we get

$$E_c(t) = \frac{\rho(\ell - x_0)}{4}\sum_{m=1}^{\infty}\dot{\bar{\phi}}_m^2(t) + \frac{T(\ell - x_0)}{4}\sum_{m=1}^{\infty}\bar{\lambda}_m^2\,\bar{\phi}_m^2(t) \qquad (4.12)$$

The work done by application of the constraint can be simply computed as

$$W_c = E_c(t_c) - E(t_c) \tag{4.13}$$

4.2.2.3 Effect of constraint removal

After removal of the constraint, the equation of motion of the string will be described by the relation

$$y_r(x,t) = \sum_{n=1}^{\infty} e^{-\zeta_n \omega_n t} \left\{ \mu_n \cos(\omega_n \sqrt{1-\zeta_n^2})t + \nu_n \sin(\omega_n \sqrt{1-\zeta_n^2})t \right\} \sin \lambda_n x \tag{4.14}$$

where

$$\omega_n \triangleq c\lambda_n, \quad \zeta_n \triangleq K/(2c\lambda_n)$$

If the constraint is applied at time $t = t_r$, we have the following conditions:

A1. $y_r(x,0) = y_c(x,t_r)$. From Eqs. (4.6) and (4.14) we can write

$$\sum_{n=1}^{\infty} \mu_n \sin \lambda_n x = \sum_{m=1}^{\infty} \bar{\phi}_m(t_r) \sin \bar{\lambda}_m(\ell - x) \tag{4.15}$$

where $\bar{\phi}_m(t)$ was defined after Eq. (4.6). Multiplying both sides by $\sin \lambda_n x$ and integrating with respect to x from 0 to ℓ, we get

$$\begin{aligned} \mu_n &= \frac{2}{\ell} \sum_{m=1}^{\infty} \bar{\phi}_m(t_r) \int_{x_0}^{\ell} \sin \bar{\lambda}_m(\ell - x) \sin \lambda_n x \; dx \\ &= \frac{2}{\ell} \sum_{m=1}^{\infty} (-1)^m \bar{\phi}_m(t_r) \frac{\bar{\lambda}_m}{\lambda_n^2 - \bar{\lambda}_m^2} \sin \lambda_n x_0 \end{aligned} \tag{4.16}$$

A2. $\dot{y}_r(x,0) = \dot{y}_c(x,t_r)$. From Eqs. (4.6) and (4.14) we can again write

$$\sum_{n=1}^{\infty} \omega_n \left(\sqrt{1-\zeta_n^2}\, \nu_n - \zeta_n\, \mu_n \right) \sin \lambda_n x = \sum_{m=1}^{\infty} \dot{\bar{\phi}}_m(t_r) \sin \bar{\lambda}_m (\ell - x) \tag{4.17}$$

Multiplying both sides by $\sin \lambda_n x$, integrating with respect to x from 0 to ℓ, we get

$$\nu_n = \frac{1}{\omega_n \sqrt{1-\zeta_n^2}} \left[\zeta_n\, \omega_n\, \mu_n + \frac{2}{\ell} \sum_{m=1}^{\infty} (-1)^m \dot{\bar{\phi}}_m(t_r) \frac{\bar{\lambda}_m}{\lambda_n^2 - \bar{\lambda}_m^2} \sin \lambda_n x_0 \right] \tag{4.18}$$

where μ_n is defined by Eq. (4.16).

Once the values of μ_n and ν_n have been determined, we update the values of A_n and B_n as follows

$$A_n = \mu_n, \qquad B_n = \nu_n, \qquad n = 1, 2, \cdots, \infty$$

The change in the energy of the string due to constraint removal can now be computed as

$$W_r = E(t_r) - E_c(t_r) \tag{4.19}$$

The update in the values of A_n and B_n also allow us to repeat the process of constraint application and removal.

4.3 Experimental Setup

4.3.1 Coil Extension Spring - A Substitute for the String

A traditional string has high damping and is not well-suited for vibration control experiments. As a substitute for the string, we used a stretched coil extension spring which has low damping. The material and geometric specifications of the spring [79] used in experiments are provided in Table 4.1:

Table 4.1: Specifications of coil extension spring

Material	Outside diameter	Inside diameter	Wire diameter
Steel	2.032 mm	1.016 mm	0.508 mm

A sample spring of free length 2.286 m (90 in) was found to have a mass of 0.034 kg. The mass per unit length of the spring is therefore $\rho_S = 0.0149$ kg/m. Using a known load, the stiffness of the spring in tension was computed to be $k_S = 150.42$ N/m. The experimental setup is shown in Fig. 4.2. In this setup, the distance between the fixed supports is $\ell = 1.64$ m. The spring clamped between these supports had a free length of 1.525 m; the tension in the spring is therefore $T = k_S \Delta = 150.42 \times (1.64 - 1.525) = 17.29$ N. The spring was given an arbitrary initial displacement and the sensor was used to measure the displacement of one point on the string - see Fig. 4.2. The sensor data was recorded for 100 sec at 1000 samples/sec. The natural frequencies of free vibration of the spring were computed from the FFT of the sensor data and are shown in Table 4.2. The data indicates $\omega_2 \approx 2\omega_1$, $\omega_3 \approx 3\omega_1$ and $\omega_4 \approx 4\omega_1$. This is characteristic of vibrating strings and therefore the coil extension spring is a good substitute for the string.

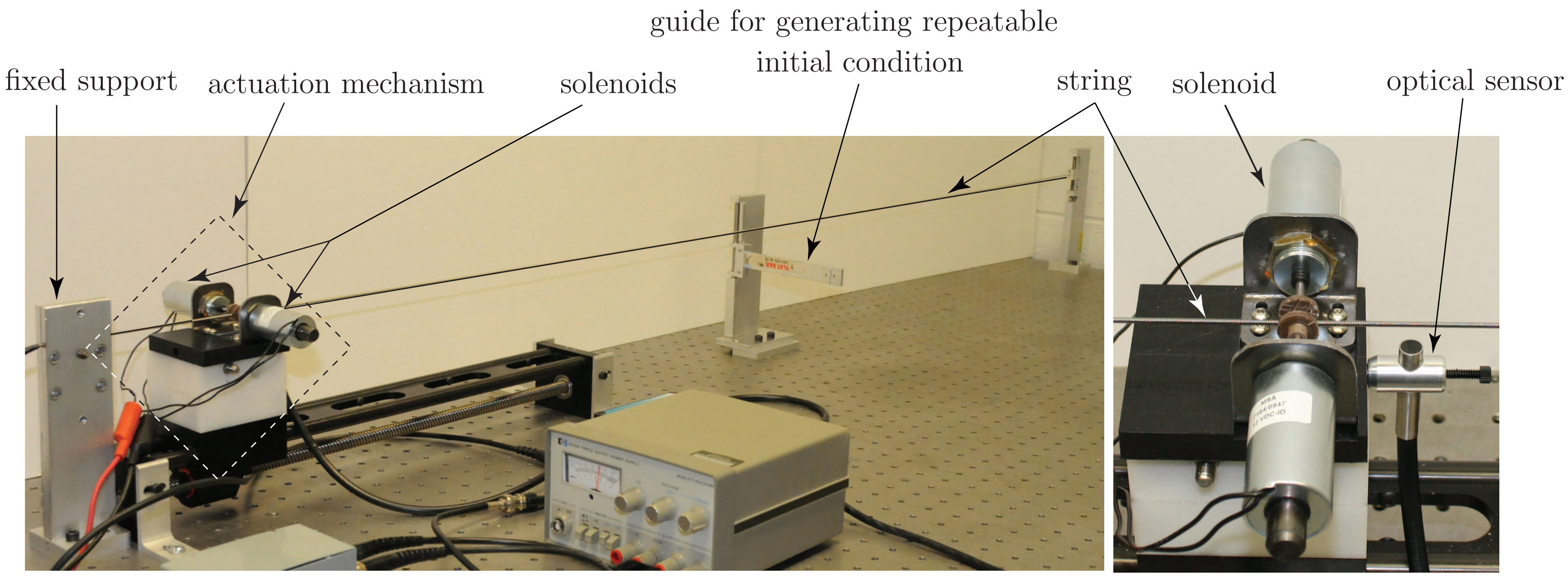

(a) (b)

Figure 4.2: (a) Experimental setup showing the string between two fixed supports and the actuation mechanism, (b) A close-up view of the actuation mechanism and sensor

Treating the spring as a string, the mass per unit length of the string was computed from the first natural frequency in Table 4.2, using the relation

$$\rho = T\left(\frac{\pi}{\ell\,\omega_1}\right)^2 = 0.0164 \ \ \mathrm{kg/m} \tag{4.20}$$

This is higher than the mass per unit length of the spring, $\rho_S = 0.0149$ kg/m. In our simulations, we will use the value of mass per unit length of the equivalent string, $\rho = 0.0164$ kg/m.

Table 4.2: Experimentally determined natural frequencies of the spring/string in rad/s

Units	ω_1	ω_2	ω_3	ω_4
rad/s	62.07	124.15	186.29	248.37
Hz	9.88	19.76	29.65	39.53

4.3.2 Internal Damping of the String

4.3.2.1 Estimation of Damping Ratio

In order to compare simulation and experimental results on vibration suppression, it is necessary to determine the internal damping of the string. To this end, we collected experimental data on the string vibrating freely in the first mode and computed the damping ratio ζ using the method of logarithmic decrement

$$\zeta = \left[1 + (2\pi/\delta)^2\right]^{-1/2}, \qquad \delta = \frac{1}{k}\ln\left(\frac{x_i}{x_{k+i}}\right)$$

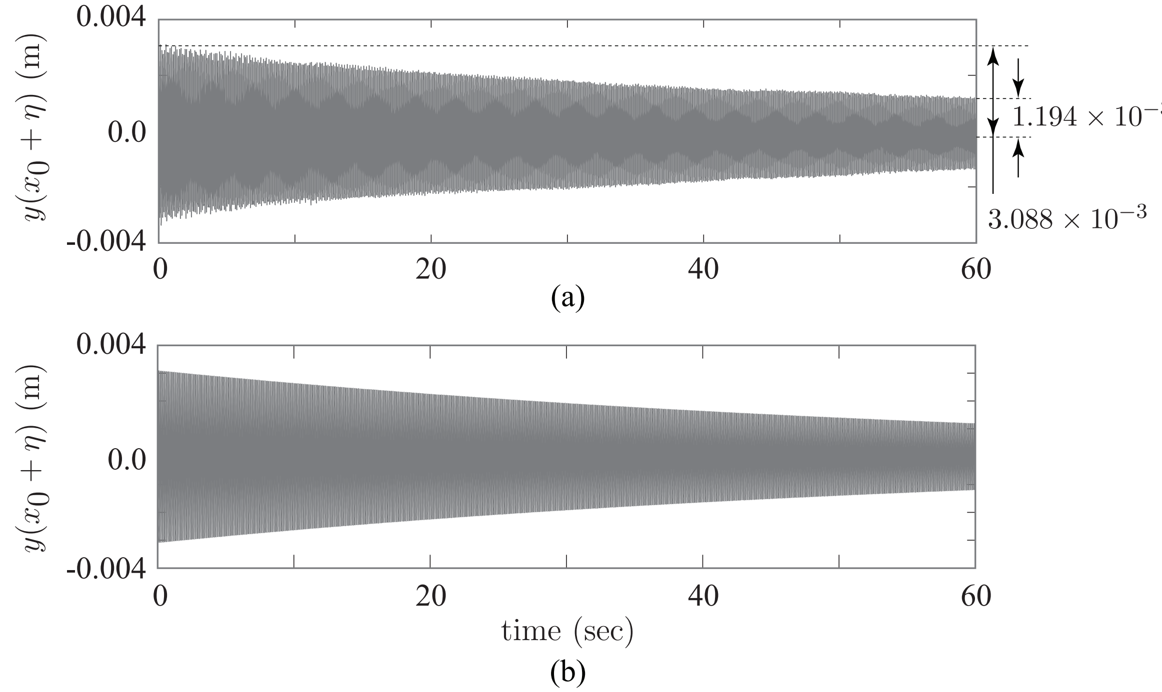

Figure 4.3: Free vibration of a string: (a) Experimental results for the string in Fig. 4.2 (b) Simulation results obtained using a damping ratio computed from the experimental results in (a)

The experimental data is shown in Fig. 4.3 (a). For this data, we had $x_i = 3.088 \times 10^{-3}$ m, $x_{k+i} = 1.194 \times 10^{-3}$ m and $k = 591$; this gives $\zeta = 2.56 \times 10^{-4}$. Using this value of ζ and values of T and ρ obtained experimentally, we simulated free vibration of the string in its first mode. The results are shown in Fig. 4.3 (b); they match quite well with the experimental results in Fig. 4.3 (a) and provide confidence in our mathematical model.

4.3.2.2 Variation of Damping Coefficient with Length

The damping ratio $\zeta = 2.56 \times 10^{-4}$ was determined experimentally for the string vibrating in its first mode. The product of the damping ratio and the natural frequency is therefore

$$\zeta\omega = 2.56 \times 10^{-4} \times 62.07 = 0.0159 \ \text{rad/s}$$

The product $\zeta\omega$ was assumed to be constant in our mathematical model since it is proportional to the damping coefficient C ($\zeta\omega = C/2\rho$). To investigate the validity of this assumption, we present experimental results on variation of the product $\zeta\omega$ with change in length of the string. The results, shown in Fig. 4.4, indicate that $\zeta\omega$ initially remains constant but increases rapidly thereafter as the length is decreased. The trend is consistently observed with three different strings, namely:

(1) string described in Section 3.1 with stiffness $k_S = 150.42$ N/m and tension $T = 17.29$ N;

(2) string with spring coil diameter smaller than that of string (1) but of higher stiffness $k_S = 284.90$ N/m and with higher tension $T = 34.50$ N; and

(3) string with spring coil diameter similar to that of string (1) and same tension as that of string (1) but of lower stiffness $k_S = 47.5$ N/m.

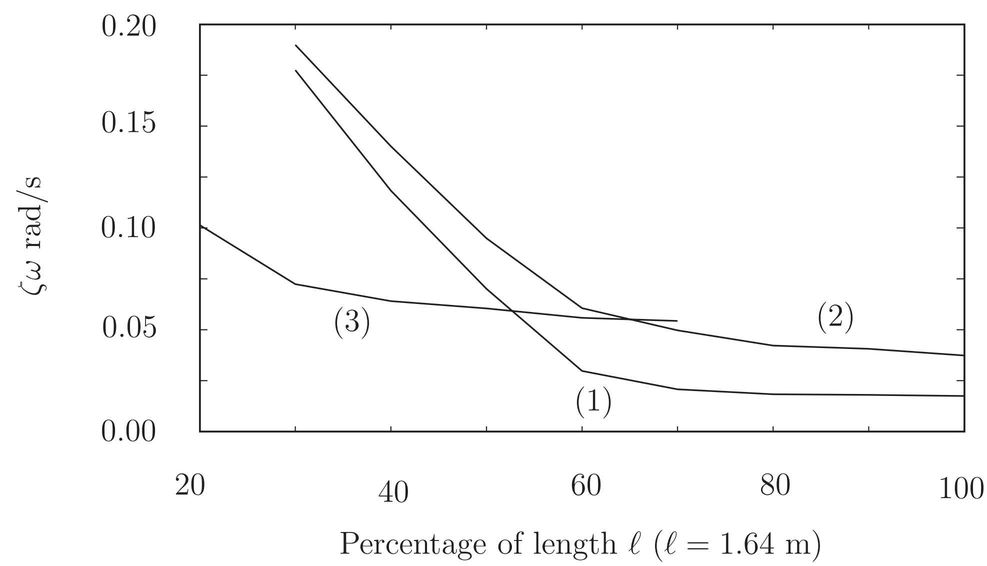

Figure 4.4: Effect of changing the length of the string on the product $\zeta\omega$ for three different strings

4.4 Simulation and Experimental Results on Vibration Suppression

For simulations, we used the mathematical model in Eq. (4.3) with the following parameter values

$$\ell = 1.64 \text{ m}, \qquad T = 17.29 \text{ N}, \qquad \rho = 0.0164 \text{ kg/m}, \qquad \zeta = 2.56 \times 10^{-4}$$

which were obtained experimentally. To be consistent with our experimental setup, we used

$$x_0 = 0.1\,\ell = 0.164 \text{ m}, \qquad \eta = 0.04 \text{ m}$$

The string was given the displacement shown in Fig. 4.5 with $d = \ell/2 = 0.82$ m and $h = 0.01$ m, and released from rest at the initial time. This initial condition, which can be mathematically described as follows

$$y(x,0) = f(x) = \begin{cases} -\dfrac{h}{d}\,x & 0 \le x \le d \\ \\ -\dfrac{h}{\ell - d}\,(\ell - x) & d \le x \le \ell \end{cases}, \qquad \dot{y}(x,0) = g(x) = 0$$

excites all modes of vibration. The modal coefficients can be determined from the expression for $y(x,t)$ in Eq. (4.3) and its derivative, as follows

$$\sum_{n=1}^{\infty} A_n \sin \lambda_n x = f(x)$$

$$\Rightarrow \qquad A_n = -\frac{2}{\ell}\left[\frac{h}{d}\int_0^d x \,\sin\frac{n\pi}{\ell}x\,dx + \frac{h}{\ell - d}\int_d^\ell (\ell - x)\sin\frac{n\pi}{\ell}x\,dx\right] = \frac{2h\ell^2}{n^2\pi^2 d(\ell - d)}\sin\frac{n\pi}{\ell}d$$

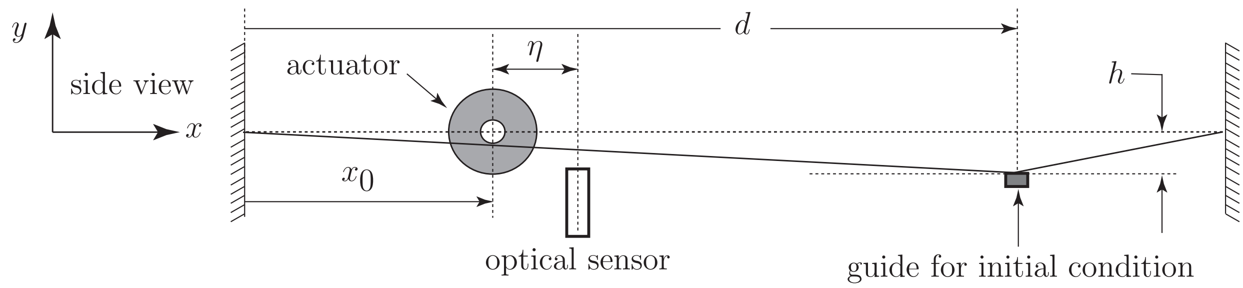

Figure 4.5: Initial displacement of the string used for both simulations and experiments. The guide for generating repeatable initial conditions in experiments can be seen in Fig. 4.2

$$\begin{aligned}
&\sum_{n=1}^{\infty}\left[\omega_n\sqrt{1-\zeta_n^2}\,B_n-\zeta_n\omega_n\,A_n\right]\sin\lambda_n x=g(x)=0\\
\Rightarrow\quad &B_n=\frac{\zeta_n}{\sqrt{1-\zeta_n^2}}A_n \qquad (4.21)
\end{aligned}$$

The constraint was applied when the sensed point on the string passes through its mean position, *i.e.*, $y(x_0+\eta)\approx 0$. The constraint was released exactly 0.5 sec after the constraint was applied. The time interval of 0.5 sec is provided to allow vibration of the string over the interval $[0, x_0)$ to dissipate naturally. In Fig. 4.6 (a), we present simulation results for $N = 12$ cycles of constraint application and removal with a time interval of 0.5 sec between cycles and with $n = 3$ modes. The experimental results are shown in Fig. 4.6 (b). The initial condition used in our experiment was identical to that used in simulations and facilitated by the guide for generating repeatable initial conditions shown in Fig. 4.2.

The following observations can be made from the simulation and experimental results in Fig. 4.6:

- The time duration of active control is almost identical in simulations and experiments, slightly greater than 12 sec. It includes 12 cycles of constraint application and removal with a minimum duration of 1.0 sec per cycle.

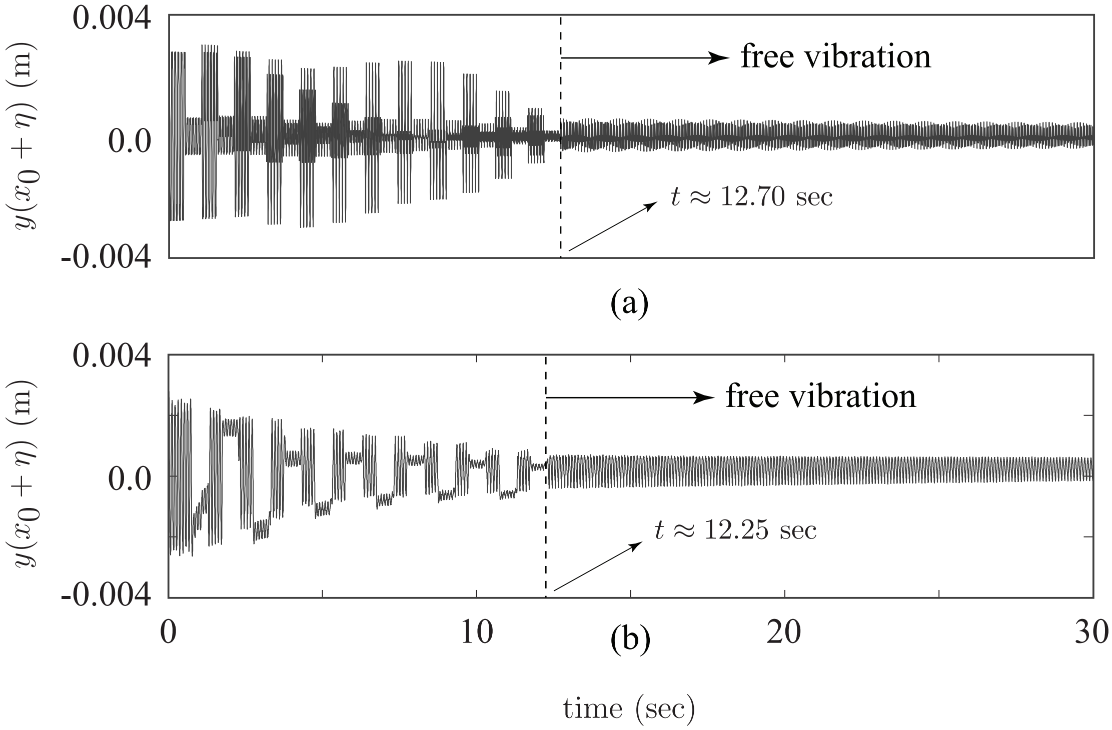

Figure 4.6: Results of vibration suppression obtained from (a) simulations and (b) experiments

- For the period of time that the constraint is active, the amplitude of vibration is significantly lower than when the constraint is not active. This is due to the fact that constraint application results in a temporary boundary at $x = x_0$ and Fig. 4.6 plots the displacement of the string at $x = x_0 + \eta$, *i.e.*, at a small distance η from this boundary.

- In simulations, the constrained string vibrates about the mean position of the unconstrained string - see plot (a), but in experiments it has a positive or a negative offset - see plot (b). This is because it is possible to apply the constraint exactly when the string is passing through its mean position in simulations; the same is difficult to achieve in experiments due to reaction time of the solenoids. It may be noted that the solenoids fail to keep the string completely constrained during the first cycle of experiments. At this time the string has a large amount of energy and the friction forces between the string and the solenoid plungers are insufficient to prevent some slipping.

- At the initial time, we had $d = 0.82$ m, $h = 0.01$ m, $x_0 = 0.164$ m and $\eta = 0.04$ m. This corresponds to $y(x_0 + \eta) = 2.48 \times 10^{-3}$ m - see Fig. 4.5. The initial amplitudes of vibration in Fig. 4.6 matches well with this number.

- The ratio of the initial amplitude of vibration to the amplitude of vibration immediately after active control is terminated is 4.29 for simulation results in plot (a) and 4.98 for experimental results in plot (b). Assuming only the first mode of vibration to be present, these numbers correspond to $\approx 94.5\%$ and $\approx 95.9\%$ of energy dissipation for simulations and experiments, respectively. The large percentage of energy dissipation is indicative of the effectiveness of the control strategy.

- The simulation results in plot (a) indicate the presence of higher modes after termination of active control. The experimental results in plot (b) indicate that only the first mode is present and the higher modes have dissipated. This suggests that the damping ratio ζ may not be constant across modes; a higher damping ratio for the higher modes may have contributed to higher energy dissipation in experiments compared to simulations.

4.5 Additional Investigations

4.5.1 Efficacy of Vibration Suppression - A Parametric Study

The efficacy of vibration suppression through constraint application and removal depends on several parameters. In this section, we present a parametric experimental study to illustrate the effect of three specific parameters, namely:

A1. (x_0/ℓ): Location of constraint from proximal boundary

A2. t_r: Duration of time for which the constraint is applied, and

A3. N: Number of times the constraint is applied and removed

on the settling time. We define the settling time as the time required for the amplitude of vibration to decay to 20% of its initial value. For a string vibrating predominantly in its first mode, this corresponds to the time required for dissipation of $\approx$ 96% of the energy. The results of settling time are presented in Table 4.3. These results indicate that larger number of cycles of constraint application and removal (higher value of N) results in smaller settling time, *i.e.*, faster vibration suppression, independent of the values of (x_0/ℓ) and t_r. Also, larger values of (x_0/ℓ) require proportionately longer time of application t_r, for the shortest settling time. It can be seen that independent of the value of N, $t_r = 0.5$ results in the the shortest settling time for $(x_0/\ell) = 0.05$, $t_r = 1.0$ results in the the shortest settling time for $(x_0/\ell) = 0.10$, and $t_r = 1.5$ results in the the shortest settling time for $(x_0/\ell) = 0.15$. This because a larger value of x_0 lowers the frequency of vibration of the constrained string segment and increases the time required for natural dissipation of energy in this segment. From the above discussion, it is clear that $t_r = 0.5$ and $N = 12$ provides the

Table 4.3: Effect of three different parameters: (x_0/ℓ), t_r, and N on the settling time

	(x_0/ℓ)=0.05		(x_0/ℓ)=0.10		(x_0/ℓ)=0.15	
t_r (sec)	$N = 6$	$N = 12$	$N = 6$	$N = 12$	$N = 6$	$N = 12$
0.5	51.61	43.44	64.52	38.12	72.21	65.32
1.0	57.42	46.63	54.70	30.43	70.46	53.18
1.5	60.32	47.44	63.66	43.22	62.44	28.07

optimal settling time for $(x_0/\ell) = 0.05$; $t_r = 1.0$ and $N = 12$ provides the optimal settling time for $(x_0/\ell) = 0.10$; and $t_r = 1.5$ and $N = 12$ provides the optimal settling time for $(x_0/\ell) = 0.15$. These three cases are highlighted in Table 4.3. Among them, $(x_0/\ell) = 0.15$ has the shortest settling time. Simulation and experimental results for shaded results in table 4.3 are presented in Figs. 4.7, 4.8 and 4.9 respectively. These figures show good match in reduction of vibration amplitude and settling time t_s.

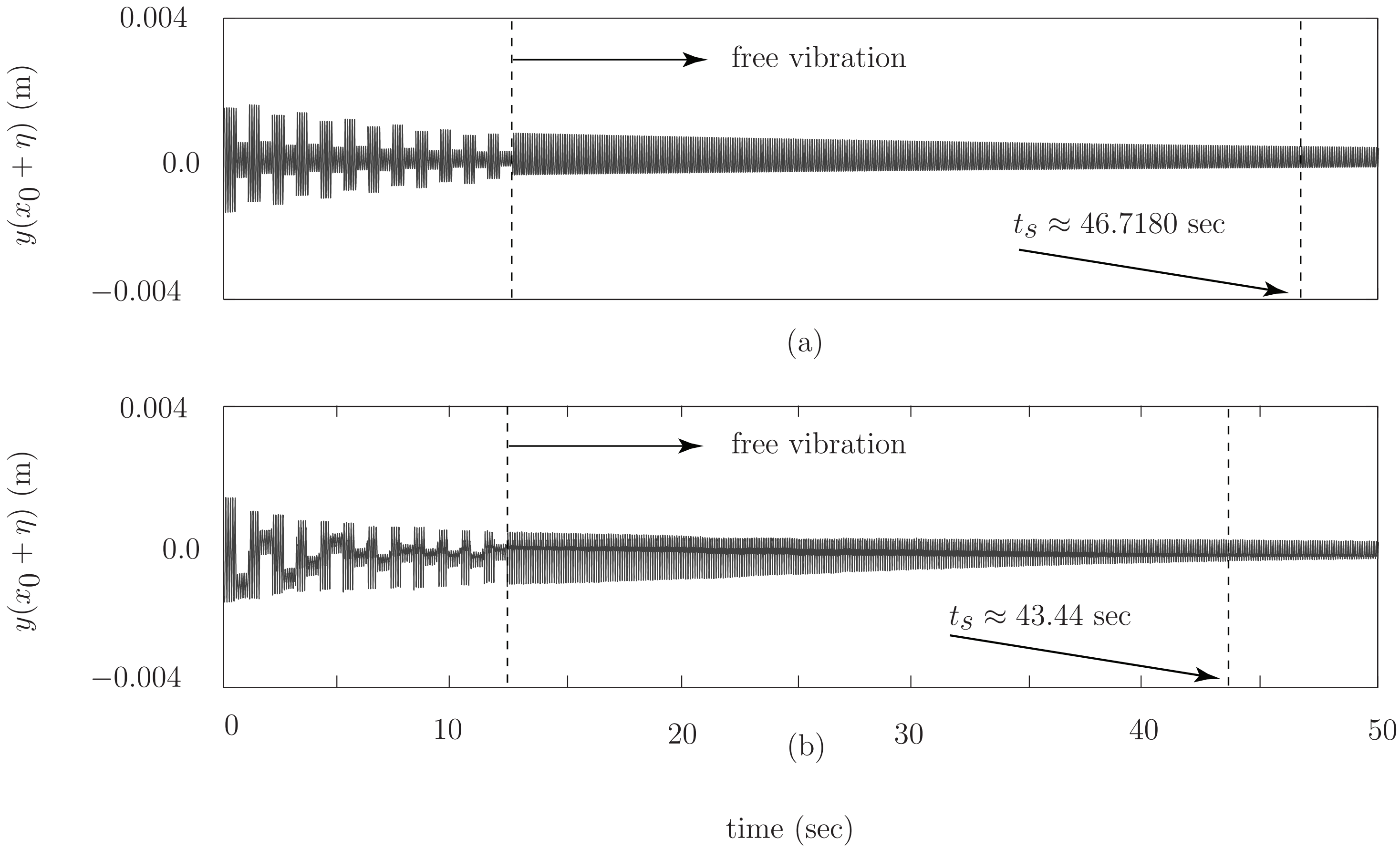

Figure 4.7: Results of vibration suppression obtained from (a) simulations and (b) experiments, with $(x_0/\ell) = 0.05$, $t_r = 0.5$ s, and $N = 12$

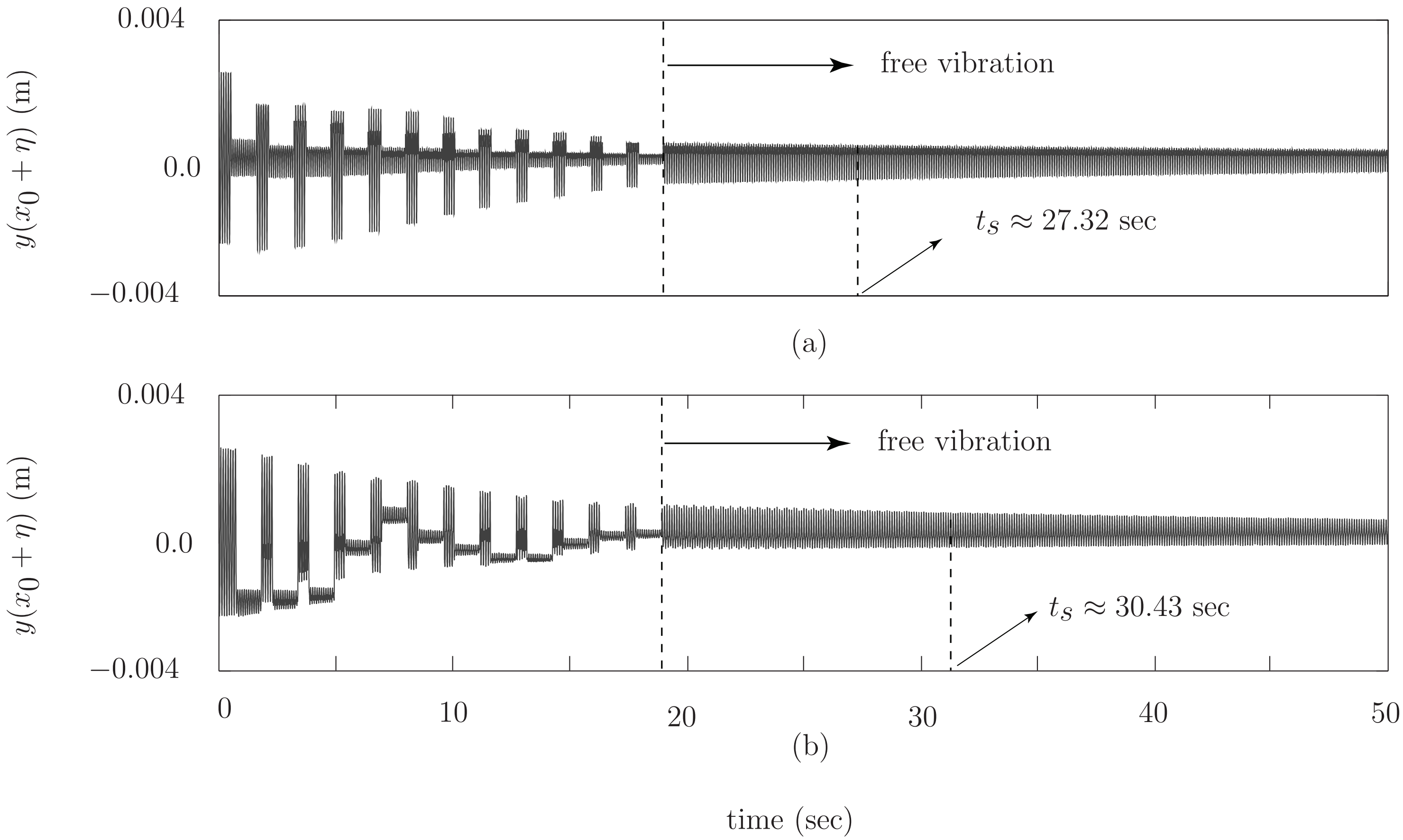

Figure 4.8: Results of vibration suppression obtained from (a) simulations and (b) experiments, with $(x_0/\ell) = 0.10$, $t_r = 1$ s, and $N = 12$

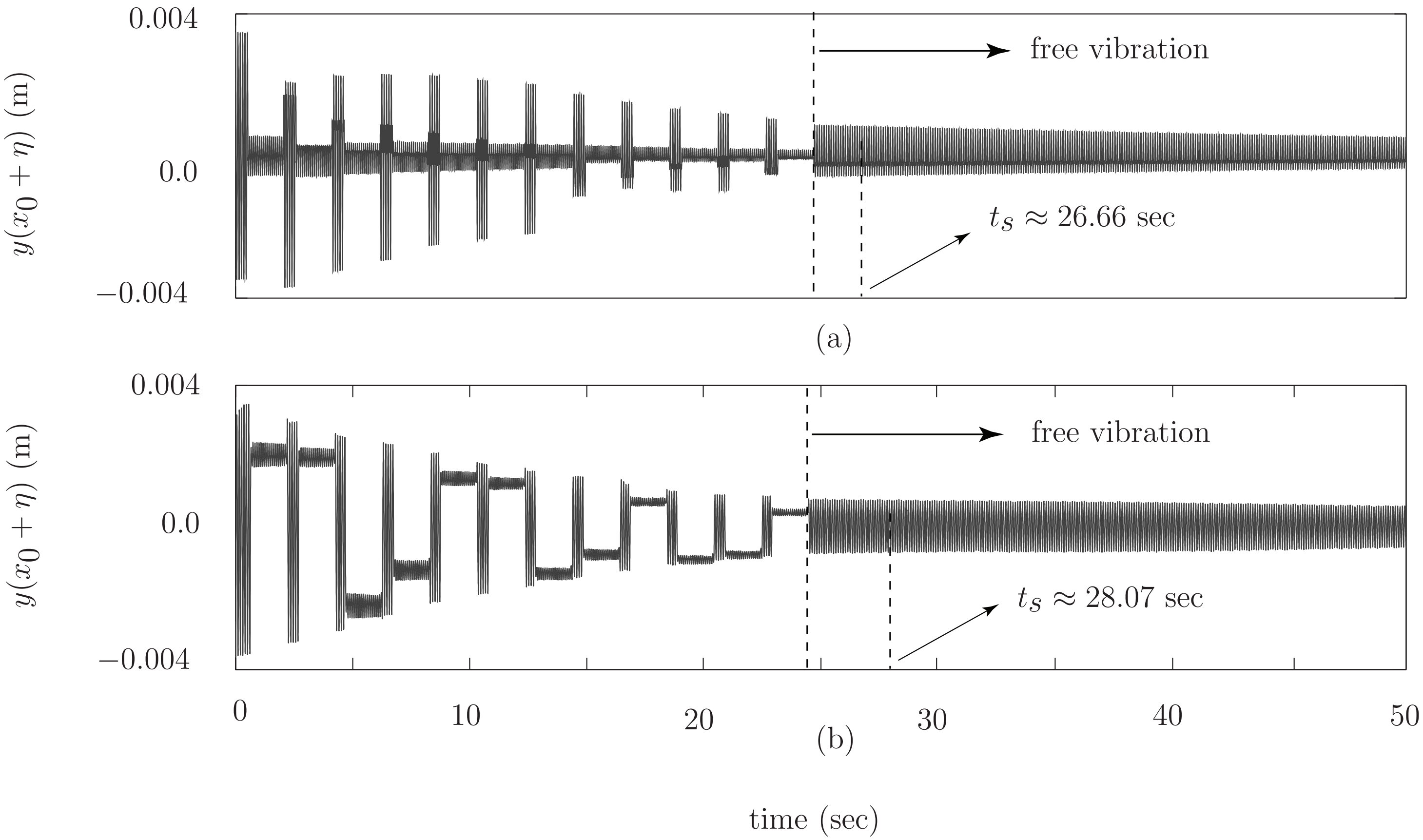

Figure 4.9: Results of vibration suppression obtained from (a) simulations and (b) experiments, with $(x_0/\ell) = 0.15$, $t_r = 1.5$ s, and $N = 12$

4.5.2 Excitation of Higher Modes

The energy dissipation mechanism proposed in this chapter relies on trapping energy in a short segment of the string, which is dissipated naturally due to high internal damping. The energy of the string is also dissipated through excitation of high-frequency modes in the longer segment of the string. The high-frequency modes are excited each time the constraint is applied or removed; this can be explained mathematically by the mapping between Fourier coefficients describing the motion of the string in the constrained and unconstrained states. The high-frequency modes also have high rates of damping, and although they do not decay out as quickly as the vibration in the short string segment, energy transfer to these modes facilitate vibration suppression.

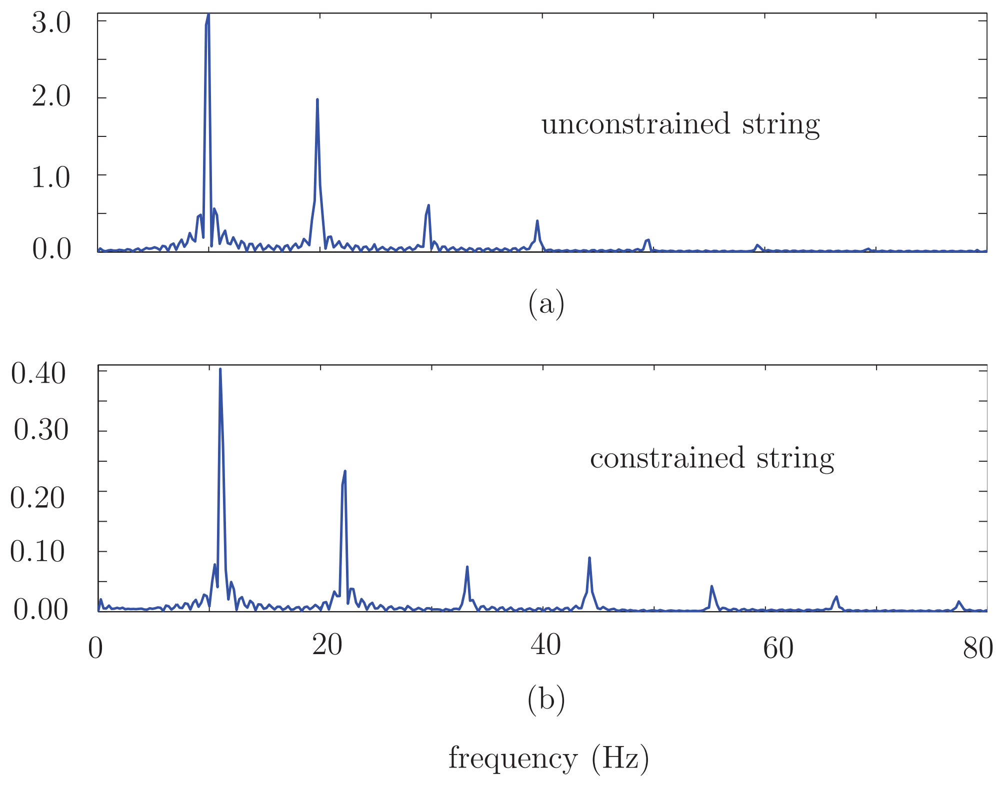

Figure 4.10: Fast Fourier-Transform results showing multiple modes of vibration of the (a) unconstrained string and (b) constrained string

We present results of fast Fourier-Transform (FFT) of the string vibration collected over 3 sec, both after application and after removal of the constraint. These plots shown in Fig. 4.8 indicate that at least six higher modes are excited. The FFT plots indicate that the frequencies of the constrained string are slightly higher than those of the unconstrained string. This is because of the shorter length of the constrained string. The amplitudes of the constrained string in the FFT plot are however lower than those of the unconstrained string. This is because the sensor is located closer to the boundary when the string is constrained than when it is unconstrained.

Chapter 5

Dynamics of a Circular Membrane with an Eccentric Circular Areal Constraint: Analysis and Accurate Simulations

The studies on vibration of constrained circular membrane are restrict to the determination of the eigenfrequencies where most of the results in the literature typically compute the first few eigenfrequencies of vibration but they do not provide a method to simulate the dynamics accurately. The simulation of the dynamics requires computation of modal coefficients using orthogonality properties of the modes. Although orthogonality properties of modes are well-known, they have not been established mathematically for constrained membranes. We present orthogonality properties of all modes of a circular membrane with an internal circular areal constraint for the first time in this chapter. The computation of the modal coefficients require accurate computation of the mode shapes and this requires proper choice of the number of angular modes. This chapter is organized as follows. A formal problem statement and a list of assumptions are provided in Section 5.1. The expression for the symmetric and antisymmetric modes are derived in Section 5.2 using Lin's analysis [46]. In Section 5.3, we establish orthogonality between the symmetric modes, the antisymmetric modes, and between symmetric and antisymmetric modes. In Section 5.4 we provide the algorithm for accurate computation of the mode shapes, and in Section 5.5 we provide the algorithm for computation of modal coefficients. The dynamics of a constrained membrane is simulated at the end of Section 5.5.

5.1 Problem Statement and Assumptions

Consider the circular membrane of radius R and outer boundary Γ_O, shown in Fig. 5.1. A circular area of radius a and boundary Γ_i, located at a distance d from the center of the membrane, has zero displacement at all times; this constrains the dynamics of the membrane. To study the vibration of the active region of the membrane, we make the following assumptions:

A1. The membrane is homogeneous and has a constant mass per unit area equal to μ. The tension in the membrane is equal to T and remains constant at all times. The membrane undergoes transverse vibration and it is not affected by gravity.

A2. The amplitude of oscillation of the membrane is small and its motion can be expressed by the standard relation in polar coordinates [75]:

$$\frac{\partial^2 Z}{\partial r^2} + \frac{1}{r}\frac{\partial Z}{\partial r} + \frac{1}{r^2}\frac{\partial^2 Z}{\partial \theta^2} = \frac{1}{c^2}\frac{\partial^2 Z}{\partial t^2}, \qquad c = \sqrt{T/\mu} \tag{5.1}$$

where $Z = Z(r, \theta, t)$ is the transverse displacement. The distance of any point P is measured from the center of the inner circle O and is denoted by r; θ denotes the angle that vector r makes with the x-axis.

A3. The transverse displacement of all points in the area enclosed by the inner circle is zero, *i.e.*, $Z(r, \theta, t) = 0$ for $r \in [0, a]$, $\theta \in [0, 2\pi]$. The displacement of the membrane is also zero along the outer boundary Γ_O.

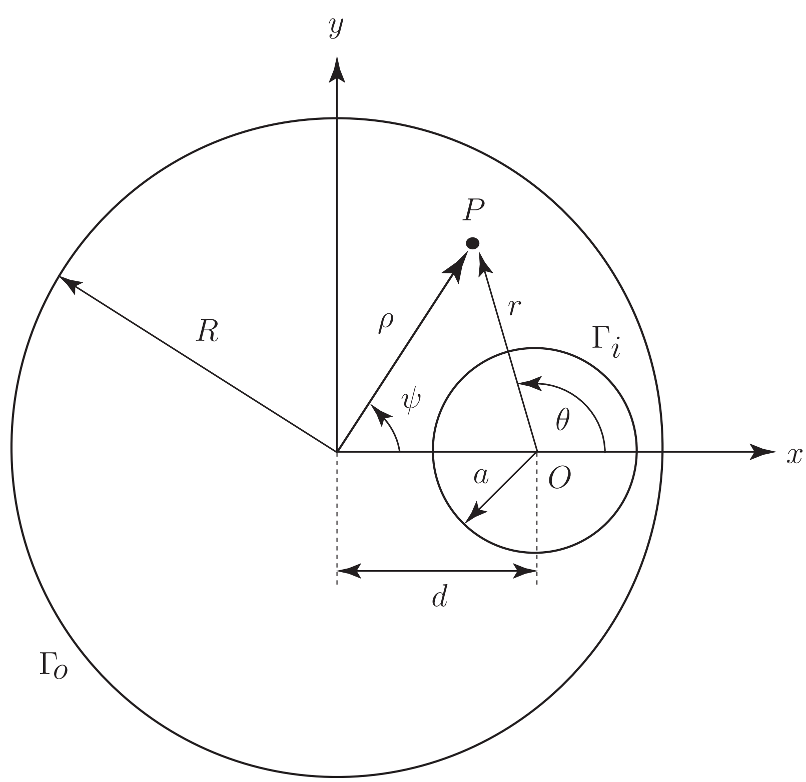

Figure 5.1: A circular membrane with an inner circular areal constraint

5.2 Background - Modes of Vibration

5.2.1 General Solution

A general solution to Eq. (5.1) is obtained by separation of variables. Assuming $Z(r, \theta, t) = \varphi(r, \theta)\, F(t)$ and rearranging terms, we get

$$\frac{1}{\varphi}\{\frac{\partial^2 \varphi}{\partial r^2} + \frac{1}{r}\frac{\partial \varphi}{\partial r} + \frac{1}{r^2}\frac{\partial^2 \varphi}{\partial \theta^2}\} = \frac{1}{c^2}\frac{1}{F}\frac{\partial^2 F}{\partial t^2} \tag{5.2}$$

Let $-k^2$ be the separation constant. Then, the right-hand side of Eq. (5.2) gives

$$\frac{1}{c^2}\frac{1}{F}\frac{\partial^2 F}{\partial t^2} = -k^2, \quad \text{or} \quad \frac{\partial^2 F}{\partial t^2} + c^2 k^2 F = 0$$

If we define the natural frequency $\omega \triangleq ck$[1], we get

$$F(t) = A \cos \omega t + B \sin \omega t \tag{5.3}$$

where A and B are constants whose values depend on initial conditions. Equating the left-hand side of Eq. (5.2) to $-k^2$ and rearranging terms, we get

$$r^2 \frac{\partial^2 \varphi}{\partial r^2} + r\frac{\partial \varphi}{\partial r} + k^2 r^2 \varphi = -\frac{\partial^2 \varphi}{\partial \theta^2} \tag{5.4}$$

To separate the radial and angular terms in Eq. (5.4), we substitute $\varphi(r, \theta) = U(r)\, V(\theta)$;

[1]The separation constant k is related to the natural frequency by the relation $k = \omega/c$ and has the unit of rad/m. Since c is a constant, the value of k is proportional to the frequency. In the sequel we will refer to k as the eigenfrequency.

this yields

$$\frac{1}{U}\{r^2\frac{\partial^2 U}{\partial r^2}+r\frac{\partial U}{\partial r}+k^2r^2\}=-\frac{1}{V}\frac{\partial^2 V}{\partial\theta^2} \tag{5.5}$$

By choosing m^2 to be the separation constant, we get

$$\frac{1}{V}\frac{\partial^2 V}{\partial\theta^2}=-m^2, \qquad \Rightarrow \qquad V(\theta)=C_m\cos m\theta+D_m\sin m\theta \tag{5.6}$$

where C_m and D_m are constants whose values depend on initial conditions. Since we have

$$V(\pi)=V(-\pi), \qquad \frac{\partial V}{\partial\theta}(\pi)=\frac{\partial V}{\partial\theta}(-\pi)$$

it can be shown that m^2 takes integer values $0, 1, 2, \cdots$. From the left-hand side of Eq. (5.5) we get

$$r^2\frac{\partial^2 U}{\partial r^2}+r\frac{\partial U}{\partial r}+(k^2r^2-m^2)U=0 \tag{5.7}$$

For any integer value of m, the general solution to Eq. (5.7) is as follows:

$$U(r)=\beta_m\,J_m(kr)+\gamma_m\,Y_m(kr)$$

where β_m and γ_m are constants, and $J_m(kr)$ and $Y_m(kr)$ are Bessel functions [75] of the first and second kind, respectively. The general solution to the equation of motion of the

[2]The integer m is the number of angular nodes. For an unconstrained membrane, it is equal to the number of diametrical lines along which the membrane has zero displacement

circular membrane can now be written as

$$Z(r,\theta,t) = \sum_{m=0}^{\infty} \{\beta_m J_m(kr) + \gamma_m Y_m(kr)\} \times \\ \{C_m \cos m\theta + D_m \sin m\theta\} \{A \cos \omega t + B \sin \omega t\} \tag{5.8}$$

The solution in Eq. (5.8) can be rewritten as

$$Z(r,\theta,t) = \left\{\varphi^s(r,\theta) + \varphi^c(r,\theta)\right\} \{A \cos \omega t + B \sin \omega t\} \tag{5.9}$$

where

$$\begin{aligned} \varphi^s(r,\theta) &= \sum_{m=1}^{\infty} \{\beta_{1m} J_m(kr) + \gamma_{1m} Y_m(kr)\} \sin m\theta \\ \varphi^c(r,\theta) &= \sum_{m=0}^{\infty} \{\beta_{2m} J_m(kr) + \gamma_{2m} Y_m(kr)\} \cos m\theta \end{aligned} \tag{5.10}$$

and $\beta_{1m} = \beta_m D_m$, $\gamma_{1m} = \gamma_m D_m$, $\beta_{2m} = \beta_m C_m$ and $\gamma_{1m} = \gamma_m C_m$. The constants in Eq. (5.9), namely, k, A, B, m, β_{1m}, γ_{1m}, β_{2m}, γ_{2m}, can be determined by applying boundary conditions and initial conditions.

5.2.2 Boundary Conditions

The circular membrane is assumed to be fixed from the outer boundary and with presence of the internal circular constraint, the outer boundary of the constraint is assumed to be fixed. The boundary conditions can be written as:

A1. The membrane has zero displacement for $r = a$. From Eq. (5.9) we get

$$Z(a, \theta, t) = \left\{\varphi^{s}(a, \theta) + \varphi^{c}(a, \theta)\right\} \{A \cos \omega t + B \sin \omega t\} = 0$$

This implies $\{\varphi^{s}(a, \theta) + \varphi^{c}(a, \theta)\} = 0$, or

$$\begin{aligned} &\sum_{m=1}^{\infty} \{\beta_{1m} J_m(ka) + \gamma_{1m} Y_m(ka)\} \sin m\theta \\ + &\sum_{m=0}^{\infty} \{\beta_{2m} J_m(ka) + \gamma_{2m} Y_m(ka)\} \cos m\theta = 0 \end{aligned} \tag{5.11}$$

A2. The membrane has zero displacement for all r values for which $\rho = R$. This implies

$$\begin{aligned} &\sum_{m=1}^{\infty} \left\{\beta_{1m} J_m(kr|_{\rho=R}) + \gamma_{1m} Y_m(kr|_{\rho=R})\right\} \sin m\theta \ + \\ &\sum_{m=0}^{\infty} \left\{\beta_{2m} J_m(kr|_{\rho=R}) + \gamma_{2m} Y_m(kr|_{\rho=R})\right\} \cos m\theta = 0 \end{aligned} \tag{5.12}$$

The solutions to Eqs. (5.11) and (5.12) were investigated by several researchers [2], [46], [47], [3] and the eigenfrequencies were determined for the even (symmetric) and the odd (antisymmetric) modes[3].

5.2.3 Even or Symmetric Modes

The symmetric modes are associated with the cosine term $\cos m\theta$ in Eq. (5.10) and are denoted by $\varphi^{c}(r, \theta)$. The superscript "c" is used to represent the cosine terms. Since the

[3]A background about simple circular unconstrained membrane can be found in appendix A.2

symmetric modes satisfy the differential equation independently, the boundary conditions in Eqs. (5.11) and (5.12) give

$$\begin{aligned}\sum_{m=0}^{\infty}\{\beta_{2m}\,J_m(ka)+\gamma_{2m}\,Y_m(ka)\}\cos m\theta=0\\ \sum_{m=0}^{\infty}\left\{\beta_{2m}\,J_m(kr|_{\rho=R})+\gamma_{2m}\,Y_m(kr|_{\rho=R})\right\}\cos m\theta=0\end{aligned}\tag{5.13}$$

Equation (5.13) cannot be solved directly for k since the second equation contains $r|_{\rho=R}$, which is a function of θ. From Fig. 5.1, we can show

$$r|_{\rho=R}=r(\theta)=\sqrt{R^2+d^2-2Rd\cos\psi}=\sqrt{R^2-d^2\sin^2\theta}-d\cos\theta\tag{5.14}$$

To solve Eq. (5.13) analytically, Lin [46] used Graf's addition formula [80] to transform the Bessel functions from (r,θ) coordinates to (ρ,ψ) coordinates. This transformation is given below

$$\begin{aligned}J_m(kr)\,e^{im\theta}&=\sum_{q=-\infty}^{\infty}J_{m+q}(k\rho)\,J_q(kd)\,e^{i(m+q)\psi}\\ Y_m(kr)\,e^{im\theta}&=\sum_{q=-\infty}^{\infty}Y_{m+q}(k\rho)\,J_q(kd)\,e^{i(m+q)\psi}\end{aligned}\tag{5.15}$$

Using the expressions in Eq. (5.15), Eq. (5.13) is rewritten as follows

$$\begin{aligned}\sum_{m=0}^{\infty}\{\beta_{2m}\,J_m(ka)+\gamma_{2m}\,Y_m(ka)\}\cos m\theta=0\\ \sum_{m=0}^{\infty}\sum_{q=-\infty}^{\infty}\left\{\beta_{2m}\,J_{m+q}(kR)+\gamma_{2m}\,Y_{m+q}(kR)\right\}J_q(kd)\,\cos(m+q)\psi=0\end{aligned}\tag{5.16}$$

Expanding the inner summation and using the property of Bessel functions, we get[4]

$$\sum_{n=0}^{\infty} \{\beta_{2n} J_n(ka) + \gamma_{2n} Y_n(ka)\} \cos n\theta = 0$$

$$\sum_{m=0}^{\infty} \sum_{n=0}^{\infty} \epsilon_n \{\beta_{2m} J_n(kR) + \gamma_{2m} Y_n(kR)\} \left\{J_{n-m}(kd) + (-1)^m J_{n+m}(kd)\right\} \cos n\psi = 0 \tag{5.17}$$

where ϵ_n is defined as

$$\epsilon_n = \begin{cases} 1/2 & \text{if } n = 0 \\ 1 & \text{if } n > 0 \end{cases}$$

Expanding Eq. (5.17) from $m = 0$ to N horizontally and from $n = 0$ to N vertically, gives the matrix equation

$$P^c X^c = 0 \tag{5.18}$$

where $P^c \in R^{(2N+2)\times(2N+2)}$ and $A \in R^{(2N+2)}$ are given by the relations

$$P^c = \begin{bmatrix} J_0(\zeta_1) & Y_0(\zeta_1) & 0 & 0 & \cdots & 0 & 0 \\ \frac{1}{2}J_0(\zeta_2)H^c_{00} & \frac{1}{2}Y_0(\zeta_2)H^c_{00} & \frac{1}{2}J_0(\zeta_2)H^c_{01} & \frac{1}{2}Y_0(\zeta_2)H^c_{01} & \cdots & \frac{1}{2}J_0(\zeta_2)H^c_{0N} & \frac{1}{2}Y_0(\zeta_2)H^c_{0N} \\ 0 & 0 & J_1(\zeta_1) & Y_1(\zeta_1) & \cdots & 0 & 0 \\ J_1(\zeta_2)H^c_{10} & Y_1(\zeta_2)H^c_{10} & J_1(\zeta_2)H^c_{11} & Y_1(\zeta_2)H^c_{11} & \cdots & J_N(\zeta_2)H^c_{1N} & Y_N(\zeta_2)H^c_{1N} \\ \vdots & \vdots & \vdots & \vdots & \ddots & \vdots & \vdots \\ 0 & 0 & 0 & 0 & \cdots & J_N(\zeta_1) & Y_N(\zeta_1) \\ J_N(\zeta_2)H^c_{N0} & Y_N(\zeta_2)H^c_{N0} & J_N(\zeta_2)H^c_{N1} & Y_N(\zeta_2)H^c_{N1} & \cdots & J_N(\zeta_2)H^c_{NN} & Y_N(\zeta_2)H^c_{NN} \end{bmatrix}$$

$$X^c = \begin{bmatrix} \beta_{20} & \gamma_{20} & \beta_{21} & \gamma_{21} & \cdots & \beta_{2N} & \gamma_{2N} \end{bmatrix}^T$$

[4]See appendix B

and where $\zeta_1 = ka$, $\zeta_2 = kR$, and $H^c_{nm} = \left\{J_{n-m}(kd) + (-1)^m J_{n+m}(kd)\right\}$. Equation (5.18) is used to solve for the eigenfrequencies k^c_i and eigenvectors X^c_i for $i = 1, 2, \cdots$. Using Eq. (5.10), the symmetric modes can be subsequently obtained as follows:

$$\varphi^c_i(r,\theta) = \beta_{20,i} \sum_{m=0}^{N} \left[\frac{\beta_{2m,i}}{\beta_{20,i}} J_m(k^c_i r) + \frac{\gamma_{2m,i}}{\beta_{20,i}} Y_m(k^c_i r)\right] \cos m\theta \tag{5.19}$$

where the terms $(\beta_{2m,i}/\beta_{20,i})$, $(\gamma_{2m,i}/\beta_{20,i})$, $m = 0, 1, \cdots, N$ are entries of the i-th eigenvector X^c_i, and $\beta_{20,i}$ is a scaling factor for the i-th symmetric mode.

5.2.4 Odd or Antisymmetric Modes

The antisymmetric modes are associated with the sine term $\sin m\theta$ in Eq. (5.10) and are denoted by $\varphi^s(r,\theta)$; the superscript "s" is used to represent the sine terms. For the symmetric modes, the boundary conditions in Eqs. (5.11) and (5.12) give

$$\begin{aligned}\sum_{m=1}^{\infty} \{\beta_{1m} J_m(ka) + \gamma_{1m} Y_m(ka)\} \sin m\theta = 0 \\ \sum_{m=1}^{\infty} \left\{\beta_{1m} J_m(kr|_{\rho=R}) + \gamma_{1m} Y_m(kr|_{\rho=R})\right\} \sin m\theta = 0\end{aligned} \tag{5.20}$$

Using Graf's addition formula [80], the boundary conditions in Eq. (5.20) can be rewritten as

$$\begin{aligned}\sum_{n=1}^{\infty} \{\beta_{1n} J_n(ka) + \gamma_{1n} Y_n(ka)\} \sin n\theta = 0 \\ \sum_{m=1}^{\infty}\sum_{n=1}^{\infty} \{\beta_{1m} J_n(kR) + \gamma_{1m} Y_n(kR)\} \left\{J_{n-m}(kd) - (-1)^m J_{n+m}(kd)\right\} \sin n\psi = 0\end{aligned} \tag{5.21}$$

Expanding Eq. (5.21) from $m = 1$ to M and $n = 1$ to M, $M = (N + 1)$, gives the matrix equation

$$P^s X^s = 0 \tag{5.22}$$

where $P^s \in R^{2M \times 2M}$ and $B \in R^{2M}$ are given by the relations

$$P^s = \begin{bmatrix} J_1(\zeta_1) & Y_1(\zeta_1) & 0 & 0 & \cdots & 0 & 0 \\ J_1(\zeta_2)H^s_{11} & Y_1(\zeta_2)H^s_{11} & J_1(\zeta_2)H^s_{12} & Y_1(\zeta_2)H^s_{12} & \cdots & J_1(\zeta_2)H^s_{1M} & Y_1(\zeta_2)H^s_{1M} \\ 0 & 0 & J_2(\zeta_1) & Y_2(\zeta_1) & \cdots & 0 & 0 \\ J_2(\zeta_2)H^s_{21} & Y_2(\zeta_2)H^s_{21} & J_2(\zeta_2)H^s_{22} & Y_2(\zeta_2)H^s_{22} & \cdots & J_2(\zeta_2)H^s_{2M} & Y_2(\zeta_2)H^s_{2M} \\ \vdots & \vdots & \vdots & \vdots & \ddots & \vdots & \vdots \\ 0 & 0 & 0 & 0 & \cdots & J_M(\zeta_1) & Y_M(\zeta_1) \\ J_M(\zeta_2)H^s_{M1} & Y_M(\zeta_2)H^s_{M1} & J_M(\zeta_2)H^s_{M2} & Y_M(\zeta_2)H^s_{M2} & \cdots & J_M(\zeta_2)H^s_{MM} & Y_M(\zeta_2)H^s_{MM} \end{bmatrix}$$

$$X^s = \begin{bmatrix} \beta_{11} & \gamma_{11} & \beta_{12} & \gamma_{12} & \cdots & \beta_{1M} & \gamma_{1M} \end{bmatrix}^T$$

and where $\zeta_1 = ka$, $\zeta_2 = kR$, and $H^s_{nm} = \{J_{n-m}(kd) - (-1)^m J_{n+m}(kd)\}$. Equation (5.22) is used to solve for the eigenfrequencies k^s_i and eigenvectors X^s_i for $i = 1, 2, \cdots$. Using Eq. (5.10), the symmetric modes can be subsequently obtained as follows:

$$\varphi^s_i(r, \theta) = \beta_{11,i} \sum_{m=1}^{M} \left[\frac{\beta_{1m,i}}{\beta_{11,i}} J_m(k^s_i r) + \frac{\gamma_{1m,i}}{\beta_{11,i}} Y_m(k^s_i r) \right] \sin m\theta \tag{5.23}$$

where the terms $(\beta^i_{1m}/\beta^i_{11})$, $(\gamma^i_{1m}/\beta^i_{11})$, $m = 1, 2, \cdots, M$ are entries of the i-th eignevector X^s_i, and β^i_{11} is a scaling factor for the i-th antisymmetric mode.

From the expressions in Eqs. (5.19) and (5.23) it can be seen that each mode shape of a constrained membrane φ_i is a summation of terms that are a function of m, *i.e.*, each mode shape depends on all the angular nodes. This is different from unconstrained membranes where each mode shape is associated with a specific angular node only and is denoted by $\varphi_{i,m}$, *i.e.*, a pair of subscripts are used to identify the mode shape. Since each mode shape is associated with an eigenfrequency, the eigenfrequencies of unconstrained membranes are denoted by $k_{i,m}$ whereas the eigenfrequencies of constrained membranes are denoted by k_i.

In the literature, the subscripts for frequencies and mode shapes of unconstrained membranes are numbered starting with zero, *i.e.*, i, $m = 0, 1, 2, \cdots$. In a slight deviation from this tradition, the frequencies and mode shapes of constrained membranes have been numbered starting with one in this chapter, *i.e.*, $i = 1, 2, 3, \cdots$.

5.3 Orthogonality of Modes

The differential equation in Eq. (5.2) is related to the eigenfrequency k as follows

$$\frac{1}{\varphi}\{\frac{\partial^2\varphi}{\partial r^2} + \frac{1}{r}\frac{\partial\varphi}{\partial r} + \frac{1}{r^2}\frac{\partial^2\varphi}{\partial\theta^2}\} = \frac{1}{c^2}\frac{1}{F}\frac{\partial^2 F}{\partial t^2} = -k^2$$

and can be rewritten in the form

$$\frac{1}{r}\frac{\partial}{\partial r}\left[r\frac{\partial\varphi}{\partial r}\right] + \frac{1}{r^2}\frac{\partial^2\varphi}{\partial\theta^2} + k^2\varphi = 0 \tag{5.24}$$

Let k_i and k_j be the i-th and j-th eigenfrequency associated with the modes φ_i and φ_j, respectively. Each of the modes φ_i and φ_j may be symmetric or anti-symmetric. For these two modes, Eq. (5.24) can be written as follows

$$\frac{1}{r}\frac{\partial}{\partial r}\left[r\frac{\partial \varphi_i}{\partial r}\right] + \frac{1}{r^2}\frac{\partial^2 \varphi_i}{\partial \theta^2} + k_i^2 \varphi_i = 0 \tag{5.25}$$

$$\frac{1}{r}\frac{\partial}{\partial r}\left[r\frac{\partial \varphi_j}{\partial r}\right] + \frac{1}{r^2}\frac{\partial^2 \varphi_j}{\partial \theta^2} + k_j^2 \varphi_j = 0 \tag{5.26}$$

Multiplying Eq. (5.25) by φ_j and Eq. (5.26) by φ_i and subtracting one from the other, we get

$$\frac{1}{r}\left\{\frac{\partial}{\partial r}\left[r\frac{\partial \varphi_i}{\partial r}\right]\varphi_j - \frac{\partial}{\partial r}\left[r\frac{\partial \varphi_j}{\partial r}\right]\varphi_i\right\} + \frac{1}{r^2}\left\{\frac{\partial^2 \varphi_i}{\partial \theta^2}\varphi_j - \frac{\partial^2 \varphi_j}{\partial \theta^2}\varphi_i\right\} + \left\{k_i^2 - k_j^2\right\}\varphi_i\varphi_j = 0 \tag{5.27}$$

Integrating Eq. (5.27) over the active region of membrane now gives

$$\begin{aligned} &\int_0^{2\pi}\int_a^{r|_{\rho=R}}\left\{\frac{\partial}{\partial r}\left[r\frac{\partial \varphi_i}{\partial r}\right]\varphi_j - \frac{\partial}{\partial r}\left[r\frac{\partial \varphi_j}{\partial r}\right]\varphi_i\right\} drd\theta \\ + \quad &\int_0^{2\pi}\int_a^{r|_{\rho=R}}\frac{1}{r}\left\{\frac{\partial^2 \varphi_i}{\partial \theta^2}\varphi_j - \frac{\partial^2 \varphi_j}{\partial \theta^2}\varphi_i\right\} drd\theta \\ + \quad &\left\{k_i^2 - k_j^2\right\}\int_0^{2\pi}\int_a^{r|_{\rho=R}}\varphi_i\varphi_j \; rdrd\theta = 0 \end{aligned} \tag{5.28}$$

Integration of the first term by parts gives

$$\int_0^{2\pi}\int_a^{r|_{\rho=R}}\left\{\frac{\partial}{\partial r}\left[r\frac{\partial \varphi_i}{\partial r}\right]\varphi_j - \frac{\partial}{\partial r}\left[r\frac{\partial \varphi_j}{\partial r}\right]\varphi_i\right\} drd\theta =$$

$$\int_0^{2\pi}\left[r\frac{\partial \varphi_i}{\partial r}\varphi_j - r\frac{\partial \varphi_j}{\partial r}\varphi_i\right]_{r=a}^{r|_{\rho=R}} d\theta - \int_0^{2\pi}\int_a^{r|_{\rho=R}}\left[\frac{\partial \varphi_i}{\partial r}\frac{\partial \varphi_j}{\partial r} - \frac{\partial \varphi_j}{\partial r}\frac{\partial \varphi_i}{\partial r}\right] rdrd\theta$$

Since both φ_i and φ_j are zero for $r = a$ and r values where $\rho = R$, the first term on the right-hand side of the above equation is zero. The second term on the right-hand side of the above equation is zero trivially and this implies

$$\int_0^{2\pi}\int_a^{r|_{\rho=R}} \frac{1}{r}\left\{\frac{\partial^2\varphi_i}{\partial\theta^2}\varphi_j - \frac{\partial^2\varphi_j}{\partial\theta^2}\varphi_i\right\} drd\theta + \left\{k_i^2 - k_j^2\right\}\int_0^{2\pi}\int_a^{r|_{\rho=R}} \varphi_i\varphi_j \; rdrd\theta = 0 \tag{5.29}$$

The first term in Eq. (5.29) is given by the expression

$$\int_0^{2\pi}\int_a^{r|_{\rho=R}} \frac{1}{r}\left\{\frac{\partial^2\varphi_i}{\partial\theta^2}\varphi_j - \frac{\partial^2\varphi_j}{\partial\theta^2}\varphi_i\right\} drd\theta \tag{5.30}$$

where the limits of integration correspond to the unconstrained area of the membrane in Fig. 5.1. In Eq. (5.30), the integration is first carried out with respect to r and then with respect to θ. For the first integration, the upper limit of r is expressed as a function of θ; this functional dependence of r on θ is given by Eq. (5.14) and shown in Fig. 5.2 (a). We evaluate the expression in Eq. (5.30) by changing the order of integration. This requires θ to be expressed as a function of r, which is obtained from the geometry in Fig. 5.1:

$$\theta = \theta(r) = \cos^{-1}\left[\frac{R^2 - r^2 - d^2}{2rd}\right], \qquad \theta \in [0, \pi] \tag{5.31}$$

The area of integration is redrawn in Fig. 5.2 (b) and the integral in Eq. (5.30) is expressed as the sum of the following three terms:

$$\begin{aligned} &\int_a^{R-d}\int_{-\pi}^{+\pi} \frac{1}{r}\left\{\frac{\partial^2\varphi_i}{\partial\theta^2}\varphi_j - \frac{\partial^2\varphi_j}{\partial\theta^2}\varphi_i\right\} d\theta dr \\ +&\int_{R-d}^{R+d}\int_{-\pi}^{-\theta(r)} \frac{1}{r}\left\{\frac{\partial^2\varphi_i}{\partial\theta^2}\varphi_j - \frac{\partial^2\varphi_j}{\partial\theta^2}\varphi_i\right\} d\theta dr \\ +&\int_{R-d}^{R+d}\int_{+\theta(r)}^{+\pi} \frac{1}{r}\left\{\frac{\partial^2\varphi_i}{\partial\theta^2}\varphi_j - \frac{\partial^2\varphi_j}{\partial\theta^2}\varphi_i\right\} d\theta dr \end{aligned} \tag{5.32}$$

where $\theta(r)$ is defined by Eq. (5.31). For each of the three terms in Eq. (5.32), the inner

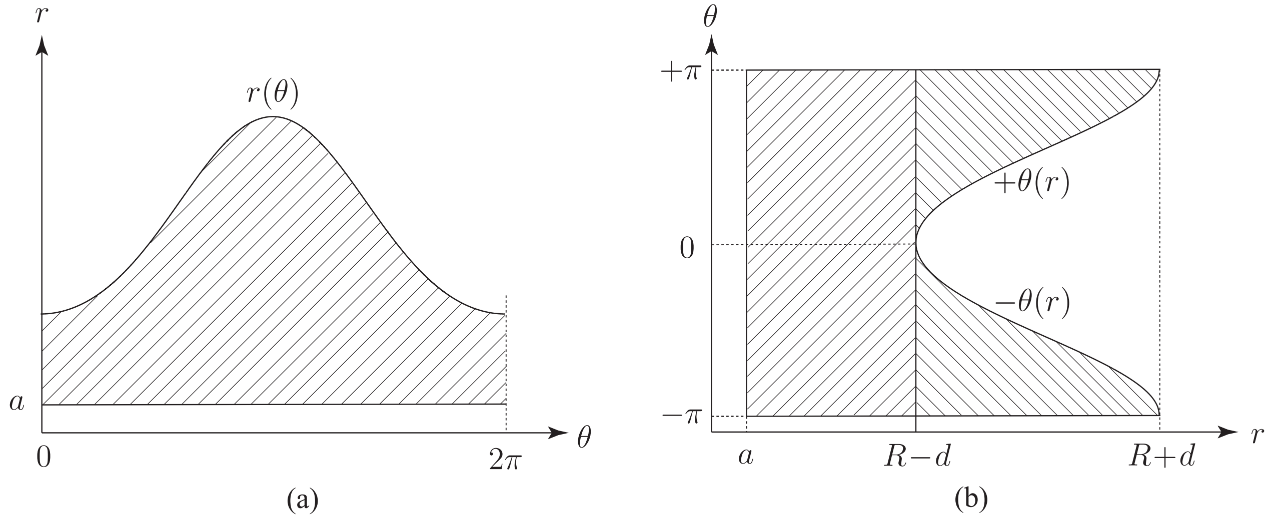

Figure 5.2: Shaded region showing the area of integration for the two cases where the integration is done (a) first with respect to r and then with respect to θ, and (b) first with respect to θ and then with respect to r

integration with respect to θ by parts, gives

$$\begin{aligned}\int_\theta \left[\frac{\partial^2\varphi_i}{\partial\theta^2}\varphi_j - \frac{\partial^2\varphi_j}{\partial\theta^2}\varphi_i\right] d\theta &= \left[\frac{\partial\varphi_i}{\partial\theta}\varphi_j - \frac{\partial\varphi_j}{\partial\theta}\varphi_i\right]_{\theta_l}^{\theta_u} - \int_\theta \left[\frac{\partial\varphi_i}{\partial\theta}\frac{\partial\varphi_j}{\partial\theta} - \frac{\partial\varphi_j}{\partial\theta}\frac{\partial\varphi_i}{\partial\theta}\right] d\theta \\ &= \left[\frac{\partial\varphi_i}{\partial\theta}\varphi_j - \frac{\partial\varphi_j}{\partial\theta}\varphi_i\right]_{\theta_l}^{\theta_u} \end{aligned} \tag{5.33}$$

where θ_l and θ_u denote the lower and upper limits of θ. Using Eq. (5.33), the three terms in Eq. (5.32) can be simplified to the form

$$\begin{aligned}\int_a^{R-d} \frac{1}{r}\left[\frac{\partial\varphi_i}{\partial\theta}\varphi_j - \frac{\partial\varphi_j}{\partial\theta}\varphi_i\right]_{-\pi}^{+\pi} dr &+ \int_{R-d}^{R+d} \frac{1}{r}\left[\frac{\partial\varphi_i}{\partial\theta}\varphi_j - \frac{\partial\varphi_j}{\partial\theta}\varphi_i\right]_{-\pi}^{-\theta(r)} dr \\ &+ \int_{R-d}^{R+d} \frac{1}{r}\left[\frac{\partial\varphi_i}{\partial\theta}\varphi_j - \frac{\partial\varphi_j}{\partial\theta}\varphi_i\right]_{+\theta(r)}^{+\pi} dr\end{aligned}$$

Since $\theta = +\theta(r)$ and $\theta = -\theta(r)$ describe the outer boundary of the membrane where $\varphi_i =$

$\varphi_j = 0$ for all i and j, the above integrals simplify to the form

$$\begin{aligned}
& \int_a^{R-d} \frac{1}{r} \left[\frac{\partial \varphi_i}{\partial \theta} \varphi_j - \frac{\partial \varphi_j}{\partial \theta} \varphi_i \right]_{-\pi}^{+\pi} dr \\
+ & \int_{R-d}^{R+d} \frac{1}{r} \left[\frac{\partial \varphi_i}{\partial \theta} \varphi_j - \frac{\partial \varphi_j}{\partial \theta} \varphi_i \right]_{-\pi}^{+\pi} dr \\
= & \int_a^{R+d} \frac{1}{r} \left[\frac{\partial \varphi_i}{\partial \theta} \varphi_j - \frac{\partial \varphi_j}{\partial \theta} \varphi_i \right]_{-\pi}^{+\pi} dr
\end{aligned} \tag{5.34}$$

Now consider the three separate cases:

A1. <u>Modes φ_i and φ_j are both symmetric:</u> Using Eq. (5.19), both $(\partial \varphi_i / \partial \theta)$ and $(\partial \varphi_j / \partial \theta)$ can be expressed in the form

$$\frac{\partial \varphi_i}{\partial \theta} = \sum_{m=0}^{\infty} (.) \sin m\theta, \qquad \frac{\partial \varphi_j}{\partial \theta} = \sum_{m=0}^{\infty} (.) \sin m\theta$$

Since their values are zero at $\theta = \pm\pi$, the integral in Eq. (5.34) is identically zero.

A2. <u>Modes φ_i and φ_j are both anti-symmetric:</u> It can be see from Eq. (5.23) that φ_i and φ_j have the form

$$\varphi_i = \sum_{m=0}^{\infty} (.) \sin m\theta, \qquad \varphi_j = \sum_{m=0}^{\infty} (.) \sin m\theta$$

Since their values are zero at $\theta = \pm\pi$, the integral in Eq. (5.34) is identically zero.

A3. <u>Mode φ_i is symmetric and mode φ_j is anti-symmetric:</u> Using Eqs. (5.19) and (5.23) it can be shown that both the terms $(\partial \varphi_i / \partial \theta)\varphi_j$ and $(\partial \varphi_j / \partial \theta)\varphi_i$ are zero at $\theta = \pm\pi$, and therefore the integral in Eq. (5.34) is identically zero.

This proves that the integral in Eq. (5.30) is zero for any two distinct modes φ_i and φ_j, irrespective of whether they are both symmetric, both antisymmetric, or one of them is symmetric and the other is antisymmetric. From Eq. (5.29) we can now conclude

$$\int_0^{2\pi} \int_a^{r|_{\rho=R}} \varphi_i \varphi_j \; r dr d\theta = 0, \qquad i \neq j \tag{5.35}$$

which is the orthogonality condition for a pair of distinct modes.

5.4 Accurate Computation of Eigenfrequencies and Mode Shapes

5.4.1 Computational Algorithm

We present an algorithm for numerical computation of the eigenfrequencies and their corresponding mode shapes. The algorithm is identical for symmetric and antisymmetric modes and therefore we discuss it here for the symmetric modes only. The algorithm first computes all eigenfrequencies k_i^c, $i = 1, 2, \cdots$, that are less than a user-specified maximum eigenfrequency $k_{\max}^c$. The interval $[0, k_{\max}^c]$ is divided into small segments of length Δk and the eigenfrequencies within each segment are computed separately. The number of eigenfrequencies that show up within each segment depend on the value of N, which is related to the size of the matrix P^c in Eq. (5.18). Starting from zero, increasing the value of N typically results in larger number of zero crossings of the determinant P^c (see Fig. 5.3), and hence a larger number of eigenfrequencies within a specific segment. Beyond a certain value of N, the number of eigenfrequencies in a given segment will not change. At this point, increasing

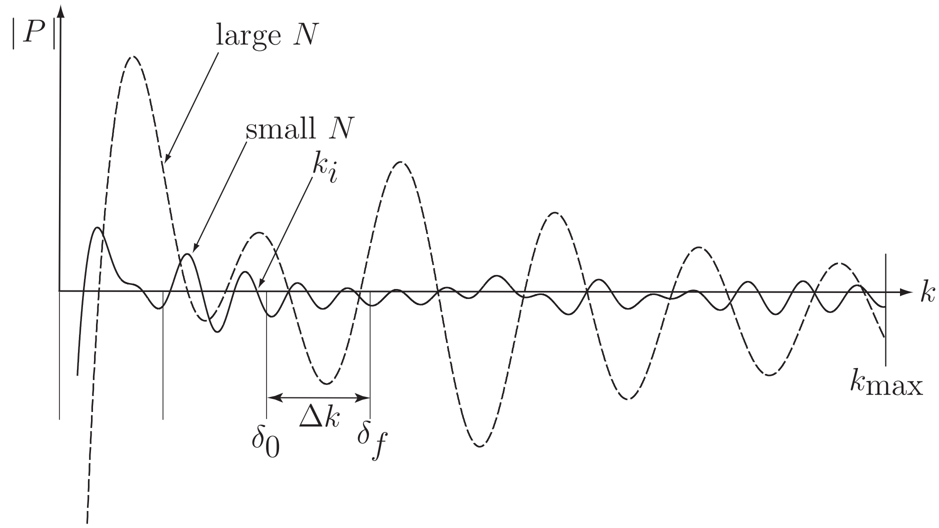

Figure 5.3: The eigenfrequencies are the zero crossings of the determinant of the matrix P^c for symmetric modes, and P^s for antisymmetric modes

the value of N produces very small changes in the values of the eigenfrequencies but such changes can result in significant improvement or loss of accuracy of the associated mode shapes. The flowchart shown in Fig. 5.8 provides the algorithm for computing all eigenfrequencies in the interval $[0, k^c_{\max}]$, and accurately computing the mode shape associated with each eigenfrequency through proper choice of N. A brief summary of the algorithm is provided next.

The interval $[0, k^c_{\max}]$ is divided into small segments of length Δk. For any given segment, the boundaries of the segment are denoted by δ_0 and δ_f. The value of k is changed in increments of δ (small number) from δ_0 to δ_f, and zero crossings of $\mid P^c \mid$ are stored as potential eigenfrequencies. For a given segment, this procedure is repeated by increasing N, $N \in \{0, 1, 2, \cdots, N_{\max}\}$, till no additional zero crossings occur and the mode shapes associated with the eigenfrequencies have been computed accurately. The mode shapes are computed using Eq. (5.19) and are checked for accuracy by verifying $\varphi^c_i = 0$ along the inner and outer boundary of the membrane. The procedure is repeated for each segment till the maximum user-specified value of $k = k_{\max}$ is reached.

In the literature, several methods have been proposed for computing the eigenfrequency and mode shapes of constrained membranes. Most of these methods are well suited to computing the first few eigenfrequencies and mode shapes only. For simulation of the dynamics of a constrained membrane, it is necessary to accurately compute many frequencies and mode shapes; this is difficult to compute using existing methods due to singularity. For example, Nagaya [2], Singh and Kothari [47], and Singh, et al. [3] proposed to combine the two equations for symmetric modes in Eq. (5.13) into the following single equation

$$\sum_{m=0}^{\infty} \beta_{2m} \left\{ J_m(kr|_{\rho=R}) - \frac{J_m(ka)}{Y_m(ka)} Y_m(kr|_{\rho=R}) \right\} \cos m\theta = 0 \tag{5.36}$$

This procedure reduces the dimension of the coefficient matrix by a factor of two and reduces the computational burden but presence of Bessel function of the second kind, $Y_m(ka)$, in the denominator makes it prone to singularity. This problem become critical during computation of higher frequencies.

The eigenfrequencies and mode shapes of the antisymmetric modes can be computed using the algorithm in Fig. 5.4 by replacing P^c, k_i^c, and φ_i^c with P^s, k_i^s, and φ_i^s, respectively, and N with M. P^s is defined in Eq. (5.22) and φ_i^s is defined in Eq. (5.23).

5.4.2 Numerical Results

We use the algorithm in Section 5.4.1 to accurately compute the eigenfrequencies and mode shapes of a constrained membrane with $R/a = 0.25$ and $d/a = 1.0$. This problem was considered in the literature [1], [2], [47] and the results were summarized by Singh, et al. [3]. We compare these results with those obtained using our algorithm, implemented with

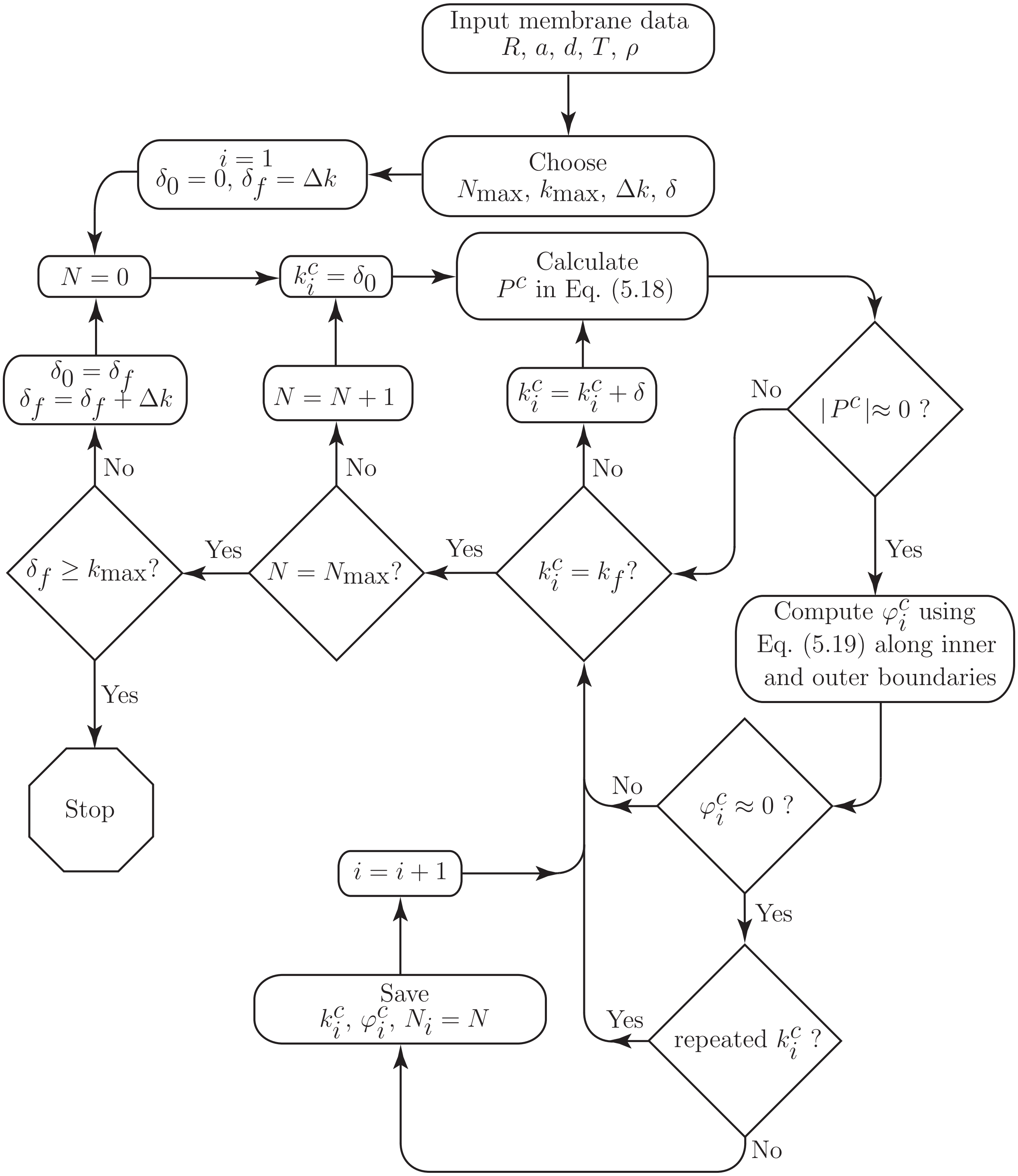

Figure 5.4: Algorithm for computing eigenfrequencies and mode shapes for symmetric modes

$k_{\max} = 10a$ and $\Delta k = k_{\max}$. Table 5.1 shows the non-dimensional fundamental antisymmetric frequencies for the constrained membrane obtained using our algorithm; the value of

Table 5.1: First eight non-dimensional frequencies of antisymmetric modes of constrained membrane with $a/R = 0.25$ and $d/a = 1.0$. The results in parenthesis are from [1], [2], and [3], and the star superscript indicates frequencies with accurate mode shapes computed using our algorithm

M	$k_1^c a$	$k_2^c a$	$k_3^c a$	$k_4^c a$	$k_5^c a$	$k_6^c a$	$k_7^c a$	$k_8^c a$
1	1.1119	2.1342	-	-	-	-	-	-
2	1.0636	1.4307	1.9199	-	-	-	-	-
3	1.0661	1.3811	1.6875	1.9290	2.3177	-	-	-
4	1.0660	1.3850	1.6557	1.9288	1.9473	2.3280	-	-
5	1.0660*	1.3848	1.6591	1.9275	1.9296	2.2195	2.3292	-
6	1.0660*	1.3848	1.6589	1.9284	1.9312	2.2083	2.3288	2.4982
7	1.0660*	1.3848*	1.6589	1.9284	1.9311	2.2101	2.3288	2.4916
8	1.0660*	1.3848*	1.6589*	1.9284	1.9311	2.2099	2.3288	2.4928
9	1.0660*	1.3848*	1.6589*	1.9284*	1.9311*	2.2099	2.3288	2.4927
10	1.0660*	1.3848*	1.6589*	1.9284*	1.9311*	2.2099	2.3288*	2.4927
11	1.0660*	1.3848*	1.6589*	1.9284*	1.9311*	2.2099*	2.3288*	2.4927
12	1.0660*	1.3848*	1.6589*	1.9284*	1.9311*	2.2099*	2.3288*	2.4927*
13	1.0660*	1.3848*	1.6589*	1.9284*	1.9311*	2.2099*	2.3288*	2.4927*
40	1.0647	1.3822	1.6572	1.9272	1.9297	2.2072	2.3272	2.4922
-	(1.0659)	(1.3848)	(1.6589)	(1.9283)	-	-	-	-
-	(1.0500)	(1.3800)	-	-	-	-	-	-

M is gradually increased till all modes are accurately computed. As mentioned in Section 5.4.1, the accuracy of each mode shape is verified by computing the displacement of 100 points along the inner and outer membrane boundaries. For accuracy, the displacement of the membrane at all these points must satisfy $\epsilon \leqslant 10^{-4}$. In Table 5.1, eigenfrequencies associated with accurate mode shapes (this depends on correct choice of M) have a star superscript. The eigenfrequencies obtained from the literature are presented in separate rows at the bottom of the table and are placed within parenthesis. The following observations can be made from the results presented in Table 5.1:

A1. It is not possible to identify all the eigenfrequencies in an interval using a small value of M. Increasing the value of M helps in identifying more eigenfrequencies and $M \geq 6$

identifies all eight eigenfrequencies in this particular example.

A2. For $M = 6$, all eigenfrequencies are identified but only the first eigenfrequency has an accurate mode shape. Increasing the value of M results in a larger number of accurate mode shapes and $M = 12$ results in accurate computation of all mode shapes.

A3. A large value of M is not guaranteed to result in accurate mode shapes. For example, $M = 13$ gives all accurate mode shapes but none of the mode shapes are accurate for $M = 40$. This is because of the sensitivity of the Bessel functions. This justifies the need for increasing M gradually rather than choosing a pre-specified large integer.

A4. Although all the mode shapes can be accurately computed using $M = 12$, the computational burden can be significantly reduced by using the lowest value of M for each eigenfrequency that gives an accurate mode shape. For example, the mode shape for $k_1^c a$ should be computed using $M = 5$, the mode shape for $k_2^c a$ should be computed using $M = 7$, and so on.

A5. The eigenfrequencies in the literature have values that are very close to those obtained by our algorithm. However, these small errors result in large errors in the shape of the modes, which will violate boundary and orthogonality conditions. This will be discussed further later.

We next present results for different sizes and locations of the constraint in the membrane. The specific values of a/R and d/a used are taken from Singh, et al. [3]. Table 5.2 presents the first five non-dimensional frequencies of symmetric modes of the constrained membranes and values of N used to compute the corresponding mode shapes. For a given set of a/R and d/a values, the first row contains eigenfrequencies and N values that correspond to accurate mode shapes. The procedure for obtaining accurate eigenfrequencies and mode shapes was discussed in Section 5.4.1. The second row contains eigenfrequencies that are

Table 5.2: First five non-dimensional frequencies of symmetric modes of constrained membranes and values of N used to compute the mode shapes. For a given set of a/R and d/a values, the first row contains values that correspond to accurate mode shapes. The second row contain values that are closest to those presented in the literature - the eigenfrequencies are underlined to indicate that the corresponding mode shapes are inaccurate. The results from the literature [1], [2], [3] are presented in the following rows with eigenfrequencies in parenthesis

a/R	d/a	$k_1^c a$	N	$k_2^c a$	N	$k_3^c a$	N	$k_4^c a$	N	$k_5^c a$	N
0.5	0.2	2.7348	5	3.2374	6	3.6531	7	3.9346	8	4.2482	8
		$\underline{2.7348}$	3	$\underline{3.2373}$	4	$\underline{3.6531}$	5	$\underline{3.9346}$	6	$\underline{4.2482}$	6
		(2.7348)	-	(3.2373)	-	(3.6530)	-	(3.9346)	-	(4.2482)	-
		(2.7520)	-	(3.2500)	-	(3.6680)	-	(3.9370)	-		
	0.4	2.4053	5	3.0862	7	3.6973	9	4.2487	10	4.6704	9
		$\underline{2.4053}$	4	$\underline{3.0862}$	5	$\underline{3.6973}$	6	$\underline{4.2487}$	8	$\underline{4.6704}$	5
		(2.4053)	-	(3.0862)	-	(3.6972)	-	(4.2487)	-	(4.6704)	-
		(2.4300)	-	(3.0860)	-	(3.6950)	-	(4.2500)	-		
	0.6	2.1536	6	2.9451	8	3.6598	9	4.1455	8	4.3194	11
		$\underline{2.2081}$	1	$\underline{2.9429}$	4	$\underline{3.6505}$	5			$\underline{4.4738}$	3
		(2.2800)	-	(2.9310)	-	(3.6620)	-			(4.4320)	-
	0.8	1.9570	6	2.8256	8	3.5975	11	3.7439	11	4.3140	12
		$\underline{1.9537}$	2	$\underline{2.8109}$	3	$\underline{3.5779}$	5			$\underline{4.4424}$	6
		(1.9340)	-	(2.8130)	-	(3.5620)	-			(4.4250)	
	1.0	1.8001	7	2.7236	9	3.4187	9	3.5358	12	4.2690	13
		$\underline{1.8001}$	4	$\underline{2.7239}$	5	$\underline{3.4183}$	5			$\underline{4.3044}$	7
		(1.8000)	-	(2.7240)	-	(3.4180)	-			(4.3750)	-
0.25	1	0.8681	5	1.2305	6	1.4817	10	1.6789	8	1.6882	8
		$\underline{0.8680}$	2	$\underline{1.2305}$	4	$\underline{1.4817}$	5	$\underline{1.6789}$	6	$\underline{1.6882}$	6
		(0.8680)	-	(1.2305)	-	(1.4817)	-	(1.6788)	-	(1.6881)	-
		(0.8720)	-	(1.2200)	-	(1.4400)	-				
	2	0.7456	8	1.1967	10	1.4521	8	1.5610	11	1.8897	12
		$\underline{0.7456}$	3	$\underline{1.1966}$	5	$\underline{1.4521}$	6	$\underline{1.5610}$	7	$\underline{1.8898}$	8
		(0.7455)	-	(1.1966)	-	(1.4521)	-	(1.5609)	-	(1.8898)	-
		(0.7430)	-	(1.2040)	-	(1.4620)	-				
	3	0.6674	9	1.1024	11	1.3636	12	1.5074	13	1.7571	12
		$\underline{0.6690}$	3	$\underline{1.1129}$	3	$\underline{1.3660}$	4				
		(0.6700)	-	(1.1230)	-	(1.3670)	-				

closest to values presented in the literature; these eigenfrequencies are obtained by gradually increasing N till the error between the computed value and the value in the literature is minimum. In all cases, the error is minimum for a value of N for which the mode shape is inaccurate - this is indicated by the underlined eigenfrequencies. The eigenfrequencies in parenthesis are taken from the literature [3] and are presented in the third and fourth rows. The following observations can be made from the results presented in Table 5.2 pertaining to accurate eigenfrequencies and mode shapes:

A1. Lower values of N are required to compute lower eigenfrequencies, and vice versa. This can also be observed from the data presented in Table 5.1.

A2. Lower values of N are required for lower values of d, *i.e.*, constraints located farther from the center of the membrane, and vice versa.

A3. Higher values of N are required for smaller values of a, *i.e.*, constraints of smaller size, and vice versa.

The effect of N on the accuracy of eigenfrequencies was first observed by Nagaya [2], who used $8 \leq N \leq 12$ to confine the error to $\approx 0.5\%$. Such choice of N may indeed result in accurate computation of the eigenfrequency but there is no guarantee that the mode shape will be accurate. The accuracy of the mode shape depends on the size and location of the constraint, as discussed above, and incorrect choice of N can result in significant error in the mode shape even when the eigenfrequency is computed accurately. This is illustrated with the help of Fig. 5.5, which shows the accurate and inaccurate mode shapes for $k_3^c a$ for $a/R = 0.5$ and $d/a = 0.6, 0.8$, and 1.0. It should be noted that the eigenfrequencies corresponding to these accurate and inaccurate mode shapes, shown in Table 5.2, indicate negligible error. For example, for $a/R = 0.5$ and $d/a = 0.8$, the error in the eigenfrequency is only

$$\frac{3.5975 - 3.5620}{3.5975} \times 100 \approx 1\%$$

but the mode shapes in Fig. 5.5 (b) are significantly different; and of course, the inaccurate mode shape does not satisfy the boundary conditions. Similar observations can be made for the cases $a/R = 0.5$, $d/a = 0.6$ and $a/R = 0.5$, $d/a = 1.0$. For these cases, the error in the eigenfrequency is $\approx -0.06\%$ and $\approx 0.02\%$, respectively but the corresponding mode shapes are significantly different. We complete this section with numerical results for an example where the size of the constraint is small and the location of the constraint is far away from the center of the membrane, *i.e.*, a/R is small and d/a is large. For such cases, it is difficult to obtain the eigenfrequencies and mode shapes accurately because the Bessel functions are sensitive to large values of d and small values of a. Despite this sensitivity, our algorithm was able to compute the first twenty modes of a membrane with $a/R = 0.1$ and $d/a = 9.0$. The first symmetric mode and the sixteenth symmetric mode of the membrane are shown in Fig. 5.6 together with the non-dimensional eigenfrequencies and the required value of N. Note that $N = 18$ was required for computing the sixteenth mode accurately. Figure 5.7 shows more mode shapes with $d/a = 2.0$.

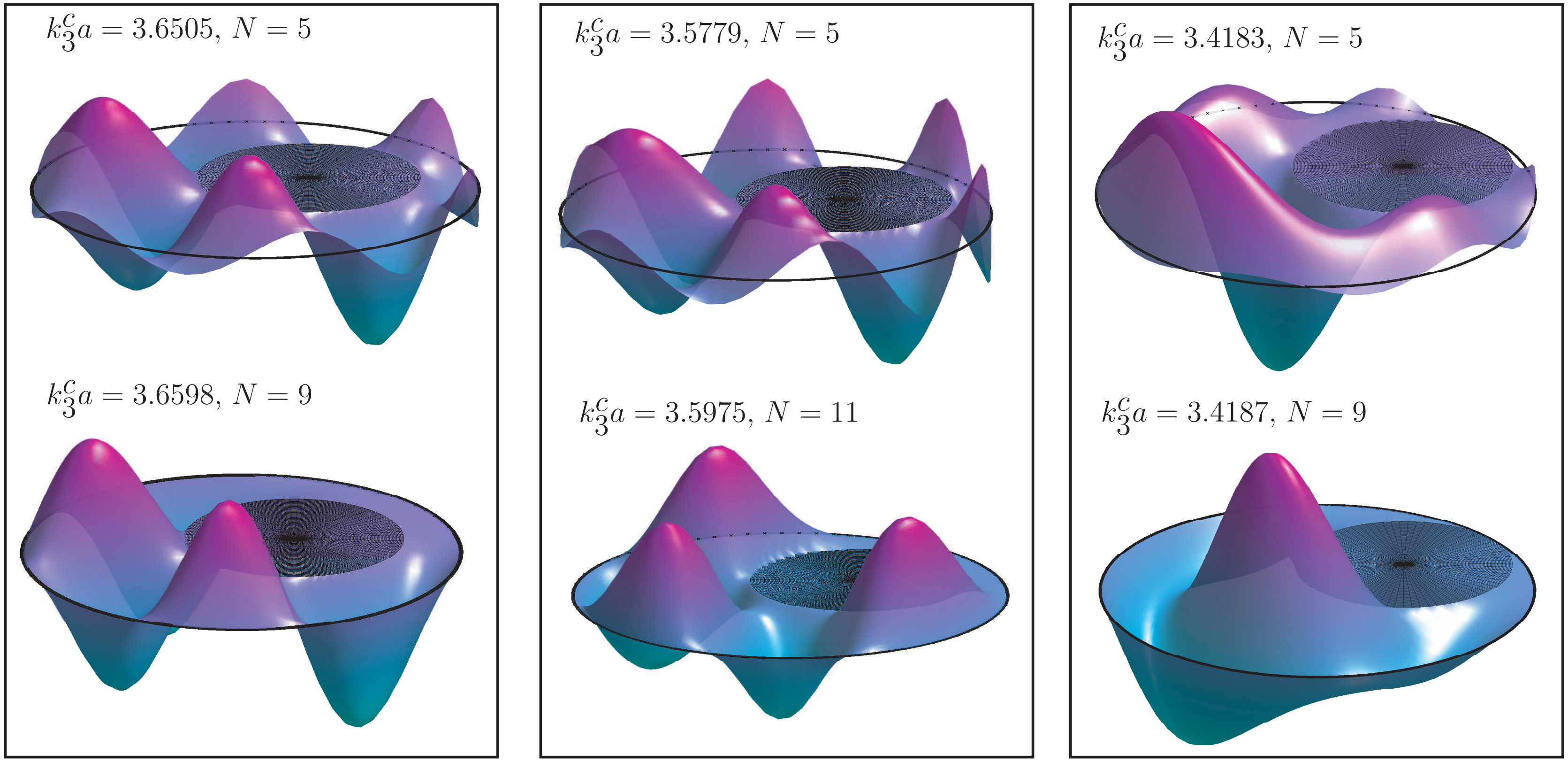

(a) (b) (c)

Figure 5.5: Mode shapes $k_3^c a$ for constrained membranes in Table 5.2 with $a/R = 0.5$ and (a) $d/a = 0.6$ (b) $d/a = 0.8$ (c) $d/a = 1.0$. For each of these three cases, the inaccurate mode shapes are shown above the accurate mode shapes

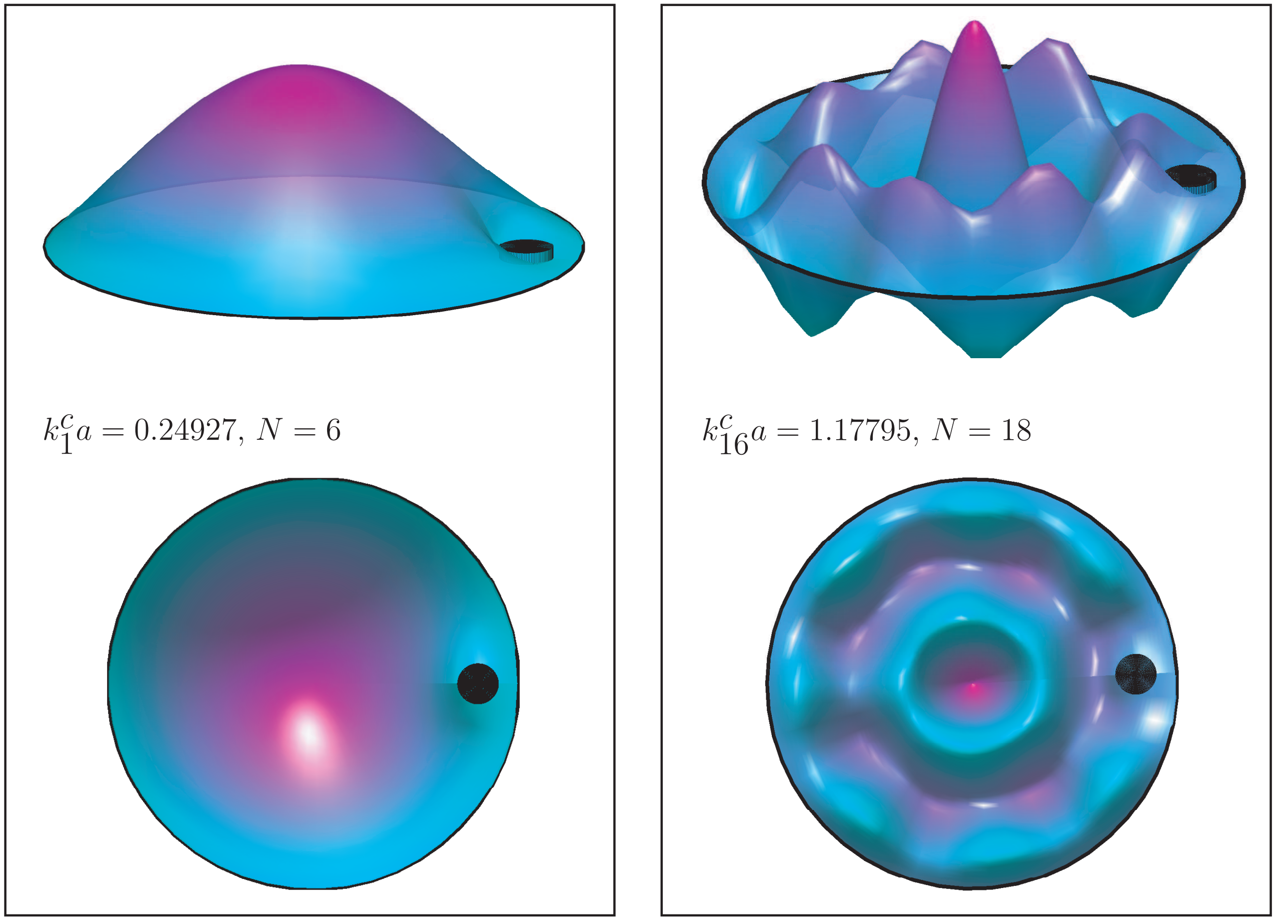

(a) (b)

Figure 5.6: First symmetric mode and sixteenth symmetric mode of a constrained membrane with $a/R = 0.1$ and $d/a = 9.0$. For both these cases, the isometric view is placed above the top view and the value of N required for accuracy is shown

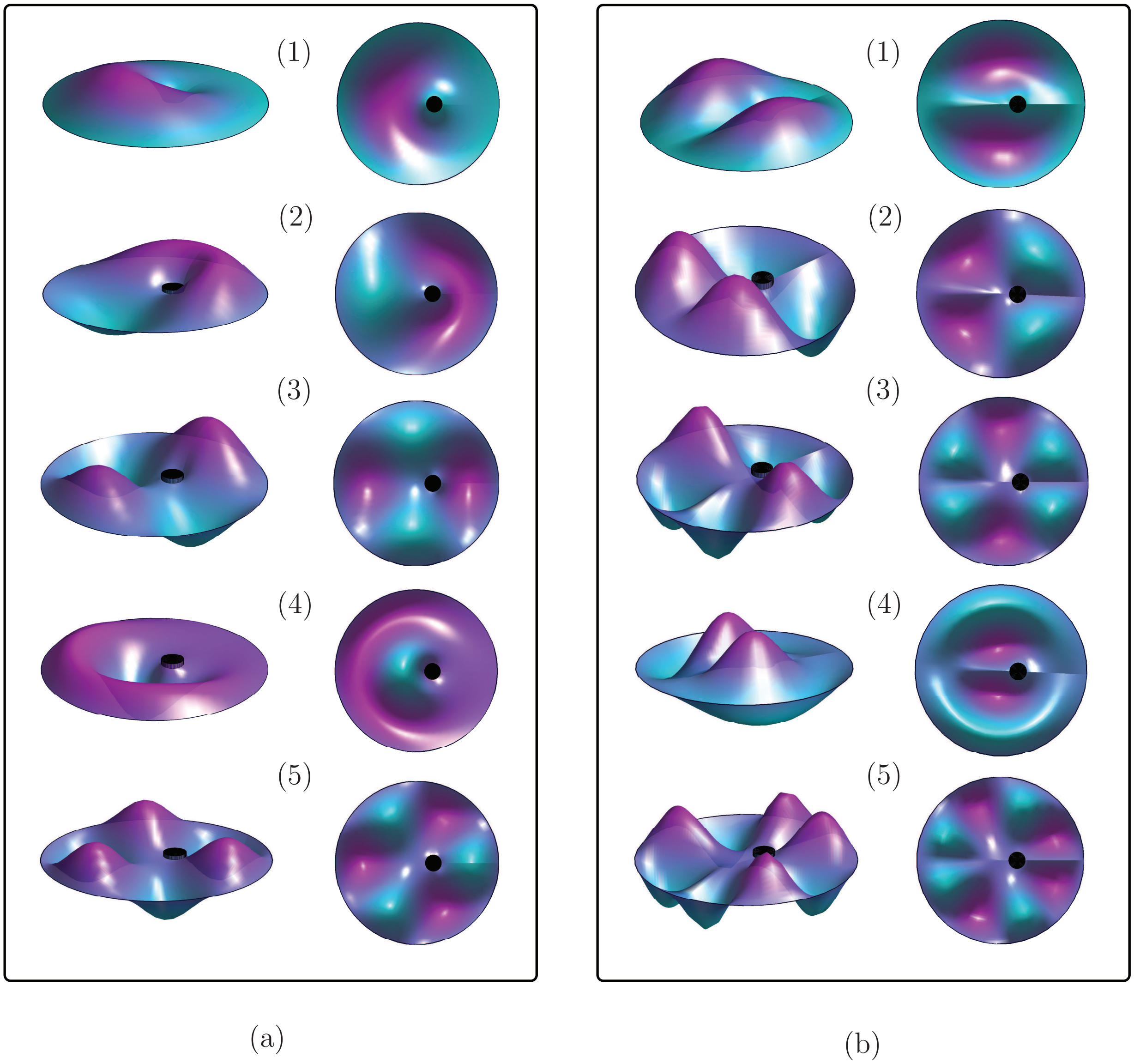

Figure 5.7: First five modes of a membrane with $a/R = 0.1$ and $d/a = 2.0$ (a) Antisymmetric modes (b) Symmetric modes. For both, the isometric view is placed next the top view

5.5 Simulation of Constrained Membrane Dynamics

5.5.1 Computation of Modal Coefficients

From the general form of the dynamics of the membrane given in Eq. (5.9), the complete solution can be written as follows

$$
\begin{aligned}
Z_C(r,\theta,t) = &\sum_{i=0}^{\infty} \varphi_i^c(k_i^c r,\theta)(A_{1i}\cos\omega_i^c t + B_{1i}\sin\omega_i^c t) \\
&+ \sum_{j=1}^{\infty} \varphi_j^s(k_j^s r,\theta)(A_{2j}\cos\omega_i^s t + B_{2j}\sin\omega_j^s t)
\end{aligned}
\tag{5.37}
$$

where φ_i^c, φ_i^s are defined in Eqs. (5.19) and (5.23), respectively, and $\omega_i^c = ck_i^c$, $\omega_j^s = ck_j^s$, $i,j = 1,2,\cdots$. The initial conditions are assumed to be

$$
Z(r,\theta,0) = G(r,\theta), \qquad \dot{Z}(r,\theta,0) = H(r,\theta)
$$

Applying the displacement initial conditions to Eq. (5.37), we get

$$
\sum_{i=1}^{\infty} A_i^c\,\varphi_i^c + \sum_{j=1}^{\infty} A_j^s\,\varphi_j^s = G(r,\theta) \tag{5.38}
$$

Multiplying Eq. (5.38) by φ_i^c, integrating both sides over the unconstrained area of the membrane, and using the orthogonality condition in Eq. (5.35), we get

$$
A_i^c = \left[\int_0^{2\pi}\int_a^{r|_{\rho=R}} G(r,\theta)\,\varphi_i^c\, r dr d\theta\right] \Big/ \left[\int_0^{2\pi}\int_a^{r|_{\rho=R}} (\varphi_i^c)^2\, r\, dr d\theta\right], \quad i = 1,2,\cdots \tag{5.39}
$$

Multiplying Eq. (5.38) by φ_i^s, integrating both sides over the unconstrained area of the membrane, and using the orthogonality condition in Eq. (5.35), we get

$$A_j^s = \left[\int_0^{2\pi} \int_a^{r|_{\rho=R}} G(r,\theta)\, \varphi_i^s\, r dr d\theta \right] / \left[\int_0^{2\pi} \int_a^{r|_{\rho=R}} (\varphi_i^s)^2\, r\, dr d\theta \right], \quad j = 1, 2, \cdots \tag{5.40}$$

Applying the velocity initial conditions to Eq. (5.37), we get

$$\sum_{i=1}^{\infty} B_i^c\, \omega_i^c\, \varphi_i^c + \sum_{j=1}^{\infty} B_j^s\, \omega_j^s\, \varphi_j^s = H(r,\theta) \tag{5.41}$$

By repeating the same procedure as above, the remaining modal coefficients can be obtained as

$$B_i^c = \frac{1}{\omega_i^c} \left[\int_0^{2\pi} \int_a^{r|_{\rho=R}} H(r,\theta)\, \varphi_i^c\, r dr d\theta \right] / \left[\int_0^{2\pi} \int_a^{r|_{\rho=R}} (\varphi_i^c)^2\, r\, dr d\theta \right], \quad i = 1, 2, \cdots \tag{5.42}$$

$$B_j^s = \frac{1}{\omega_i^s} \left[\int_0^{2\pi} \int_a^{r|_{\rho=R}} H(r,\theta)\, \varphi_i^s\, r dr d\theta \right] / \left[\int_0^{2\pi} \int_a^{r|_{\rho=R}} (\varphi_i^s)^2\, r\, dr d\theta \right], \quad j = 1, 2, \cdots \tag{5.43}$$

The integrals in Eqs. (5.39), (5.40), (5.42) and (5.43) are of the form

$$\int_0^{2\pi} \int_a^{g(\theta)} f(r,\theta) dr d\theta$$

where $g(\theta) = r|_{\rho=R} = \sqrt{R^2 - d^2 \sin^2\theta} - d\cos\theta$. Through change of variables $x = \theta$ and

$r = [(1-y)a + yg(x)]$ the integrals are changed to the form

$$\int_0^{2\pi} \int_0^1 f\,[(1-y)a + yg(x), x]\,[g(x) - a]dydx = \int_0^{2\pi} \int_0^1 h(y,x)\,dy\,dx$$

The integrations are performed numerically using a n-point Gaussian quadrature rule as follows

$$\int_0^{2\pi} \int_0^1 h(y,x)\,dy\,dx = \frac{\pi}{2} \int_{-1}^1 \int_{-1}^1 h(\zeta,\eta)\,d\eta\,d\zeta = \frac{\pi}{2} \sum_{i=1}^{n} \sum_{j=1}^{n} w_i w_j\, h(\zeta_i, \eta_j) \tag{5.44}$$

where $x = \pi(\eta+1)$, $y = (\zeta+1)/2$, w_i and w_j are the weights, and ζ_i and η_j are the integration points respectively. Since Bessel functions are very sensitive to numerical integration, accurate computation of the modal coefficients requires correct choice of the number of integration points in Eq. (5.44). An algorithm for properly choosing n and accurately computing the modal coefficients is described by the flow chart in Fig. 5.8, which is self-explanatory.

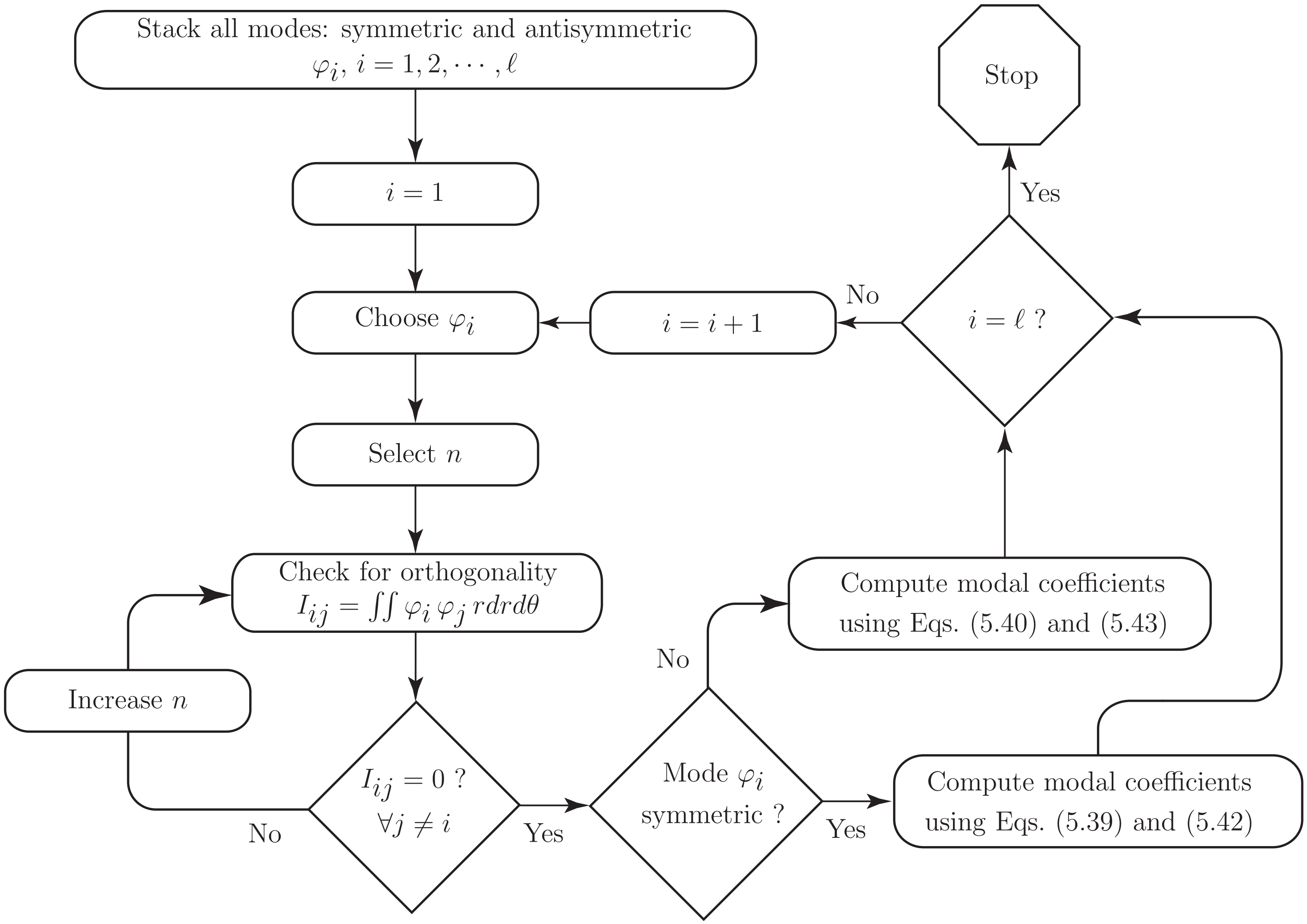

Figure 5.8: Algorithm for computing modal coefficients

5.5.2 Numerical Results Verifying Orthogonality

In Section 5.4.2 we showed that results in the literature provide reasonably accurate eigenfrequencies but the associated mode shapes are inaccurate and as such do not satisfy the boundary conditions. In this section we show that these inaccurate modes do not satisfy the orthogonality condition; the accurate modes satisfy the orthogonality conditions but requires proper choice of the number of integration points n. The number of integration points can be chosen properly by following the algorithm described by the flowchart in Fig. 5.8. We consider constrained membranes with $a/R = 0.5$ and $d/a = 0.6, 0.8, 1.0$; these cases were presented in Table 5.2. For this membrane, the third symmetric mode φ_3^c and fourth symmetric mode φ_4^c are used to check for orthogonality. In particular, we check the orthogonality of φ_4^c (accurate mode shape) with both φ_3^c (accurate mode shape) and $\underline{\varphi_3^c}$ (inaccurate mode shape). The results are presented in Table 5.3.

Table 5.3: Checking orthogonality between the accurate and inaccurate third symmetric mode and the accurate fourth symmetric mode of constrained membranes with $a/R = 0.5$ and $d/a = 0.6, 0.8, 1.0$. The inaccurate third symmetric mode is underlined

d/a	0.6		0.8		1.0	
n	$< \underline{\varphi_3^c}, \varphi_4^c >$	$< \varphi_3^c, \varphi_4^c >$	$< \underline{\varphi_3^c}, \varphi_4^c >$	$< \varphi_3^c, \varphi_4^c >$	$< \underline{\varphi_3^c}, \varphi_4^c >$	$< \varphi_3^c, \varphi_4^c >$
4	0.0091	0.0149	-0.0221	-0.0465	0.0560	-0.3005
8	-0.0366	-0.0821	-0.0621	-0.1769	-0.0171	0.1715
12	0.0142	-0.0080	-0.0069	-0.0514	0.0107	0.0327
16	0.0056	0.0081	0.0187	0.0427	0.0026	0.0222
20	-0.0013	0.0011	-0.0080	0.0184	0.0030	0.0244
24	-0.0015	0.0000	-0.0061	0.0025	0.0019	0.0058
28	-0.0016	0.0000	-0.0068	0.0002	0.0021	0.0006
32	-0.0016	0.0000	-0.0067	0.0000	0.0022	0.0000

To show the orthogonality between symmetric-symmetric and symmetric-antisymmetric modes, we consider a membrane with $a/R = 0.1$ and $d/a = 0, 4, 8$. The results are shown in Table 5.4. It is clear that accurate computation of the mode shapes require proper choice of the number of integration points n. The number of integration points depends on the size and location of the constraint and can be chosen using the flowchart in Fig. 5.8. It may be mentioned that symmetric-antisymmetric modes are orthogonal for small values of n and higher values of n are required to satisfy orthogonality between symmetric-symmetric and antisymmetric-antisymmetric modes.

Table 5.4: Number of integration points n required to achieve orthogonality between symmetric-symmetric and symmetric-antisymmetric modes of constrained membranes with $a/R = 0.1$ and $d/a = 0, 4, 8$

d/a	0		4		8	
n	$\langle \varphi_4^c, \varphi_5^c \rangle$	$\langle \varphi_4^c, \varphi_5^s \rangle$	$\langle \varphi_4^c, \varphi_5^c \rangle$	$\langle \varphi_4^c, \varphi_5^s \rangle$	$\langle \varphi_4^c, \varphi_5^c \rangle$	$\langle \varphi_4^c, \varphi_5^s \rangle$
4	-0.0013	0.0000	-0.3009	0.0000	-0.0746	0.0000
8	0.0013	0.0000	0.2686	0.0000	0.0215	0.0000
12	0.0000	0.0000	-0.1659	0.0000	0.0293	0.0000
16	0.0000	0.0000	-0.0741	0.0000	0.0182	0.0000
20	0.0000	0.0000	-0.0086	0.0000	0.0224	0.0000
24	0.0000	0.0000	-0.0004	0.0000	0.0100	0.0000
28	0.0000	0.0000	0.0000	0.0000	0.0020	0.0000
32	0.0000	0.0000	0.0000	0.0000	0.0002	0.0000
36	0.0000	0.0000	0.0000	0.0000	0.0000	0.0000

5.5.3 Simulation of Free Vibration

In this section, we simulate the motion of a constrained membrane subjected to an initial condition for different cases. The membrane is assumed to have the following specifications

$R = 1$ m,

$\mu = 0.25$ kg.m^{-2},

$T = 1$ N.m^{-1}

- **Case 1** : $a/R = 0.12$ and $d/R = 0.88$ and the initial conditions are represented as

$$H(r,\theta) = 0, \qquad G(r,\theta) = 0.1(r-a)^8(r - r(\theta)), \qquad r \geq a$$

where $r(\theta) = \sqrt{R^2 - d^2\sin^2\theta} - d\cos\theta$

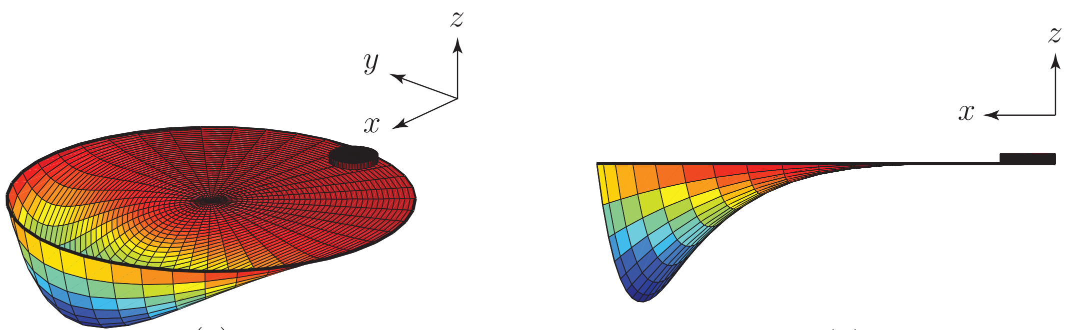

(a) (b)

Figure 5.9: Initial displacement of the membrane described in case 1

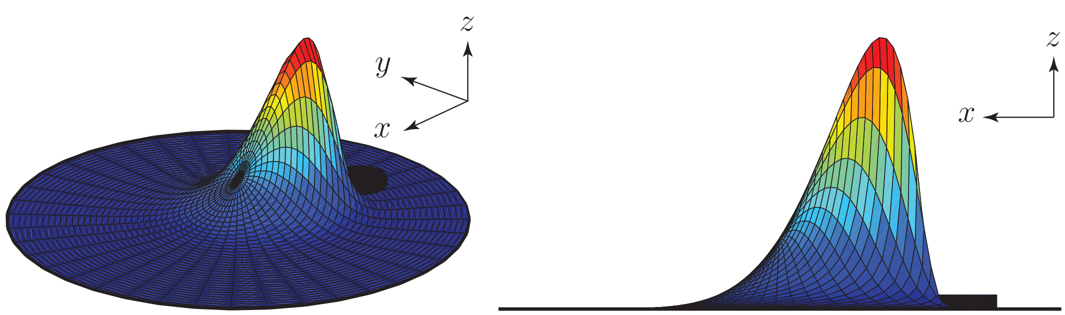

(a) (b)

Figure 5.10: Initial displacement of the membrane described in case 2

- **Case 2** : $a/R = 0.12$ and $d/R = 0.66$ and the initial conditions are represented as

$$H(r,\theta) = 0, \qquad G(r,\theta) = \frac{3}{5}(r-a)(r - r(\theta))^8, \qquad r \geq a$$

- **Case 3** : In this case, the membrane is assumed to be unconstrained and vibrating in its first mode. As it passes through the mean position, the constraint is applied and held fixed for all future time with $a/R = 0.1$ and $d/R = 0.4$. The position and velocity of the unconstrained membrane are given by the expressions

$$Z(r, \theta, t) = J_0(k_1^c \rho) \cos \omega_1^c t, \qquad \dot{Z}(r, \theta, t) = -\omega_1^c J_0(k_1^c \rho) \sin \omega_1^c t$$

where $\rho \triangleq \sqrt{r^2 + d^2 + 2rd \cos \theta}$ is defined in Fig. 5.1, $k_1^c R = 2.405$ and is obtained from the first zero of the Bessel function J_0, $\omega_1^c \triangleq \sqrt{T/\rho}\, k_1^c$, and $t = 0$ denotes the initial time when the membrane is released from rest. At $t = \pi/2\omega_1^c$, the membrane passes through the mean position and the constraint is applied. The initial conditions for the constrained membrane are therefore

$$G(r, \theta) = 0, \qquad H(r, \theta) = \begin{cases} -\omega_1^c J_0(k_1^c \rho) & : \quad a < r \leq \sqrt{R^2 - d^2 \sin^2 \theta} - d \cos \theta \\ 0 & : \quad 0 \leq r \leq a \end{cases}$$

The dynamics of the membrane was simulated using 16 symmetric and 16 antisymmetric modes. Fig. 5.11 shows the evolution of the motion for the membrane in case 1, where the isometric and side views are showed for each snapshot and the beginning of the motion is showed in Fig. 5.11 (a) and continues in Fig. 5.11 (b). The simulation of membrane in case 2 is shown in Fig. 5.12, where the motion starts in Fig. 5.12 (a) and continues in Fig. 5.12 (b) and Fig. 5.12 (c) respectively. Fig. 5.13 shows the evolution in motion of the membrane described in case 3 over one cycle of its motion . It is clear from the snapshots that both internal and external boundary conditions are satisfied and this is indicative of the accuracy of the simulations.

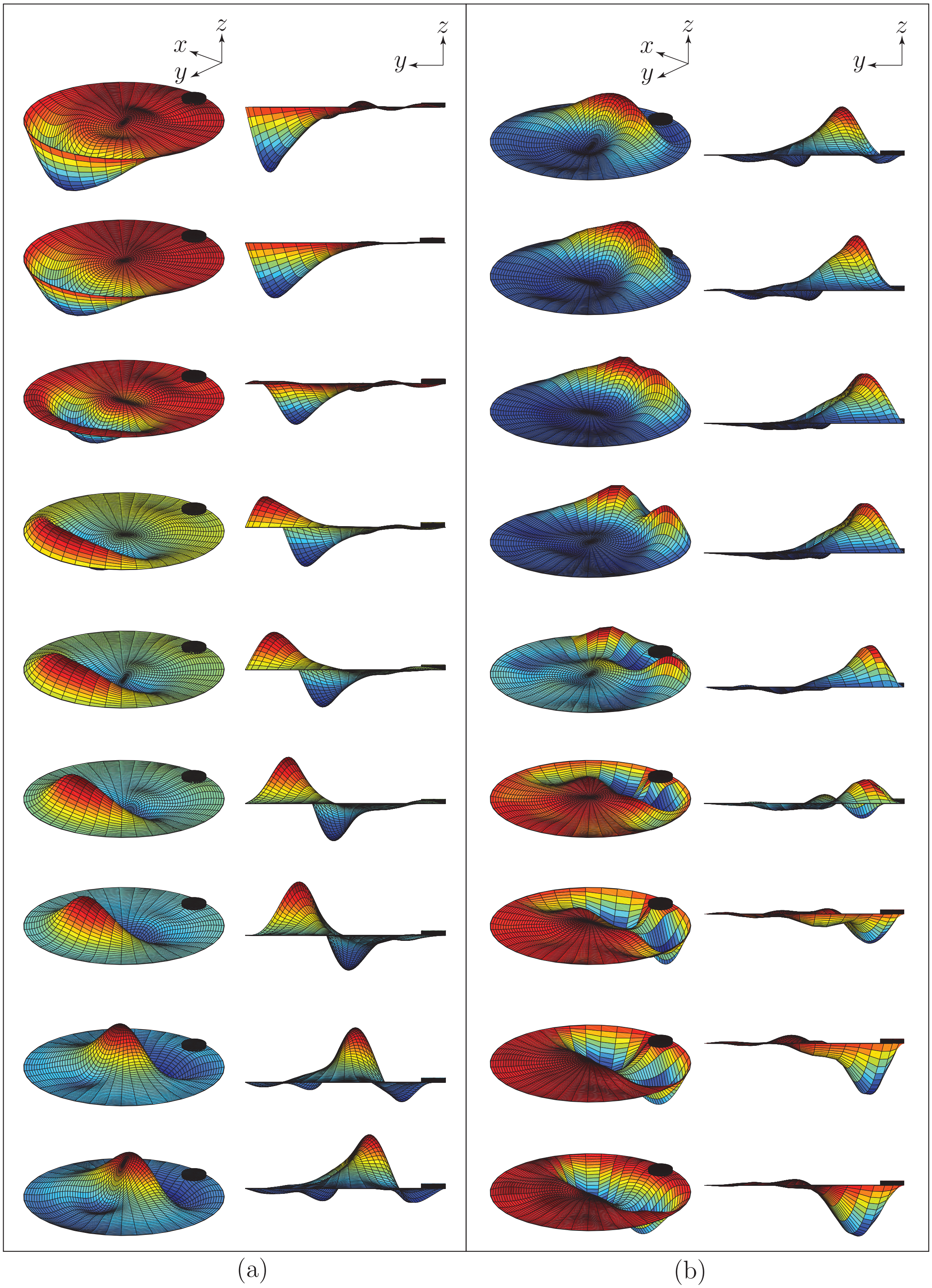

Figure 5.11: Snapshots of the membrane described in case 1 during one second of its vibration

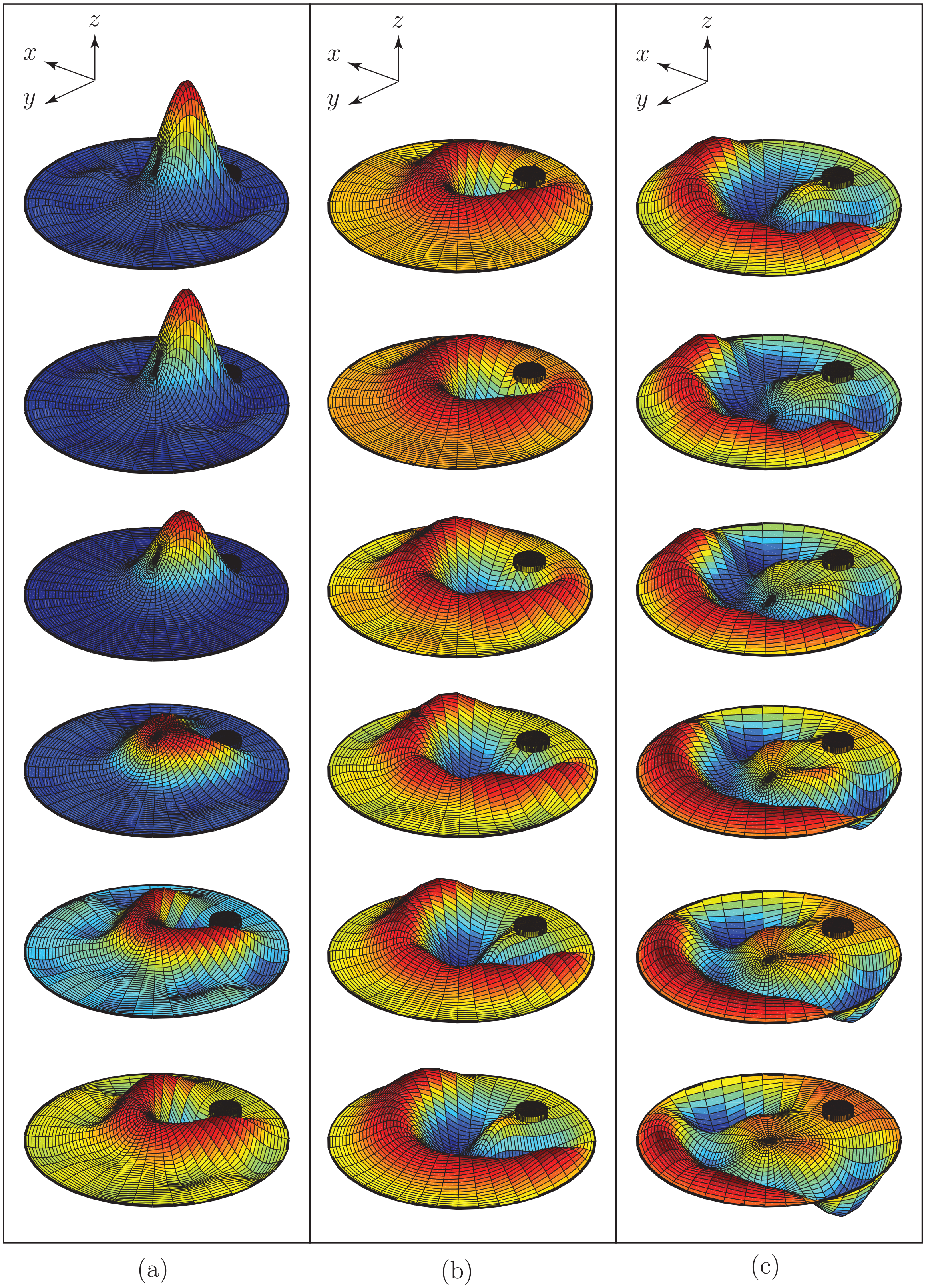

Figure 5.12: Snapshots of the membrane described in case 2 during one second of its vibration

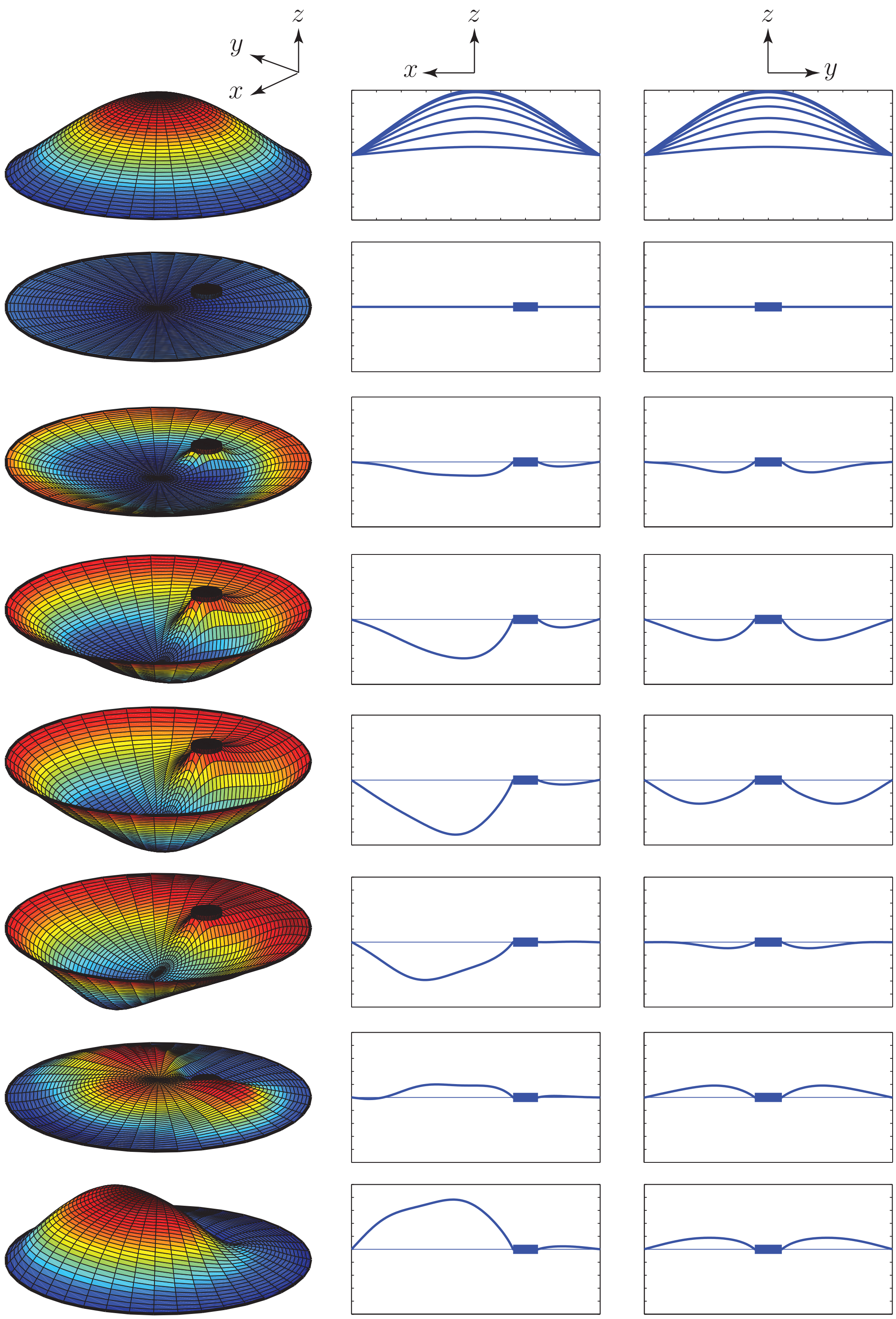

Figure 5.13: Snapshots of the membrane described in section case 3 during one cycle of its vibration

Chapter 6

Vibration Control of a Circular Membrane Using An Areal Constraint

6.1 Introduction

In this chapter we use the accurate dynamics analysis and simulation procedure presented in Chapter 5 to investigate the effect of constraint application and removal on the energetics of a vibrating membrane. The constraint is assumed to be circular and applied suddenly at an arbitrary time during free vibration of the membrane, which is vibrating in its fundamental mode. The energetics of the membrane due to constraint application is investigated for different sizes and locations of the constraint. This chapter is organized as follows: A formal problem statement and a list of assumptions are provided in Section 6.2. Assuming that the membrane is vibrating in its fundamental mode, we use analytical methods in Section 6.3 to study the dynamics of the membrane and change in its energy after application of the constraint. The dynamics of the membrane and change in its energy after removal of the constraint is studied in Section 6.4. In Section 6.5 we present numerical simulation results for one cycle of constraint application and removal - these results indicate that the energy of the membrane can increase or decrease depending on the time of application of the constraint. In Section 6.6 we repeat the analyses of Sections 6.3 and 6.4 for arbitrary initial conditions of the membrane and develop different control strategies to suppress the vibration of the membrane. Numerical simulation results are then presented to demonstrate the efficacy of the control strategies.

6.2 Problem Statement and Assumptions

Consider a circular membrane of radius R initially vibrating freely in its fundamental mode as shown in Fig. 6.2 (a). Assume a circular areal constraint of radius a to be applied instantaneously near the boundary of the membrane as shown Fig. 6.2 (b) at some arbitrary time $t = t_C$ during the motion of the membrane. The constraint is assumed to be applied during membrane motion at a distance d from the center of the membrane as shown in Fig. 6.2 (c). We investigate the effect of applying the constraint on the total energy under the following simplifying assumptions:

A1. The membrane is homogeneous and has a constant mass per unit area denoted by μ. The tension in the membrane is equal to T and remains constant at all times.

A2. The membrane is initially vibrating in its fundamental mode. This assumption will be removed and a general displacement profile of the membrane will be assumed in Section 6.6.

A3. The amplitude of oscillation of the membrane is small and therefore the equation of motion of the membrane can be expressed by the standard relation in polar coordinates [75]

$$\frac{\partial^2 Z_0}{\partial \rho^2} + \frac{1}{\rho}\frac{\partial Z_0}{\partial \rho} + \frac{1}{\rho^2}\frac{\partial^2 Z_0}{\partial \psi^2} = \frac{1}{c^2}\frac{\partial^2 Z_0}{\partial t^2} \tag{6.1}$$

where $Z_0 = Z_0(\rho, \psi, t)$ is the transversal displacement of the freely vibrating membrane and $c^2 = T/\mu$. The distance ρ is measured from the center of the membrane, and ψ is the angle that ρ makes with the x-axis as shown in Fig. 6.1.

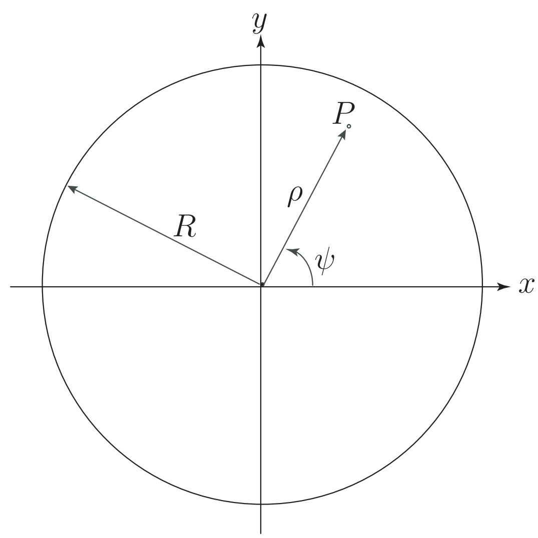

Figure 6.1: Circular membrane with radius R .

A4. The membrane has no internal damping, *i.e.*, the energy of the membrane will remain conserved during free vibration.

A5. At time $t = t_C$, the areal constrained is applied instantaneously as shown in Fig. 6.2 (b), at a distance d from the center of the membrane. The application of the constraint imposes an areal zero-displacement over a small region of the vibrating membrane. The displacement and velocity of the membrane over the remaining region of the membrane remains unchanged immediately after application of the constraint.

A6. At time $t = t_r$, $t_r > t_c$, the constraint is instantaneously moved back to its original position, *i.e.*, the constraint is removed to the outside of the membrane. The displacement and velocity of the membrane over the unconstrained region of the membrane remains unchanged immediately after removal of the constraint.

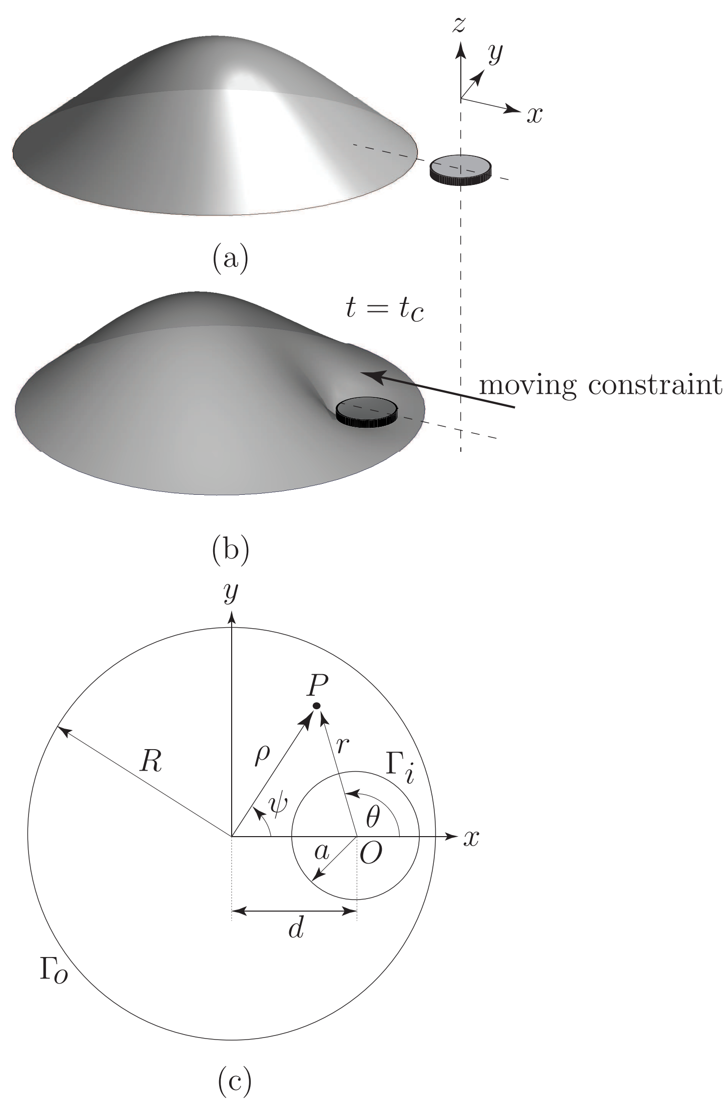

Figure 6.2: (a) A vibrating membrane (b) A zero-displacement circular constraint is applied to the membrane at time $t = t_c$ over a small region of the membrane (c) Geometry of the membrane and the applied constraint after constraint application

6.3 Effect of Applying Constraint on the Dynamics of the Membrane

6.3.1 Equation of motion after application of the constraint

The geometry of the membrane and the constraint is shown in Fig. 6.2 (c). To investigate the dynamics of the constrained membrane, we transform the coordinates of membrane from (ρ, ψ) to (r, θ) where both of the coordinates systems are shown in Fig. 6.2 (c), and the governing differential equation can be written as

$$\frac{\partial^2 Z_c}{\partial r^2} + \frac{1}{r}\frac{\partial Z_c}{\partial r} + \frac{1}{r^2}\frac{\partial^2 Z_c}{\partial \theta^2} = \frac{1}{c^2}\frac{\partial^2 Z_c}{\partial t^2} \tag{6.2}$$

where $Z = Z(r, \theta, t)$ is the transversal displacement. The distance r is measured from the center of the inner circle, O, and θ is the angle that r forms with the x-axis as shown in Fig. 6.2. The accurate dynamics analysis of the constrained membrane in (r, θ) coordinates is discussed in detail in Chapter 5 and the general solution is obtained in Eq. (5.37) as:

$$\begin{aligned} Z_c(r,\theta,t) = &\sum_{i=0}^{\infty} \varphi_i^c(k_i^c r, \theta)(A_{1i}\cos\omega_i^c t + B_{1i}\sin\omega_i^c t) \\ &+ \sum_{j=1}^{\infty} \varphi_j^s(k_j^s r, \theta)(A_{2j}\cos\omega_i^s t + B_{2j}\sin\omega_j^s t) \end{aligned} \tag{6.3}$$

where $\varphi_i^c(k_i^c r, \theta)$ and $\varphi_j^s(k_j^s r, \theta)$ are the symmetric and antisymmetric shape functions, which are presented in Eqs. (5.19) and (5.23). Also, k_i^c and k_j^s are the symmetric and antisymmetric eigenfrequencies of the constrained membrane. The model coefficients A_{1i}, B_{1i}, A_{2j} and B_{2j} are to be determined by applying the initial conditions.

6.3.2 Initial Conditions

The membrane is initially vibrating in the its first mode as:

$$Z_0(\rho, \psi, t) = A_0 J_0(k_{00}\rho) \cos \omega_{00} t \tag{6.4}$$

where A_0 is the maximum amplitude of oscillation. The constraint is applied at an arbitrary time t_c and therefore the initial conditions are

A1. The displacement of the membrane can be written as follows

$$Z_c(r, \theta, 0) = \begin{cases} A_0\, J_0(k_{00}\rho)\, \cos \omega_{00}\, t_c & : \quad a < r \leq \sqrt{R^2 - d^2 \sin^2 \theta} - d \cos \theta \\ 0 & : \quad 0 \leq r \leq a \end{cases} \tag{6.5}$$

Applying the initial conditions to Eqs. (6.3) and (6.4), we get

$$\sum_{i=0}^{\infty} A_{1i} \varphi_i^c(k_i^c r, \theta) + \sum_{j=1}^{\infty} A_{2j} \varphi_j^s(k_j^s r, \theta) = A_0 J_0(k_{00}\rho) \cos \omega_{00} t_c \tag{6.6}$$

To obtain the coefficients A_{1j} and A_{2j}, we use the orthogonality conditions between modes, where the orthogonality conditions between distinct modes are obtained in Eq. (5.35). By multiplying Eq. (6.6) with φ_i^c and integrating both sides over the effective membrane surface and using the orthogonality condition presented in Eq. (5.35), we get

$$A_{1i} = \frac{A_0 \cos \omega_{00} t_c}{\kappa_c} \int_0^{2\pi} \int_a^{r(\theta)} J_0(k_{00}\rho)\, \varphi_i^c\, r\, dr\, d\theta \tag{6.7}$$

where

$$\kappa_C = \int_0^{2\pi} \int_a^{r(\theta)} (\varphi_i^c)^2 r\, dr\, d\theta \tag{6.8}$$

Multiplying Eq. (6.6) with φ_j^s and integrating both sides over the effective membrane surface and using the orthogonality conditions in Eq. (5.35), gives

$$A_{2j} = \frac{A_0 \cos \omega_{00} t_c}{\kappa_S} \int_0^{2\pi} \int_a^{r(\theta)} J_0(k_{00}\rho)\ \varphi_j^s\, r\, dr\, d\theta \tag{6.9}$$

where

$$\kappa_S = \int_0^{2\pi} \int_a^{r(\theta)} (\varphi_j^s)^2 r\, dr\, d\theta \tag{6.10}$$

A2. The velocity of the membrane can be written as follows

$$\frac{\partial Z_C(r,\theta,0)}{\partial t} = \begin{cases} \dfrac{\partial Z_0(\rho,\psi,t_c)}{\partial t} & : \quad a < r \leq \sqrt{R^2 - d^2 \sin^2\theta} - d\cos\theta \\ 0 & : \quad 0 \leq r \leq a \end{cases} \tag{6.11}$$

$$\Rightarrow \sum_{i=0}^{\infty} B_{1i}\omega_i^c \varphi_i^c + \sum_{j=1}^{\infty} B_{2j}\omega_j^s \varphi_j^s \quad = \quad -\omega_{00}\, A_0\, J_0(k_{00}\rho)\, \sin \omega_{00} t_c \tag{6.12}$$

By multiplying Eq. (6.12) with φ_i^c and integrating both sides over the membrane surface and using the orthogonality conditions in Eq. (5.35), we get

$$B_{1i} = \frac{-\,\omega_{00}\, A_0 \sin \omega_{00} t_c}{\omega_i^c \kappa_C} \int_0^{2\pi} \int_a^{r(\theta)} J_0(k_{00}\rho)\ \varphi_i^c\, r\, dr\, d\theta \tag{6.13}$$

By multiplying Eq. (6.12) with φ_i^s and integrating both sides over the effective membrane surface and using the orthogonality condition presented in Eq. (5.35), we get

$$B_{2j} = \frac{-\,\omega_{00}\,A_0 \sin \omega_{00} t_c}{\omega_j^s \kappa_s} \int_0^{2\pi} \int_a^{r(\theta)} J_0(k_{00}\rho)\; \varphi_j^s \, r \, dr \, d\theta \tag{6.14}$$

6.3.3 Membrane Energy Before Application of Constraint

The total energy of the circular membrane in polar coordinates can be written as[1]

$$\begin{aligned} E &= \frac{\mu}{2} \iint\limits_A \left(\frac{\partial Z(r,\theta,t)}{\partial t} \right)^2 r \, dr \, d\theta \\ &+ \frac{T}{2} \iint\limits_A \left\{ \left(\frac{\partial Z(r,\theta,t)}{\partial r} \right)^2 + \frac{1}{r^2} \left(\frac{\partial Z(r,\theta,t)}{\partial \theta} \right)^2 \right\} r \, dr \, d\theta \end{aligned} \tag{6.15}$$

Where μ is the mass per unit area of the membrane and T is the tension per unit length. The initial energy of membrane can be given by rewriting Eq. (6.15) in (ρ, ψ) coordinates and with integrating over the membrane area as follows:

$$\begin{aligned} E_0 &= \frac{\mu}{2} \int_0^{2\pi} \int_0^R \left(\frac{\partial Z_0(\rho,\psi,t)}{\partial t} \right)^2 \rho \, d\rho \, d\psi \\ &+ \frac{T}{2} \int_0^{2\pi} \int_0^R \left\{ \left(\frac{\partial Z_0(\rho,\psi,t)}{\partial \rho} \right)^2 + \frac{1}{\rho^2} \left(\frac{\partial Z_0(\rho,\psi,t)}{\partial \psi} \right)^2 \right\} \rho \, d\rho \, d\psi \end{aligned} \tag{6.16}$$

[1]See appendix C

By differentiating Eq. (6.4) with respect to t, ρ and ψ, we get

$$\begin{aligned} \frac{\partial Z_0(\rho,\psi,t)}{\partial t} &= -A_0\omega_0 J_0(k_o\rho)\sin\omega_0 t \\ \frac{\partial Z_0(\rho,\psi,t)}{\partial \rho} &= -A_0 k_o J_1(k_o\rho)\cos\omega_0 t \\ \frac{\partial Z_0(\rho,\psi,t)}{\partial \psi} &= 0 \end{aligned} \tag{6.17}$$

Inserting Eqs. (6.17) in Eq. (6.16) leads to

$$\begin{aligned} E_0 &= \frac{\mu}{2}\int_0^{2\pi}\int_0^R \left(-A_0\omega_0 J_0(k_o\rho)\sin\omega_0 t\right)^2 \rho\, d\rho\, d\psi \\ &+ \frac{T}{2}\int_0^{2\pi}\int_0^R \left(-A_0 k_o J_1(k_o\rho)\cos\omega_0 t\right)^2 \rho\, d\rho\, d\psi \end{aligned}$$

Note that

$$\int_0^R J_n^2(k\rho)\,\rho\, d\rho = \frac{R^2}{2}\left\{J_n^2(kR) - J_{n-1}(kR)J_{n+1}(kR)\right\} \tag{6.18}$$

and $J_{-1}(k_oR) = -J_1(k_oR)$, $\omega_0 = ck_0$, $T = c^2\mu$, and $J_0(k_oR) = 0$. Then the total energy before the constraint application is

$$E_0 = \frac{T\pi}{2}\left(A_0 k_0 J_1(k_oR)\right)^2 \tag{6.19}$$

6.3.4 Membrane Energy After Application of Constraint

In this section we investigate the energy of the membrane after the application of the constraint. The equation of membrane motion after the constraint application is obtained by $Z_c(r,\theta,t)$ in Eq. (6.3), hence, the total energy of the membrane after constraint application can be given by using Eq. (6.15), and integrating over the constrained membrane area as follows

$$
\begin{aligned}
E_C &= \frac{T}{2}\int_0^{2\pi}\int_a^{r(\theta)}\left\{\left(\frac{\partial Z_C(r,\theta,t)}{\partial r}\right)^2+\frac{1}{r^2}\left(\frac{\partial Z_C(r,\theta,t)}{\partial \theta}\right)^2\right\} r\,dr\,d\theta \\
&+ \frac{\mu}{2}\int_0^{2\pi}\int_a^{r(\theta)}\left(\frac{\partial Z_C(r,\theta,t)}{\partial t}\right)^2 r\,dr\,d\theta \qquad (6.20)
\end{aligned}
$$

By differentiating Eq. (6.4) with respect to t, r and θ, we get

$$
\begin{aligned}
\frac{\partial Z_C(r,\theta,t)}{\partial t} &= \sum_{i=0}^{\infty}\omega_i^c\varphi_i^c(k_i^c r,\theta)(-A_{1i}\sin\omega_i^c t+B_{1i}\cos\omega_i^c t) \\
&+ \sum_{j=1}^{\infty}\omega_j^s\varphi_j^s(k_j^s r,\theta)(-A_{2j}\sin\omega_i^s t+B_{2j}\cos\omega_j^s t)
\end{aligned}
$$

$$
\begin{aligned}
\frac{\partial Z_C(r,\theta,t)}{\partial r} &= \sum_{i=0}^{\infty}\frac{\partial\varphi_i^c(k_i^c r,\theta)}{\partial r}(A_{1i}\cos\omega_i^c t+B_{1i}\sin\omega_i^c t) \\
&+ \sum_{j=1}^{\infty}\frac{\varphi_j^s(k_j^s r,\theta)}{\partial r}(A_{2j}\cos\omega_i^s t+B_{2j}\sin\omega_j^s t) \qquad (6.21)
\end{aligned}
$$

where,

$$
\begin{aligned}
\frac{\partial\varphi_i^c(k_i^c r,\theta)}{\partial r} &= \sum_{m=0}^{N+1}\left[\beta_{2m}^i\frac{\partial J_m(k_i^c r)}{\partial r}+\gamma_{2m}^i\frac{\partial Y_m(k_i^c r)}{\partial r}\right]\cos m\theta \\
\frac{\varphi_j^s(k_j^s r,\theta)}{\partial r} &= \sum_{m=1}^{N}\left[\beta_{1m}^j\frac{\partial J_m(k_j^s r)}{\partial r}+\gamma_{1m}^j\frac{\partial Y_m(k_j^s r)}{\partial r}\right]\sin m\theta \qquad (6.22)
\end{aligned}
$$

where, in general,

$$\frac{\partial J_m(kr)}{\partial r} = \frac{k}{2}\left[J_{m-1}(kr) - J_{m+1}(kr)\right]$$
$$\frac{\partial Y_m(kr)}{\partial r} = \frac{k}{2}\left[Y_{m-1}(kr) - Y_{m+1}(kr)\right] \tag{6.23}$$

Also,

$$\begin{aligned}\frac{\partial Z_c(r,\theta,t)}{\partial \theta} &= \sum_{i=0}^{\infty} \frac{\partial \varphi_i^c(k_i^c r,\theta)}{\partial \theta}(A_{1i}\cos\omega_i^c t + B_{1i}\sin\omega_i^c t) \\ &+ \sum_{j=1}^{\infty} \frac{\partial \varphi_j^s(k_j^s r,\theta)}{\partial \theta}(A_{2j}\cos\omega_i^s t + B_{2j}\sin\omega_j^s t)\end{aligned} \tag{6.24}$$

where

$$\frac{\partial \varphi_i^c(k_i^c r,\theta)}{\partial \theta} = \sum_{m=0}^{N} -m\left[\beta_{2m}^i J_m(k_i^c r) + \gamma_{2m}^i Y_m(k_i^c r)\right]\sin m\theta$$
$$\frac{\partial \varphi_j^s(k_j^s r,\theta)}{\partial \theta} = \sum_{m=1}^{N+1} m\left[\beta_{1m}^j J_m(k_j^s r) + \gamma_{1m}^j Y_m(k_j^s r)\right]\cos m\theta \tag{6.25}$$

The total energy of the membrane after the application of the constraint E_c can be calculated by inserting the equations (6.21-6.25) into Eq. (6.20) and integrating numerically. The work done by the constraint W_d and the percentage change in energy are expressed as:

$$W_d = E_c - E_0 \tag{6.26}$$

$$\%\text{Change in Energy} = \frac{E_c - E_0}{E_0} \times 100 \tag{6.27}$$

6.4 Effect of Removing Constraint on the Dynamics of the Membrane

6.4.1 Equation of motion after removal of the constraint

We analyse the dynamics of the membrane after constraint removal. Assume the constraint is removed at an arbitrary time $t = t_r$ after application of the constraint, such that $t_r > t_c > 0$. When the constraint is removed, the membrane vibrates freely according to the equation of motion of an unconstrained membrane. The equation of motion of simple unconstrained membrane can be obtained by solving the PDE in Eq. (6.1). Assume $\bar{Z}_f(\rho, \psi, t)$ is the transverse displacement of the membrane after the removal of the constraint, and the governing differential equation becomes

$$\frac{\partial^2 \bar{Z}_f}{\partial \rho^2} + \frac{1}{\rho}\frac{\partial \bar{Z}_f}{\partial \rho} + \frac{1}{\rho^2}\frac{\partial^2 \bar{Z}_f}{\partial \psi^2} = \frac{1}{c^2}\frac{\partial^2 \bar{Z}_f}{\partial t^2} \tag{6.28}$$

The general solution of Eq. (6.28) is given by using the separation of variables and it can be written as[2]

$$\begin{aligned}\bar{Z}_f(\rho, \psi, t) &= \sum_{q=0}^{\infty}\sum_{i=0}^{\infty} J_q(k_{qi}\rho)(C_{qi}\cos\omega_{qi}t + D_{qi}\sin\omega_{qi}t)\cos q\psi \\ &+ \sum_{q=1}^{\infty}\sum_{i=1}^{\infty} J_q(k_{qi}\rho)(E_{qi}\cos\omega_{qi}t + F_{qi}\sin\omega_{qi}t)\sin q\psi \end{aligned} \tag{6.29}$$

where k_{qi} represents the eigenfrequencies of the unconstrained membrane and $\omega_{qi} = c\,k_{qi}$ and the model coefficients C_{qi}, D_{qi}, E_{qi} and F_{qi} are constants to be determined by applying

[2]See Appendix A.2

the initial conditions. When the constraint is removed at $t = t_r$, previous motion of the constrained membrane represents the initial conditions for the upcoming membrane motion after constraint removal. Thus, the initial conditions can be written as:

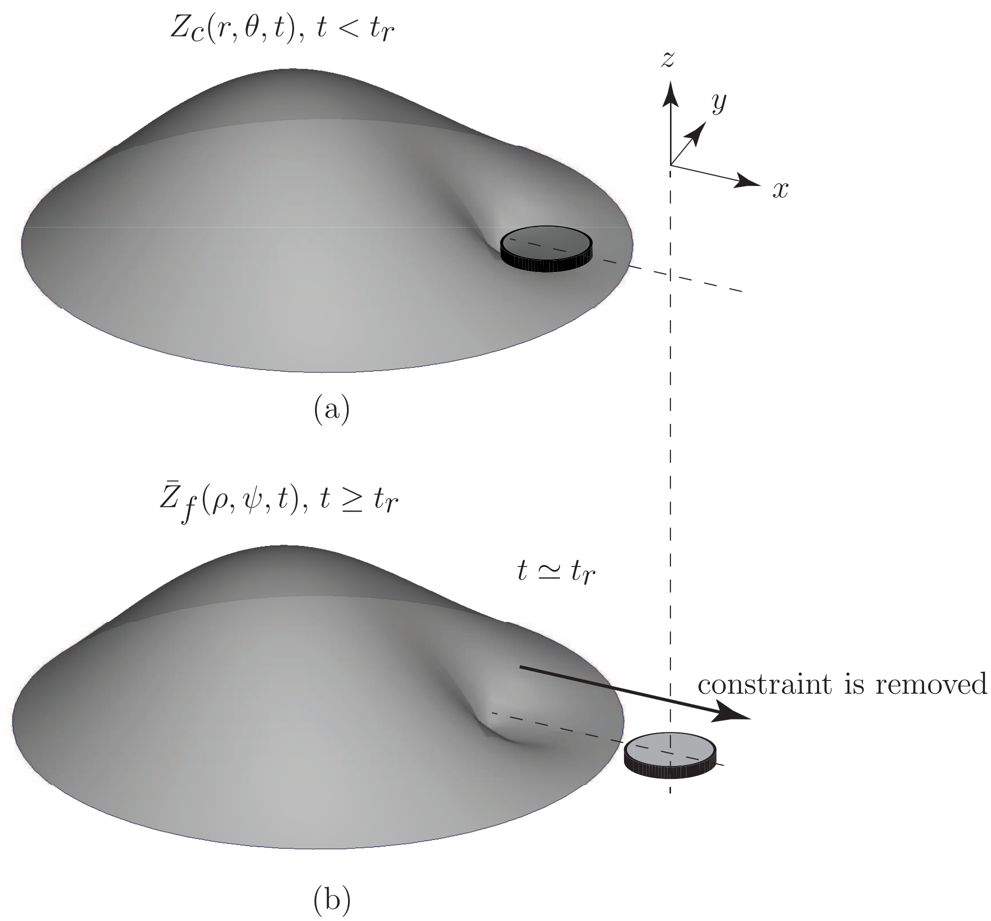

Figure 6.3: (a) A vibrating constrained membrane (b) The circular constraint is removed from the membrane at time $t \simeq t_r$

A1. The displacement of the membrane can be obtained by applying the initial conditions to Eqs. (6.3) and (6.29) as follows

$$\bar{Z}_f(\rho, \psi, 0) = \begin{cases} Z_C(r, \theta, t_r) & : \quad a < r \leq \sqrt{R^2 - d^2 \sin^2 \theta} - d \cos \theta \\ 0 & : \quad 0 \leq r \leq a \end{cases} \tag{6.30}$$

then

$$Z_c(r,\theta,t_r) \;=\; C_{00}J_0(k_{00}\rho) + \sum_{q=1}^{\infty}\sum_{i=1}^{\infty} J_q(k_{qi}\rho)\left(C_{qi}\cos q\psi + E_{qi}\sin q\psi\right) \tag{6.31}$$

Note that the orthogonality conditions for unconstrained membrane are:

$$\begin{aligned}
&\int_0^R J_q(k_{qi}\rho)J_q(k_{qj}\rho)\rho d\rho = 0, \quad i \neq j \\
&\int_0^{2\pi} \sin m\psi\, \sin q\psi\; d\psi = \int_0^{2\pi} \cos m\psi\, \cos q\psi\, d\psi = 0, \quad q \neq m \\
&\int_0^{2\pi} \cos m\psi\, \sin q\psi\, d\psi = 0, \quad \forall q, m
\end{aligned} \tag{6.32}$$

By multiplying Eqs. (6.31) by $J_0(k_{00}\rho)$ and integrating both sides over the membrane surface and using the orthogonality condition presented in Eq(6.32), we get

$$C_{00} = \frac{1}{2\pi\, \triangle_{00}} \int_0^{2\pi}\int_0^R Z_c(r,\theta,t_r)J_0(k_{00}\rho)\,\rho\, d\rho\, d\psi \tag{6.33}$$

where $\triangle_{00}= \int_0^R J_0^2(k_{00}\rho)\,\rho\, d\rho$, and note that from Eq. (6.18) we can write

$$\triangle_{qi}= \int_0^R J_n^2(k_{qi}\rho)\,\rho\, d\rho = \frac{R^2}{2}\left\{J_n^2(k_{qi}R) - J_{n-1}(k_{qi}R)J_{n+1}(k_{qi}R)\right\} \tag{6.34}$$

By repeating the procedure above after multiplying Eq. (6.31) by $J_q(k_{qj}\rho)\cos m\psi$ and

$J_q(k_{qj}\rho)\sin m\psi$ respectively, and integrating over the membrane area, we get

$$C_{qi} = \frac{1}{\pi \triangle_{qi}} \int_0^{2\pi} \int_0^R Z_c(r,\theta,t_r) J_q(k_{qi}\rho) \cos q\psi \;\rho\, d\rho\, d\psi$$
$$E_{qi} = \frac{1}{\pi \triangle_{qi}} \int_0^{2\pi} \int_0^R Z_c(r,\theta,t_r) J_q(k_{qi}\rho) \sin q\psi \;\rho\, d\rho\, d\psi \qquad (6.35)$$

A2. The velocity of the membrane can be written as

$$\frac{\partial \bar{Z}_f(\rho,\psi,0)}{\partial t} = \begin{cases} \dfrac{\partial Z_c(r,\theta,t_r)}{\partial t} & : \quad a < r \leq \sqrt{R^2 - d^2\sin^2\theta} - d\cos\theta \\ 0 & : \quad 0 \leq r \leq a \end{cases} \qquad (6.36)$$

this gives

$$D_{00}\,\omega_{00}\, J_0(k_{00}\rho) + \sum_{q=1}^{\infty}\sum_{i=1}^{\infty} \omega_{qi} J_q(k_{qi}\rho)\left(D_{qi}\cos q\psi + F_{qi}\sin q\psi\right) = \frac{\partial Z_c(r,\theta,t_r)}{\partial t} \qquad (6.37)$$

Following the procedure in which the coefficients in Eqs. (6.33) and (6.35) were obtained, we get

$$D_{00} = \frac{1}{2\pi\omega_{00}\,\triangle_{00}} \int_0^{2\pi} \int_0^R \frac{\partial Z_c(r,\theta,t_r)}{\partial t} J_0(k_{00}\rho)\,\rho\, d\rho\, d\psi$$
$$D_{qi} = \frac{1}{\pi\omega_{qi}\,\triangle_{qi}} \int_0^{2\pi} \int_0^R \frac{\partial Z_c(r,\theta,t_r)}{\partial t} J_q(k_{qi}\rho)\cos q\psi \;\rho\, d\rho\, d\psi$$
$$F_{qi} = \frac{1}{\pi\omega_{qi}\,\triangle_{qi}} \int_0^{2\pi} \int_0^R \frac{\partial Z_c(r,\theta,t_r)}{\partial t} J_q(k_{qi}\rho)\sin q\psi \;\rho\, d\rho\, d\psi \qquad (6.38)$$

One can note that the variables in the integrations in Eqs. (6.33), (6.35),and (6.38) are different (ρ, ψ and r, θ). In addition, the integrations should be performed by excluding the area covered by the constraint because it has zero displacement and zero velocity. Excluding the constrained area by using $(\rho, \psi\ )$ coordinates is quite challenging. Therefore, we change the order of the integrations and the variables of the integration will be (r, θ) coordinates system only. We can unify the integrations variables by using the relationships between $(\rho, \psi$ and $r, \theta\ )$, where from Fig. 6.2 we can write

$$\rho = \sqrt{d^2 + r^2 + 2\,r\,d\cos\theta}, \quad \psi = \cos^{-1}\left(\frac{d + r\ \cos\theta}{\rho}\right) \tag{6.39}$$

The area of the membrane is constant and can be obtained by

$$Area = \int_0^{2\pi}\int_0^{r(\theta)} r\,dr\,d\theta = \int_0^{2\pi}\int_0^{R} \rho\,d\rho\,d\psi$$

Using Eq. (6.39) and integrating over the area with $(r\,dr\,\theta)$ instead of $(\rho\,d\rho\,d\psi)$ we can get

$$\begin{aligned}\int_0^{2\pi}\int_0^{R} h(r,\theta,t_r)\,J_0(k_{00}\rho)\,\rho\,d\rho\,d\psi \quad &+ \quad \iint\limits_{A_C} 0\ \ J_0(k_{00}\rho)\,\rho\,d\rho\,d\psi \\ &= \int_0^{2\pi}\int_a^{r(\theta)} h(r,\theta,t_r)\,J_0(k_{00}\rho(\theta))\,r\,dr\,d\theta\end{aligned}$$

where $h(r,\theta,t_r)$ could be $Z_C(r,\theta,t_r)$ or $\dfrac{\partial Z_C(r,\theta,t_r)}{\partial t}$.

6.4.2 Membrane Energy After Removal of Constraint

The total energy of the membrane after constraint removal can be obtained by using Eq. (6.15), and integrating over the unconstrained membrane area

$$
\begin{aligned}
E_r &= \frac{T}{2}\int_0^{2\pi}\int_0^R \left\{ \left(\frac{\partial \bar{Z}_f(\rho,\psi,t)}{\partial \rho}\right)^2 + \frac{1}{\rho^2}\left(\frac{\partial \bar{Z}_f(\rho,\psi,t)}{\partial \psi}\right)^2 \right\} \rho \, d\rho \, d\psi \\
&+ \frac{\mu}{2}\int_0^{2\pi}\int_0^R \left(\frac{\partial \bar{Z}_f(\rho,\psi,t)}{\partial t}\right)^2 \rho \, d\rho \, d\psi \qquad (6.40)
\end{aligned}
$$

The derivatives of $\bar{Z}_f(\rho,\psi,t)$ with respect to ρ ,ψ and t are obtained from Eq. (6.29) as follows

$$
\begin{aligned}
\frac{\partial \bar{Z}_f(\rho,\psi,t)}{\partial \rho} &= \sum_{q=1}^{\infty}\sum_{i=1}^{\infty} \frac{\partial J_q(k_{qi}\rho)}{\partial \rho} \left\{ f_{qi}^c(t)\cos q\psi + f_{qi}^s(t)\sin q\psi \right\} \\
\frac{\partial \bar{Z}_f(\rho,\psi,t)}{\partial \psi} &= \sum_{q=1}^{\infty}\sum_{i=1}^{\infty} qJ_q(k_{qi}\rho) \left\{ -f_{qi}^c(t)\sin q\psi + f_{qi}^s(t)\cos q\psi \right\} \\
\frac{\partial \bar{Z}_f(\rho,\psi,t)}{\partial t} &= \sum_{q=1}^{\infty}\sum_{i=1}^{\infty} J_q(k_{qi}\rho) \left\{ \frac{df_{qi}^c(t)}{dt}\cos q\psi + \frac{df_{qi}^s(t)}{dt}\sin q\psi \right\} \qquad (6.41)
\end{aligned}
$$

where

$$
\begin{aligned}
\frac{\partial J_m(k_{qi}\rho)}{\partial \rho} &= \frac{k_{qi}}{2}\left[J_{m-1}(k_{qi}\rho) - J_{m+1}(k_{qi}\rho) \right] \\
f_{qi}^c(t) &= C_{qi}\cos\omega_{qi}t + D_{qi}\sin\omega_{qi}t \\
f_{qi}^s(t) &= E_{qi}\cos\omega_{qi}t + F_{qi}\sin\omega_{qi}t \\
\frac{df_{qi}^c(t)}{dt} &= \omega_{qi}\left(-C_{qi}\sin\omega_{qi}t + D_{qi}\cos\omega_{qi}t \right) \\
\frac{df_{qi}^s(t)}{dt} &= \omega_{qi}\left(-E_{qi}\sin\omega_{qi}t + F_{qi}\cos\omega_{qi}t \right) \qquad (6.42)
\end{aligned}
$$

By inserting Equations (6.43) and (6.42) in Eq. (6.40), and using the numerical integration described in Eq. (5.44), the total energy of the membrane after constraint removal can be obtained.

6.5 Simulation of One Cycle of Constraint Application and Removal

In this section we present numerical simulations for the circular vibrating membrane subjected to a sudden areal constraint for different time of constraint applications t_c and constraint sizes and locations. Consider a circular membrane oscillating in the first mode as follows:

$$Z_0(\rho, \psi, t) = A_0 J_0(k_{00}\, \rho) \cos(\omega_{00})t \tag{6.43}$$

where the specifications of the membrane are :

$$R = 1 \text{ m}, \qquad \mu = 0.25 \text{ kg/m}^2, \qquad \text{T} = 1 \text{ N/m}$$

and $k_{00} = 2.4048$ m $^{-1}$, $A_0 = 0.1$ m and $\omega_{00} = 4.8096$ rad/sec

From ω_{00} we can obtain the time period which is 1.3064 sec and Fig. 6.3 (a) shows the shape of the membrane at different instants of time over the interval $t \in [0, 0.6532]$ sec. The membrane is in its maximum potential energy configuration at $t = 0$ sec and $t = 0.6532$ sec, and maximum kinetic energy configuration at $t = 0.3266$ sec when the membrane passes through the mean position.

We first present simulation results for percentage change in energy due to constraint of size $a/R = 0.1$ and locations $d/R \in \{0.0, 0.6, 0.9\}$ and $t_C \in [0.24, 0.42]$ sec as shown in Fig. 6.4 (b). The simulation is performed using 16 symmetric and 16 antisymmetric modes. The results, shown in Fig. 6.4 (b), indicate that the energy of the membrane increases if the constraint is applied when the membrane is far away from the mean position, and decreases if the constraint is applied when the membrane is near its mean position, irrespective of the value of d. Same result can be observed for different constraint size ($a/R = 0.12$) and locations $d/R \in \{0.0, 0.44, 0.88\}$ as shown in Fig 6.4 (c). The results also show that larger constraint causes more change (increase/decrease) in the total energy, as expected. Similar observation were made in our previous work on vibration suppression of string using a scabbard-like actuator, presented in Chapter 3.

The results can be explained as follows. When the constraint is applied and an area of the membrane is brought to rest, the kinetic energy of the seized membrane is removed. However, the potential energy in the membrane is increased due to sudden change in the slope adjacent to the constraint. The potential energy increases more as the constraint is applied when the membrane is far away form the mean position, and hence, the total energy is increased. When the constraint is applied as the membrane passes through the mean position, the change in potential energy is almost zero and the kinetic of the area seized by the constraint is lost, hence the total energy of the membrane is reduced. In addition, the kinetic energy is proportional to the area of the membrane which is covered by the constraint, and therefore, larger constraint size causes higher energy reduction when the constraint is applied as the membrane passes through the mean position. That is because the velocity of the constrained area is higher when the it is located close to the center of the membrane. For the same value of t_C, a smaller value of d results in a higher decrease in total energy when the constraint is applied as the membrane passes through the mean position. The general statement of energy reduction condition can be stated as: *The maximum energy reduction occurs when the constraint is applied as the membrane passes through its mean position . The energy loss due to the loss of kinetic energy of the membrane area which is covered by the constraint* . We can use this condition to apply and remove the constraint sequentially, or move the constraint over the membrane area to reduce the total energy of the membrane.

Next we investigate the change in energy of the membrane due to removal of the constraint. We compute the values of E_C and E_r, which equal the energy of the membrane before and after removal of the constraint respectively. Using Eqs. (6.20), E_C is computed for 16 symmetric and 16 antisymmetric modes. We fix the value of the energy before the constraint removal E_C and we compute E_r from Eq. (6.40) with varying the number of Fourier coefficients. From this data (see Table 6.1) it is clear that E_C and E_r approach each other as the number of Fourier coefficients increase. Although the data corresponds to the specific case of $d/R = 0.88$, $a/R = 0.12$ and $t_r = 0.4$ sec, the same trends can be observed for all values of d/R, a/R and t_r. In the next section we investigate the effect of application of the constraint on the dynamics of the membrane with arbitrary initial conditions such that sequential application and removal of constraints can be explored as a strategy for vibration suppression.

Table 6.1: Comparison of values of E_r with a fixed value of $E_C = 2.4455$ J for constrained membrane with $d/R = 0.88$, $a/R = 0.12$ and $t_r = 0.4$ sec

No. of Fourier coefficients	E_r (J)	error %
10	2.4176	-1.1428
30	2.4335	-0.4903
64	2.4365	-0.3683
80	2.4391	-0.2604

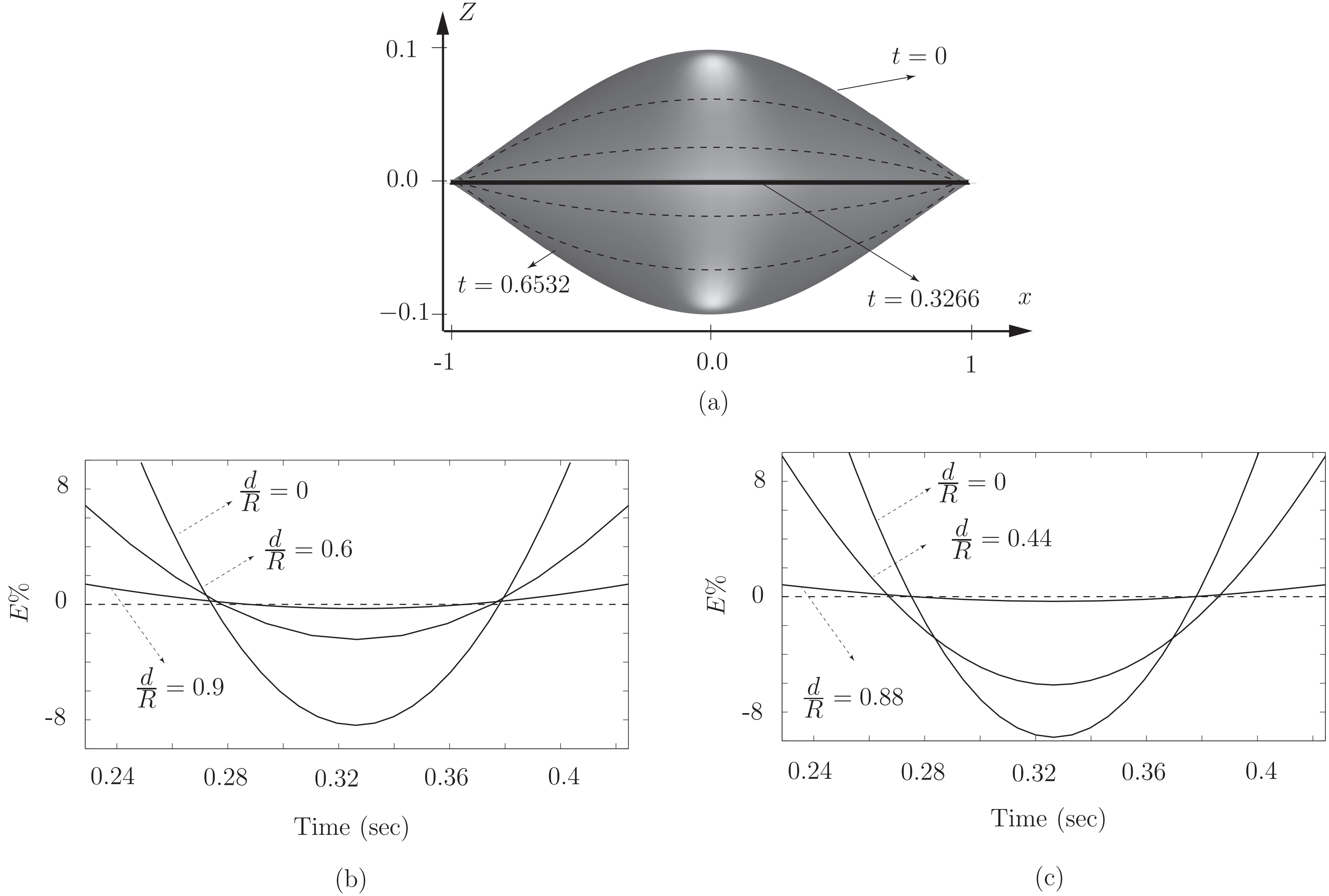

Figure 6.4: Percentage change in total energy of the membrane due to application of the constraint of different size of values of of d and to. (a) position of the membrane at different time instants. (b) $a/R = 0.1$ (c) $a/R = 0.12$

6.6 Sequential Application and Removal of Constraints

6.6.1 Dynamics of membrane with arbitrary initial conditions

The analysis in this chapter thus far is based on a membrane that initially vibrates in its the fundamental mode. We extend the analysis to include arbitrary initial vibration of the membrane. The equation of motion of unconstrained membrane that includes all possible initial conditions can be written as

$$\begin{aligned} Z_O(\rho, \psi, t) &= \sum_{q=0}^{\infty}\sum_{i=0}^{\infty} J_q(k_{qi}\rho)(\alpha_{qi}\cos\omega_{qi}t + \beta_{qi}\sin\omega_{qi}t)\cos q\psi \\ &+ \sum_{q=1}^{\infty}\sum_{i=1}^{\infty} J_q(k_{qi}\rho)(\Gamma_{qi}\cos\omega_{qi}t + \delta_{qi}\sin\omega_{qi}t)\sin q\psi \end{aligned} \tag{6.44}$$

which is similar to Eq(6.29) and satisfies the boundary conditions of unconstrained membrane, and the coefficients α_{qi}, β_{qi}, Γ_{qi} and δ_{qi} are known. By using Eq. (6.15), the initial energy of the membrane can be written as

$$\begin{aligned} \bar{E}_O &= \frac{T}{2}\int_0^{2\pi}\int_0^R \left\{\left(\frac{\partial Z_O(\rho,\psi,t)}{\partial\rho}\right)^2 + \frac{1}{\rho^2}\left(\frac{\partial Z_O(\rho,\psi,t)}{\partial\psi}\right)^2\right\}\rho\, d\rho\, d\psi \\ &+ \frac{\mu}{2}\int_0^{2\pi}\int_0^R \left(\frac{\partial Z_O(\rho,\psi,t)}{\partial t}\right)^2 \rho\, d\rho\, d\psi \end{aligned} \tag{6.45}$$

where it is identical to E_r in Eq. (6.40), and the same calculation procedure for E_r can be used to obtain E_O. The equation of motion of the membrane after constraint application can be written as

$$\bar{Z}_C(r,\theta,t) = \sum_{i=0}^{\infty} \bar{\varphi}_i^c(k_i^c r, \theta)\, f_i^c(t) + \sum_{j=1}^{\infty} \bar{\varphi}_j^s(k_j^s r, \theta)\, f_j^s(t) \tag{6.46}$$

where $f_i^c(t) = \bar{A}_{1i} \cos \omega_i^c t + \bar{B}_{1i} \sin \omega_i^c t$ and $f_j^s(t) = \bar{A}_{2j} \cos \omega_i^s t + \bar{B}_{2j} \sin \omega_j^s t$. Equation (6.46) is identical to Eq. (6.3) except that φ_i^c, φ_j^s, A_{1i}, A_{2i}, B_{1j}, and B_{2j} are replaced by $\bar{\varphi}_i^c$, $\bar{\varphi}_j^s$, $\bar{A}_{1i}$, $\bar{A}_{2i}$, $\bar{B}_{1j}$, and $\bar{B}_{2j}$. The coefficients $\bar{A}_{1i}$, $\bar{A}_{2i}$, $\bar{B}_{1j}$, and $\bar{B}_{2j}$ are determined from the initial conditions by repeating the procedure used in Section 6.3.1. Without loss of generality, the time is reset from $t = t_C$ to $t = 0$, and the displacement and velocity of the membrane given by

$$\begin{aligned} \bar{Z}_C(r, \theta, 0) &= Z_O(\rho, \psi, t_C) \\ \frac{\partial \bar{Z}_C(r, \theta, 0)}{\partial t} &= \frac{\partial Z_O(\rho, \psi, t_C)}{\partial t} \end{aligned} \tag{6.47}$$

By using Eqs. (6.44), (6.46) and (6.47) and following the same procedure used in Section 6.3.1, we can write

$$\begin{aligned} \bar{A}_{1i} &= \frac{1}{\kappa_C} \int_0^{2\pi} \int_a^{r(\theta)} Z_O(\rho, \psi, t_C)\ \bar{\varphi}_i^c\, r\, dr\, d\theta \\ \bar{A}_{2j} &= \frac{1}{\kappa_S} \int_0^{2\pi} \int_a^{r(\theta)} Z_O(\rho, \psi, t_C)\ \bar{\varphi}_j^s\, r\, dr\, d\theta \\ \bar{B}_{1i} &= \frac{1}{\omega_i^c \kappa_C} \int_0^{2\pi} \int_a^{r(\theta)} \frac{\partial Z_O(\rho, \psi, t_C)}{\partial t}\ \bar{\varphi}_i^c\, r\, dr\, d\theta \\ \bar{B}_{2j} &= \frac{1}{\omega_j^s \kappa_S} \int_0^{2\pi} \int_a^{r(\theta)} \frac{\partial Z_O(\rho, \psi, t_C)}{\partial t}\ \bar{\varphi}_j^s\, r\, dr\, d\theta \end{aligned} \tag{6.48}$$

The total energy of the membrane after constraint application is

$$\begin{aligned} \bar{E}_C &= \frac{T}{2} \int_0^{2\pi} \int_a^{r(\theta)} \left\{ \left(\frac{\partial \bar{Z}_C(r, \theta, t)}{\partial r} \right)^2 + \frac{1}{r^2} \left(\frac{\partial \bar{Z}_C(r, \theta, t)}{\partial \theta} \right)^2 \right\} r\, dr\, d\theta \\ &+ \frac{\mu}{2} \int_0^{2\pi} \int_a^{r(\theta)} \left(\frac{\partial \bar{Z}_C(r, \theta, t)}{\partial t} \right)^2 r\, dr\, d\theta \end{aligned} \tag{6.49}$$

6.6.2 Control strategies for vibration suppression

Similar to the vibrating string subjected to a constraint applied by a scabbard-like (see Chapter 3), the simulation results in Section 6.5 show that the maximum reduction in energy of the membrane is achieved if the constraint is applied when the displacement of the membrane is zero over the area $r \leq a$. For arbitrary initial conditions, the displacement of the membrane can be uniformly zero over a small area adjacent to the constraint at some given time, and therefore, energy reduction can be ensured by choosing a small distance that the constraint moves. We investigate three different control strategies for the vibration suppression of a circular membrane. These different control strategies are presented in next three sections.

6.6.3 Simple Application and Removal of Constraint

In this section we investigate energy dissipation due to simple application and removal of the areal constraint. The constraint is applied at a distance d from the center of the membrane during its motion, and then removed to its original location outside the membrane as shown in Fig 6.5 (b). We use the energy reduction condition from Section 6.5 to compute the total energy of the vibrating membrane through sequential application and removal of the constraint. Assume that the membrane is initially vibrating freely with arbitrary initial conditions as in Eq. (6.44). A set of sensors are mounted on the mechanism applying the constraint to sense the displacements of the membrane of the circular area $\bar{\Omega}$ to which the constraint will be applied, see Fig. 6.5 (b). When the displacement of the sensed area $\bar{\Omega}$ is approximately zero, the constraint is applied, and after some arbitrary time t_r the constraint is removed and the procedure will be repeated.

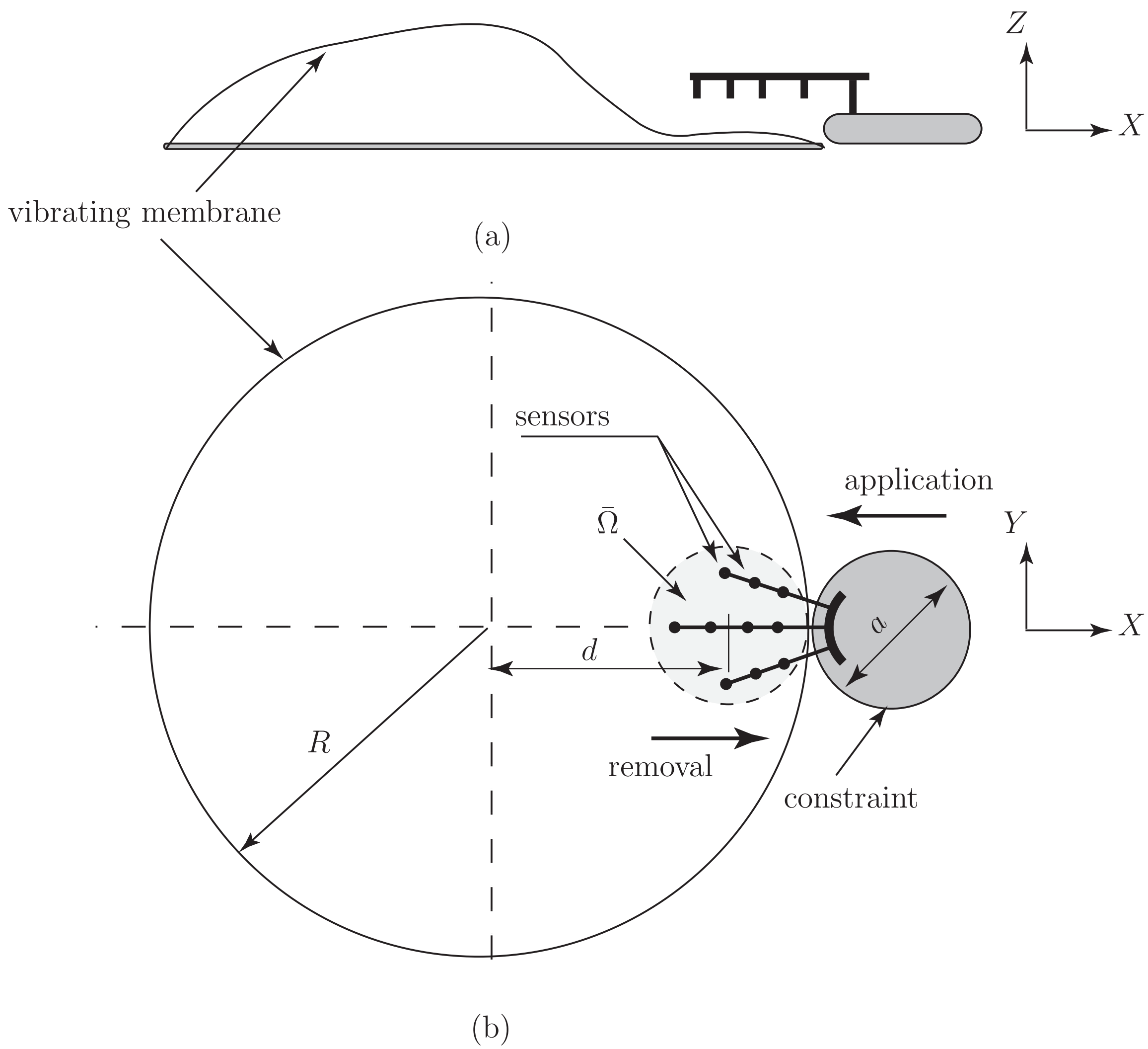

Figure 6.5: Sensing mechanism for simple application and removal of constraint (a) side view. (b) top view

The procedure of simple application and removal of the constraint can be summarized as follows:

A1. The membrane initially vibrates freely and its equation of motion is given by $Z_p(\rho, \psi, t) = Z_o(\rho, \psi, t)$, where $Z_o(\rho, \psi, t)$ is presented in Eq. (6.44) and p denotes the number of times the constraint has applied. The initial energy E_0 of the membrane is computed by using Eq. (6.16).

A2. When the displacement of sensed area $\bar{\Omega}$ is ≈ 0, then $t = t_c^{(p)}$ and the constraint is applied.

A3. Reset the time $t = 0$ and find the equation of the motion of the membrane after constraint application $\bar{Z}_c(r, \theta, t)$ which is presented in Eq. (6.46). The procedure presented in Section 6.6.1 is used to obtain the model coefficients as follows :

$$
\begin{aligned}
\bar{A}_{1i}^{(p)} &= \frac{1}{\kappa_c} \int_0^{2\pi} \int_a^{r(\theta)} Z_p(\rho, \psi, t_c^{(p)})\ \bar{\varphi}_i^c\, r\, dr\, d\theta \\
\bar{A}_{2j}^{(p)} &= \frac{1}{\kappa_s} \int_0^{2\pi} \int_a^{r(\theta)} Z_p(\rho, \psi, t_c^{(p)})\ \bar{\varphi}_j^s\, r\, dr\, d\theta \\
\bar{B}_{1i}^{(p)} &= \frac{1}{\omega_i^c \kappa_c} \int_0^{2\pi} \int_a^{r(\theta)} \frac{\partial Z_p(\rho, \psi, t_c^{(p)})}{\partial t}\ \bar{\varphi}_i^c r\, dr\, d\theta \\
\bar{B}_{2j}^{(p)} &= \frac{1}{\omega_j^s \kappa_s} \int_0^{2\pi} \int_a^{r(\theta)} \frac{\partial Z_p(\rho, \psi, t_c^{(p)})}{\partial t}\ \bar{\varphi}_j^s r\, dr\, d\theta
\end{aligned}
$$

where κ_c and κ_s are presented in Eqs. (6.8) and (6.10) respectively.

A4. Compute the total membrane energy after constraint application $\bar{E}_c^{(p)}$ by using Eq. (6.49) and then compute the energy reduction by

$$E\% = \frac{E_O - \bar{E}_C^{(p)}}{E_O} \times 100 \tag{6.50}$$

A5. Let the constrained membrane vibrate freely (starting from $t = 0$) and let the constraint be removed after some arbitrary time $t = t_r^{(p)}$.

A6. Reset the time $t = 0$, and use the previous displacement and velocity of the constrained membrane $\bar{Z}_C(r, \theta, t_r^{(p)})$ as initial conditions to find the equation of motion after constraint removal $\bar{Z}_f^{(p+1)}(\rho, \psi, t)$, which is presented in Eq. (6.29). The procedure presented in Section 6.4.1 is used to calculate the modal coefficients, as follows

$$\begin{aligned}
C_{00}^{(p+1)} &= \frac{1}{2\pi \bigtriangleup_{00}} \int_0^{2\pi} \int_0^R \bar{Z}_C^{(p)}(r, \theta, t_r^{(p)})\, J_0(k_{00}\rho)\, \rho \, d\rho \, d\psi \\
C_{qi}^{(p+1)} &= \frac{1}{\pi \bigtriangleup_{qi}} \int_0^{2\pi} \int_0^R \bar{Z}_C^{(p)}(r, \theta, t_r^{(p)})\, J_q(k_{qi}\rho)\, \cos q\psi \;\rho \, d\rho \, d\psi \\
E_{qi}^{(p+1)} &= \frac{1}{\pi \bigtriangleup_{qi}} \int_0^{2\pi} \int_0^R \bar{Z}_C^{(p)}(r, \theta, t_r^{(p)})\, J_q(k_{qi}\rho)\, \sin q\psi \;\rho \, d\rho \, d\psi \\
D_{00}^{(p+1)} &= \frac{1}{2\pi\omega_{00} \bigtriangleup_{00}} \int_0^{2\pi} \int_0^R \frac{\partial \bar{Z}_C^{(p)}(r, \theta, t_r^{(p)})}{\partial t}\, J_0(k_{00}\rho)\, \rho \, d\rho \, d\psi \\
D_{qi}^{(p+1)} &= \frac{1}{\pi\omega_{qi} \bigtriangleup_{qi}} \int_0^{2\pi} \int_0^R \frac{\partial \bar{Z}_C^{(p)}(r, \theta, t_r^{(p)})}{\partial t}\, J_q(k_{qi}\rho)\, \cos q\psi \;\rho \, d\rho \, d\psi \\
F_{qi}^{(p+1)} &= \frac{1}{\pi\omega_{qi} \bigtriangleup_{qi}} \int_0^{2\pi} \int_0^R \frac{\partial \bar{Z}_C^{(p)}(r, \theta, t_r^{(p)})}{\partial t}\, J_q(k_{qi}\rho)\, \sin q\psi \;\rho \, d\rho \, d\psi
\end{aligned}$$

A7. Update the equation of the unconstrained membrane motion by setting $Z_P(\rho, \psi, t) = \bar{Z}_f^{(p+1)}(\rho, \psi, t)$ and increase the counter , where $p = p + 1$ and go to step 2.

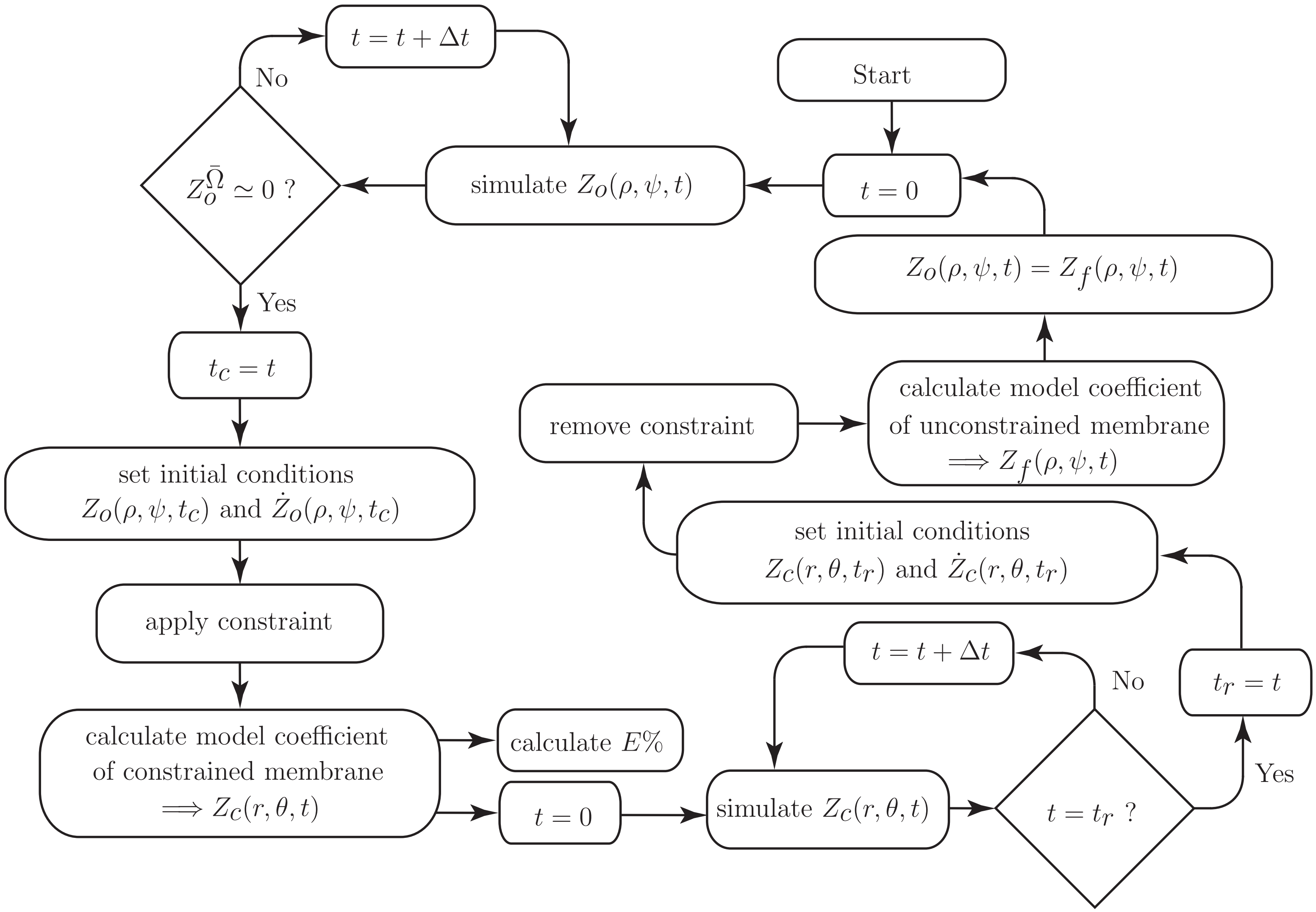

Figure 6.6: Flowchart for simple application and removal of constraint strategy

Note that simple constraint application and removal requires computing the eigenfrequencies and mode shapes for only one time and storing it and using it offline during sequential application and removal of constraint. A flowchart for the procedure described in this section is shown in Fig 6.6.

6.6.4 Radial Constraint Application

In this section we study effect of moving the constraint radially on the energy of the membrane. The constraint is first applied near the membrane, boundary at a distance d_1 from the center of the membrane and then moved towards the center of the membrane at a distance d_2, where $d_2 < d_1$ and so on till the constraint reaches a prescribed distance d_p such that $d_p < \cdots < d_2 < d_1$ as shown in Fig. 6.7 (b). Thereafter, the constraint is moved back to a distance d_{p-1} and then d_{p-2} and so on till the constraint comes back to its original location at a distance d_1. The sensing mechanism for this case is shown in Fig. 6.7, where the sensors record the displacement of the area $\bar{\Omega}$ which lies on the path of the constraint movement (on X-axis). The case of radial constraint motion is more complicated than the simple constraint application and removal case. The change of the constraint location implies computation of eigenfrequencies and mode shapes for each application distance d during the constraint movement. When the constrained is moved from its location at d_1 to its location at d_2, the coordinate system changes, see Fig. 6.8. As a result, computation of modal coefficients of the new location requires integration over the entire membrane area excluding both constraint areas $\bar{\Omega}_1$ and $\bar{\Omega}_2$. This is because $\bar{\Omega}_1$ represents an area of zero initial displacement and velocity for the new constraint location at d_2 and the upcoming motion is restricted to the area outside $\bar{\Omega}_2$.

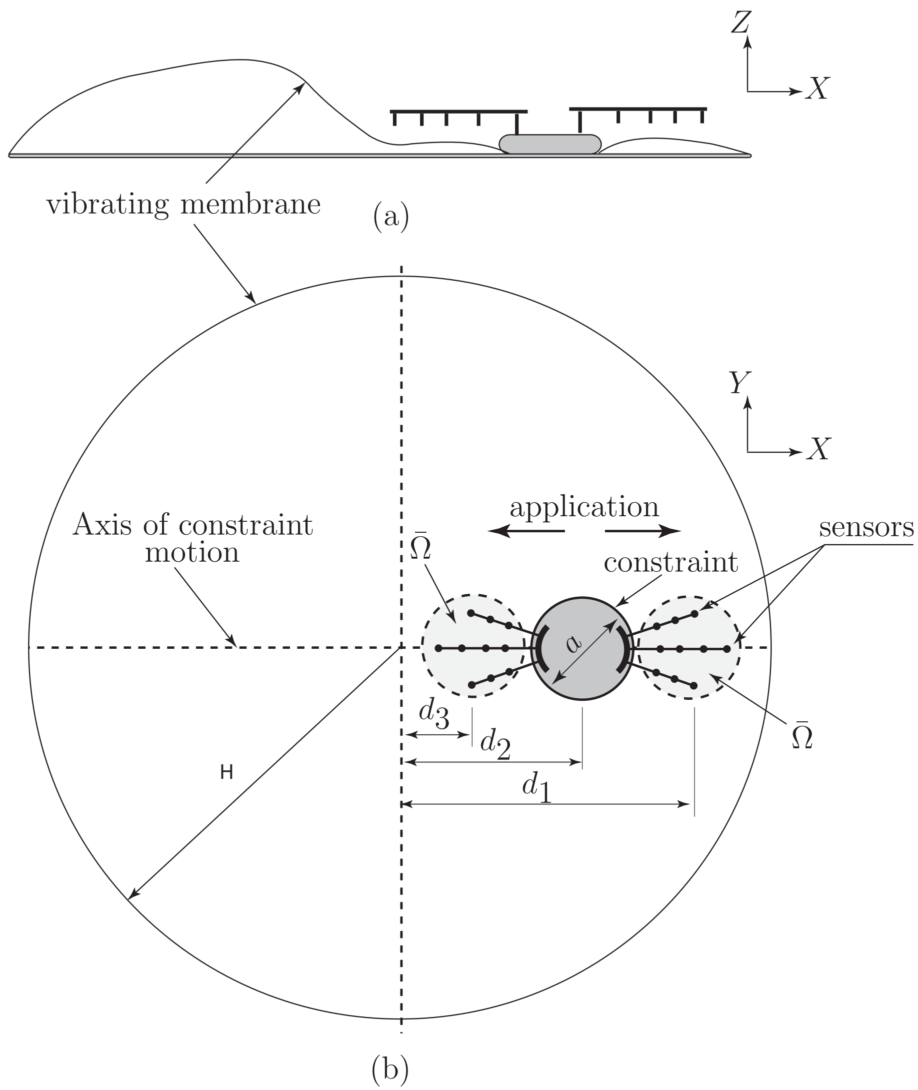

Figure 6.7: Sensing mechanism and path of constraint motion for radial constraint motion (a) side view. (b) top view.

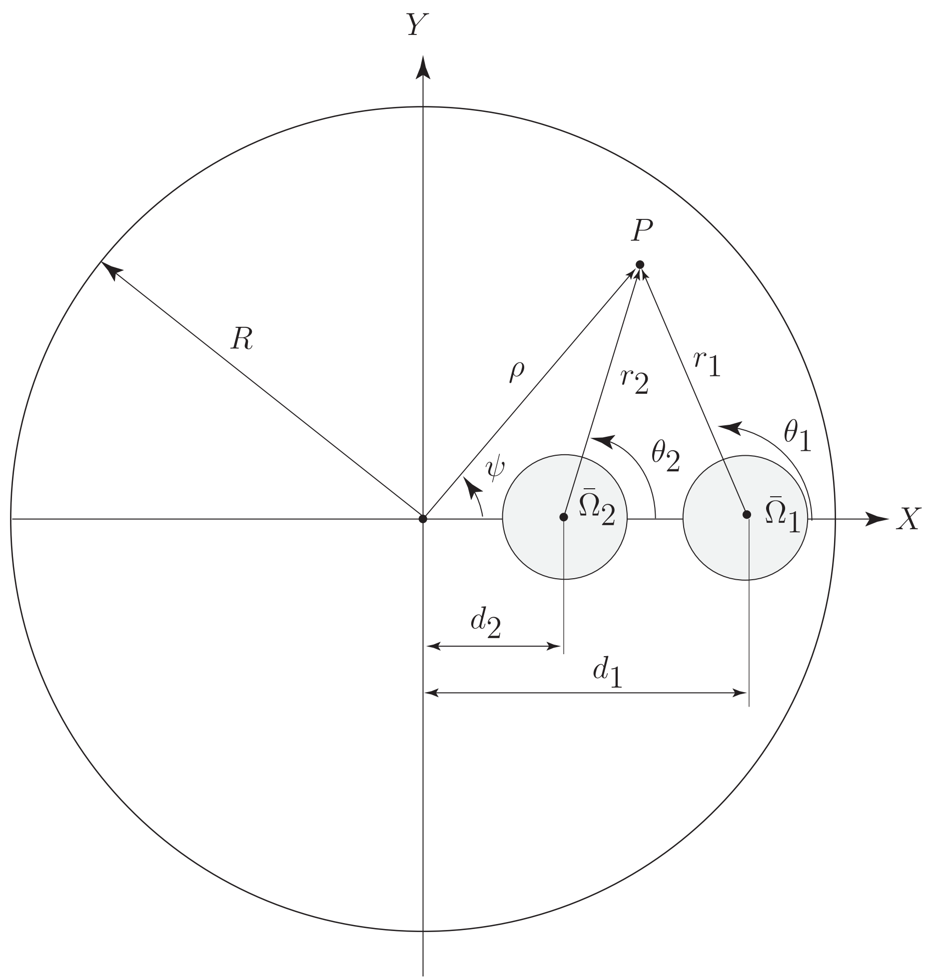

Figure 6.8: The coordinates of two different locations of a constraint moved from location at d_1 to location at d_2.

It is quite difficult to exclude both $\bar{\Omega}_1$ and $\bar{\Omega}_2$ mathematically, and therefore we use an alternative method by storing the initial conditions of the previous motion (d_1 location with r_1, θ_1 coordinates system) in the (ρ, ψ) coordinates system then transfer the initial conditions into new coordinates r_2, θ_2 which are associated with the new constraint location d_2. The procedure of the constraint movement can be summarized as follows:

A1. The membrane is initially vibrates freely and the equation of motion $Z_o(\rho, \psi, t)$ is presented in Eq. (6.44). The initial energy E_0 of the membrane is computed by using Eq. (6.16).

A2. When the displacement of sensed area $\bar{\Omega}_1$ is ≈ 0, then $t = t_c^{(1)}$ and the constraint is applied.

A3. Reset the time $t = 0$ and find the equation of the motion of the membrane after constraint application $\bar{Z}_c(r_1, \theta_1, t)$ which is presented in Eq. (6.46) with replacing (r, θ) by (r_1, θ_1). The procedure presented in Section 6.6.1 is used to obtain the model coefficients at constraint location d_1 as follows

$$\begin{aligned}
\bar{A}_{1i}^{(1)} &= \frac{1}{\kappa_c^{(1)}} \int_0^{2\pi} \int_a^{r(\theta_1)} Z_o(\rho, \psi, t_c^{(1)})\ (\bar{\varphi}_i^c)^{(1)}\, r_1\, dr_1\, d\theta_1 \\
\bar{A}_{2j}^{(1)} &= \frac{1}{\kappa_s^{(1)}} \int_0^{2\pi} \int_a^{r(\theta_1)} Z_o(\rho, \psi, t_c^{(1)})\ (\bar{\varphi}_j^s)^{(1)}\, r_1\, dr_1\, d\theta_1 \\
\bar{B}_{1i}^{(1)} &= \frac{1}{(\omega_i^c)^{(1)} \kappa_c^{(1)}} \int_0^{2\pi} \int_a^{r(\theta_1)} \frac{\partial Z_o(\rho, \psi, t_c^{(1)})}{\partial t}\ (\bar{\varphi}_i^c)^{(1)}\, r_1\, dr_1\, d\theta_1 \\
\bar{B}_{2j}^{(1)} &= \frac{1}{(\omega_j^s)^{(1)} \kappa_s^{(1)}} \int_0^{2\pi} \int_a^{r(\theta_1)} \frac{\partial Z_o(\rho, \psi, t_c^{(1)})}{\partial t}\ (\bar{\varphi}_j^s)^{(1)}\, r_1\, dr_1\, d\theta_1
\end{aligned}$$

Where the subscript (1) indicates that the calculations are associated with constraint location d_1. Set the counter $p = 1$.

A4. Compute the total membrane energy after constraint application $\bar{E}_c^{(p)}$ by using Eq. (6.49) and then compute the energy reduction by using Eq. (6.50).

A5. Let the constrained membrane vibrate freely and when the displacement of sensed area $\bar{\Omega}_{p+1}$ is ≈ 0, then $t = t_r^{(p)}$ and the constraint is removed. The initial conditions are stored in the (ρ, ψ) coordinates system by setting the time $t = 0$, and finding the equation of motion after constraint removal $\bar{Z}_f^{(p)}(\rho, \psi, t)$ which is presented in Eq. (6.29). By using similar procedure to that presented in Section 6.4.1, the modal coefficients of the unconstrained motion can be obtained as

$$
\begin{aligned}
C_{00}^{(p)} &= \frac{1}{2\pi \, \triangle_{00}} \int_0^{2\pi} \int_0^R \bar{Z}_c^{(p)}(r_p, \theta_p, t_r^{(p)}) \, J_0(k_{00}\rho) \, \rho \, d\rho \, d\psi \\
C_{qi}^{(p)} &= \frac{1}{\pi \, \triangle_{qi}} \int_0^{2\pi} \int_0^R \bar{Z}_c^{(p)}(r_p, \theta_p, t_r^{(p)}) \, J_q(k_{qi}\rho) \, \cos q\psi \;\, \rho \, d\rho \, d\psi \\
E_{qi}^{(p)} &= \frac{1}{\pi \, \triangle_{qi}} \int_0^{2\pi} \int_0^R \bar{Z}_c^{(p)}(r_p, \theta_p, t_r^{(p)}) \, J_q(k_{qi}\rho) \, \sin q\psi \;\, \rho \, d\rho \, d\psi \\
D_{00}^{(p)} &= \frac{1}{2\pi\omega_{00} \, \triangle_{00}} \int_0^{2\pi} \int_0^R \frac{\partial \bar{Z}_c^{(p)}(r_p, \theta_p, t_r^{(p)})}{\partial t} \, J_0(k_{00}\rho) \, \rho \, d\rho \, d\psi \\
D_{qi}^{(p)} &= \frac{1}{\pi\omega_{qi} \, \triangle_{qi}} \int_0^{2\pi} \int_0^R \frac{\partial \bar{Z}_c^{(p)}(r_p, \theta_p, t_r^{(p)})}{\partial t} \, J_q(k_{qi}\rho) \, \cos q\psi \;\, \rho \, d\rho \, d\psi \\
F_{qi}^{(p)} &= \frac{1}{\pi\omega_{qi} \, \triangle_{qi}} \int_0^{2\pi} \int_0^R \frac{\partial \bar{Z}_c^{(p)}(r_p, \theta_p, t_r^{(p)})}{\partial t} \, J_q(k_{qi}\rho) \, \sin q\psi \;\, \rho \, d\rho \, d\psi
\end{aligned}
$$

where $\triangle_{qi}$ is presented in Eq. (6.34).

A6. Transfer the initial conditions stored in (ρ, ψ) coordinates system (from step 5) to (r_{p+1}, θ_{p+1}) which represents the coordinates system of the new constraint location at d_{p+1}. Reset the time $t = 0$ and find the equation of the motion of the membrane after constraint application $\bar{Z}_C(r_{p+1}, \theta_{p+1}, t)$ which is presented in Eq. (6.46) with replacing (r, θ) by (r_{p+1}, θ_{p+1}). The procedure presented in Section 6.6.1 is used to obtain the model coefficients at constraint location d_{p+1}, except the initial conditions are considered at $t = 0$ instead of $t = t_C$ as follows

$$
\begin{aligned}
\bar{A}_{1i}^{(p+1)} &= \frac{1}{\kappa_C^{(p+1)}} \int_0^{2\pi} \int_a^{r(\theta_{p+1})} \bar{Z}_f^{(p)}(\rho, \psi, 0)\, (\bar{\varphi}_i^c)^{(p+1)}\, r_{p+1}\, dr_{p+1}\, d\theta_{p+1} \\
\bar{A}_{2j}^{(p+1)} &= \frac{1}{\kappa_S^{(p+1)}} \int_0^{2\pi} \int_a^{r(\theta_{p+1})} \bar{Z}_f^{(p)}(\rho, \psi, 0)\, (\bar{\varphi}_j^s)^{(p+1)}\, r_{p+1}\, dr_{p+1}\, d\theta_{p+1} \\
\bar{B}_{1i}^{(p+1)} &= \frac{1}{\Sigma_C} \int_0^{2\pi} \int_a^{r(\theta_{p+1})} \frac{\partial \bar{Z}_f^{(p)}(\rho, \psi, 0)}{\partial t}\, (\bar{\varphi}_i^c)^{(p+1)}\, r_{p+1}\, dr_{p+1}\, d\theta_{p+1} \\
\bar{B}_{2j}^{(p+1)} &= \frac{1}{\Sigma_S} \int_0^{2\pi} \int_a^{r(\theta_{p+1})} \frac{\partial \bar{Z}_f^{(p)}(\rho, \psi, 0)}{\partial t}\, (\bar{\varphi}_j^s)^{(p+1)}\, r_{p+1}\, dr_{p+1}\, d\theta_{p+1}
\end{aligned}
$$

Where $\Sigma_S = (\omega_j^s)^{(p+1)} \kappa_S^{(p+1)}$ and $\Sigma_C = (\omega_i^c)^{(p+1)} \kappa_C^{(p+1)}$. The subscript $(p+1)$ indicates the calculations of mode shapes and eigenfrequencies are performed when the constraint at d_{p+1}.

A7. Update last equation of the constrained membrane motion to be initial motion for the next constraint location by setting $\bar{Z}_C(r_p, \theta_p, t) = \bar{Z}_C(r_{p+1}, \theta_{p+1}, t)$ and define the new constraint location d_{p+2} and go to step 4. Note that for each constraint location, the integrations require the following relationship

$$
\rho = \sqrt{d_p^2 + r_p^2 + 2\, r_p^2\, d_p^2 \cos\theta_p}, \qquad \psi = \cos^{-1}\left(\frac{d_p + r_p\, \cos\theta_p}{\rho}\right)
$$

A flowchart for the procedure described in this section is shown in Fig. 6.9.

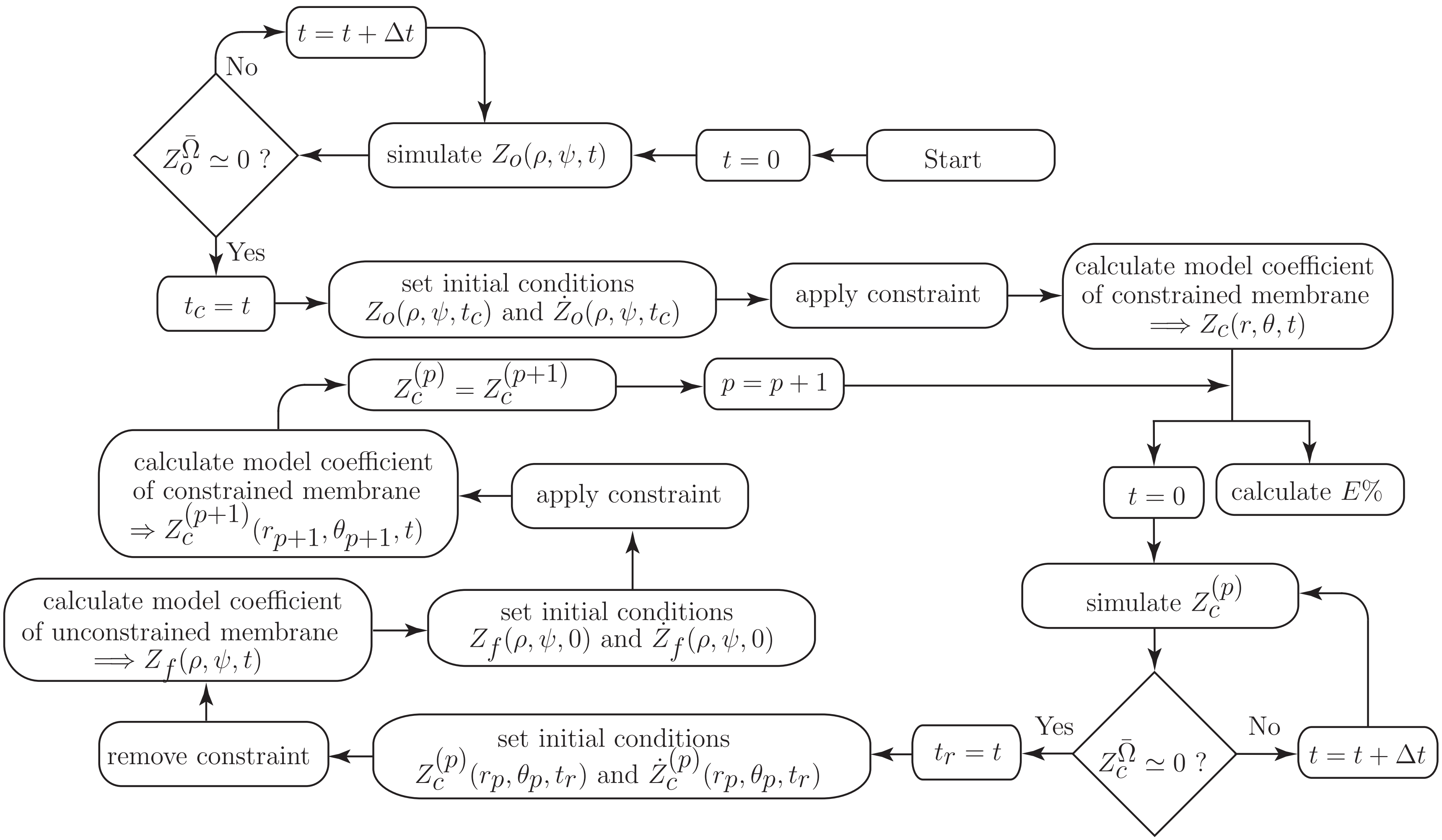

Figure 6.9: Flowchart for radial application of constraint strategy, for each p increment, new constraint location d_p is defined and the eigenfrequencies and mode shapes are calculates at this location

6.6.5 Circumferential Constraint Application

In this section we study vibration suppression in the membrane due to circumferential motion of the constraint. The constraint is first applied on the X-axis near the membrane boundary at a distance d from the center of the membrane and then the constraint is moved along a circular path around the membrane center at location of (d, ϕ_1) from the center of the membrane, where $\phi_1 > 0$. Thereafter, the constraint is moved further to new location on the circular path at (d, ϕ_2) such that $\phi_2 > \phi_1$ till the constraint reaches a prescribed location at (d, ϕ_p) such that $\phi_p > \cdots > \phi_2 > \phi_1$ as shown in Fig. 6.11. When the constraint location is at (d, ϕ_1), the eigenfrequencies and the mode shapes of symmetric and antisymmetric modes should be computed according to the inclined coordinates system (x_1, y_1) as shown Fig. 6.11.

Similar to the case of radial constraint motion, the case of circumferential constraint motion is more complicated than the simple constraint application and removal method. When the constraint is moved from location $(d, 0)$ to the new location (d, ϕ_1),the coordinate system changes as shown in Fig. 6.11. As a result and similar to radial constraint motion, computing of modal coefficients of the new location requires integration over the entire membrane area while excluding the two constraints areas $\bar{\Omega}_0$ and $\bar{\Omega}_1$. That is because $\bar{\Omega}_0$ represents an area of zero initial displacement and velocity for the new constraint location at (d, ϕ_1) and the upcoming motion is restricted to the area outside $\bar{\Omega}_1$. Similar to the radial motion case, we use an alternative method by storing the initial conditions of the previous motion ($d, 0$ location with r_0, θ_0 coordinates system) in the (ρ, ψ) coordinates system then transfer it to the new constraint location (d, ϕ_1 location with r_1, θ_1 coordinates system).

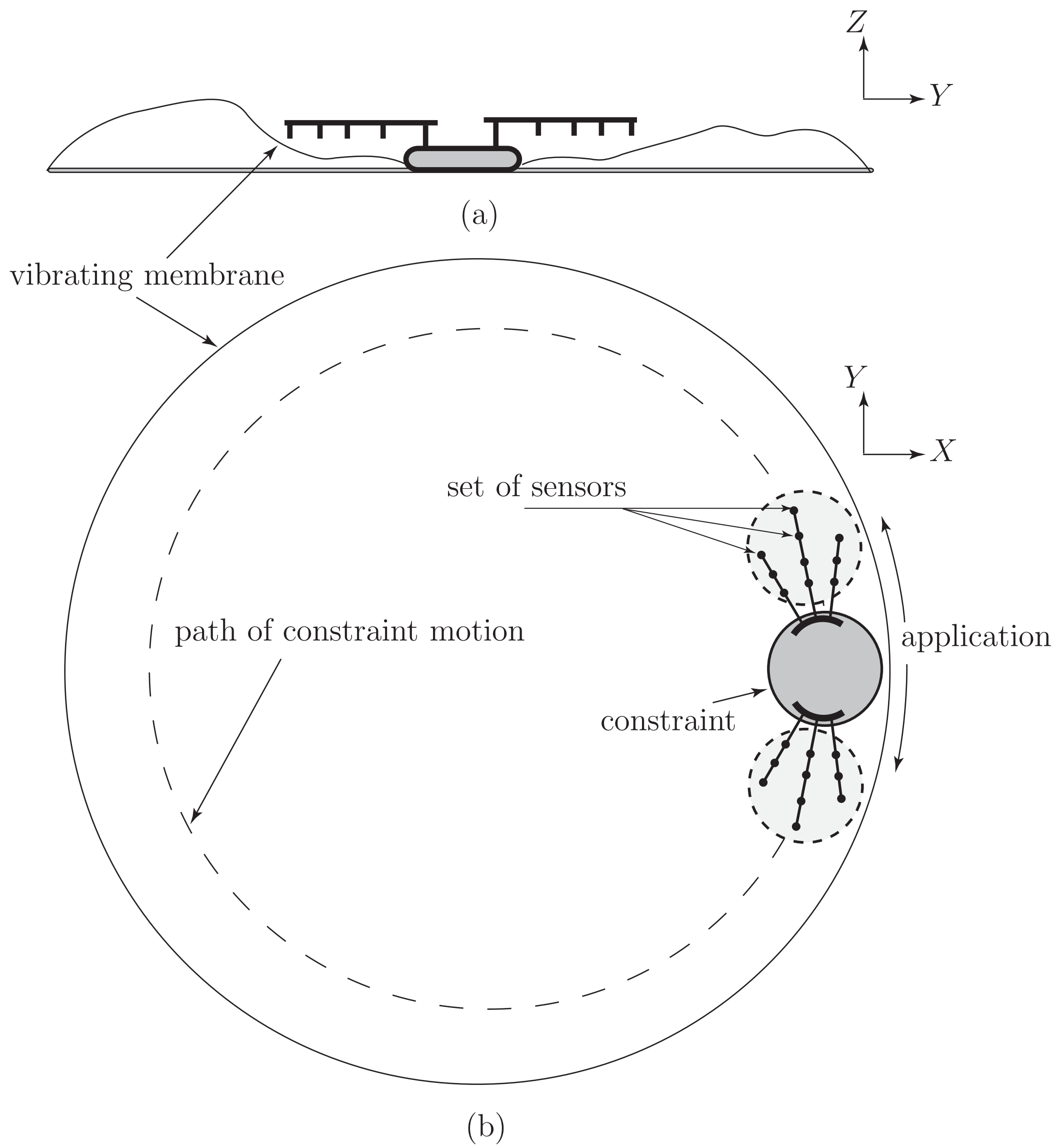

Figure 6.10: Sensing mechanism for circumferential constraint motion (a) back side view. (b) top view

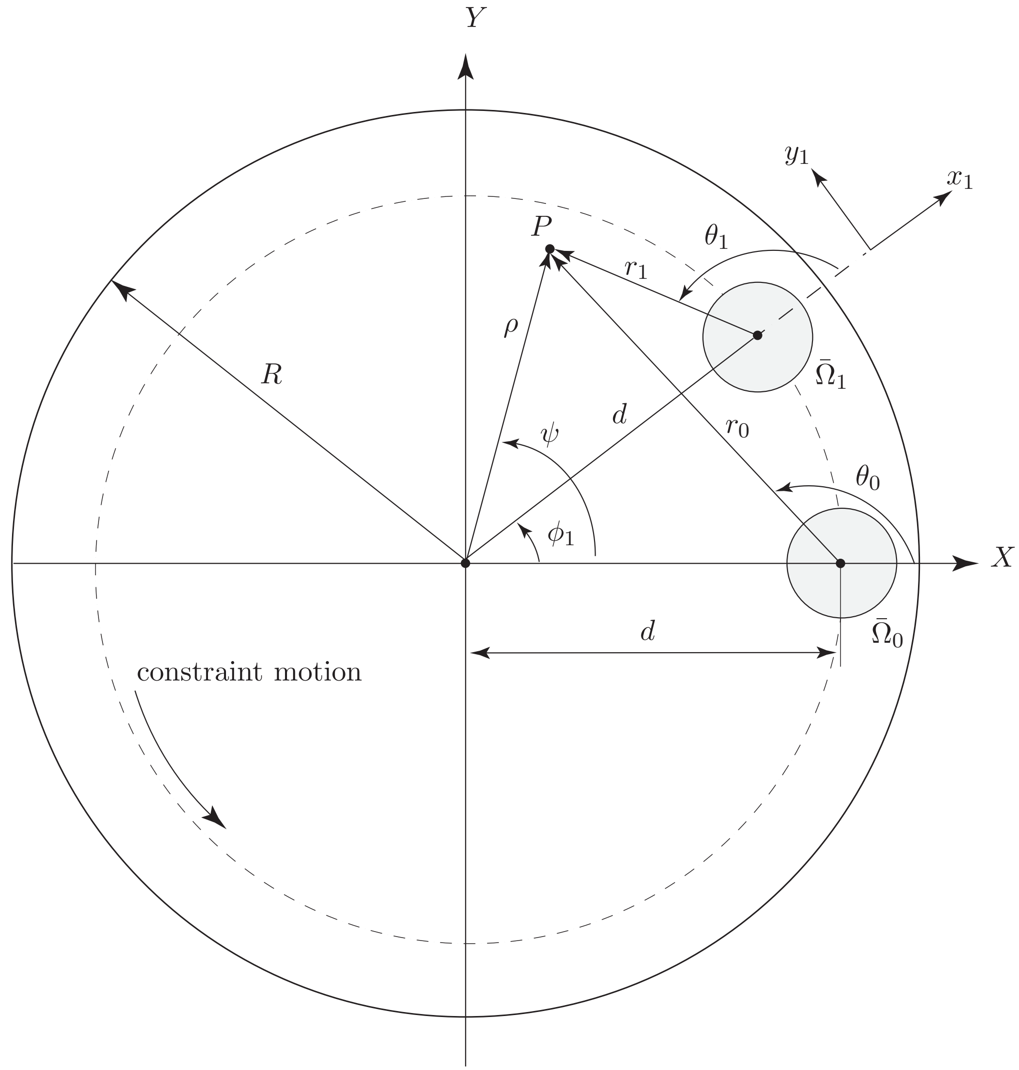

Figure 6.11: The coordinates systems of two different locations of a constraint moved in a circular path from location $(d, 0)$ to (d, ϕ_1)

The procedure of the constraint movement can be summarized as follows

A1. The membrane is initially vibrates freely and the equation of motion $Z_O(\rho, \psi, t)$ is presented in Eq. (6.44). The initial energy E_0 of the membrane is computed by using Eq. (6.16).

A2. When the displacement of sensed area $\bar{\Omega}_0$ is ≈ 0, then $t = t_c^{(0)}$ and the constraint is applied.

A3. Reset the time $t = 0$ and find the equation of the motion of the membrane after constraint application $\bar{Z}_C(r_0, \theta_0, t)$ which is presented in Eq. (6.46) with replacing (r, θ) by (r_0, θ_0). The procedure presented in Section 6.6.1 is used to obtain the model coefficients at constraint location (d, ϕ_0)=$(d, 0)$ as follows

$$\bar{A}_{1i}^{(0)} = \frac{1}{\kappa_c^{(0)}} \int_0^{2\pi} \int_a^{r(\theta_0)} Z_O(\rho, \psi, t_c^{(0)})\ (\bar{\varphi}_i^c)^{(0)}\, r_0\, dr_0\, d\theta_0$$

$$\bar{A}_{2j}^{(0)} = \frac{1}{\kappa_s^{(0)}} \int_0^{2\pi} \int_a^{r(\theta_0)} Z_O(\rho, \psi, t_c^{(0)})\ (\bar{\varphi}_j^s)^{(0)}\, r_0\, dr_0\, d\theta_0$$

$$\bar{B}_{1i}^{(0)} = \frac{1}{(\omega_i^c)^{(0)} \kappa_c^{(0)}} \int_0^{2\pi} \int_a^{r(\theta_0)} \frac{\partial Z_O(\rho, \psi, t_c^{(0)})}{\partial t}\ (\bar{\varphi}_i^c)^{(0)}\, r_0\, dr_0\, d\theta_0$$

$$\bar{B}_{2j}^{(0)} = \frac{1}{(\omega_j^s)^{(0)} \kappa_s^{(0)}} \int_0^{2\pi} \int_a^{r(\theta_0)} \frac{\partial Z_O(\rho, \psi, t_c^{(0)})}{\partial t}\ (\bar{\varphi}_j^s)^{(0)}\, r_0\, dr_0\, d\theta_0$$

Where the subscript (0) indicates that the calculations are performed at the location (d, ϕ_0) where $\phi_0 = 0$. Set the counter $p = 1$.

A4. Compute the total membrane energy after constraint application $\bar{E}_C^{(p)}$ by using Eq. (6.49) and then compute the energy reduction by using Eq. (6.50)

A5. When the displacement of sensed area $\bar{\Omega}_p$ is ≈ 0, the constraint is removed and $t = t_r^{(p)}$. and the initial conditions are stored in (ρ, ψ) coordinates system by setting the time $t = 0$, and finding the equation of motion after constraint removal $\bar{Z}_f^{(p)}(\rho, \psi, t)$ which is presented in Eq. (6.29). By using similar procedure to that presented in section 6.4.1, the modal coefficients of the unconstrained motion can be obtained as

A6. Transfer the initial conditions stored in (ρ, ψ) coordinates system (from step 5) to (r_{p+1}, θ_{p+1}) which represents the coordinates system of the new constraint location at (d, ϕ_{p+1}).

A7. Reset the time $t = 0$ and find the equation of the motion of the membrane after constraint application $\bar{Z}_C(r_{p+1}, \theta_{p+1}, t)$ which is presented in Eq. (6.46) with replacing (r, θ) by (r_{p+1}, θ_{p+1}). The procedure presented in Section 6.6.1 is used to obtain the model coefficients at constraint location d, ϕ_{p+1}, except the initial conditions are considered at $t = 0$ instead of $t = t_C$ as follows

$$
\begin{aligned}
\bar{A}_{1i}^{(p+1)} &= \frac{1}{\kappa_C^{(p+1)}} \int_0^{2\pi} \int_a^{r(\theta_{p+1})} \bar{Z}_f^{(p)}(\rho, \psi, 0)\, (\bar{\varphi}_i^c)^{(p+1)}\, r_{p+1}\, dr_{p+1}\, d\theta_{p+1} \\
\bar{A}_{2j}^{(p+1)} &= \frac{1}{\kappa_S^{(p+1)}} \int_0^{2\pi} \int_a^{r(\theta_{p+1})} \bar{Z}_f^{(p)}(\rho, \psi, 0)\, (\bar{\varphi}_j^s)^{(p+1)}\, r_{p+1}\, dr_{p+1}\, d\theta_{p+1} \\
\bar{B}_{1i}^{(p+1)} &= \frac{1}{\Sigma_C} \int_0^{2\pi} \int_a^{r(\theta_{p+1})} \frac{\partial \bar{Z}_f^{(p)}(\rho, \psi, 0)}{\partial t}\, (\bar{\varphi}_i^c)^{(p+1)}\, r_{p+1}\, dr_{p+1}\, d\theta_{p+1} \\
\bar{B}_{2j}^{(p+1)} &= \frac{1}{\Sigma_S} \int_0^{2\pi} \int_a^{r(\theta_{p+1})} \frac{\partial \bar{Z}_f^{(p)}(\rho, \psi, 0)}{\partial t}\, (\bar{\varphi}_j^s)^{(p+1)}\, r_{p+1}\, dr_{p+1}\, d\theta_{p+1}
\end{aligned}
$$

where $\Sigma_S = (\omega_j^s)^{(p+1)} \kappa_S^{(p+1)}$ and $\Sigma_C = (\omega_i^c)^{(p+1)} \kappa_C^{(p+1)}$.

A8. Update last equation of the constrained membrane motion to be initial motion for the next constraint location by setting $\bar{Z}_C(r_p, \theta_p, t) = \bar{Z}_C(r_{p+1}, \theta_{p+1}, t)$ and define the new constraint location (d, ϕ_{p+1}) and go to step 4. A flowchart for the procedure described in this section is shown in Fig 6.12. Note that for each constraint location, the integrations require the following relationship

$$\rho = \sqrt{d^2 + r_p^2 + 2\, r_p^2\, d^2 \cos\theta_p}, \qquad \psi = \cos^{-1}\left(\frac{d + r_p\, \cos\theta_p}{\rho}\right) + \phi_p$$

6.6.6 Numerical simulations

In this section we present numerical simulations for the three control strategies presented in Sections (6.6.3), (6.6.4) and (6.6.5). For all of the three control strategies we assume that the membrane is initially vibrating in its fundamental mode and the equation of motion is $Z_0(\rho, \psi, t) = A_0 J_0(k_{00}\, \rho) \cos(\omega_{00})t$, where, $k_{00} = 2.4048$ m $^{-1}$, $A_0 = 0.1$ m and $\omega_{00} =$ 4.8096 rad/sec and the specifications of the membrane and constraint are :

$$\frac{a}{R} = 0.12, \qquad R = 1 \text{ m}, \qquad \mu = 0.25 \text{ kg/m}^2, \qquad \mathrm{T} = 1 \text{ N/m}$$

We simulate 10 cycles of constraint application and removal for all of the three control strategies with 16 symmetric and 16 antisymmetric modes. First, we simulate one cycle of constraint application and removal for the simple application and removal of the constraint strategy presented in Section 6.6.3 with $d/R = 0.88$, i.e the constraint is adjacent to the boundary. The constraint is applied when the sensed area $\bar{\Omega}_p$ passes through the mean position and removed when $\bar{\Omega}_p$ at its maximum amplitude.

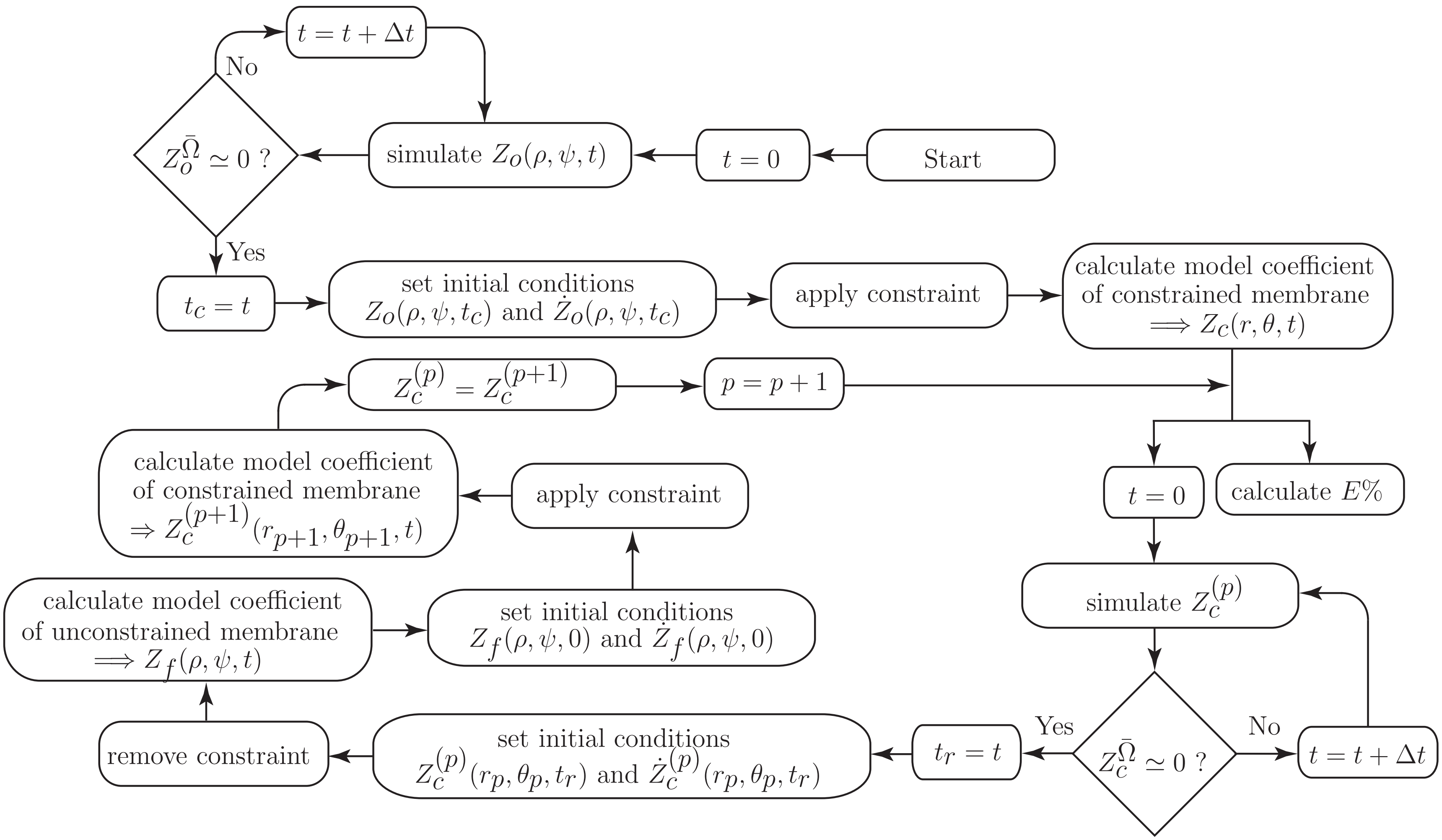

Figure 6.12: Flowchart for circumferential application of constraint strategy, for each p increment, new constraint location (angle ϕ_p) is defined and the eigenfrequencies and mode shapes are calculates at this location

In the redial constraint application strategy discussed in Section 6.6.4, the constraint is moved radially forward (toward the membrane center) and backward (toward the outer boundary). At the beginning, the constraint is applied at the earliest instant of time adjacent to the outer membrane boundary i.e. at a distance $d/R = 0.88$ when the forward sensors record approximately zero displacements and the constrained membrane continues vibrating freely. Next earliest instant of time when the forward sensors record zero displacements, the constraint is moved forward to a distance $d/R = 0.66$ (the previous location is adjacent to the next location) and process is repeated till the constraint reaches a distance $d/R = 0.44$ and then the constraint is moved backward gradually till it reaches the outer boundary at a distance $d/R = 0.88$ in similar way by using the records of backward sensors. The circumferential constraint application strategy discussed in Section 6.6.5 is simulated with an angular increments of $\phi = 2\tan^{-1}(a/d)$ with $d/R = 0.88$ and $a/R = 0.12$, where the constraint moves circumferentially adjacent to the outer boundary of the membrane. At the beginning, the constraint is applied at the earliest instant of time adjacent to the outer membrane boundary i.e. at a distance $d/R = 0.88$ then the constraint is moved counter-clockwise incrementally, that is the next constraint location is adjacent to the previous constraint location where$\phi = 15.53^{\circ}$.

Figure 6.14 shows displacement and percentage energy loss $E\%$ of the membrane at the end of the first cycle, 6 cycles and after completion of 10 cycles of constraint application and removal for the three control strategies. Table 6.2 shows comparison between the three constraint application strategies. It is clear form the data that the simple constraint application and removal strategy results in significantly higher reduction in energy in comparison to radial and circumferential constraint application. Although constraint removal does not change the overall energy of the membrane, the configuration of the membrane at the time of constraint removal determines how energy of the constrained membrane is redistributed over the entire membrane area; and this has a significant effect on the rate of energy reduction in subsequent cycles of constraint application. Figure 6.13 shows the snapshots of the first cycle of constraint application and removal. It can be seen clearly that the removal of constraint as the the membrane in its maximum displacement, generates a bump that implies excitation of higher modes similar to our observation in the case of string vibration presented in Chapter 3. Exciting higher modes implies increasing of the velocities distribution over some small areas that is implicitly included on the area of the membrane. The energy lost is proportional to the kinetic energy of constrained area Ω, and the kinetic energy is proportional to the velocity of Ω, therefore, exciting higher modes increases the velocity over the area Ω which implies increasing in the kinetic energy and, hence, the energy lost is higher.

Table 6.2: Comparison of percentage energy loss of the membrane for the three different constraint applications strategies (A) simple (B) radial (C) circumferential, over 10 constraint applications

No.	1	2	3	4	5	6	7	8	9	10
(A)	0.305	2.247	4.425	6.000	8.110	10.278	12.102	14.035	16.834	17.180
(B)	0.305	1.203	2.236	2.945	3.289	5.479	6.692	7.182	9.292	11.548
(C)	0.305	0.498	0.606	0.844	0.867	1.251	1.158	1.295	1.3635	1.483

The energy reduction in radial constraint application is less than the simple application strategy but higher than the circumferential motion strategy. This can be explained as follows; in the radial and circumferential motion, the removal time t_r can not be chosen arbitrary like the simple application and removal case. Rather, in radial and circumferential constraint motion the constraint is moved when the sensor record zero displacement on the adjacent area, in fact each constraint motion step in these two cases represents application to the new constraint location and removal for the previous constraint location simultaneously. Hence, exciting higher modes is not guaranteed in these two cases, as a result the total energy reduction will depend on the kinetic energy stored in constrained part. Furthermore, the velocity over the area Ω increases inherently when the constraint approaches toward the center of the membrane. Hence, in the radial constraint application case the energy is reduced due to velocity increasing over the constrained area. In the circumferential motion case the amount of kinetic energy removed by the constraint applications is small for two reasons. First, the velocity over the area to be constrained Ω near the boundary is inherently low, as a result, the amount of the kinetic energy of Ω is small. Second, the choosing of the constraint removal time t_r is not arbitrary like the simple case, i.e the constraint is moved when the membrane is at the minimum deformation and therefore higher modes are not excited.

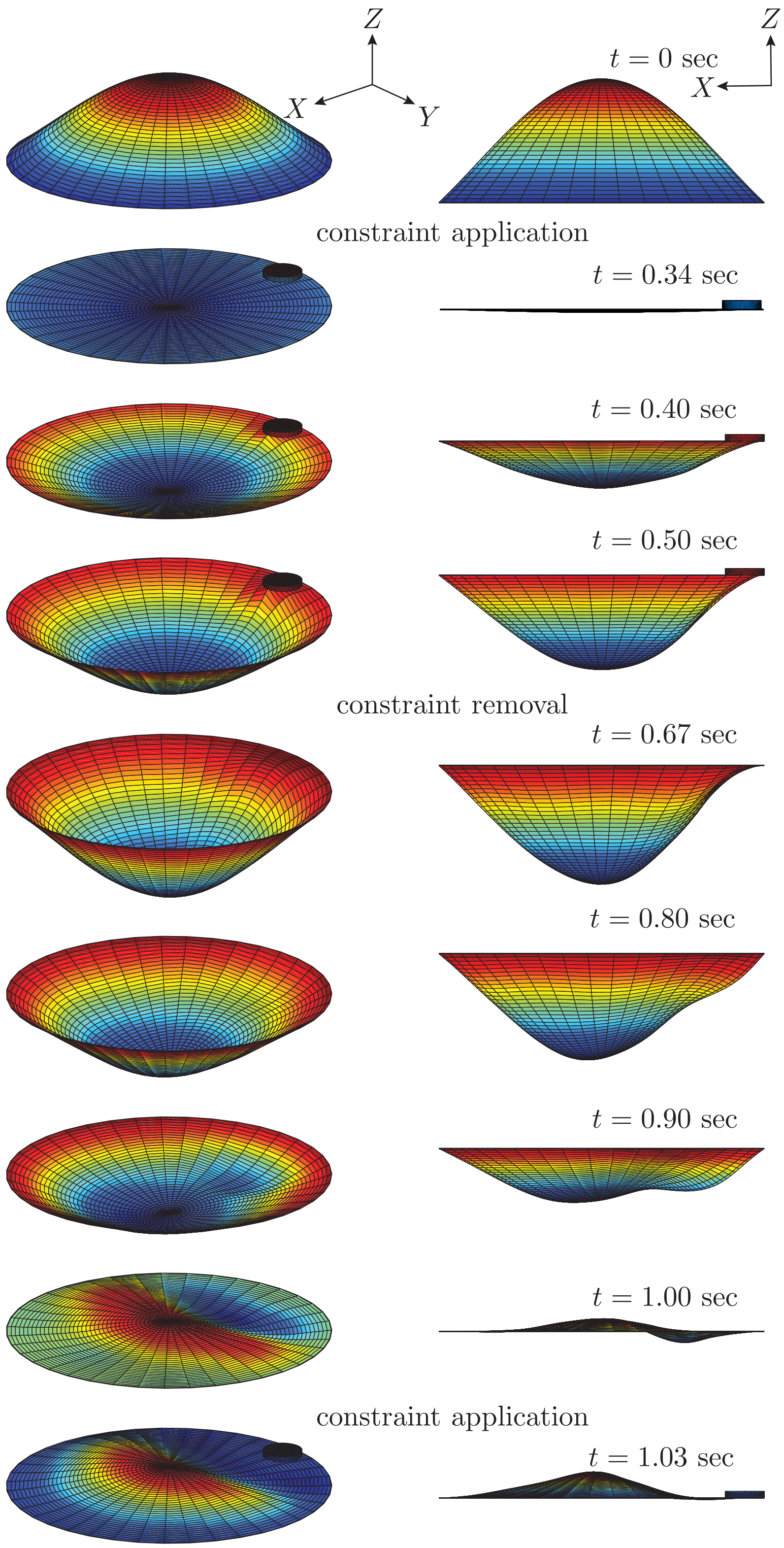

Figure 6.13: Snapshots of one cycle for simple constraint application and removal strategy

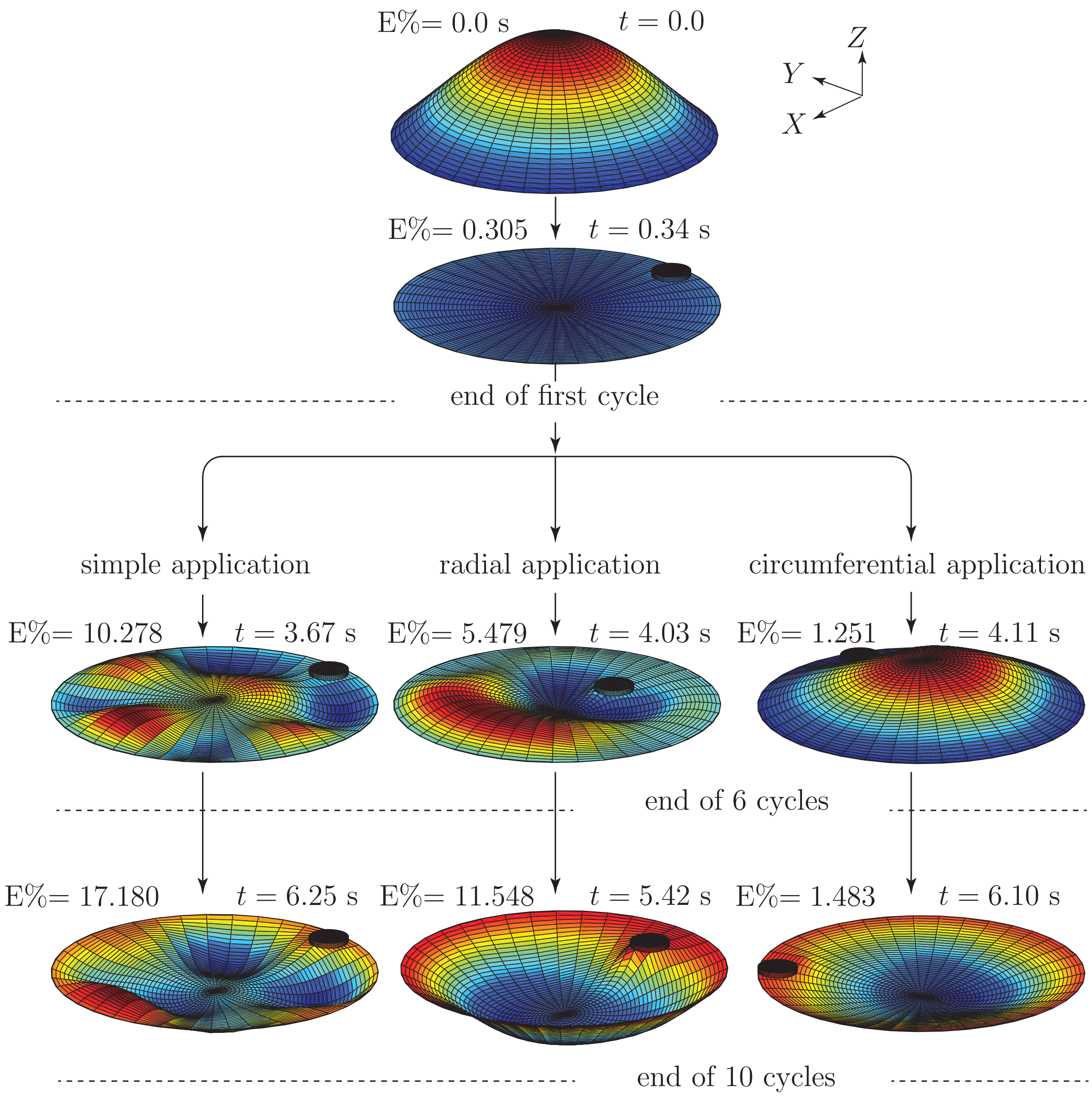

Figure 6.14: Displacement and percentage energy loss $E\%$ of the membrane at the end of the first cycle, 6 cycles and after completion of 10 cycles of constraint application and removal for cases; simple, radial and circumferential applications of constraint

Chapter 7

Conclusion Remarks and Future Work

In this dissertation, we investigated the vibration control of continuous systems, namely string and circular membrane, using boundary constraint. The problem of vibrating string subjected to fixed constraint represented by a rigid obstacle located at one boundary is investigated first. The energy dissipation in the string due to wrapping around the obstacle is investigated and it is shown that the energy dissipation can be increased by changing the orientation of the obstacle, where the obstacle is considered as passive mechanism. Second, the problem of vibrating string subjected to moving constraint is investigated. The constraint is represented by a scabbard that is applied and removed at one of the string boundaries. The effect of application and removal of the constraint on the total energy of the string is investigated. The results show that the total energy can be reduced based on the time of constraint application. Based on energy reduction condition, a semi-active control strategy is presented to suppress the string vibration by applying and removing the constraint sequentially. The semi-active control strategy is verified experimentally and the results from experiment and simulation matched well.

The vibration control of circular membrane using areal constraint is investigated third in two parts. The first part includes investigating the accuracy of the dynamics of circular membrane with the presence of eccentric areal constraint for arbitrary initial conditions. The second part includes investigation of the effect of application and removal of the areal constraint on the energy of the membrane. The results show that the total energy can be reduced by applying the constraint as the membrane passes through the mean position. Based on energy reduction condition, three different semi-active control strategies are presented and efficacy of each strategy is investigated. In the next sections we discuss the entire work with details.

7.1 Vibration of a String Wrapping and Unwrapping Around an Obstacle

In Chapter 2 we investigated the problem of a string vibrating against a smooth obstacle. The obstacle is located at one of the boundaries and the string is assumed to wrap and unwrap around the obstacle during vibration. Assuming linear behavior of the string, an analytical model was developed for computing its geometry at each time step by bookkeeping the energy. The wrapping of the obstacle is modeled by a series of perfectly inelastic collisions between the obstacle and adjacent segments of the string and unwrapping is assumed to be energy conserving. The geometry of the string is determined iteratively starting from an initial configuration where the string is vibrating in a single mode and is not in contact with the obstacle. The obstacle can be regarded as a passive mechanism for vibration suppression in which the energy lost during each cycle of oscillation depends on the energy content of the string at the beginning of the cycle. Numerical simulation results are provided for the string vibrating in different modes for circular- and elliptic-shaped obstacles. The loss of energy is found to be greater for higher modes of oscillation and for obstacles that induce greater length of wrapping.

Since the energy dissipation is proportional to the length of string wrapping around the obstacle, the energy dissipation can be increased by adding another obstacle at the boundary of the string. Also, the obstacle geometry can have potential non-linear effect on the vibration of the string. Another non-linearity effect can be presented due to the large amplitude of the string vibration or due to inhomogeneity of the mass distribution along the string. Further investigation on the non-linearity effect lies in the scope of our future work.

7.2 Semi-Active Control for String Vibration

The dynamics of a vibrating string subjected to a constraint at one boundary is investigated in Chapter 3. The constraint is applied by a scabbard that moves a small distance along the mean position of the string. The scabbard is moved instantaneously such that the position and velocity of the string outside the scabbard is unaffected immediately after application of the constraint, whereas the length of the string covered by the scabbard is brought to rest. The constraint is removed by moving the scabbard back to its original position and the change in energy of the string is investigated for different values of scabbard travel distance and time of application of the constraint. Analytical and numerical simulation results are first provided for the string vibrating in the first mode, and then for a more general case where the string has arbitrary initial conditions. The results show that the energy of the string can increase or decrease depending on the time of application of the constraint for a given distance of travel of the scabbard. This provides the opportunity for semi-active control of vibration of the string through direct physical interaction, using the scabbard as an actuator. A simple feedback control strategy is proposed and numerical simulation results are presented. These results indicate that although removal of the constraint does not change the energy of the string, the effectiveness of the control strategy depends on the time of removal of the constraint.

In Chapter 4 we presented an experimental verification to the idea of the scabbard-like actuator method. The control strategy relies on sequential application and removal of a zero displacement constraint at one point on the string near its boundary. Application of the constraint results in rapid dissipation of vibration energy of the string segment that lies between the point of application of the constraint and the proximal boundary. Removal of the constraint redistributes the energy of the string over its entire length and allows the cycle of constraint application and removal to be repeated for suppression of vibration. A linear model of the string with damping was used to simulate the effect of constraint application and removal; the damping in the model was based on experimentally-determined values. Simulation results showed that a few cycles of constraint application and removal can suppress the vibration of the string rapidly. This result was corroborated by experiments using an extension coil spring which behaves like a lightly damped string. The displacement of the string was sensed using an optical sensor and the constraint was applied by a pair of solenoids. Both simulation and experimental results establish the efficacy of our simple control strategy. This simple semi-active control strategies can be used for vibration suppression of strings and tendons used in space applications such as tensegrity structures where rigid pre-compressed members (usually bars) are connected by pre-tensioned cables or strings or tendons [81].

7.3 Dynamics and Vibration Control of Membrane

Chapter 5 presented investigation on the dynamics of a circular membrane with an internal eccentric circular areal constraint. The membrane is assumed to be fixed at its outer boundary and the areal constraint is assumed to impose zero displacement over the entire internal circular area. This problem has been investigated by several researchers but prior efforts have been limited to solving for the first few eigenfrequencies; the orthogonality property of the modes have not been established and the procedure for computing the mode shapes or simulating the dynamics has not been presented. In this chapter we establish the orthogonality property of the symmetric and antisymmetric modes of the constrained membrane and provide a systematic method for computing the eigenfrequencies and mode shapes accurately. It is shown that the number of terms in the series expansion plays a critical role in accurate computation of the mode shapes. While fewer terms result in truncation errors, too many terms lead to numerical errors due to high sensitivity of the Bessel functions. An algorithm is presented to choose the appropriate number of terms and the importance of the algorithm is demonstrated through examples where fewer or more terms result in accurate eigenfrequencies but inaccurate mode shapes. The orthogonality conditions established in this chapter are used to determine modal coefficients for dynamics simulations. This however requires proper choice of the number of numerical integration points. An algorithm is presented to determine the appropriate number of numerical integration points which is shown to depend on the size and location of the areal constraint. Using the two algorithms for determination of the mode shapes and computation of the modal coefficients, the dynamics of a constrained membrane is accurately simulated; the accuracy of the simulations can be verified from the boundary conditions. The tools developed for simulation of constrained membrane dynamics, presented in this chapter, can be used to study the vibration of membrane structures and the efficacy of control methodologies for vibration mitigation.

The energetics of circular membrane subjected to eccentric areal constraint is investigated in Chapter 6 . The constraint of radius a is assumed to be applied at a distance d form the center of the membrane arbitrary time t_O during the membrane motion. Under the assumptions of small displacements and linearity, it was shown that application of the constraint can increase or decrease the total energy of the membrane depending on the time of application of the constraint. It was shown that the maximum energy reduction occurs when the constraint is applied as the membrane passes through the mean position. Furthermore, larger constraint size causes higher increasing/decreasing in total energy, and higher value of eccentricity d leads to less energy reduction and vice versa. Cyclic application and removal of constraint will result in vibration suppression when the constraint is always applied at times when it removes energy from the membrane.

Since the problem of vibrating membrane is two dimensional problem, the constraint can be moved in many different directions. Three different constraint movement directions are investigated for the optimal vibration suppression for the membrane. The three directions of constraint movement are ; (1) simple application and removal of constraint (2) radial constraint motion (3) circumferential constraint motion. Among the three constraint motion strategies, the simple application and removal of constraint is the best strategy where the energy is reduced significantly with comparison to radial and circumferential constraint motion. Radial constraint motion reduces energy more than the circumferential constraint motion. The methodology can be used for vibration control of membranes and other continuous structures through physical interaction with a relatively small section of the structure near the boundary. The control mechanisms of our control strategies for the vibrating strings and membranes are simple and do not require complicated feedback control design, thus, our semi-active control strategies can be used in many different applications such as large membrane mirror and antennas used in space application. The semi-active control strategies presented in this work can be modified to be used in some non-linear problems in vibration of continuous systems and such studies are in the scope of out future work.

APPENDICES

Appendix A

Vibration of Circular Membrane: Preliminary

A.1 Bessel Functions

One of the varieties of special functions which are encountered in the solution of physical problems is the class of functions called Bessel functions. They are solutions to a very important differential equation, the Bessel equation [80] :

$$x^2 \frac{d^2 y}{dx^2} + x \frac{dy}{dx} + (x^2 - n^2) = 0 \tag{A.1}$$

Where n could be any integer (the order of the Bessel function). The Bessel function could have the following forms:

Bessel functions of the first kind $J_n(x)$

$$J_n(x) = \sum_{m=0}^{\infty} \frac{(-1)^m}{m!\Gamma[m+n+1]} (\frac{1}{2}x)^{2m+n} \tag{A.2}$$

$$J_n(x) = \frac{1}{\pi} \int_0^{\pi} \cos(n\tau - x\sin(\tau))d\tau. \tag{A.3}$$

Bessel functions of the second kind $Y_n(x)$

$$Y_v(x) = \frac{J_v(x)\cos(v\pi) - J_{-v}(x)}{\sin(v\pi)} \tag{A.4}$$

Where v is not an integer, and for v is an integer n we have

$$\begin{aligned} Y_n(x) = &-\frac{(\frac{1}{2}x)^{-n}}{\pi} \sum_{k=0}^{n-1} \frac{(n-k-1)!}{k!} (\frac{1}{4}x^2)^k + \frac{2}{\pi} ln(\frac{1}{2}x) J_n(x) \\ &-\frac{(\frac{1}{2}x)^{n}}{\pi} \sum_{k=0}^{n-1} [\varphi_o(k+1) + \varphi_o(n+k+1)] \frac{(-\frac{1}{4}x^2)^k}{k!(n+k)!} \end{aligned} \tag{A.5}$$

Where φ_o is the digamma function.

The first and second kind Bessel function have the following properties

$$J_{-n}(x) = (-1)^n J_n(x) \tag{A.6}$$

$$Y_{-n}(x) = (-1)^n Y_n(x) \tag{A.7}$$

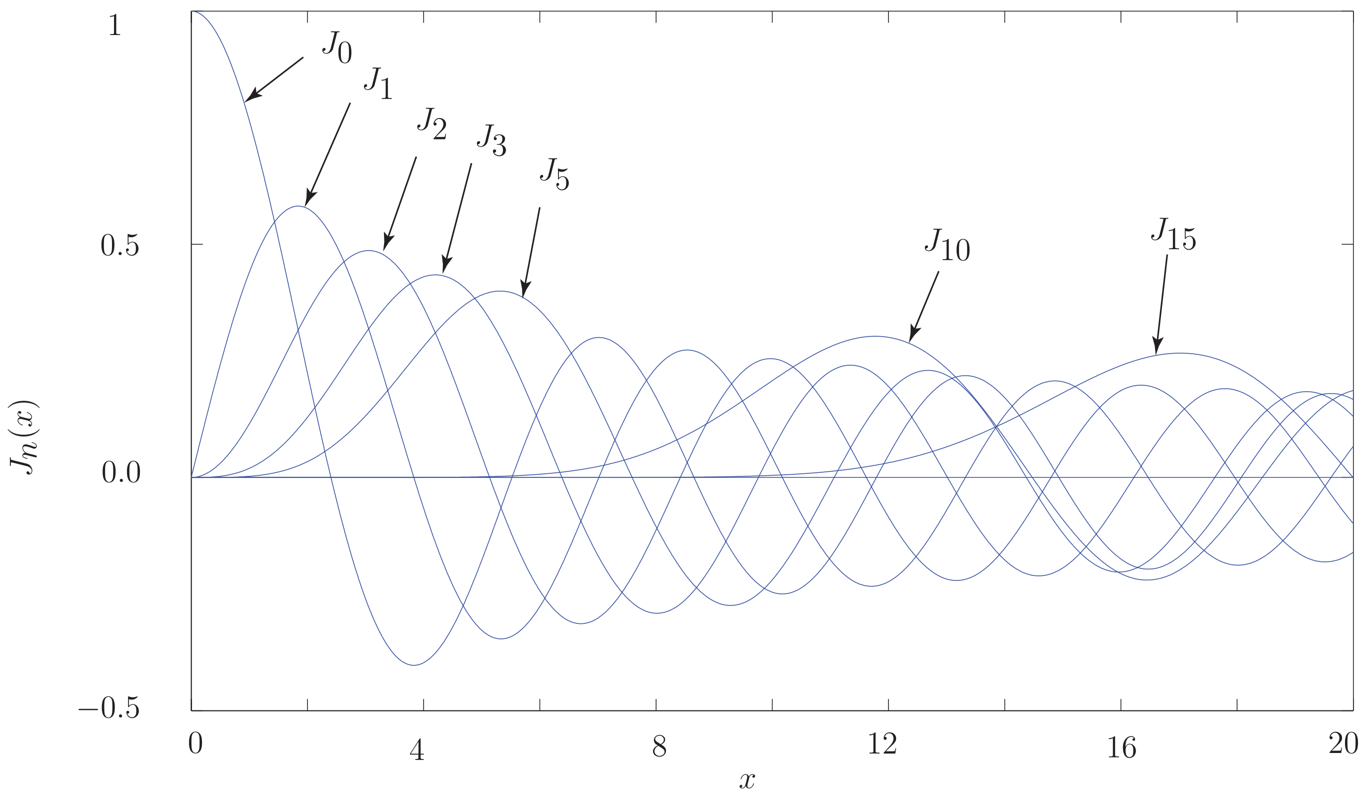

Figure A.1: Bessel functions of the first kind $J_n(x)$

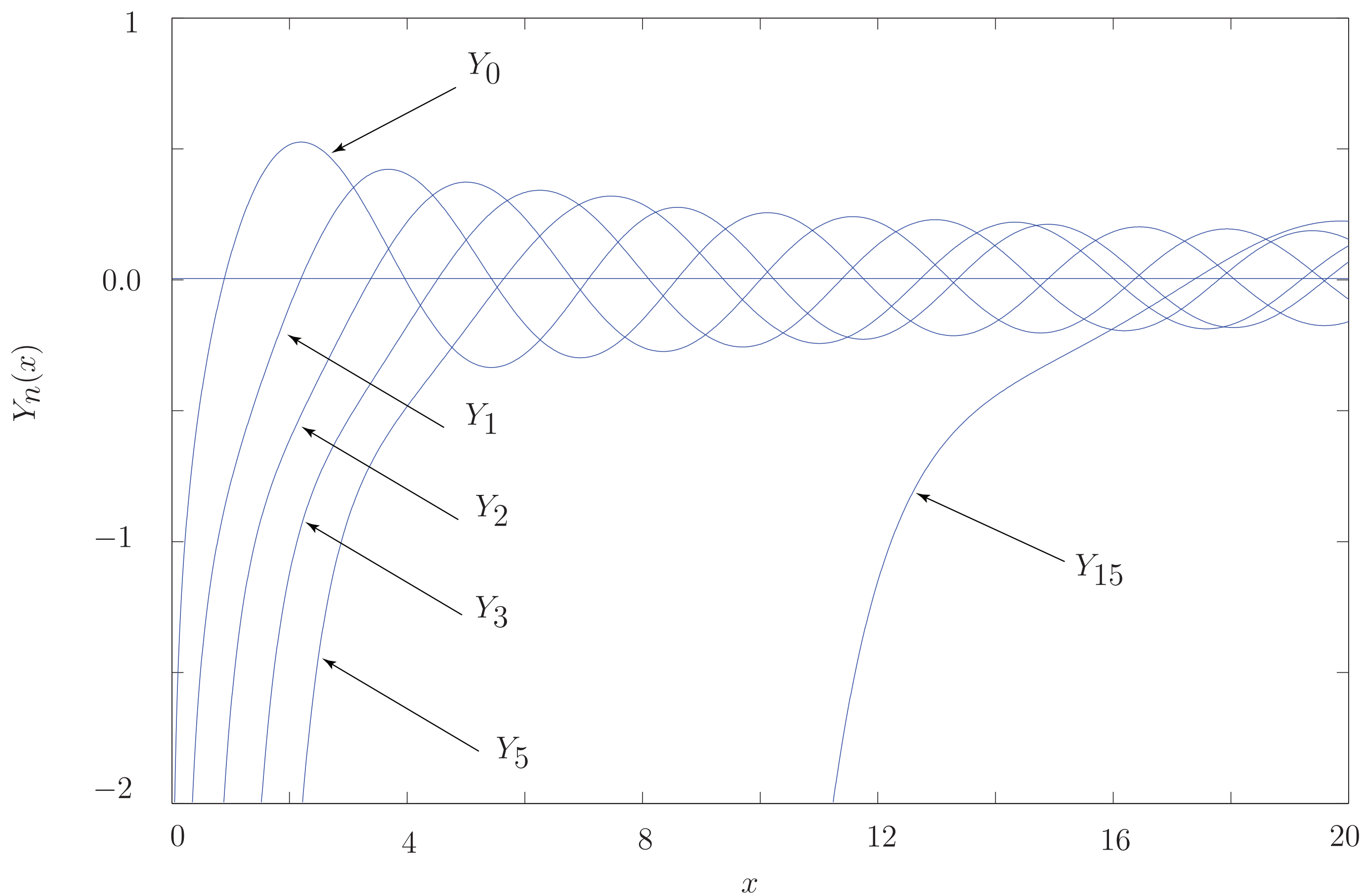

Figure A.2: Bessel functions of the second kind $Y_n(x)$

A.2 Vibration of Circular Membranes

Consider a circular membrane of the radius R as shown in Fig. A.3

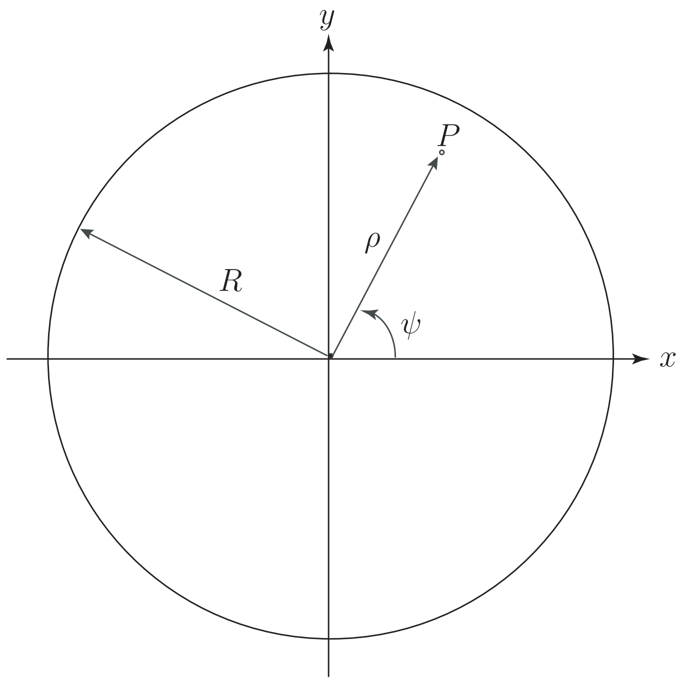

Figure A.3: Circular membrane with radius R .

The governing differential equation for the vibrating membrane is given as [75]

$$\frac{\partial^2 Z}{\partial \rho^2} + \frac{1}{\rho}\frac{\partial Z}{\partial \rho} + \frac{1}{\rho^2}\frac{\partial^2 Z}{\partial \psi^2} = \frac{1}{c^2}\frac{\partial^2 Z}{\partial t^2} \tag{A.8}$$

Where $Z = Z(\rho, \psi, t)$ is the transversal displacement (perpendicular to the page in Fig. A.3, and $c^2 = T/\mu$. Where T is the tension in the membrane and μ is the mass density per unit area.

General Solution

The solution for Eq. (A.8) can be obtained by applying separation of the variables.

$$Z(\rho, \psi, t) = \sum_{m=0}^{\infty} \{\beta_m J_m(k\rho) + \gamma_m Y_m(k\rho)\} \{C_m \cos m\psi + D_m \sin m\psi\} \{A \cos \omega t + B \sin \omega t\} \tag{A.9}$$

Boundary conditions

The boundary conditions are associated with the spatial variables r and ψ, therefore, we apply the boundary conditions to $V(\rho, \psi)$ only.

A1. At $r = 0$, $V(0, \psi) = \{\beta J_m(0) + \gamma Y_m(0)\}\{C_m \cos m\psi + D_m \sin m\psi\}$, but $Y_m(0) = \infty$ and it is not suitable because there is finite value for $V(0, \psi)$, which requires that $\gamma = 0$.

A2. The membrane is fixed at $r = R$ or $V(R, \psi) = \{\beta J_m(kR)\}\{C_m \cos m\psi + D_m \sin m\psi\} = 0$

Now, the only term left to satisfy $V(R, \psi) = 0$ is the zeros of the Bessel function $J_m(kR)$. There will be many zeros (intersections with x-axis), let the value of the first intersection of the $J_m(\gamma)$ occurs at γ_{m1} and the second intersection at γ_{m2} and so on. Then $k_{nm}R = \gamma_{nm} \Longrightarrow k_{nm} = \frac{\gamma_{nm}}{R}$.

Then

$$V(\rho, \psi) = \sum_{m=0}^{\infty} \sum_{n=1}^{\infty} J_m(\gamma_{mn} \frac{\rho}{R})\{C_{mn} \cos m\psi + D_{mn} \sin m\psi\} \tag{A.10}$$

and the form of $Z(\rho, \psi, t)$ becomes

$$Z(\rho, \psi, t) = \sum_{m=0}^{\infty} \sum_{n=1}^{\infty} J_m(\gamma_{mn} \frac{\rho}{R})\{T^c_{mn}(t) \cos m\psi + T^s_{mn}(t) \sin m\psi\} \tag{A.11}$$

where

$$T^c_{mn}(t) = A_{mn} \cos \omega_{mn} t + B_{mn} \cos \omega_{mn} t \tag{A.12}$$

and

$$T^{s}_{mn}(t) = C_{mn}\cos\omega_{mn}t + D_{mn}\cos\omega_{mn}t \tag{A.13}$$

The coefficients A_{mn}, B_{mn} ,C_{mn} and D_{mn} are to be determined by apply the initial conditions and $\omega_{mn} = c\gamma_{mn}\frac{r}{R}$. Equation (A.11) represents the eigenfunction of the membrane, and the eigen frequencies ω_{nm} in Eq. (A.12) can be obtained by $\omega_{nm} = ck_{nm} = c\gamma_{mn}\frac{r}{R}$, where γ_{mn} can be obtained form the zeros of the Bessel function and table (A.1) shows some values for γ_{mn}.

Figure A.4 shows some different possible shape modes. And it is clear that there are angular

Table A.1: Some values for γ_{mn} which is zeros for Bessel function $J_m(\gamma_{nm})$.

n \ m	0	1	2	3	4
1	2.4048	3.8317	5.1356	6.3802	7.5883
2	5.5201	7.0156	8.4172	9.7610	11.0647
3	8.6537	10.1735	11.6198	13.0152	14.3725
4	11.7915	13.3237	14.7960	16.2235	17.6160

and redial nodes, where m refers to number of angular nodes and n refers to number of redial nodes.

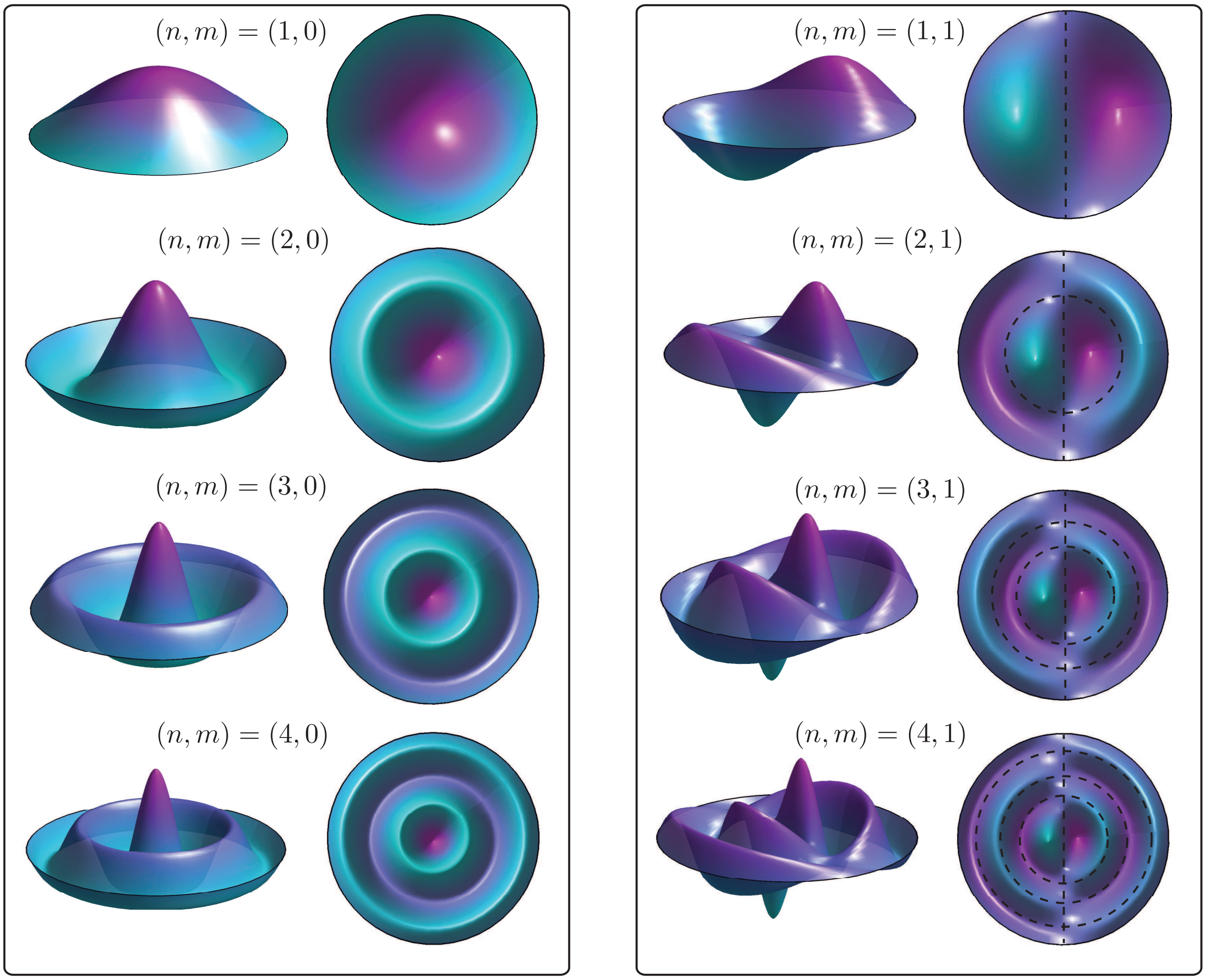

(a) (b)

Figure A.4: Fundamental modes of circular membrane with (a) First four redial nodes and no angular nodes (b) First four redial nodes and one angular nodes .

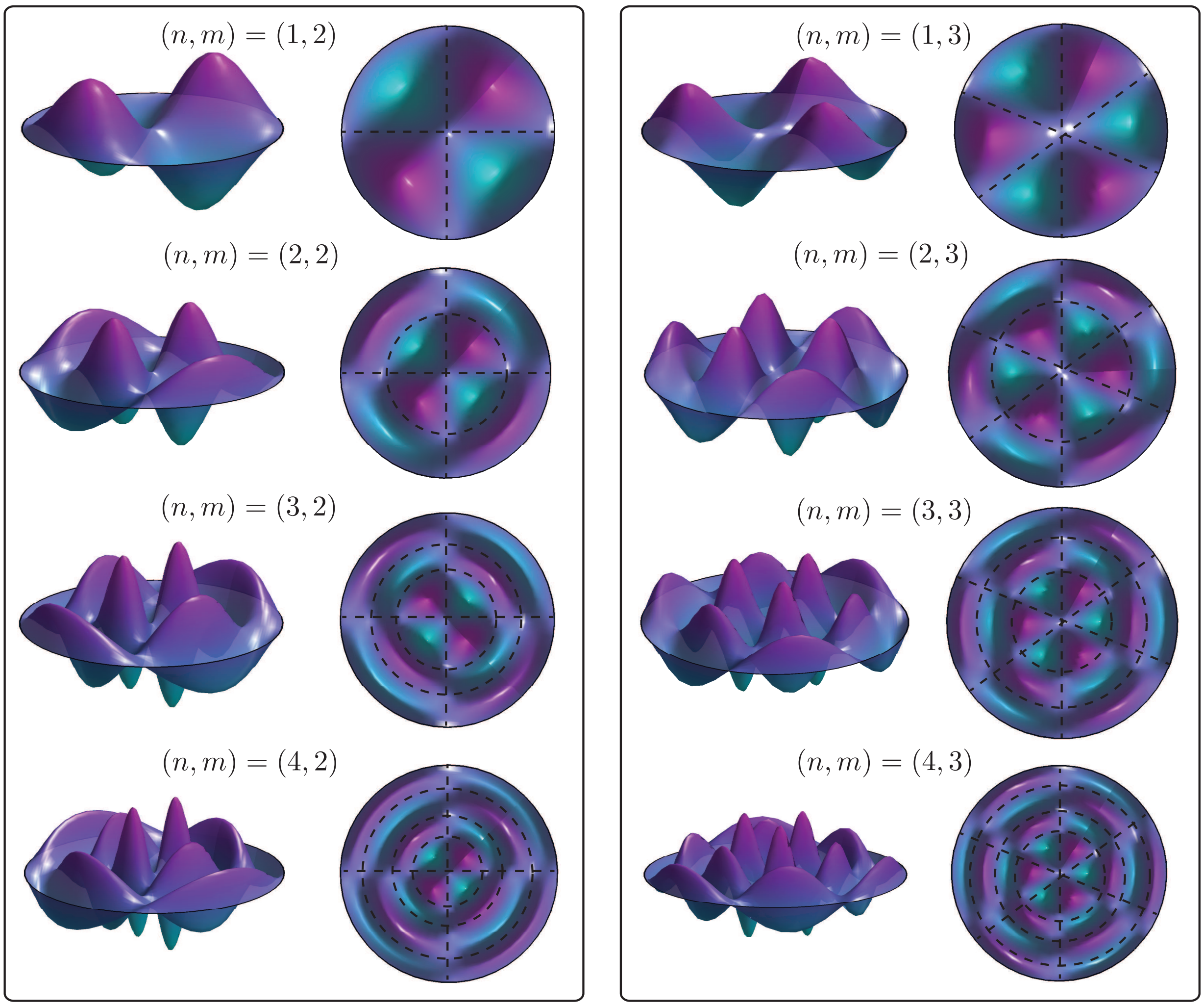

(a) (b)

Figure A.5: Fundamental modes of circular membrane with (a) First four redial nodes and two angular nodes (b) First four redial nodes and three angular nodes .

Appendix B

Change of Summation Indices

We have the following double summation

$$\sum_{m=0}^{\infty}\sum_{q=-\infty}^{\infty}\Big\{\beta_{2m}\,J_{m+q}(kR)+\gamma_{2m}\,Y_{m+q}(kR)\Big\}\,J_q(kd)\,\cos(m+q)\psi=0 \tag{B.1}$$

we define $n = m + q$, the

$$\sum_{m=0}^{\infty}\sum_{n=-\infty}^{\infty}\{\beta_{2m}\,J_n(kR)+\gamma_{2m}\,Y_n(kR)\}\,J_{n-m}(kd)\,\cos(n)\psi=0 \tag{B.2}$$

note that

$$\sum_{n=-\infty}^{\infty}H_n=\sum_{n=0}^{\infty}H_n+\sum_{n=-\infty}^{-1}H_n=\sum_{n=0}^{\infty}\epsilon_n(H_n+H_{-n}) \tag{B.3}$$

where ϵ_n is defined as

$$\epsilon_n = \begin{cases} 1/2 & \text{if } n = 0 \\ 1 & \text{if } n > 0 \end{cases}$$

using Eq. (B.5) in Eq. (B.2) leads to

$$\begin{aligned} &\sum_{m=0}^{\infty} \sum_{n=0}^{\infty} \{\beta_{2m} J_n(kR) + \gamma_{2m} Y_n(kR)\} J_{n-m}(kd) \cos(n)\psi \\ &+ \left\{\beta_{2m} J_{-n}(kR) + \gamma_{2m} Y_{-n}(kR)\right\} J_{-n-m}(kd) \cos(-n)\psi \end{aligned} \tag{B.4}$$

From the properties of Bessel functions, we have

$$J_{-\nu}(x) = (-1)^{\nu} J_{\nu}(x), \qquad Y_{-\nu}(x) = (-1)^{\nu} Y_{\nu}(x)$$

Then Eq. (B.1) finally becomes

$$\sum_{m=0}^{\infty} \sum_{n=0}^{\infty} \epsilon_n \{\beta_{2m} J_n(kR) + \gamma_{2m} Y_n(kR)\} \left\{J_{n-m}(kd) + (-1)^m J_{n+m}(kd)\right\} \cos n\psi = 0 \tag{B.5}$$

For the double summation with sine term, we can use the same procedure to prove that

$$\sum_{m=1}^{\infty} \sum_{q=-\infty}^{\infty} \left\{\beta_{1m} J_{m+q}(kR) + \gamma_{1m} Y_{m+q}(kR)\right\} J_q(kd) \sin(m+q)\psi = 0 \tag{B.6}$$

can be written as

$$\sum_{m=1}^{\infty} \sum_{n=1}^{\infty} \{\beta_{1m} J_n(kR) + \gamma_{1m} Y_n(kR)\} \left\{J_{n-m}(kd) - (-1)^m J_{n+m}(kd)\right\} \sin n\psi = 0 \tag{B.7}$$

Appendix C

Energy of Circular Membrane

The total energy of the membrane in Cartesian coordinates is obtained as [82]

$$E = \iint\limits_{A} \left\{ \frac{\mu}{2} \left(\frac{\partial Z(x,y,t)}{\partial t} \right)^2 + \frac{T}{2} \left(\frac{\partial Z(x,y,t)}{\partial x} \right)^2 + \frac{T}{2} \left(\frac{\partial Z(x,y,t)}{\partial y} \right)^2 \right\} dx\, dy \qquad \text{(C.1)}$$

We have

$$\begin{aligned} \frac{\partial z}{\partial x} &= \frac{\partial z}{\partial r}\,\frac{\partial r}{\partial x} + \frac{\partial z}{\partial \theta}\,\frac{\partial \theta}{\partial x} = \frac{\partial z}{\partial r}\,\cos\theta - \frac{\partial z}{\partial \theta}\,\frac{\sin\theta}{r} \\ \frac{\partial z}{\partial y} &= \frac{\partial z}{\partial r}\,\frac{\partial r}{\partial y} + \frac{\partial z}{\partial \theta}\,\frac{\partial \theta}{\partial y} = \frac{\partial z}{\partial r}\,\sin\theta + \frac{\partial z}{\partial \theta}\,\frac{\cos\theta}{r} \end{aligned} \qquad \text{(C.2)}$$

where $r = \sqrt{x^2 + y^2}$ and

$$\frac{\partial r}{\partial x} = \cos x, \qquad \frac{\partial r}{\partial y} = \cos y, \qquad \frac{\partial \theta}{\partial x} = -\frac{\sin\theta}{r}, \qquad \frac{\partial \theta}{\partial y} = \frac{\cos\theta}{r}$$

By squaring the equations in Eq. (C.1), we get

$$
\begin{aligned}
\left(\frac{\partial z}{\partial x}\right)^2 &= \left(\frac{\partial z}{\partial r}\right)^2 \cos^2\theta - \frac{1}{r}\frac{\partial z}{\partial r}\frac{\partial z}{\partial \theta}\cos\theta\sin\theta + \left(\frac{\partial z}{\partial \theta}\right)^2 \frac{\sin^2\theta}{r^2} \\
\left(\frac{\partial z}{\partial y}\right)^2 &= \left(\frac{\partial z}{\partial r}\right)^2 \sin^2\theta + \frac{1}{r}\frac{\partial z}{\partial r}\frac{\partial z}{\partial \theta}\cos\theta\sin\theta + \left(\frac{\partial z}{\partial \theta}\right)^2 \frac{\cos^2\theta}{r^2}
\end{aligned}
\tag{C.3}
$$

By adding the equations in Eq. (C.3) we get

$$
\left(\frac{\partial z}{\partial x}\right)^2 + \left(\frac{\partial z}{\partial y}\right)^2 = \left(\frac{\partial z}{\partial r}\right)^2 + \frac{1}{r^2}\left(\frac{\partial z}{\partial \theta}\right)^2
$$

Note that $dx\,dy = r\,dr\,d\theta$, then the energy expression in Eq.(C.1) becomes

$$
\begin{aligned}
E &= \frac{\mu}{2}\iint\limits_A \left(\frac{\partial Z(r,\theta,t)}{\partial t}\right)^2 r\,dr\,d\theta \\
&+ \frac{T}{2}\iint\limits_A \left\{\left(\frac{\partial Z(r,\theta,t)}{\partial r}\right)^2 + \frac{1}{r^2}\left(\frac{\partial Z(r,\theta,t)}{\partial \theta}\right)^2\right\} r\,dr\,d\theta
\end{aligned}
\tag{C.4}
$$

BIBLIOGRAPHY

BIBLIOGRAPHY

[1] H. Yee and N. Audeh, “Cutoff frequencies of eccentric waveguides,” *IEEE Transactions on Microwave Theory and Techniques*, vol. 14, no. 10, pp. 487 – 493, 1966.

[2] N. K., “Vibration of a membrane having a circular outer boundary and an eccentric circular inner boundary,” *Journal of Sound and Vibration*, vol. 50, no. 4, pp. 545 – 551, 1977.

[3] V. A. S. G. P. Singh, G. S. and L. S. Kothari, “Comments on free transverse vibrations of uniform circular plates and membranes with eccentric holes,” *Journal of Sound and Vibration*, vol. 100, no. 1, pp. 141–145, 1985.

[4] “The spartan 207 inflatable antenna http://www.nasaimages.org/.”

[5] C. Citrini, “The energy theorem in the impact of a string vibrating against a pointshaped obstacle,” *Atti Accad. Naz. Lincei Rend.*, vol. 59, pp. 143–148, 1977.

[6] L. Amerio, “Continuous solutions of the problem of a string vibrating against an obstacle,” *Rendiconti del Seminario Mathematico della Universita di Padova*, vol. 59, no. , pp. 67–96, 1978.

[7] Michelle and Schatzman, “A hyperbolic problem of second order with unilateral constraints: The vibrating string with a concave obstacle,” *Journal of Mathematical Analysis and Applications*, vol. 73, no. 1, pp. 138 – 191, 1980.

[8] A. Haraux and H. Cabannes, “Almost periodic motion of a string vibrating against a straight fixed obstacle,” *Nonlinear Analysis, Theory, Methods and Applications*, vol. 7, no. 2, pp. 129–141, 1983.

[9] R. Burridge, J. Kappraff, and C. Morshedi, “The sitar string, a vibrating string with a one-sided inelastic constraint,” *SIAM Journal on Applied Mathematics*, vol. 42, no. 6, pp. 1231–1251, 1982.

[10] A. Bamberger and M. Schatzman, “New results on the vibrating string with a continuous obstacle,” *SIAM Journal of Mathematical Analysis*, vol. 14, no. 3, pp. 560–595, 1983.

[11] J. Ahn, “A vibrating string with frictionless dynamic impact,” *Applied Numerical Mathematics*, vol. 57, pp. 861–884, 2007.

[12] M. Frontini and L. Gotusso, “Numerical study of the motion of a string vibrating against an obstacle by physical discretization,” *Applied Mathematical Modeling*, vol. 14, pp. 489–494, 1990.

[13] A. Krishnaswamy and J. Smith, “Methods for simulating string collisions with rigid spatial obstacles,” in *IEEE Workshop on Applications of Signal Processing to Audio and Acoustics*, pp. 233 – 236, 2003.

[14] S. M. Han and M. A. Grosenbaugh, “Nonlinear free vibration of a cable against a straight obstacle,” *Journal of Sound and Vibration*, vol. 273, pp. 337–361, 2004.

[15] D. N. Dutt and B. S. Ramakrishna, “Vibration control of stretched strings by an external distributed force,” *Journal of Sound and Vibration*, vol. 57, no. 4, pp. 603–606, 1978.

[16] D. N. Dutt and B. S. Ramakrishna, “Application of optimization methods to vibration control of stretched strings,” *Journal of Sound and Vibration*, vol. 57, no. 4, pp. 499–514, 1978.

[17] J. Issa, R. Mukherjee, A. R. Diaz, and S. W. Shaw, “Modal disparity and its experimental verification,” *Journal of Sound and Vibration*, vol. 311, no. 35, pp. 1465 – 1475, 2008.

[18] J. Issa, R. Mukherjee, and A. R. Diaz, “Energy dissipation in dynamical systems through sequential application and removal of constraints,” *Journal of Dynamic Systems, Measurement, and Control*, vol. 131, no. 2, p. 021011, 2009.

[19] P. Hbrard and A. Henrott, “Optimal shape and position of the actuators for the stabilization of a string,” *Systems and Control Letters*, vol. 48, no. 34, pp. 199 – 209, 2003.

[20] A. D. Myshkis, “Vibrations of the string with energy dissipation and impulsive feedback support,” *Nonlinear Analysis*, vol. 26, no. 7, pp. 1271 – 1278, 1996.

[21] W. D. Zhu and N. A. Zheng, "Exact response of a translating string with arbitrarily varying length under general excitation," *Applied Mathematics and Computation*, vol. 75, no. 3, 2008.

[22] S. Shahruz and D. Kurmaji, "Vibration suppression of a nonlinear axially moving string by boundary control," *Journal of Sound and Vibration*, vol. 201, no. 1, pp. 145 – 152, 1997.

[23] R.-F. Fung, J.-W. Wu, and S.-L. Wu, "Exponential stabilization of an axially moving string by linear boundary feedback," *Automatica*, vol. 35, no. 1, pp. 177 – 181, 1999.

[24] T. cheng Li, Z. chao Hou, and J. feng Li, "Stabilization analysis of a generalized nonlinear axially moving string by boundary velocity feedback," *Automatica*, vol. 44, no. 2, pp. 498 – 503, 2008.

[25] K. Do and J. Pan, "Boundary control of transverse motion of marine risers with actuator dynamics," *Journal of Sound and Vibration*, vol. 318, no. 45, pp. 768 – 791, 2008.

[26] H. K. Khalil, *Nonlinear Systems, 3rd Ed.* Prentice Hall, New York, NY., 2002.

[27] F. ZHANG, D. DAWSON, S. NAGARKATTI, and C. RAHN, "Boundary control for a general class of non-linear string-actuator systems," *Journal of Sound and Vibration*, vol. 229, no. 1, pp. 113 – 132, 2000.

[28] J. Lu, M. Crocker, and P. Raju, "Active vibration control using wave control concepts," *Journal of Sound and Vibration*, vol. 134, no. 2, pp. 364 – 368, 1989.

[29] A. D. Myshkis, "Active wave control of string near fixed boundary," *ASME Journal of Vibration and Acoustics*, vol. 130, no. 1, 2008.

[30] C. TAN and S. YING, "Active wave control of the axially moving string: Theory and experiment," *Journal of Sound and Vibration*, vol. 236, no. 5, pp. 861 – 880, 2000.

[31] W. Zhang and L.-Q. Chen, "Vibration control of an axially moving string system: Wave cancellation method," *Applied Mathematics and Computation*, vol. 175, no. 1, pp. 851 – 863, 2006.

[32] N. Tanaka and Y. Kikushima, "Active wave control of a flexible beam fundamental characteristics of an active-sink system and its verification," *Journal of Sound and Vibration*, vol. 35, no. 2, pp. 499–514, 1992.

[33] C. Baicu, C. Rahn, and B. Nibali, "Active boundary control of elastic cables: Theory and experiment," *Journal of Sound and Vibration*, vol. 198, no. 1, pp. 17 – 26, 1996.

[34] M. Sosa, A. Carneiro, J. Colafemina, and O. Baffa, "A new magnetic probe to study the vibration of the tympanic membrane," *Journal of Magnetism and Magnetic Materials*, vol. 226230, no. 2, pp. 2067 – 2069, 2001.

[35] E. J. Ruggiero and D. J. Inman, "Modeling and vibration control of an active membrane mirror," *Smart Materials and Structures*, vol. 18, p. 095027, 2009.

[36] K. Miyano, "Surface tension measured by vibrating membranes: An application to smectic-a and -b phases," *Phys. Rev. A*, vol. 26, pp. 1820–1823, 1982.

[37] G. Percin, T. S. Lundgren, and B. T. Khuri-Yakub, "Controlled ink-jet printing and deposition of organic polymers and solid particles," *Applied Physics Letters*, vol. 73, pp. 2375–2378, 1998.

[38] H. Y. Yee and N. F. Audeh, "Uniform waveguides with arbitrary cross sections considered by the point-matching method," *Institute of Electrical and Electronic Engineers Transactions MTT13*, pp. 847–851, 1965.

[39] J. Davies and C. Muilwyk, "Numerical solution of uniform hollow waveguides with boundaries of arbitrary shape," *Proceedings of the Institution of Electrical Engineers*, vol. 113, no. 2, pp. 277 –284, 1966.

[40] C. W and Steele, "Numerical computation of electric and magnetic fields in a uniform waveguide of arbitrary cross section," *Journal of Computational Physics*, vol. 3, no. 1, pp. 148 – 153, 1968.

[41] P. Arlett, A. Bahrani, and O. Zienkiewicz, "Application of finite elements to the solution of helmholtz's equation," *Proceedings of the Institution of Electrical Engineers*, vol. 115, no. 12, pp. 1762 –1766, 1968.

[42] N. Gass, "Solution of the three dimensional scalar helmholtz equation by a finite element formulation," *ZAMM - Journal of Applied Mathematics and Mechanics / Zeitschrift fr Angewandte Mathematik und Mechanik*, vol. 57, no. 2, pp. 95–99, 1977.

[43] P. Laura, "A simple method for the determination of cutoff frequencies of waveguides with arbitrary cross sections," *Proceedings of the IEEE*, vol. 54, no. 10, pp. 1495 – 1497, 1966.

[44] M.J. and Hine, "Eigenvalues for a uniform fluid waveguide with an eccentric-annulus cross-section," *Journal of Sound and Vibration*, vol. 15, no. 3, pp. 295 – 305, 1971.

[45] R. Bulley and B. Davies, "Computation of approximate polynomial solutions to te modes in an arbitrarily shaped waveguide," *IEEE Transactions on Microwave Theory and Techniques*, vol. 17, no. 8, pp. 440 – 446, 1969.

[46] L. W.H., "Free transverse vibrations of uniform circular plates and membranes with eccentric holes," *Journal of Sound and Vibration*, vol. 81, no. 3, pp. 425 – 435, 1982.

[47] G. S. Singh and L. S. Kothari, "On the solution of the two-dimensional helmholtz equation," *Journal of Mathematical Physics*, vol. 25, no. 3, pp. 810–811, 1984.

[48] K. Nagaya and Y. Hai, "Free vibration of composite membranes with arbitrary shape," *Journal of Sound and Vibration*, vol. 100, no. 1, pp. 123 – 134, 1985.

[49] S. Noga, "Free transverse vibration analysis of an elastically connected annular and circular double-membrane compound system," *Journal of Sound and Vibration*, vol. 329, no. 9, pp. 1507 – 1522, 2010.

[50] A. Arokiasamy, "Simulation of vibrations of rectangular and square membranes using computer graphics," *Simulation Modelling Practice and Theory*, vol. 10, no. 12, pp. 3 – 12, 2002.

[51] E. Alvarado-Anell, M. Sosa, and M. A. Moreles, "Computational study of forced oscillations in a membrane," *REVISTA MEXICANA DE FISICA*, vol. 51, no. 2, pp. 102–107, 2005.

[52] E. Alvarado-Anell, M. Sosa, and M. A. Moreles, "Numerical simulation of the dynamical properties of the human tympanum," *REVISTA MEXICANA DE FISICA*, vol. 54, no. 2, pp. 135–140, 2008.

[53] A. BHIDE, "Computer simulation of human tympanic membrane," *The Journal of Laryngology and Otology*, vol. 106, pp. 878–881, 1992.

[54] P. A. A. Laura and R. H. Gutierrez, "Determination of the fundamental eigenvalue of a rhombic membrane with a concentric circular hole," *Journal of Sound and Vibration*, vol. 153, no. 1, pp. 176–179, 1992.

[55] L. H. Wu and C. Y. Wang, "Fundamental frequencies of a circular membrane with a centered strip," *Journal of Sound and Vibration*, vol. 239, no. 2, pp. 363–368, 2001.

[56] S. W. Kang and J. M. Lee, "Free vibration analysis of composite rectangular membranes with an oblique interface," *Journal of Sound and Vibration*, vol. 251, no. 3, pp. 505–517, 2002.

[57] J. Chen, S. Kao, W. Lee, and Y. Lee, "Eigensolutions of the helmholtz equation for a multiply connected domain with circular boundaries using the multipole trefftz method," *Engineering Analysis with Boundary Elements*, vol. 34, no. 5, pp. 463 – 470, 2010.

[58] V. H. Cortinez and P. A. A. Laura, "Vibrations of non-homogeneous rectangular membranes," *Journal of Sound and Vibration*, vol. 156, no. 2, pp. 217–225, 1992.

[59] F. F. Cap, "Eigenfrequencies of membranes of arbitrary boundary and with varying surface mass density," *Applied Mathematics and Computation*, vol. 124, pp. 319–329, 2001.

[60] C. Zhao and G. P. Stevens, "A practical error estimator for finite element predicted natural frequencies of membrane vibration problems," *Journal of Sound and Vibration*, vol. 195, no. 5, pp. 739–756, 1996.

[61] I. P. A. R. Stanford, B. and W. Shyy, "Fixed membrane wings for micro air vehicles: Experimental characterization, numerical modeling, and tailoring," *Progress in Aerospace Sciences*, vol. 44, pp. 258–294, 2008.

[62] T. X. I. E. G. R. B. K. S. S. Song, A. and B. K., "Aeromechanics of membrane wings with implications for animal flight," *AIAA Journal*, vol. 46, no. 8, 2008.

[63] G. M. S. W. Z. Rojratsirikul, P. and I. Gursul, "Flow-induced vibrations of low aspect ratio rectangular membrane wings," *Journal of Fluids and Structures*, vol. 27, no. 8, pp. 1296–1309, 2011.

[64] D. A. Wang and H. H. Ko, "Piezoelectric energy harvesting from flow-induced vibration," *Journal of Micromechanics and Microengineering*, vol. 20, no. 2, 2010.

[65] J. J. Allen and A. J. Smits, "Energy harvesting eel," *Journal of Fluids and Structures*, vol. 15, no. 3, pp. 629–640, 2011.

[66] Q. Wang, "Wave propagation in a piezoelectric coupled cylindrical membrane shell," *International Journal of Solids and Structures*, vol. 38, no. 4647, pp. 8207 – 8218, 2001.

[67] C. H. Jenkins and U. A. Korde, "Membrane vibration experiments: An historical review and recent results," *Journal of Sound and Vibration*, vol. 295, no. 35, pp. 602 – 613, 2006.

[68] R. P. Grosso and M. Yellin, "The membrane mirror as an adaptive optical element," *The Optical Society of America*, vol. 67, no. 3, pp. 399–406, 1977.

[69] I. Jo, "On the optimal control of circular membranes," *Acta Mathematica Hungarica*, vol. 58, pp. 365–376, 1991.

[70] I. Jo, "On the control of a rectangular membrane," *Acta Mathematica Hungarica*, vol. 59, pp. 25–32, 1992.

[71] D. M. James, B. G. Patrick, S. Chodimella, D. Marker, and B. deBlonk, "Design and testing of a one-meter membrane mirror with active boundary control," vol. 5899, p. 58990Z, SPIE, 2005.

[72] M. V. Aguanno, F. Lakestani, M. P. Whelan, and M. J. Connelly, "Heterodyne speckle interferometer for full-field velocity profile measurements of a vibrating membrane by electronic scanning," *Optics and Lasers in Engineering*, vol. 45, no. 6, pp. 677 – 683, 2007.

[73] S. Tliba, "Control of a vibrating axisymmetric membrane using piezoelectric tranducers," vol. 18, 2011.

[74] J. M. E. Tarazaga, P. A. and D. J. Inman, "Vibro-acoustics of a pressurized optical membrane," *Mechanical Systems and Signal Processing*, vol. 30, pp. 373–392, 2012.

[75] E. Kreyzig, *Advanced Engineering Mathematics 9th Ed.* John Wiley and Sons, Hoboken, NJ, 1993.

[76] L. Meirovitch, *Elements of Vibration Analysis.* McGraw Hill, New York, NY.

[77] E. Kashy, D. A. Johnson, J. McIntyre, and S. L. Wolfe, "Transverse standing waves in a string with free ends," *American Journal of Physics*, vol. 65, no. 4, pp. 310–313, 1997.

[78] A. W. Leissa and M. S. Qatu, *Vibration of Continuous Systems, 1st Edition.* Mc-Graw Hill Professional, 2011.

[79] "http://www.drtempleman.com/spring-guides.htm."

[80] G. N. Watson, *A Treatise on the Theory of Bessel Functions.* Cambridge University Press, 1958.

[81] I. J. Oppenheim and W. O. Williams, "Vibration of an elastic tensegrity structure," *European Journal of Mechanics - A/Solids*, vol. 20, no. 6, pp. 1023 – 1031, 2001.

[82] L. N. Virgin, *Vibration of Axially Loaded Structures.* Cambridge University Press, 2007.